

Reconstruction and Visualization
of Neuronal Pathways
from Diffusion Tensor Data

Rekonstruktion und Visualisierung
neuroner Bahnen aus Diffusionstensor-Daten

Der Technischen Fakultät der
Universität Erlangen–Nürnberg
zur Erlangung des Grades

DOKTOR–INGENIEUR

vorgelegt von

Dipl.–Inf. Dorit Merhof

Erlangen — 2007

Als Dissertation genehmigt von
der Technischen Fakultät
der Universität Erlangen–Nürnberg

Tag der Einreichung:	29.06.2007
Tag der Promotion:	08.10.2007
Dekan:	Prof. Dr.–Ing. J. Huber
Berichterstatter:	Prof. Dr. G. Greiner Prof. Dr.–Ing. B. Preim

Revision 1.0
©2007, Copyright Dorit Merhof
All Rights Reserved
Alle Rechte vorbehalten

Abstract

For diagnosis and surgical planning, magnetic resonance imaging (MRI) has become an important source of medical data. About a decade ago, a novel MRI technique called diffusion tensor imaging (DTI) evolved. Due to its ability to reflect the location and structure of fibrous tissue such as white matter *in vivo*, this technique has gained increasing interest in different research disciplines.

For neurosurgery, DTI data is of high value since information about the location and the course of white matter tract systems is provided, thus supporting the anatomical information obtained from MRI. White matter tracts, i.e. motor or sensory pathways, are important structures within the human brain. In order to avoid neurological deficits after brain surgery, these fiber tracts must remain intact.

However, the reconstruction of neuronal structures from DTI data is a non-trivial task due to the complex tensor information that is captured per voxel. For this reason, extensive research has been conducted in recent years in order to develop techniques for the processing and visualization of DTI tensor data.

This work contributes to current research and introduces new techniques for the reconstruction and visualization of white matter tracts. The different approaches were developed in collaboration with neurosurgeons and are intended to support preoperative planning and intraoperative guidance in surgical interventions. For this purpose, a DTI toolbox comprising dataset processing, tensor reconstruction, filtering techniques, fiber tracking and connectivity analysis, hull algorithms and different visualization approaches has been developed.

In the future, the research currently conducted in the field of DTI will contribute to the further improvement of planning in neurosurgery and to the reduction of the inherent risk of postoperative neurological deficits for the patients.

Contents

Abstract	i
Contents	iii
List of Figures	vii
List of Tables	ix
List of Code Examples	xi
Acknowledgements	xiii
I Introduction	1
1 Background and overview	3
1.1 Motivation	3
1.2 Contribution	4
1.3 Overview	6
2 Neurosurgery: History, disease patterns, and operative procedures	9
2.1 History of neurosurgery	9
2.2 Disease patterns treated in neurosurgery	10
2.3 Neurosurgical procedures	11
2.3.1 Clinical setup in the operating room	11
2.3.2 Navigation in image-guided neurosurgery	12
2.4 Neuroanatomy	14
2.5 Imaging techniques applied in neurosurgery	16
2.5.1 Physical background	16
2.5.2 Magnetic resonance imaging (MRI)	18
2.5.3 Functional magnetic resonance imaging (fMRI)	19

2.5.4	Diffusion tensor imaging (DTI)	20
2.5.5	Imaging parameters and image data	20
II	Reconstruction of neuronal structures	23
3	Tensor reconstruction and processing	25
3.1	The Stejskal-Tanner equation	25
3.2	Diffusion tensor reconstruction	26
3.3	Quantifying tensor shape	27
3.3.1	Tensor eigensystem	27
3.3.2	Diffusion ellipsoids	28
3.3.3	Scalar metrics	28
3.4	Tensor interpolation	30
3.5	Tensor filtering	31
3.5.1	Gaussian filter	32
3.5.2	Two-class Gaussian weighting	33
3.5.3	Best-neighbor filter	34
3.5.4	Results	35
3.6	Discussion	36
4	Fiber tracking	39
4.1	Basics about tracking algorithms	39
4.1.1	Streamline propagation and tensor deflection	40
4.1.2	Tract-selection techniques	44
4.2	Local regularization filters	45
4.2.1	Local filter window	46
4.2.2	Gaussian local regularization filter	46
4.2.3	Moving least-squares filter	47
4.2.4	Results	48
4.3	Fiber tracking using evenly spaced streamlines	50
4.3.1	Standard approach for evenly spaced streamlines	51
4.3.2	Adaptive control of the separating distance	53
4.3.3	ROI based tracking using evenly spaced streamlines	55
4.4	Directional Volume Growing	56
4.4.1	Algorithm for directional volume growing	56
4.4.2	Results	57
4.5	Discussion	59
5	Connectivity analysis between functional regions	63
5.1	Previous work	63
5.2	Connectivity analysis based on pathfinding	64
5.2.1	A* algorithm	64

5.2.2	Domain restriction	67
5.2.3	Grid for partitioning the search space	67
5.2.4	Cost function	68
5.2.5	Minimum cost path	70
5.2.6	Multiple start and goal voxels	70
5.2.7	Heuristic	70
5.2.8	Efficient implementation	71
5.3	Results	72
5.3.1	Quality analysis	72
5.3.2	Computing time	73
5.4	Discussion	75
6	Generation of hulls	77
6.1	Tetrahedralization and 3D Alpha Shapes	78
6.1.1	3D Delaunay Tetrahedralization	78
6.1.2	3D Alpha Shapes	79
6.1.3	Results	80
6.2	Isosurfaces	81
6.2.1	Rasterization	81
6.2.2	Volume filtering	82
6.2.3	Surface Extraction	82
6.2.4	Surface filtering	83
6.2.5	Results	85
6.3	Construction of a safety margin	88
6.4	Discussion	90
7	Distortion correction	93
7.1	Distortion artifacts of DTI-EPI data	93
7.2	Previous work	94
7.3	Non-linear registration	95
7.3.1	Similarity measure	95
7.3.2	Optimization	96
7.3.3	3D free-form deformation	96
7.3.4	Registration framework	98
7.4	Experimental setup	98
7.5	Results	100
7.6	Discussion	103
III	Visualization	107
8	Visualization of fibers	109
8.1	Color transfer functions	109

8.2	Visualization based on lines	111
8.2.1	Illuminated streamlines	111
8.2.2	Adaptive transparency	115
8.3	Visualization based on triangle strips and point sprites	116
8.3.1	Previous work	117
8.3.2	Hybrid visualization approach	117
8.3.3	Results	123
8.4	Discussion	125
9	Visualization of hulls	127
9.1	Lighting	127
9.2	Transparency	128
10	Multimodal visualization of DTI- and MR-Data	129
10.1	Multimodal visualization based on direct volume rendering	129
10.1.1	Tagged volumes	130
10.1.2	Volume clipping	130
10.1.3	Fusion	131
10.2	Results	132
10.3	Discussion	132
IV	Conclusion	135
11	Summary	137
12	Outlook	141
	Bibliography	143

List of Figures

2.1	Neurosurgical procedure	11
2.2	Setup of neuronavigation system	13
2.3	Spin orientation in magnetic field	14
2.4	Spin orientation in magnetic field	15
2.5	Spin orientation in magnetic field	17
2.6	Net magnetization and RF pulse	18
2.7	Relaxation processes	19
3.1	Diffusion ellipsoid	28
3.2	Barycentric space coordinates of diffusion tensor	30
3.3	Gaussian smoothing	32
3.4	Two-class Gaussian weighting filter	34
3.5	Best-neighbor filter	35
4.1	Schematic outline of fiber tracking	42
4.2	Schematic outline of tensor deflection	43
4.3	Boolean operators for tract selection	45
4.4	Local filter window	46
4.5	Pyramidal tract reconstructed with oriented filters	49
4.6	Comparison of integration schemes and local filters	50
4.7	Fiber tracking based on evenly spaced streamlines	53
4.8	Adaptive distance control for tracking using evenly spaced streamlines	54
4.9	ROI based tracking using evenly spaced streamlines	55
4.10	Conventional volume growing	58
4.11	Reconstructed pyramidal tract based on directional volume growing	59
5.1	Schematic outline of the A* algorithm	66
5.2	Expansion of search space	68
5.3	Tensor probability profiles	69
5.4	Pathfinding vs. fiber tracking in tumor patients	74
6.1	View through OR microscope	77
6.2	Hulls based on 3D Delaunay tetrahedralization	79
6.3	Hulls based on 3D tetrahedralization and comparison with fiber tracking	80

6.4	Effect of 3D Gaussian volume filtering	82
6.5	Initial iso-surface resulting from Marching Cubes	83
6.6	Surface filtering with scale-dependent Laplace filter	84
6.7	Hull for the arcuate fasciculus in a brain-tumor patient	85
6.8	Hulls for pyramidal tract and corpus callosum in brain-tumor patient . . .	86
6.9	Hulls for the pyramidal tract in four patients	87
6.10	Expanded hulls for optic and pyramidal tract	89
7.1	DTI distortions in a patient dataset	99
7.2	Measurement of displacement after non-linear registration	100
7.3	Distortion measurement results in a patient dataset	101
7.4	Measured distortions, averaged for population of 14 patients	102
8.1	Color transfer functions for fiber visualization	110
8.2	Definition of the normal vector for illuminated streamlines	112
8.3	Tracking of the whole brain visualized with illuminated streamlines . . .	114
8.4	Streamlines visualized with adaptive transparency	116
8.5	Construction of a triangle strip	118
8.6	Illumination of triangle strip simulated using 1D texture	119
8.7	Usage of RGB-texture to draw and illuminate point sprite	120
8.8	Usage of RGB-texture to draw and illuminate point sprite	121
8.9	Visualization of fiber tracts using point sprites	122
8.10	Profile of a tube depending on viewing direction	122
8.11	Flipping triangles for a segment in viewing direction	123
8.12	Terminating textured quads	123
8.13	Fiber tracking rendered with hybrid approach	125
9.1	Illumination of hulls	127
9.2	Semi-transparent visualization of hulls	128
10.1	Direct volume rendering with tagged volumes	130
10.2	Direct volume rendering with volume clipping	131

List of Tables

2.1	Image data parameters	21
2.2	DTI gradient directions	21
3.1	Computing times for global filtering	36
4.1	Accuracy and computing time for oriented filters	49
5.1	Complexity of different data structures	71
5.2	Evaluation connectivity analysis	73
5.3	Performance and expansion of search grid for connectivity analysis	74
6.1	Evaluation of distance between fiber tract and hull surface	88
7.1	Summarized susceptibility distortions for 14 patient datasets	103
8.1	Frame rates for illuminated lines	114
8.2	Frame rates for hybrid visualization approach	124
10.1	Frame rates for multimodal visualization	132

List of Code Examples

4.1	Pseudocode for fiber tracking.	41
5.1	Pseudocode for A* algorithm.	65

Acknowledgements

First of all, I would like to express my gratitude to my supervisor Prof. Günther Greiner for supporting and encouraging my work. I greatly appreciated his kind advice as well as the freedom I was given to develop my own ideas. His profound scientific knowledge, his cooperation and his friendly and cordial relationship have made an invaluable contribution to the success of this thesis - thank you very much!

Furthermore, I am very grateful to Prof. Bernhard Preim from the Otto-von-Guericke-University, Magdeburg, who kindly agreed to review this thesis. The wide variety of working areas covered by his institute and his fair and motivating attitude make him an exceptional person in medical research.

Additionally, I would like to thank PD Dr.-Ing. Peter Hastreiter, PD Dr. med. Christopher Nimsy, Prof. Marc Stamminger, Prof. Rudolf Fahlbusch and Prof. Michael Buchfelder for initiating the C9 project, SFB 603. It has been very interesting to work for this project due to the motivating medical background and the wide variety of different aspects and working areas.

PD Dr. med. Christopher Nimsy deserves my special gratitude for providing valuable ideas as well as suggestions for improvements from the medical point of view. I am also very grateful to PD Dr. med. Oliver Ganslandt and Dr. hum. biol. Peter Grummich for sharing with me their deep understanding of brain function, and also to Dr. med. Thilo Hammen for answering my questions about brain anatomy. Dr. techn. Andreas Stadlbauer was a valuable source of information on MR physics and imaging sequences, and Stefanie Kreckel deserves my gratitude for MR data acquisition. I am also very grateful to Markus Friebe, Chair of Multimedia Communications and Signal Processing, who kindly provided suggestions for filtering the diffusion tensor data. Furthermore, I am much obliged to Betsy Nießner for proofreading this thesis.

Last but not least, I thank all my colleagues at the Chair of Computer Graphics. It has really been a pleasure to work in such a team! Especially my former colleagues Dr.-Ing. Grzegorz Soza and Fernando Vega took part in many fruitful discussions and contributed to the success of this work. Additionally, I am very grateful to my Diploma and Master students Ezgi Bingöl, Laura Cojocar, Florian Eckert, Mirco Richter and Markus Sonntag for their interest in this research area and for the good relationship.

Finally, I would like to express my deep love and gratitude to my family and my fiancé Markus Lindner for supporting and motivating me throughout my work.

Dorit Merhof

Part I
Introduction

Chapter 1

Background and overview

1.1 Motivation

The medical imaging techniques available today are a powerful tool for understanding basic anatomical and physiological relationships and for accurate and reproducible diagnosis. For this reason, modern imaging and image processing techniques provide important support for a wide variety of clinical applications. Magnetic resonance imaging (MRI) is a non-invasive imaging technique preferably applied for organs and tissue, resulting in scalar-valued slice images. For diagnosis and planning in surgery as well as for navigation applications, MRI is a valuable source of information. For the processing and visualization of MRI data, a wide variety of techniques including 3D visualization and segmentation approaches have been developed.

Within the last decade, a further MRI technique denoted as *diffusion tensor imaging (DTI)* has been established. DTI measures diffusion of water, which originates from the random motion of molecules due to thermal energy. In fibrous tissue such as the white matter¹ of the nervous system, diffusion is restricted to a preferred direction. From the diffusion measurements, it is possible to draw conclusions about the underlying tissue structure. This makes it possible to analyze brain function and structure *in vivo*, which is of interest for different areas in research and medical application. The diffusion characteristics measured with DTI support the diagnosis of acute ischemic stroke, degenerative diseases such as Alzheimer's disease or psychiatric disorders such as schizophrenia. In neuroanatomy and neurosurgery, the DTI measurements serve as a basis for the reconstruction of white matter structures.

However, the processing and visualization of DTI data is a non-trivial task due to the complexity of the acquired data. Instead of a scalar value, a whole diffusion tensor is available per voxel which describes the local diffusion properties. The challenges of reconstructing and visualizing white matter tracts based on DTI data comprise the design of meaningful scalar metrics, adequate reconstruction algorithms, as well as compre-

¹White matter contains nerve fibers (axons) which are responsible for information transmission. The axons are surrounded by myelin, which has a whitish appearance.

hensive visualization techniques.

In this work, reconstruction and visualization techniques based on DTI data are presented, which are adapted to the requirements of neurosurgery. For diagnosis and planning in neurosurgery, DTI possesses a high degree of potential for the prevention of injury to white matter tracts during surgery, thus avoiding postoperative neurological deficits. For this reason, pioneering clinics have discovered the benefit of DTI data and started to use reconstructed tract systems for preoperative planning as well as for intraoperative visualization in combination with a neuronavigation system.

The goal of this work was to find an improved method of combining the contradictory aims of neurosurgery, which are full tumor resection on the one hand, as well as preservation of function on the other. For this purpose, novel reconstruction and visualization techniques are presented which assist the neurosurgeon during preoperative planning as well as intraoperatively.

1.2 Contribution

The main contributions of this work comprise different techniques for reconstructing and visualizing white matter structures for clinical application. The research results have been partly published in conference proceedings and journals [79-95]. In particular, the following contributions are presented and discussed in this work:

(1) RECONSTRUCTION – TENSOR FILTERING

In spite of imaging protocols where several measurements are averaged, the diffusion tensor data still suffers from imaging noise. In order to alleviate noise, filters known from video processing were applied. Since a video sequence and a sequence of slice images share some equivalence, the benefits of video filters were exploited for smoothing of DTI data.

(2) RECONSTRUCTION – FIBER TRACKING

Fiber tracking approaches are commonly applied for reconstructing fiber bundles from DTI data. In this context, the concept of evenly spaced streamlines was adapted and employed in order to control the density of the fibers, depending on the local diffusion anisotropy values. Additionally, an alternative technique for reconstructing white matter tracts based on directional volume growing was developed.

(3) RECONSTRUCTION – CONNECTIVITY ANALYSIS

For cortical regions where thin and diverging fiber bundles are located, the directional information inherent to the diffusion tensors is less pronounced. For this reason, an alternative approach for reconstructing white matter tracts between functional areas was developed. The initial algorithm based on A* pathfinding as well as major improvements including a more sophisticated cost function and a refined search grid are presented and discussed.

(4) RECONSTRUCTION – HULL SURFACES

Fiber tracking or connectivity algorithms usually generate bundles of lines that represent the shape of a fiber tract. However, for intraoperative visualization using a neuronavigation system, hull surfaces are more appropriate and serve as a basis for boundary curves which are superimposed on the OR microscope image. Based on experiences with surface meshes [84-86], different techniques for generating hulls are presented, comprising an approach based on tetrahedralization as well as a technique using isosurfaces.

(5) RECONSTRUCTION – DISTORTION CORRECTION

The EPI sequences commonly used for DTI acquisitions suffer from distortion artifacts. As a result, the reconstructed fiber tracts are spatially displaced. In order to correct the distortions for application in a navigational setup, a non-linear registration approach was applied. The processing steps as well as the registration results were evaluated and are discussed.

(6) VISUALIZATION – FIBER TRACKING

For the visualization of reconstructed fiber bundles, different approaches were developed. Depending on the local diffusion anisotropy, transparent rendering of fibers was applied in order to visually emphasize dominant tract systems. Additionally, in conjunction with the approach for connectivity analysis, different color transfer functions were developed which encode local cost function or anisotropy values. For the visualization of fibers, a novel hybrid approach based on triangle strips and point sprites was developed. The resulting visualizations provide high visual quality, and enable real-time visualization for a large number of fibers.

(7) VISUALIZATION – HULL SURFACES

For visualizing the hull surfaces, per-pixel lighting as well as semi-transparent visualization were implemented. Both techniques make it possible to investigate the structure of the hulls in detail and to monitor the quality of the hull visually. The approaches for visualizing the hulls were developed in conjunction with the hull reconstruction algorithms.

(8) VISUALIZATION – MULTIMODAL VISUALIZATION

In order to visualize reconstructed fiber tracts, respective hulls and functional areas obtained from fMRI in their anatomical context, multimodal visualization with standard MR data is required. Respective visualization techniques and their benefits for application in neurosurgery were investigated.

The development of reconstruction and visualization techniques for DTI data is an active area of research. For this reason, the algorithms and visualization techniques presented are not to be regarded as the ultimate solution to the current problems, but as contributions to an ongoing research process. The individual chapters contribute different methods for processing DTI data, which were developed with regard to application

in neurosurgery. The potential success of each method is discussed at the end of each chapter. So far, the results are promising, even though comprehensive clinical evaluations are still in progress.

1.3 Overview

In this work, a collection of novel methods for reconstructing and visualizing white matter tracts from DTI data is presented. This thesis is divided into three parts: The first part (Chapters 1 and 2) provides an introduction and outlines the medical background of neurosurgery. The second part (Chapters 3 to 7) comprises different reconstruction approaches based on DTI data. The third part (Chapters 8 to 10) addresses visualization techniques that were developed in order to achieve appropriate visualization of the reconstructed structures for medical application.

Part I – Chapter 2 outlines the medical background of neurosurgical procedures. It starts with a short review of the history of neurosurgery, outlines disease patterns treated in neurosurgery and gives an introduction to the clinical setup in the operating room, including neuronavigation. The chapter concludes with a brief description of the imaging techniques applied in neurosurgery.

Part II – Chapter 3 explains the basics about tensor reconstruction. The chapter continues with approaches for quantifying tensor shape, for tensor interpolation and for tensor filtering. Since fundamental information about tensor reconstruction and processing is provided, this chapter serves as a basis for subsequent parts of the thesis.

Part II – Chapter 4 provides an introduction to fiber tracking algorithms comprising streamline tracking, tensor deflection and tract selection techniques. An approach for oriented filters is explained, which is a local filtering method, in contrast to the global filters of Chapter 3. Subsequently, advanced approaches are described comprising evenly spaced streamlines for controlling the spacing between single fibers and an alternative approach denoted as directional volume growing.

Part II – Chapter 5 describes an approach for reconstructing neuronal structures between functional areas, such as Broca's and Wernicke's speech areas. Since the diffusion anisotropy is less pronounced in cortical and subcortical regions, an alternative approach is presented which takes into account the whole diffusion tensor information. The approach is based on pathfinding and takes advantage of a search grid and a cost function based on the tensor information in order to reconstruct possible neuronal connections.

Part II – Chapter 6 addresses the problem of representing the fiber tracking and connectivity analysis results from Chapter 4 and 5 in an intraoperative setting. Since line presentations superimposed on the OR microscope view would be confusing rather than helpful, an alternative representation is required. For this purpose, different hull approaches are presented in this chapter. The hulls serve as a basis for boundary curves

superimposed on the focus plane of the OR microscope, which are much more appropriate for intraoperative visualization.

Part II – Chapter 7 addresses the problem of image distortions resulting from the EPI sequences commonly used for DTI image acquisition. The chapter starts with a description of the distortions encountered for EPI imaging. In the further course of the chapter, the non-linear registration approach is described which is applied in order to correct the distortions. Finally, results are presented and discussed that demonstrate the benefit of this correction approach.

Part III – Chapter 8 presents different techniques for visualizing the fiber bundles obtained from fiber tracking or connectivity analysis. Adaptive transparency depending on the local diffusion anisotropy is introduced, resulting in opaque major tract systems and rather transparent small fiber bundles. This visualization technique helps to focus attention on major tract systems and ensures that they are not hidden by small fiber bundles. Another aspect which has to be considered is the coloring of the fibers. In order to convey additional information such as the local anisotropy value, appropriate color encoding schemes are presented. Finally, the chapter presents a hybrid visualization approach for fibers based on triangle strips and point sprites, which provides high visual quality and yet efficient rendering.

Part III – Chapter 9 presents some information about the visualization of hulls. Lighting as well as transparency are important tools in order to visualize the shape and the quality of the hulls with respect to the underlying fiber tracts.

Part III – Chapter 10 presents and discusses multimodal visualization of anatomical data together with fiber tracts and hulls reconstructed from DTI data as well as functional information. Simultaneous visualization of white matter structures and anatomical data provides important information about the location of white matter tracts with respect to surrounding anatomy for preoperative planning.

Chapter 2

Neurosurgery: History, disease patterns, and operative procedures

Neurosurgery comprises the surgical treatment of diseases related to the nervous system, i.e. the brain, the spinal cord and the peripheral nervous system. This section starts with an overview of the history of neurosurgery (Section 2.1), followed by an outline of the disease patterns that necessitate neurosurgical treatment (Section 2.2). Furthermore, the setup in the operating room is described including the neuronavigation system (Section 2.3). The anatomical structure of the brain as well as functional areas and white matter structures are surveyed in Section 2.4. An introduction to the different imaging techniques applied in neurosurgery for diagnosis, planning and neuronavigation is given in Section 2.5.

2.1 History of neurosurgery

Procedures related to neurosurgery date back to the earliest ages of human history. Thousands of years ago, the art of trepanation where holes are drilled into the skull and small pieces of bone are removed, was practiced as part of ritual actions. According to bone healing observed in trepanated skulls, patients survived these procedures and went on to live for some time afterwards.

Several important advancements for surgery in general were developed in the 19th century. Up to the middle of the 19th century, wound sepsis had been a major problem in relation to surgical interventions, resulting in the death of half of the patients after successful surgical treatment. The risk of postoperative infection was greatly reduced by the carbolic spray invented in 1869 by Joseph Lister and the steam sterilizing technique for surgical instruments and dressings presented by Robert Koch in 1878. The introduction of anesthesia by William T. G. Morton reduced the problem of pain and paved the way for more time-consuming and difficult surgical procedures.

Based on these developments, neurosurgery became an independent discipline at the turn of the 19th century. One of the first pioneers in neurosurgery was Victor Hors-

ley (Great Britain), who specialized in surgery and physiology and developed many practical neurosurgical techniques. In the United States, Harvey Cushing dedicated his practice mainly to surgical interventions concerning the brain and developed many basic surgical techniques. In the field of diagnosis and treatment of brain tumors, he is considered to be a pioneer of modern surgery. Among other achievements and research results, he propagated the technique of x-ray imaging for diagnosis and has contributed to the localization of cortical areas such as the sensory and motor cortex using electrical stimuli.

Following these initial steps, the gradual advance of knowledge related to neuroanatomy and neurophysiology combined with technical progress enabled the systematic treatment of diseases related to the peripheral and central nervous system. Today, modern neurosurgery provides excellent treatments for neurosurgical diseases. Innovative operating techniques and instruments such as OR microscopes, intraoperative imaging, neuronavigation systems or computer-assisted planning systems constantly improve the safety and efficiency of neurosurgical procedures. Nevertheless, open questions and further challenges remain, necessitating various research activities in this field of medicine.

2.2 Disease patterns treated in neurosurgery

The diseases treated in neurosurgery primarily include disorders of the brain, the spinal cord and the peripheral nervous system. Since the focus of this work is on brain surgery, this overview is restricted to disorders involving the brain. Disease patterns of the human brain are related to the different cell types and vascular structures dedicated to function and supply of the brain.

In general, the cells of the human brain are classified into *neuronal* and *non-neuronal* cells. The cell bodies and dendrites of neuronal cells are denoted as *grey matter* and form the convoluted surface (*cortex*) of the brain. The axons of the neuronal cells form the *white matter* that descends deep into the brain. *Glia cells* are non-neuronal cells that provide support and nutrition to the neuronal cells. *Astrocytes* are glia cells that anchor neurons to their blood supply and play a dominant role in nourishing the neuronal cells. Another type of glia cells, *oligodendrocytes*, form the myelin sheath of axons with their cell membrane. As a result, the myelin sheath provides insulation to the axon and electrical signals are propagated more efficiently. *Ependymal cells* are a further type of glia cells which form the border of fluid-filled cavities within the brain and help to keep the cerebrospinal fluid circulating.

Disease patterns of the human brain that are treated operatively mainly comprise arterial-venous malformations as well as brain tumors originating from the different cell types. The arterial-venous diseases comprise cavernoma, which are malformations of a vein, as well as cerebral aneurysms, where a weak vascular wall results in a bulge of the vessel, which may rupture. Brain tumors are classified according to the cell type showing abnormal cell division resulting in tumor growth. Most primary brain tumors (not

metastatic cancers) originate from glia cells and are therefore denoted as *gliomas*. They are further classified as astrocytomas, oligodendrocytomas or ependymomas. Brain tumors are further distinguished with respect to their malignance. According to the shape and the growth properties of the tumor cells, a grade between I and IV is determined according to the World Health Organization (WHO) brain tumor classification scheme introduced in 1993. Grade I refers to less malignant tumors with a slow growth; grade IV tumors are aggressive and grow fast.

2.3 Neurosurgical procedures

Diseases of the human brain such as arterial-venous malformations or brain tumors often necessitate surgical intervention such as resection. In this section, the setup of modern operating rooms (OR) (Section 2.3.1) including navigation in image-guided neurosurgery (Section 2.3.2) is explained.

2.3.1 Clinical setup in the operating room

The Department of Neurosurgery, Erlangen, Germany, is one of the pioneering clinics equipped with intraoperative high-field MR imaging. Intraoperative imaging essentially contributes to safe and precise surgery. MR imaging is commonly used for brain tumor diagnosis and is applied intraoperatively for immediate quality control in order to determine the extent of tumor removal. In addition to that, intraoperative MR imaging allows for the compensation of brain shift by updating the navigation system with intraoperative data.

The intraoperative MR scanner (Figure 2.1, (a)) is installed in an operating room with radiofrequency shielding. During surgery, the patient is positioned on a rotating surgical table (b) allows positional changes. The view of the OR microscope (c) as well as preoperative data are displayed by monitors mounted on the ceiling (d).



Figure 2.1: Setup in the operating room. Attached to the MR scanner (a), a rotating surgical table (b) allows positional changes. The view of the OR microscope (c) as well as preoperative data are displayed by monitors mounted on the ceiling (d).

cal table (Figure 2.1, (b)) which is attached to the high-field MR scanner. The table can be locked in various positions and the tabletop is suited for MR imaging. For intraoperative MR scans, the table is rotated in front of the scanner and the tabletop with the patient on top of it moves into the scanner. For surgery, the table is rotated in order to position the patient's head at the 0.5-mT line. Since the OR microscope (Figure 2.1, (c)) and the surgeon's chair are not fully MR compatible, they are positioned outside the 0.5-mT line and are mechanically attached to the wall for safety reasons. Two monitors mounted on a ceiling arm (Figure 2.1, (d)) show the images from the microscope as well as further visualizations prepared preoperatively. The camera of the navigation system used for neurosurgical guidance is mounted on the ceiling, as well as the touch screen for software control of the navigation system.

A neurosurgical procedure starts with the preparation of the patient for surgery. After anesthesia, the patient is moved to the operating table, and the head is attached to the head holder. The screws of the head holder fixate the bone of the skull in order to assure that the head does not move during surgery, for the patient's own safety. In a next step, the setup of the neuronavigation system is performed based on an initial MR scan and identification of fiducial markers (Section 2.3.2). Additionally, preoperative planning data such as functional information is registered onto the acquired MR data in order to make it available for neuronavigation. As soon as the precision of the navigation setup has been verified, surgery starts. For surgical intervention, the surgeon takes advantage of the operating microscope which is equipped with strong lights that help to distinguish different tissues. Additionally, the neuronavigation system is able to display the border lines of the tumor as well as other important structures, such as speech areas or white matter tracts that have been determined preoperatively, in the focus plane of the microscope. The surgeon is thus able to avoid damaging these eloquent structures in order to prevent postoperative deficits. Intermediate MR scans are acquired for quality control in order to verify the current surgery result.

2.3.2 Navigation in image-guided neurosurgery

A navigation system provides the surgeon with information about the position of surgery tools with respect to image data of the patient. In the case of neurosurgery, the relevant tool that has to be tracked is the OR microscope. The neuronavigation system determines the position of the focus plane of the OR microscope in relation to the patient in order to superimpose additional information obtained from preoperative planning on the microscope image.

For this purpose, the neuronavigation system uses a stereo camera in order to monitor the position of the microscope. Additionally, the spatial position of the patient's head has to be known to the system. This is determined during the navigational setup: As soon as the patient is prepared for surgery with the skull fixed in the MR-compatible head holder, skin-adhesive fiducial markers are attached to the skin of the patient's head (Figure 2.2, left, see arrow) and an initial MR scan is acquired (Figure 2.2, middle).

The operating table is then rotated and locked at the surgery position. For the setup of the neuronavigation system, each marker is identified with a navigation pointer and assigned to the respective fiducial marker in the 3D MR scan in order to relate the MR data to the patient. The navigation pointer and a reference array mounted on the head frame (Figure 2.2, right, see arrows) are filmed by the stereo camera. The pins attached to the pointer and the reference array are extracted from the camera images by a pattern-recognition software and are used to compute the spatial position of the patient's head. By tracking the microscope position, it is now possible to relate the focus plane of the OR microscope to the corresponding plane in the MR scan.



Figure 2.2: Setup of the neuronavigation system. *Left:* Fiducial markers (see arrow) are attached to the patient's skin. *Middle:* MR scan with intraoperative scanner. *Right:* Fiducial markers are touched with a pointer (see upper arrow) and are assigned to the respective marker within the MR dataset. The spherical pins attached to the pointer and to the reference array (see lower arrow) are filmed by a stereo camera and identified by a pattern-recognition software in order to compute the spatial position of the patient.

In standard neuronavigation, solely anatomical information from MR data is used. However, in neurosurgery, a major goal is to preserve functional areas of the brain during surgery. This comprises speech and motor areas on the cortex as well as deep white matter structures (see Section 2.4). For this purpose, information from preoperative functional MR imaging where eloquent brain areas are localized as well as white matter tract information has to be incorporated into the navigation system. This is accomplished by rigid registration of the preoperative planning datasets comprising all the required information with the initial MR scan for navigation setup. As a result, it is possible to show the boundary curves of eloquent structures in the focus plane of the microscope. The surgical guidance provided by this technique is of high value. It increases the safety of surgery and helps to avoid postoperative deficits due to injury of critical regions.

2.4 Neuroanatomy

So that the following chapters may be better understood, a short introduction about neuroanatomy is provided. The focus of this section is on functional areas and white matter tract systems which are often monitored during neuronavigation, thus playing an important role in the following chapters.

The human brain is a complex organ composed of about 10 billion neuronal cells. In neuroanatomy, it is commonly divided into four parts denoted as *frontal lobe*, *parietal lobe*, *occipital lobe* and *temporal lobe*, as outlined in Figure 2.3 (left).

The cell bodies of the neuronal cells form the grey matter, which is divided into functional areas responsible for information processing. In Figure 2.3 (right), important functional areas are shown: The *motor cortex* (blue) is responsible for planning and executing voluntary movements. Along the motor strip, different parts of the body are represented, with the leg area located close to the midline, and the head and face area located laterally on the brain hemisphere. The *sensory cortex* (red) is located just behind the motor cortex and processes sensory information such as touch, pain, temperature and body position received from the peripheral sensory receptors of the body. Visual reception is processed in the *visual cortex* (yellow), which is part of the occipital lobe. Speech processing involves two functional areas denoted as *Broca's and Wernicke's speech areas* (dark grey) usually located in the left hemisphere of the brain. Broca's area (also denoted as motor speech area), is primarily involved in speech production, whereas Wernicke's area (also denoted as sensory speech area) is responsible for language comprehension and processing.

The axons of neuronal cells provide information transmission between neurons. They form bundles denoted as *white matter tracts* and connect grey matter regions on the same brain hemisphere (*association fibers*) or located in both brain hemispheres (*commissural fibers*). In order to link cortical regions with the peripheral nervous system, they

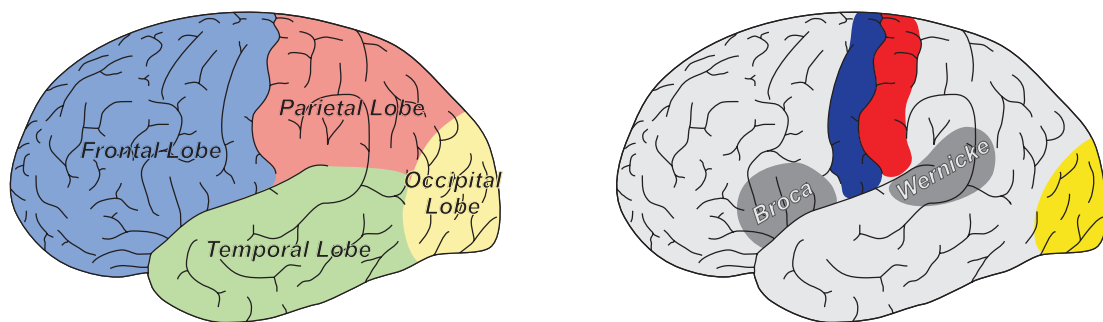


Figure 2.3: *Left*: Lobes of the human brain. *Right*: Important functional areas: Motor cortex (blue), sensory cortex (red), visual cortex (yellow), and Broca's and Wernicke's speech areas (dark grey).

may also extend down to the spinal cord (*projection fibers*). According to the cortical areas they originate from, white matter tracts can be attributed to specific function:

Pyramidal tract: An important tract system is the pyramidal tract (Figure 2.4, left), which is responsible for the transmission of motor impulses. It originates at the motor cortex and extends down to the spinal cord to synapse onto alpha motor neurons which connect to the muscles.

Corpus callosum: The corpus callosum is a tract system composed of u-shaped fibers which connect corresponding cortical areas situated in different brain hemispheres (Figure 2.4, middle). Most of the communication between both hemispheres is conducted across the corpus callosum.

Optic tract: The optic tract is part of the visual system and links the optic chiasm to the visual cortex (Figure 2.4, right). The optic chiasm is a structure, where the optic nerves from both eyes cross. Each nerve divides and half of its fibers cross over to the other hemisphere. As a result, the optic tract in each hemisphere transmits visual information from both eyes.

Arcuate fasciculus: The Broca's and Wernicke's speech areas are connected by a white matter tract system denoted as the arcuate fasciculus. This tract system is essential for correct processing and understanding of language.

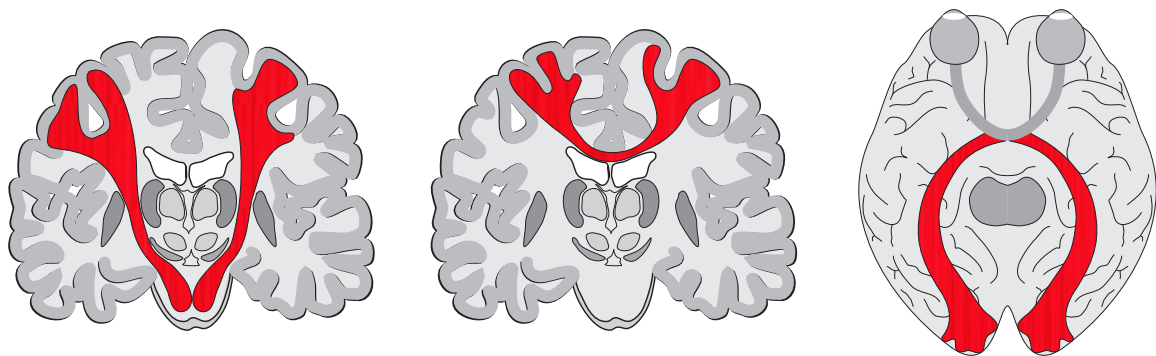


Figure 2.4: Important white matter tract systems (*from left to right*): Pyramidal tract (motor tract system), corpus callosum (connection between the two brain hemispheres), optic tract (visual pathway).

The above cortical areas and tract systems are responsible for essential motor, sensory and other integrative functions. For this reason, an important aim of surgical interventions is to preserve these structures. The next section provides an introduction to imaging techniques which are required in order to obtain information about the location of functional areas and white matter tracts of individual patients.

2.5 Imaging techniques applied in neurosurgery

This section provides an introduction to imaging techniques which play an important role in diagnosis, planning and navigation in neurosurgery. These imaging techniques are based on nuclear magnetic resonance, which is a physical phenomenon described in Section 2.5.1. In diagnosis and planning in neurosurgery, anatomical MRI scans play an important role (Section 2.5.2). Additionally, fMRI is applied in order to localize functional regions such as speech or motor areas (Section 2.5.3). In recent years, the first clinics recognized the potential of DTI (Section 2.5.5) for obtaining information about the organization of white matter structures and started to utilize DTI for preoperative planning.

2.5.1 Physical background

Atomic nuclei with an odd number of protons and neutrons, such as the hydrogen nucleus, ^1H , possess a property known as spin. This is often visualized as a spinning motion of the nucleus about its axis. In quantum mechanics, spin is represented by a magnetic spin quantum number. Due to the charge of atomic nuclei, the spinning motion induces a magnetic field which is oriented according to the direction of the spin axis. Due to their strong magnetic moment and due to their abundance in biological tissue, the hydrogen nuclei of the human body are used as a source of imaging signals in MRI. The hydrogen nucleus consists of one proton and has a spin quantum number of $1/2$, resulting in two eigenstates with slightly different energies.

In the absence of a magnetic field, the magnetic moments of the hydrogen nuclei are randomly distributed. However, if an external magnetic field \mathbf{B}_0 is applied, the nuclei align with this field. According to the two eigenstates, the nuclei are either in parallel or antiparallel state (Figure 2.5, left). However, for quantum mechanical reasons, the spin axes are not exactly aligned parallel or antiparallel with the magnetic field. They are actually set off at an angle α and precess around \mathbf{B}_0 with a characteristic frequency ω_0 known as Larmor frequency (Figure 2.5, right). For a nucleus with a given gyromagnetic ratio γ , the Larmor frequency depends on the strength of the magnetic field:

$$\omega_0 = -\gamma \cdot \mathbf{B}_0. \quad (2.1)$$

The number of spins in the parallel and antiparallel energy state depends on the temperature. For a decreasing temperature, more spins are in the lower energy state N^+ , for increasing temperature, more spins in the high energy level N^- are encountered. At blood temperature, the number of spins in the lower energy level is a bit higher compared to spins in the higher level. The ratio of spins in the lower energy level N^+ compared to spins in the upper energy level N^- is described by Boltzmann statistics, where E is the energy difference between the two states, k is the Boltzmann constant and T denotes the temperature in Kelvin:

$$\frac{N^-}{N^+} = e^{\frac{-E}{kT}}. \quad (2.2)$$

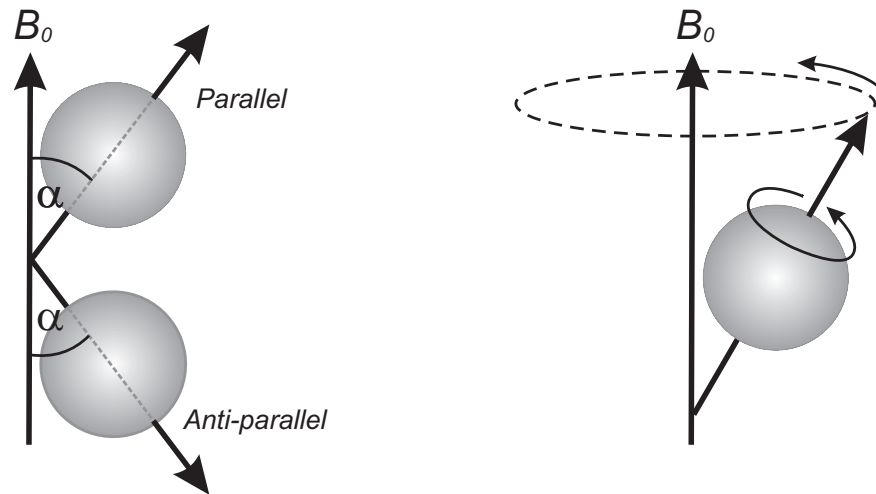


Figure 2.5: For an external magnetic field B_0 , nuclei with spin quantum number $1/2$ adopt a parallel or an antiparallel state (*left*). Each spin axis precesses around the B_0 field direction with Larmor frequency ω_0 (*right*).

In order to understand the effect of magnetic resonance, a collection of hydrogen nuclei within an external magnetic field B_0 aligned with the z -axis in 3D space is considered. The magnetic moments of the nuclei can be represented as vectors on the surface of a cone. The net magnetization M of all nuclei is in the direction of the external magnetic field as shown in Figure 2.6 (left), since the higher energy state is slightly more populated. This equilibrium state changes if radio frequency (RF) energy at the Larmor frequency is applied. RF waves have a magnetic field component, which is a property of all kinds of electromagnetic radiation. For a high-frequency magnetic field B_1 rotating with Larmor frequency ω_0 in the xy -plane, M tilts away from the direction of z , and begins to precess around the z -axis as shown in Figure 2.6 (right). The angle between the rotated direction of M and the z -axis is denoted as the *flip angle* and depends on the strength and duration of the RF pulse. Accordingly, a 90 degree pulse rotates M into the xy -plane, and a 180 degree pulse results in a net magnetization along the negative z -axis. After a RF pulse of duration t , the flip angle for constant $|B_1|$ is computed as follows:

$$\alpha = |\omega_1| \cdot t = \gamma \cdot t \cdot |B_1| \quad (2.3)$$

As soon as the RF signal is switched off, the system gradually returns to its equilibrium state with M aligned with the z -axis. This process is denoted as *relaxation*. Basically, two different relaxation processes are distinguished: *T1 relaxation* and *T2 relaxation*. $T1$ is the time constant describing the relaxation of M into its equilibrium state aligned with the z -axis. $T1$ relaxation refers to the process where nuclei dissipate their excess energy as heat to the surrounding environment (or lattice) and return to

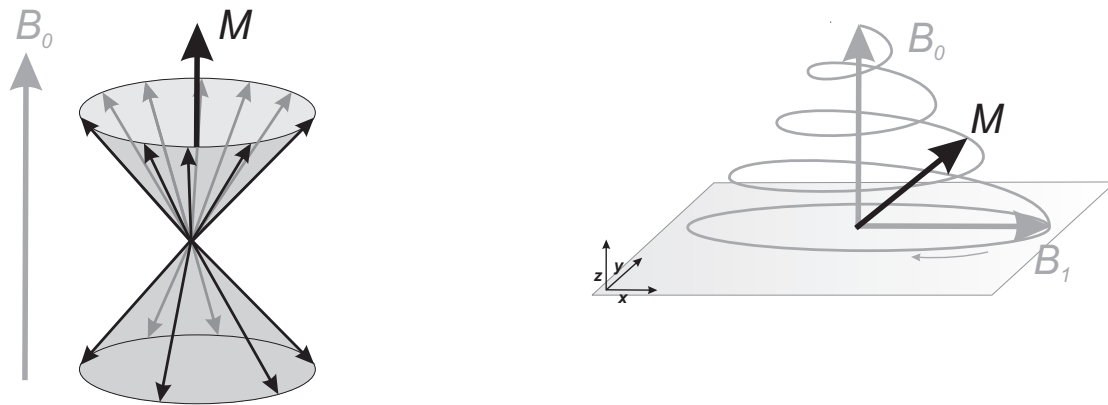


Figure 2.6: In a macroscopic sample, the net magnetization M is in the direction of the magnetic field vector B_0 (left). For a RF pulse with magnetization B_1 rotating in the xy -plane, M tilts away from the direction of B_0 and begins to rotate (right).

the equilibrium state. This process is also known as spin-lattice relaxation. T_2 is the time constant related to the relaxation of transverse magnetization due to the interacting magnetic moments of the nuclei. For this reason, this process is also called spin-spin relaxation. The interacting magnetic moments of the nuclei result in local variations of the magnetic field and cause a dephasing of the components of M within the xy -plane.

The signal that is measured in nuclear magnetic resonance results from the rotating net magnetization M after turning off the RF pulse. According to Faraday's law of magnetic induction, M induces an electromotive force in a receiver coil (Figure 2.7). Due to relaxation processes, the induced signal attenuates over time, which is denoted as *free induction decay* (FID). The magnitude of the resulting signal depends on the number of nuclei contributing to the transverse magnetization as well as on the relaxation times. This RF signal is the basis for reconstructing the MR image.

2.5.2 Magnetic resonance imaging (MRI)

The physical effect of nuclear magnetic resonance is exploited in magnetic resonance imaging (MRI) for non-invasive imaging of the human body. The concentration of water varies depending on the tissue type and leads to a varying strength of the signal.

In order to locate the sample emitting the MR signal, three gradient coils generating orthogonal magnetic fields are necessary. The first magnetic field gradient (*slice selection gradient*) is superimposed on the external magnetic field B_0 leading to a graded magnetization in z direction. As a result, the hydrogen nuclei precess at different Larmor frequencies according to Equation 2.1. If a RF pulse is applied, the hydrogen nuclei with the corresponding resonance frequency will absorb energy. Due to the magnetic field gradient, only nuclei in the respective plane perpendicular to the z -axis are selected.

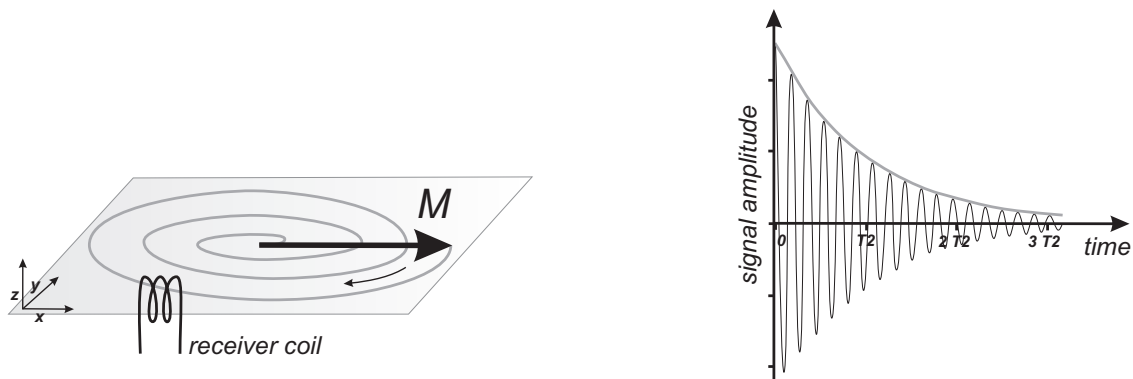


Figure 2.7: A 90 degree RF pulse tilts M to the xy -plane, where M rotates around the z -axis. Due to relaxation processes, the component of M in the xy -plane decays over time (left). This rotating magnetic field induces an alternating current in the receiver coil (right).

The thickness of the slice depends on the strength of the field gradient. The second gradient denoted as *frequency encoding gradient* is necessary in order to spatially encode the selected slice. Due to the overlapping orthogonal magnetic gradient fields, columns of hydrogen nuclei precess at slightly different Larmor frequencies. Similarly, the third gradient field (*phase encoding gradient*) encodes the third direction in three-dimensional space. The received signal is processed using a Fourier transform in order to assign signal intensities to the volume element (x, y) in the slice that has the correct phase and frequency. The grey scale representation of the signal intensities corresponds to the slice image obtained from MRI.

Standard MRI is applied in neurosurgery for diagnosis, preoperative planning and for the setup of the neuronavigation system (Section 2.3.2). For integrating relevant data into the navigation system, such as the tumor border, the location of speech or motor areas and the extent of white matter structures, an MRI dataset containing all relevant information is prepared prior to surgery.

2.5.3 Functional magnetic resonance imaging (fMRI)

Functional MRI (fMRI) provides a means of visualizing functionally activated regions of the brain. This imaging technique makes it possible to visualize physiological changes within the brain that are associated with activation of functional areas. The effect that is most frequently used for this purpose, is the blood oxygenation level dependent contrast (BOLD) effect. Increased brain activity leads to a higher demand for oxygen, which is satisfied by the vascular system supplying oxygenated haemoglobin. Since the deoxygenated haemoglobin attenuates the MR signal, a signal change related to neuronal activity can be measured.

An important application of fMRI relates to neurosurgical planning. For lesions that

are close to the motor cortex or to the speech areas, this imaging technique makes it possible to predict the exact location of functional areas and enables safe resection using the neuronavigation system.

2.5.4 Diffusion tensor imaging (DTI)

Diffusion of water molecules results from the thermal random motion, often referred to as *Brownian motion*. The MR signal is influenced by diffusion due to the phase variations when the water molecules are diffusing in an inhomogeneous magnetic field. This effect is exploited by the *Pulsed Gradient Spin Echo Sequence* introduced by Stejskal and Tanner [140]. This sequence uses two gradient pulses that are applied before and after the 180 degree refocusing pulse. The first gradient pulse induces a phase shift for static spins and is used to label the hydrogen nuclei depending on their position. After the first pulsed gradient, the spins start to dephase. The second gradient pulse is used in order to refocus the magnetization. However, during the time period between the two gradient pulses, spins have changed their location due to diffusion processes. As a result, refocusing is incomplete, leading to a signal loss. In order to determine the extent of signal loss per volume element, the measurement with diffusion gradient has to be compared with the signal acquired without diffusion gradient. Based on diffusion measurements for at least six collinear gradient directions, a diffusion tensor is reconstructed per voxel which models the local diffusion and serves as a basis for different reconstruction and visualization techniques.

In neurosurgery, DTI plays an important role in obtaining information about the location of neuronal pathways. In order to avoid neurological deficits after surgery, important tract systems dedicated to specific functions must remain intact. Since white matter consists of long, cylindrical cells, water diffusion is anisotropic in these regions resulting in a especially high signal attenuation if the field gradients are oriented along the tract direction. Consequently, the diffusion behavior of water within the human brain allows conclusions with respect to the white matter architecture, which is of high value for surgery.

2.5.5 Imaging parameters and image data

The datasets employed in this work were acquired in patients with brain lesions undergoing surgery. All the datasets were measured using a *Siemens MR Magnetom Sonata Maestro Class 1.5 Tesla* scanner. The specifications of the gradient system were a field strength of up to 40 mT/m (effective 69 mT/m) and a slew rate of up to 200 T/m/s (effective 346 T/m/s) for clinical application.

MRI: For diagnosis, planning and navigation in neurosurgery, standard T1-weighted MRI data is acquired in each patient. More precisely, an MPRAGE (magnetization prepared rapid acquisition gradient echo) sequence is applied for this purpose. The advan-

	number of voxels	voxel size in [mm ³]
MPRAGE	256 × 256 × 160	1.0 × 1.0 × 1.0
fMRI	80 × 80 × 25	3.0 × 3.0 × 3.0
DTI	128 × 128 × 60	1.875 × 1.875 × 1.9

Table 2.1: The dataset parameters, i.e. number of voxels and voxel size, for the different types of data acquired for neurosurgical intervention.

tages of MRI imaging are a high signal-to-noise ratio and a high resolution (Table 2.1). MRI imaging parameters are: TR = 2020 ms, TE = 4.38 ms.

fMRI: In patients with lesions close to functional areas, fMRI data is acquired. In order to measure activated brain areas, the patient is instructed to perform specific tasks [65]. Based on the signal intensities, activation maps are reconstructed (resolution according to Table 2.1). The functional slices are aligned to MPRAGE datasets obtained from the same patient position in order to relate them to the anatomical context. Further fMRI imaging parameters are: TR = 2470 ms, TE = 60 ms.

DTI: In the case of DTI acquisition, one reference dataset and at least six diffusion datasets are acquired. The reference dataset is measured without any gradient direction, which is equivalent to common T2 weighed MR data. For acquisition of the diffusion datasets, either six or twelve gradient directions are selected (Table 2.2). With respect to anatomical information, the reference image represents anatomical structures; the other images show diffusion properties. Due to physical limitations, the spatial resolution of DTI data is restricted to about 2 mm edge length per voxel (Table 2.1). Further DT imaging parameters are: TR = 9200 ms, TE = 86 ms, $b_{high} = 1000 \text{ s/mm}^2$, $b_{low} = 0 \text{ s/mm}^2$, 1502 Hz/Px bandwidth.

6 gradient directions	12 gradient directions
(±1 , 0 , 1)	(1 , 0 , ±0.5)
(0 , 1 , ±1)	(0 , ±0.5 , 1)
(±1 , 1 , 0)	(±0.5 , 1 , 0)
	(1 , ±0.5 , 0)
	(0 , 1 , ±0.5)
	(±0.5 , 0 , 1)

Table 2.2: Gradient directions for DTI acquisition, 6 or 12 gradient directions could be selected.

Part II

Reconstruction of neuronal structures

Chapter 3

Tensor reconstruction and processing

This chapter outlines basic computation and processing schemes for diffusion tensors. In Section 3.1, the Stejskal-Tanner formula for diffusive attenuation is described which serves as physical basis for diffusion measurements. The computation of diffusion tensors is outlined in Section 3.2. Based on this tensor data, different methods for quantifying characteristics of a tensor have been developed in previous research. In Section 3.3, a selection of scalar metrics is reviewed, which will be used in further chapters. Another important question which is considered in Section 3.4 relates to tensor interpolation, which is important for most further processing steps such as fiber tracking. The last topic covered in this chapter is tensor filtering, which is addressed in Section 3.5.

3.1 The Stejskal-Tanner equation

The Bloch equations [13] describe many phenomena in nuclear magnetic resonance and have been modified by Torrey in order to include the effects of diffusion and flow processes [144]. This results in the first-order differential Bloch-Torrey equation

$$\frac{\partial M_+}{\partial t} = -i|\omega_0| M_+ - i\gamma \mathbf{G} \mathbf{r} M_+ - M_+/T_2 + \nabla D \nabla M_+, \quad (3.1)$$

where $M_+ = m_x + im_y$ is the complex representation of transverse magnetization in the xy -plane precessing with Larmor frequency ω_0 , γ is the gyromagnetic ratio, \mathbf{r} is the spin position vector, T_2 is the spin-spin relaxation time, and D is the apparent diffusion coefficient. \mathbf{G} is the linear magnetic field gradient, which is composed of a steady gradient \mathbf{g}_0 due to inhomogeneities of the laboratory magnetic field, and a superimposed gradient \mathbf{g} .

For a spin-echo experiment as described in Section 2.5.5, the Bloch-Torrey equation can be solved using a substitution suggested by Stejskal and Tanner [140]. On the assumption that the direction of the gradient \mathbf{g} is not changed during the experiment, and is much larger than other gradients \mathbf{g}_0 , the resulting equation is further simplified. As a result, the Stejskal-Tanner formula for diffusive attenuation [140] relates the attenuated

signal of the spin-echo experiment S to the signal S_0 obtained in absence of diffusion gradients:

$$S = S_0 \exp \left(-\gamma^2 \delta^2 |\mathbf{g}|^2 \left(\Delta - \frac{\delta}{3} \right) D \right) = S_0 \exp (-bD) . \quad (3.2)$$

The b-factor $b = \gamma^2 \delta^2 |\mathbf{g}|^2 \left(\Delta - \frac{\delta}{3} \right)$ is the diffusion weighting factor [72], where δ is the duration of the diffusion sensitizing gradient pulse, $|\mathbf{g}|$ is the strength of the gradient pulses and Δ is the duration between the two gradient pulses (the time constant $\tau = \Delta - \delta/3$ is the effective diffusion time, the correction $\delta/3$ relates to the time when the gradients are on).

This equation applies to isotropic diffusion, where D is independent of the direction of the gradients. For the case of anisotropic, restricted diffusion, a more general form of Equation 3.2 taking into account the gradient direction is necessary. For this purpose, Stejskal introduced the rank-2 real symmetric diffusion tensor \mathbf{D} and replaced the diffusion term $\nabla D \nabla M_+$ in Equation 3.1 with $\nabla \mathbf{D} \nabla M_+$ [139]. Basser [4] adapted this formalism in order to measure diffusion in biological tissues, where the signal attenuation is described by:

$$S = S_0 \exp \left(-b \mathbf{g}^T \mathbf{D} \mathbf{g} \right) . \quad (3.3)$$

Comparison of Equation 3.2 and 3.13 yields the relation:

$$D(\mathbf{g}) = \mathbf{g}^T \mathbf{D} \mathbf{g} . \quad (3.4)$$

The rank-2 real symmetric diffusion tensor \mathbf{D} is able to describe anisotropic Gaussian diffusion which is observed in fibrous biological tissues such as white matter or muscle tissue.

3.2 Diffusion tensor reconstruction

Since the diffusion tensor \mathbf{D} is a real Hermitian positive definite matrix, it has 6 unique coefficients:

$$\mathbf{D} = \begin{pmatrix} D_{xx} & D_{xy} & D_{xz} \\ D_{xy} & D_{yy} & D_{yz} \\ D_{xz} & D_{yz} & D_{zz} \end{pmatrix} \quad (3.5)$$

In order to reconstruct a diffusion tensor for each voxel of a volume dataset, at least seven MR acquisitions are necessary. This comprises six acquisitions with non-collinear gradient directions $\mathbf{g}_i, i = 1..6$, and an acquisition without gradient which provides the unattenuated reference dataset. For each voxel, the system of equations

$$S_i = S_0 \exp \left(-b \mathbf{g}_i^T \mathbf{D} \mathbf{g}_i \right) , i = 1..6 \quad (3.6)$$

has to be solved, where S_0 corresponds to the grey value of the respective voxel in the reference dataset, and S_i to the grey value in the gradient dataset with gradient direction g_i . In the case of six diffusion datasets, a unique solution for the system of equations exists; for more acquisitions a linear regression approach has to be applied.

3.3 Quantifying tensor shape

Diffusion tensors reflect the structure of underlying white matter, such as the density or the directional similarity of fibers and are therefore a meaningful measure of fiber-tract organization. However, the complex information provided by the diffusion tensor as a whole is difficult to interpret. For this reason, approaches have been developed to quantify a tensor and to relate the measure of diffusion properties to the structure of tissue. In this section, the eigensystem of the tensor (Section 3.3.1) as well as its physical interpretation (Section 3.3.2) is presented and scalar invariants for tensor quantification are outlined (Section 3.3.3).

3.3.1 Tensor eigensystem

Each diffusion tensor is characterized by its principal diffusivity directions (i.e. eigenvectors $v_i, i = 1, 2, 3$) and the corresponding diffusion coefficients (i.e. eigenvalues $\lambda_i, i = 1, 2, 3$). Due to the symmetry of the diffusion tensor, the eigenvectors are perpendicular to each other and the eigenvalues are real and positive. The decomposition of the diffusion tensor D into eigenvalues and eigenvectors is known as eigen decomposition and satisfies the following equation:

$$Dv = \lambda v \quad (3.7)$$

which can be rewritten as

$$(D - \lambda I)v = 0 \quad (3.8)$$

where I is the identity matrix. This equation has non-trivial solutions, if the following determinant is equal to zero:

$$\det(D - \lambda I) = 0. \quad (3.9)$$

The cubic equation in 3.9 provides the eigenvalues of D ; the eigenvectors are obtained by substituting each eigenvalue into Equation 3.8 and by solving the resulting system of equations. The eigenvalues are typically ordered in descending order, i.e. $\lambda_1 \geq \lambda_2 \geq \lambda_3$. They provide information about the anisotropy of a tensor which is an indicator for white matter structures. In the case of eigenvalues with similar value $\lambda_1 \approx \lambda_2 \approx \lambda_3$, isotropic diffusion is encountered which occurs in tissue with cell bodies or in fluid-filled cavities such as the ventricles. If one eigenvalue predominates over the others, i.e. $\lambda_1 \gg \lambda_2 \approx \lambda_3$, white matter structures showing a strong anisotropic diffusion

characteristic are encountered. However, in the case of crossing or branching fibers, intermediate tensor characteristics may occur, where two eigenvalues of comparable size are much greater than the third one $\lambda_1 \approx \lambda_2 \gg \lambda_3$. The associated eigenvectors indicate the principal diffusion directions.

3.3.2 Diffusion ellipsoids

The diffusion tensor characterizes the Gaussian diffusion within a voxel, where the eigenvectors indicate the directions of main diffusion, and the eigenvalues the associated diffusivities. Based on the eigensystem, the Gaussian diffusion can be represented graphically by a diffusion ellipsoid [5]. The axes of the ellipsoid correlate with the directions of the eigenvectors, and their length is proportional to the square roots of the corresponding eigenvalues (Figure 3.1). In the coordinate system spanned by the eigenvectors v_1, v_2 and v_3 , the diffusion ellipsoid is calculated as follows [5]:

$$\left(\frac{x}{\sqrt{2\lambda_1\tau}}\right)^2 + \left(\frac{y}{\sqrt{2\lambda_2\tau}}\right)^2 + \left(\frac{z}{\sqrt{2\lambda_3\tau}}\right)^2 = 1. \quad (3.10)$$

The physical interpretation of the diffusion ellipsoid relates to the isoprobability surface of diffusion. For a spin located at the origin of the ellipsoid at $t = 0$, the ellipsoid surface represents possible locations (x, y, z) of equal probability at $t = \tau$ after Gaussian diffusion.

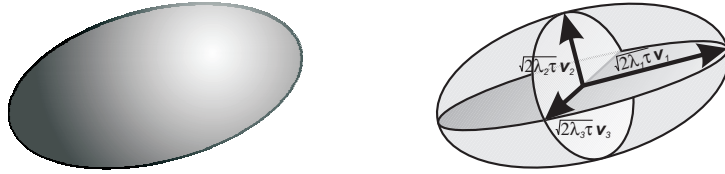


Figure 3.1: The eigenvectors v_i and eigenvalues λ_i of the diffusion tensor define the diffusion ellipsoid. The ellipsoid surface is the isoprobability surface of Gaussian diffusion after a time interval τ .

As an alternative, the axes are often scaled according to the eigenvalues (instead of their square roots) in medical applications [155, 60, 34]. This refers to a direct visualization of the eigensystem and emphasizes anisotropy, but lacks physical interpretation. Additionally, alternative tensor glyphs such as cylinders and superquadrics have been proposed in order that the shape of the tensor may be better conveyed [155, 60].

3.3.3 Scalar metrics

In order to summarize the geometrical properties of the diffusion tensor, different rotationally invariant scalar metrics have been presented. The complex tensor information

is reduced to a meaningful scalar value and facilitates 2D visualization. Based on these values, different regions of the brain can be compared with respect to their diffusion characteristics. In the literature, various metrics have been defined. In the following, the tensor trace $\text{tr}(\mathbf{D})$, the fractional anisotropy $\text{FA}(\mathbf{D})$ and the barycentric space coordinates c_l , c_p and c_s are presented, which are referred to in this thesis.

Tensor trace

The tensor trace $\text{tr}(\mathbf{D})$ is a physical measure of the overall amount of diffusion within a voxel. In fluid-filled cavities such as the ventricles, a high value is observed which is in contrast to brain tissue, where the total diffusion is low. According to empirical observations, this measure is essentially constant within healthy brain tissue [118].

$$\text{tr}(\mathbf{D}) = \lambda_1 + \lambda_2 + \lambda_3 \quad (3.11)$$

Fractional anisotropy

The fractional anisotropy $\text{FA}(\mathbf{D})$ is related to the coherence of oriented structures and describes a directional bias of diffusion. It is defined in terms of the eigenvalue variance according to [7]:

$$\text{FA}(\mathbf{D}) = \sqrt{\frac{3}{2}} \sqrt{\frac{(\lambda_1 - \langle \lambda \rangle)^2 + (\lambda_2 - \langle \lambda \rangle)^2 + (\lambda_3 - \langle \lambda \rangle)^2}{\lambda_1^2 + \lambda_2^2 + \lambda_3^2}}, \quad (3.12)$$

where $\langle \lambda \rangle = 1/3 (\lambda_1 + \lambda_2 + \lambda_3)$ is the mean of the eigenvalues. Essentially, the numerator is the standard deviation of the eigenvalues, which characterizes the ratio of the anisotropic part of \mathbf{D} to its isotropic part. The denominator contains the norm of the tensor. FA as a whole provides the fraction of diffusion that refers to anisotropic diffusion. The value of FA varies between 0 (isotropic diffusion) and 1 (complete anisotropic diffusion).

Barycentric space coordinates

Another set of scalar metrics characterizes a tensor in terms of three basic tensor shapes which are associated with linear, planar and spherical diffusion [154, 153]. In the linear case, the corresponding diffusion ellipsoid is cigar-shaped and diffusion in the direction of the eigenvector corresponding to the largest eigenvalue dominates (i.e. $\lambda_1 \gg \lambda_2 \approx \lambda_3$). In the planar case the diffusion ellipsoid is flat, which corresponds to diffusion in a plane spanned by the eigenvectors with respective eigenvalues λ_1 and λ_2 (i.e. $\lambda_1 \approx \lambda_2 \gg \lambda_3$). In the spherical case, the shape of the tensor is a sphere and no preferred diffusion direction exists (i.e. $\lambda_1 \approx \lambda_2 \approx \lambda_3$). Depending on the tensor eigenvalues, a metric will be high if the tensor shape correlates with the corresponding diffusion characteristic. The metrics associated with linear c_l , planar c_p and spherical c_s diffusion are defined as follows:

$$c_l = \frac{\lambda_1 - \lambda_2}{\lambda_1 + \lambda_2 + \lambda_3}$$

$$c_p = \frac{2(\lambda_2 - \lambda_3)}{\lambda_1 + \lambda_2 + \lambda_3}$$

$$c_s = \frac{3\lambda_3}{\lambda_1 + \lambda_2 + \lambda_3}$$

$$c_l + c_p + c_s = 1$$

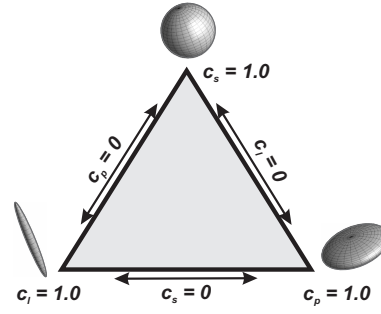


Figure 3.2: Barycentric coordinate space spanned by the three basic tensor shapes.

According to [61, 62], these metrics can be considered as coordinates in a barycentric space which is spanned by the three basic tensor shapes, as shown in Figure 3.2. Each point in the barycentric space corresponds to a possible tensor shape, and the associated anisotropy metrics (c_l, c_p, c_s) are the point's barycentric space coordinates.

3.4 Tensor interpolation

During DTI acquisition, diffusion values are measured for each voxel, leading to a diffusion tensor that characterizes the average diffusion behavior per voxel. However, for different reconstruction algorithms based on DTI data such as fiber tracking, it is desirable to obtain a tensor at arbitrary coordinates within the dataset. In principle, three different possibilities for DTI interpolation exist:

- (1) **Dataset interpolation:** Interpolation of the diffusion datasets prior to tensor computation and further metric computations.
- (2) **Tensor interpolation:** Component-wise interpolation of the tensor matrix entries.
- (3) **Eigensystem interpolation:** Interpolation of the eigenvalues and eigenvectors, which are the basis for further reconstruction and visualization approaches.

With regard to computational effort, the most convenient kind of interpolation would be the eigensystem interpolation, which is carried out at the end of the processing pipeline. In the case of tensor interpolation, it would be necessary to compute the eigensystem anew for each interpolated tensor. In the case of dataset interpolation, even each interpolated tensor must be computed anew. However, as far as maintaining the diffusion characteristics is concerned, it may be anticipated that dataset interpolation is the most careful and for this reason the most accurate method of interpolation.

This issue has been thoroughly investigated in [62], where the differences between the three interpolation methods were analyzed. For this purpose, a start and an end voxel were defined in a brain dataset, and the intermediate samples were obtained by

the different interpolation techniques. For each interpolation technique, the barycentric space coordinates of the intermediate samples were computed. The resulting interpolation paths within barycentric space were then compared for the different interpolation approaches. As a result, the interpolation paths for dataset and tensor interpolation track each other closely, whereas the path for eigensystem interpolation differs significantly. From this evaluation, it can be concluded that tensor interpolation is a good trade-off between accuracy and computing times.

3.5 Tensor filtering

In image and data processing, filtering techniques play an important role in reducing imaging noise. Like other MRI sequences, DTI suffers from partial volume effects and various artifacts which lead to corrupted diffusion measurements. Biological effects such as varying drain of cerebro-spinal fluid add further noise to the data. For this reason, different techniques for noise reduction have been presented for DTI data. Previous work mainly addresses regularization of the major eigenvectors and eigenvalues [27, 77]. In combination with fiber tracking, stochastic approaches adding uncertainty to the propagation direction [11] and local filters [160] have been investigated. However, as outlined in Section 3.4, operations on the tensor data should be performed either on the data itself or component-wise on the tensors.

For this reason, a set of global filters was implemented in this work, which smooth the reconstructed tensors. The filtering results were also published in [83]. Filtering is performed component-wise, i.e. each component of the tensors is considered separately. The filter is first applied to all entries D_{xx} of the tensors, then to all entries D_{xy} , and so on, which is equivalent to smoothing different scalar datasets. For comparison, a standard Gaussian filter was implemented. Additionally, two powerful filters originally developed for video processing were chosen for noise reduction. Since a volume dataset consists of slices, and the changes from slice to slice are only slight, there is a certain equivalence between a video and scrolling through a medical slice dataset. For this reason, the benefits of video filters were exploited for smoothing of DTI data.

In Section 3.5.1, the standard Gaussian filter implemented in this work is presented. The first video filter, the two-class Gauss weighting filter [42], is outlined in Section 3.5.2. It computes the difference between the tensor entry of a voxel and its neighboring voxels. Depending on the similarity of these values each neighbor is weighted. In this way, similar values have a higher contribution to the filtered value. The second video filter is a best-neighbor filter [161] which works in a similar way, as described in Section 3.5.3. Surrounding neighbors are sorted according to the difference of values. Only the best-matching third of the sorted neighbors is equally weighted and contributes to the filtered value of the center voxel.

3.5.1 Gaussian filter

Gaussian filtering is one of the most common filter techniques. Gaussian smoothing is based on the Gaussian distribution, which in 1D is represented as follows:

$$G(x) = \frac{1}{\sqrt{2\pi}\sigma} e^{-\frac{x^2}{2\sigma^2}}, \quad (3.13)$$

where σ is the standard deviation of the distribution, and the distribution has a mean of zero, i.e. it is centered at $x = 0$. Based on the Gaussian distribution, the corresponding 3D volume filter is a smoothing operator for volume datasets, which blurs the image data and removes noise. The degree of smoothing is determined by σ , where the noticeable influence of the neighborhood increases with a larger σ . Since the dataset is stored as a collection of discrete voxel values, a discrete approximation of the Gaussian function is required, which is denoted as *filter kernel*. The filter kernel is then convoluted with each dataset value, resulting in the Gaussian filtered dataset.

The computational effort for convolution is reduced by convolving the whole dataset in x -, y -, and z -direction with a 1D filter kernel. Since the equation for the 3D isotropic Gaussian is separable into x , y and z components, this provides an identical result to that obtained by convoluting once with a 3D kernel.

In Figure 3.3, the smoothing results of the Gaussian kernel are shown by means of FA datasets. The original dataset (left) shows a noisy structure which vanishes with increasing filter kernel sizes (middle, right). However, the edges and structures in the filtered images disappear as well, which is also reflected by a lower average and maximum FA value after filtering.

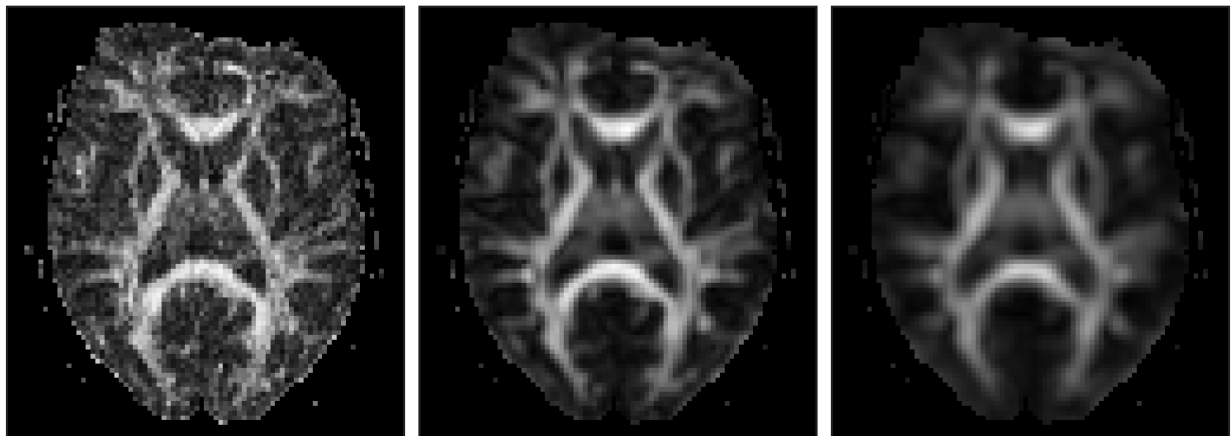


Figure 3.3: FA slice of dataset before smoothing (*left*), after Gaussian smoothing with a filter kernel of size three (*middle*) and of size five (*right*).

3.5.2 Two-class Gaussian weighting

A variation of the Gaussian filter which aims at better preserving edges is the *two-class Gaussian weighting (TCGW)* filter [42]. In contrast to Gaussian filtering, where the weight of a neighbor voxel depends on the spatial distance to the center voxel, in the case of the TCGW filter the impact of a neighbor voxel on the filtering result depends on the difference between the values of neighbor and center voxel.

Depending on the local intensity values, voxels are classified as edge or as non-edge voxels. For non-edge voxels, Gaussian weighting coefficients are computed, while edge voxels are excluded from filtering. For the classification of a voxel with grey value x_1 , the grey values x of the surrounding voxels within the 3D filter window are considered, where

$$\mathbf{x} = (x_2, \dots, x_N)^T \quad (3.14)$$

and $N = n \times n \times n$ is the vector size, depending on the filter kernel size n . The difference vector Δ stores the difference values of the filter window voxels with respect to the center voxel with grey value x_1 according to

$$\Delta = (|x_2 - x_1|, \dots, |x_N - x_1|)^T. \quad (3.15)$$

Based on this difference vector, the center voxel is classified as an edge or a non-edge voxel. For this purpose, each difference value Δ_i is compared to a threshold value T . For edge voxels, the filter weight w_i is set to zero; for non-edge voxels, the filter weight w_i is computed according to Gaussian filtering, resulting in the weight vector w , where σ is half the filter kernel size:

$$\mathbf{w} = (w_2, \dots, w_N)^T \quad \text{with} \quad w_i = \begin{cases} 0, & \Delta_i > T \text{ (edge voxel)} \\ e^{-\frac{\Delta_i^2}{2\sigma^2}}, & \Delta_i \leq T \text{ (non-edge voxel)} \end{cases}. \quad (3.16)$$

The resulting weights ensure that only non-edge voxels with a similar value compared to the center voxel are considered for filtering. For voxels within the filter window showing a significant deviation from the center value, the respective weight is set to zero and the value of this voxel has no impact on the filtering result. Based on these weights, the filtered value y for the original image value x_1 is:

$$y = \frac{\mathbf{w}^T \cdot \mathbf{x}}{\sum_i w_i} \quad (3.17)$$

As a result, TCGW filtering provides better preservation of edges, as shown in Figure 3.4. However, compared to standard Gaussian filtering, a greater computational effort is required, since an individual 3D filter window has to be computed for each voxel.

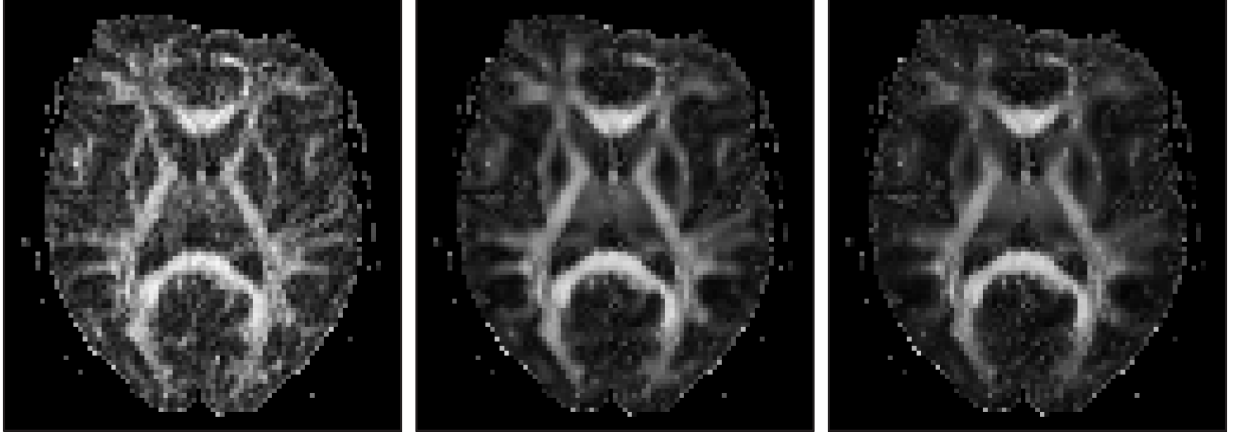


Figure 3.4: FA slice of dataset before smoothing (*left*), after TCGW smoothing with a filter kernel of size three (*middle*) and of size five (*right*).

3.5.3 Best-neighbor filter

The intention of the *best-neighbor* (BN) filter [161] is similar to the TCGW filter presented before. The BN filter sorts the values within the filter window according to the difference to the center voxel. The filter weights a value within the filter window according to the sorting order, resulting in a higher impact of voxels with similar value.

For this purpose, a vector x comprising all surrounding values within the filter window around the voxel with value x_i and a difference vector Δ are generated according to Equation 3.14 and 3.15. The entries of x are then sorted in ascending order according to the difference values in Δ , providing the sorted vector

$$\mathbf{x}' = (x'_2, \dots, x'_N)^T, \quad (3.18)$$

where $|x'_i - x_1| < |x'_{i+1} - x_1|$, $i = 2, \dots, N - 1$. Depending on the position within the sorted vector, each entry x'_i is weighted with a corresponding weight w_i . The filtered value y is computed as follows:

$$y = \frac{1}{\sum_i w_i} \sum_i w_i x'_i. \quad (3.19)$$

In our implementation, only the best third of the values within the filter window is used in order to compute the filtered value, i.e. $w_i = 0$ for $i > N/3$. The contributing values are weighted with constantly decreasing weights w_i . The smoothing results presented in Figure 3.5 show, that edges are well preserved while noise is suppressed.

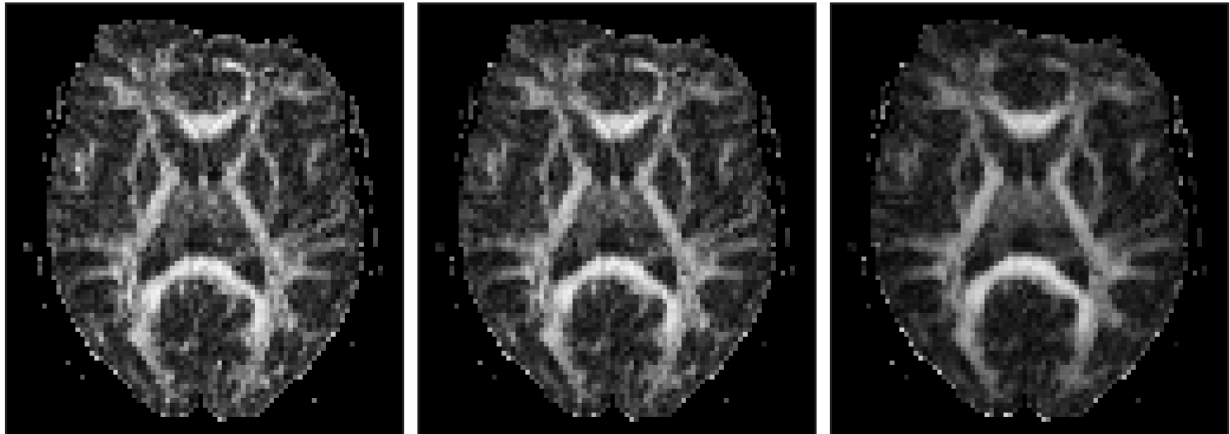


Figure 3.5: FA slice of dataset before smoothing (*left*), after best-neighbor smoothing with a filter kernel of size three (*middle*) and of size five (*right*).

3.5.4 Results

The FA images in Figures 3.3, 3.4 and 3.5 show the impact of global filtering on the diffusion tensor data. All three filters are able to suppress noise, which is clearly visible in comparison to the unfiltered FA slices. However, while Gaussian filtering merely smears the FA values, edges are much better preserved using the TCGW or the BN filtering technique. Comparison of Figure 3.4 and 3.5 shows that the BN filter provides a more conservative smoothing result, compared to the TCGW filter. This can be attributed to the truncation of values within the filter window, which diverge too much from the center value.

If global filtering techniques are applied prior to tract reconstruction algorithms such as the approaches outlined in Chapters 4 and 5, it can be observed that the resulting paths are smoother. However, global filtering tends to lower the local FA values. Since FA is commonly used as a criterion for path termination, a higher FA threshold value has to be applied for tract reconstruction.

The computing times for the different global filters were measured on a PC equipped with an Intel Pentium 4, 2.4 GHz and 512 KB RAM, and are summarized in Table 3.1. The computing times for the Gaussian filter are comparably low, which can be attributed to the fact that the Gaussian filter is based on a fixed filter kernel and is separable into 1D Gaussian kernels, which are applied separately for each dimension in 3D space. The TCGW filter constructs an individual filter window in each step, based on the difference values of the filter window voxels with respect to the center voxel. For this reason, this adaptive filter involves a higher computational cost. Similarly, the BN filter only takes into account neighbor voxels with similar values, which requires sorting of all values within the filter window. As a result, the computational effort increases further, due to the computation of difference values and due to the sorting operation.

	Filter kernel size	
	$3 \times 3 \times 3$	$5 \times 5 \times 5$
Gaussian filter	2.9 sec	4.4 sec
Two-class Gaussian weighting	11.7 sec	51.6 sec
Best-neighbor filter	24.2 sec	106.2 sec

Table 3.1: Computing times in seconds for global filtering of a diffusion tensor dataset (resolution according to Table 2.1). The computational effort for Gaussian filtering, TCGW filtering and BN filtering for different filter kernel sizes is shown.

3.6 Discussion

In this chapter, basic principles for tensor reconstruction and processing have been presented. The Stejskal-Tanner equation outlined in Section 3.1 provides the physical basis for diffusion tensor reconstruction and was adapted by [4] in order to measure diffusion in biological tissues. Thanks to this groundwork it became possible to reconstruct diffusion tensors, a topic which is reviewed in Section 3.2.

The shape of the resulting diffusion tensors provides information about the local diffusion characteristics and therefore allows conclusions about the underlying white matter. For this reason, approaches for quantifying tensor shape have been developed. They are discussed in detail in the previous work of different research groups [118, 7, 154, 153, 61, 62]. A selection of scalar metrics which are commonly used in clinical application is summarized in Section 3.3. These metrics play an important role in diffusion tensor data analysis and proved to be of high value in relation to the diagnosis of psychiatric disorders [97, 114, 125], degenerative diseases [15, 157, 138] or acute ischemic stroke [131, 19, 10]. In neuroanatomy and neurosurgery, they are commonly used in order to analyze and reconstruct white matter tracts. Since these scalar metrics have become established in many areas of application related to DTI, they are also used in the following chapters.

In Section 3.4, the topic of tensor interpolation is addressed. In order to obtain adequate diffusion tensors at intermediate positions within the dataset, appropriate interpolation schemes are required. This topic was thoroughly investigated in [62], where the quality of the interpolation result after dataset, tensor or eigensystem interpolation is assessed and compared. According to the results presented in [62], dataset interpolation provides the highest quality, closely followed by tensor interpolation. Regarding the computational cost for the different interpolation alternatives, dataset interpolation is the most, and eigensystem interpolation the least expensive method. Since tensor interpolation is nearly as accurate as dataset interpolation, but much more efficient, it provides a good trade-off between quality and computational cost. Alternative interpolation schemes such as anisotropic interpolation [20, 96] or interpolation in a nonlinear Riemannian symmetric space [26, 39] have been presented as well, but involve a high computational cost. For this reason, tensor interpolation as suggested by [62] is employed in this work.

Another important topic related to DTI tensor processing is global filtering of the tensor data. This technique is commonly applied in order to regularize the tensor field, prior to further processing. In addition to Gaussian filtering, which is thoroughly investigated in [54], two alternative approaches based on video filtering are presented and analyzed in this chapter. As shown in the respective section, these filters are better able to preserve edges, compared to the Gaussian filter. However, for all three filters, a slight decrease of the FA value can be observed, which must be taken into account when using the filtered data for further reconstruction algorithms, such as fiber tracking. In the case of voxel-based evaluations for statistical purposes, which are often assessed for the diagnosis of Alzheimer's disease or psychiatric disorders, the filter size must be carefully adjusted, as outlined by [54]. Nevertheless, the two filter techniques presented provide a regularization mechanism which ensures better preservation of the features within the data, compared to Gaussian filtering, which is achieved with an adaptive filter window which is locally assessed based on the neighbor voxels.

Overall, the techniques presented in this chapter provide fundamental tensor reconstruction, processing and filtering techniques which serve as a basis for the more advanced techniques presented in the subsequent chapters.

Chapter 4

Fiber tracking

The scalar metrics and diffusion ellipsoids presented in the previous chapter already provide insight into the diffusion data. However, directional information showing the course of the underlying white matter tracts is difficult to convey on the basis of scalar metrics, and diffusion ellipsoids are difficult to interpret.

For this reason, another class of algorithms has emerged, which are denoted as *fiber tracking*. Based on the tensor information, these approaches generate bundles of lines which approximate the course and location of white matter tracts within the human brain. However, since the scale of axons is in the range of several micrometers, compared to DTI data with a voxel size of about 2 millimeters, the trajectories obtained from fiber tracking are not able to depict single axons. Nevertheless, in the case of major white matter tracts, which consist of a collection of aligned axons, the fiber-tracking results approximate the overall shape and structure of the tract system.

This chapter starts with a survey of fiber-tracking algorithms in Section 4.1. The two most prominent approaches for fiber tracking are streamline-based techniques and tensor deflection, which are outlined in Section 4.1.1. Different tract-selection techniques are described in Section 4.1.2. In order to improve the accuracy of fiber tracking, oriented filters were implemented, as outlined in Section 4.2. Subsequently, fiber tracking based on evenly spaced streamlines is presented in Section 4.3, which was published in [91]. An advanced technique for fiber tracking is directional volume growing, which was published in [87] and which is outlined in Section 4.4. A discussion evaluating the benefit of the different techniques for medical application is provided in Section 4.5 and was partly published in [35, 106].

4.1 Basics about tracking algorithms

Fiber-tracking approaches indicate the location of white matter tracts within the human brain and have become a widely accepted technique for DTI visualization. Respective algorithms propagate lines through the tensor field, based on the local diffusion characteristics which reflect the course of the underlying white matter tracts. The resulting

fiber bundles approximate the location of neuronal fibers and are therefore a powerful tool for white matter reconstruction.

Most fiber-tracking approaches have a number of processing steps in common. First of all, seed points are selected within the volume, which may be positioned within regions of high FA, in regions of interest, or according to a specific seed-point selection scheme such as encountered in the case of evenly spaced streamlines. From each seed point, a fiber is propagated in a forward and backward direction, until certain termination criteria are met.

In each propagation step, the trajectory is extended on the basis of the underlying tensor information. In principle, two major techniques for line propagation have been established, namely *streamline propagation* [24, 99, 6] and *tensor deflection* [148, 152, 71]. In the case of streamline propagation, the tensor field is reduced to the field of the major eigenvector and streamline integration known from flow visualization is performed in the resulting vector field. Contrarily, tensor deflection takes advantage of the whole diffusion tensor and computes the new fiber direction as a product of the diffusion tensor and the last fiber direction.

In order to terminate fiber propagation, different techniques exist. A termination threshold based on FA is commonly used in order to stop propagation if the fiber leaves regions with anisotropic diffusion. Other criteria for streamline termination are a pre-defined maximum length in order to assure termination of the algorithm after a finite number of steps, or a maximum bending angle which assumes a certain straightness of the anatomical fibers. In Code Example 4.1, the pseudocode for fiber tracking in general is provided.

As an alternative, less common tracking techniques such as wavefront evolution [116, 50, 51] or probabilistic tracking [8] have been presented. The objective of these recent approaches is also to track pathways in subcortical or even cortical regions, where more isotropic tensors are present. Furthermore, regularization of the tensor data either during tracking with moving least-squares filters [160] or based on the tensor field [11, 77, 74], has been the subject of current research. The accurate treatment of crossing and branching fibers during fiber tracking is another important research topic [137, 158, 147]. An overview of different fiber-tracking techniques is provided in [100].

4.1.1 Streamline propagation and tensor deflection

Most fiber tracking algorithms take advantage of a streamline integration scheme or employ tensor deflection in order to propagate fibers. In this section, both techniques are outlined in more detail and the advantages and disadvantages of each approach are discussed.

Fiber tracking based on *streamline propagation* takes advantage of the major eigenvector of each tensor, which correlates with the direction of major diffusion. A schematic outline of streamline propagation is given in Figure 4.1. Streamline tracing is performed by stepwise integration of the diffusion field. In each step, the next position after a time

```
FiberTracking(fiberData) {  
    for (allSeedPoints) {  
        fiber = fiberData.StartNewFiber();  
        length = 0;  
        FWD = true;  
        BWD = true;  
  
        while (length < MAXLENGTH) {  
            // try to propagate fiber in fwd and bwd direction  
            success = PropagateFiber(fiber, FWD, BWD);  
  
            switch (success) {  
                case 3: length += 2;  
                case 2: length += 1;  
                       FWD = false;  
                case 1: length += 1;  
                       BWD = false;  
                case 0: break; // termination criterion reached  
            }  
        }  
    }  
}  
  
PropagateFiber(fiber, FWD, BWD) {  
    if (FWD) {  
        p = propagateForwardPoint(fiber);  
  
        if (faThreshold AND angleThreshold FULFILLED)  
            fiber.addForwardPoint(p);  
        else FWD = false;  
    }  
  
    if (BWD) {  
        p = propagateBackwardPoint(fiber);  
  
        if (faThreshold AND angleThreshold FULFILLED)  
            fiber.addBackwardPoint(p);  
        else BWD = false;  
    }  
  
    if (FWD && BWD) return 3;  
    if (BWD) return 2;  
    if (FWD) return 1;  
    return 0;  
}
```

Code Example 4.1: Pseudocode for fiber tracking.

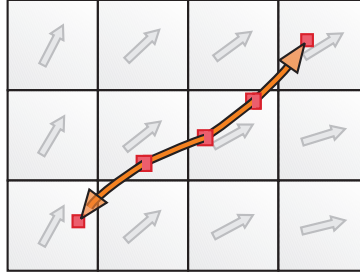


Figure 4.1: Schematic outline of fiber tracking based on streamline propagation. According to the underlying vector field, each streamline extends in forward and backward direction until a termination criterion is reached.

step Δt is computed based on the position $\mathbf{p}(t)$ and the direction of major diffusion $\mathbf{v}(\mathbf{p}(t))$ at time t :

$$\mathbf{p}(t + \Delta t) = \mathbf{p}(t) + \int_t^{t+\Delta t} \mathbf{v}(\mathbf{p}(t)) dt. \quad (4.1)$$

Since the vector field of the major eigenvectors $\mathbf{v}(\mathbf{p}(t))$ consists of experimental measurements, instead of a continuous function, numerical integration of $\mathbf{v}(\mathbf{p}(t))$ has to be performed. For this purpose, the Taylor series polynomial of $\mathbf{v}(\mathbf{p}(t))$ is constructed and employed instead of the integral in Equation 4.1. Replacing the integral with the respective Taylor series expansion yields the following equation:

$$\mathbf{p}(t + \Delta t) = \mathbf{p}(t) + \frac{\Delta t}{1!} \cdot \mathbf{v}(\mathbf{p}(t)) + \frac{(\Delta t)^2}{2!} \cdot \mathbf{v}'(\mathbf{p}(t)) + \frac{(\Delta t)^3}{3!} \cdot \mathbf{v}''(\mathbf{p}(t)) + \dots \quad (4.2)$$

In order to approximate the result of Equation 4.2, different integration schemes exist. The Euler integration scheme (also referred to as Runge-Kutta of order one) truncates Equation 4.2 after the first term of the Taylor expansion:

$$\mathbf{p}(t + \Delta t) = \mathbf{p}(t) + \Delta t \cdot \mathbf{v}(\mathbf{p}(t)) + O(\Delta t^2). \quad (4.3)$$

The resulting error $O(\Delta t^2)$ is determined according to the first term of the truncated part of the Taylor series expansion.

In order to achieve better accuracy, Runge-Kutta integration schemes of higher order [18, 120] are commonly employed. The order of the respective integration scheme denotes the number of summands of the Taylor series expansion considered for integration. The main idea behind the Runge-Kutta integration schemes is to eliminate the need for explicit computation of the derivatives in Equation 4.2. Instead, the Taylor series expansion up to some higher order is approximated by sampling the vector field at certain positions in a local neighborhood and by combining the information obtained. Implementations of the Runge-Kutta scheme for different orders are provided in [120].

In general, the higher the order of the integration scheme, the greater the accuracy of integration. However, in the case of measured data as encountered in the case of

DTI, accuracy is limited due to the discrete nature of the underlying data. For this reason, Runge-Kutta integration up to order four is commonly implemented in streamline-based fiber-tracking algorithms. An error analysis comparing different integration schemes for DTI fiber tracking is provided by [69, 70].

Fiber tracking based on streamline propagation using higher-order integration schemes makes it possible to propagate trajectories which approximate the course of underlying white matter structures. However, even higher-order integration does not prevent the streamlines from drifting away from the exact path due to numerical inaccuracies that accumulate during streamline propagation. Another limitation of fiber tracking is that bundles of crossing fibers represented by areas of planar anisotropy are not appropriately processed.

For this reason, an alternative technique denoted as *tensor deflection* was developed [148, 71, 152]. The main idea behind tensor deflection is to propagate a trajectory by multiplying the direction of the current segment d_{in} with the local diffusion tensor D , resulting in a deflected direction d_{out} indicating the direction of propagation:

$$d_{out} = D \cdot d_{in}. \quad (4.4)$$

This approach was developed in order to improve tracking results in regions with low FA, where the direction of fastest diffusion is not well defined. In areas of isotropic diffusion, the incoming direction will not be significantly deviated, whereas anisotropic tensors deflect v_{in} in the direction of the major eigenvector. This is shown in Figure 4.2, where an outline of fiber tracking based on tensor deflection is provided. The spherical tensors in the middle resulting from crossing fibers, have no impact on the propagation

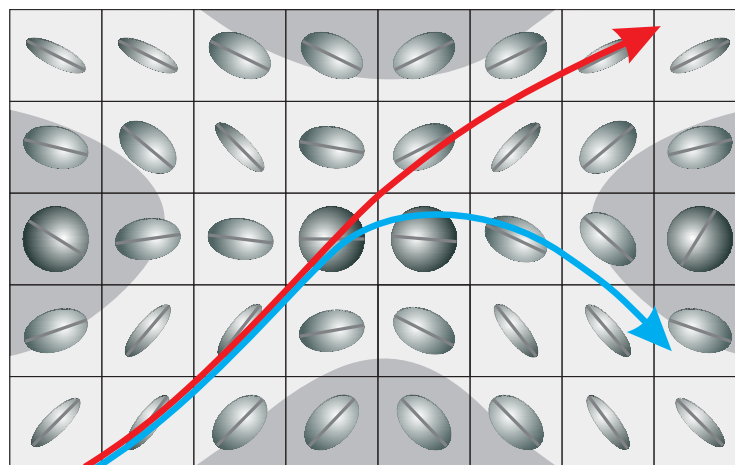


Figure 4.2: Schematic outline of fiber tracking based on tensor deflection (*red*) in comparison to streamline propagation (*blue*). Spherical tensors do not deflect the tracking direction, whereas streamline propagation follows a misleading major eigenvector.

direction in the case of tensor deflection (red). In comparison, fiber tracking based on streamline propagation (blue) follows the major eigenvectors of the spherical tensors, resulting in an erroneous path.

Fiber tracking using tensor deflection is based on the entire tensor information and takes into account both shape and orientation of the local tensor. The hope of tensor deflection is to achieve better processing of flat and rather spherical tensors, also enabling fiber tracking in cortical or sub-cortical regions. However, a closer look at the approach reveals that nevertheless severe disadvantages are encountered: First of all, the information conveyed by a spherical tensor is that all directions are equally probable. In the case of a rather spherical tensor, tensor deflection maintains the incoming fiber direction, which is not an appropriate interpretation of the tensor information, since only a single outgoing direction is considered. Furthermore, in the case of curved pathways, tensor deflection may underestimate the tract curvature [70].

For this reason, it is advisable to employ fiber tracking based on streamline propagation for the reconstruction of major tract systems, since streamline propagation achieves better preservation of the path curvature and provides more accurate results than tensor deflection [70]. For peripheral regions near the cortex, where the diffusion information is less pronounced due to crossing and diverging fibers, alternative approaches have been developed which take into account multiple directions in the case of isotropic tensors [40, 116, 8, 50, 51]. An example is the approach for connectivity analysis between functional regions presented in Chapter 5.

4.1.2 Tract-selection techniques

For the definition of separate tract systems which can be attributed to specific function, tract-selection approaches are required. A popular technique is to define regions of interest (ROIs) that cross the respective tract based on anatomical knowledge. Based on these ROIs, the fiber-tracking algorithm generates streamlines that cross the ROIs. A similar technique based on dynamic queries [1, 12] makes it possible to select specific tract systems interactively from a tracking of the whole brain, using box-shaped ROIs. In addition to that, clustering techniques have emerged which automatically generate bundles of fibers from a tracking of the whole brain [17, 98]. As a result, selection approaches provide mechanisms for fast and efficient extraction of separate tract systems.

In clinical application, regions of interest (ROIs) defined by a medical expert are preferably used for selecting specific tract systems [105]. In order to provide more flexibility for the application of ROIs, an implementation incorporating Boolean operators was chosen. Thereby, each ROI is associated with one of the Boolean operators AND, NOT or OR. In the case of the AND operator, the resulting fibers must cross the respective ROI. The NOT operator suppresses all fibers crossing the associated ROI, and the OR operator ensures that a fiber either runs through this OR ROI or through one of the other OR ROIs. As a result, this technique allows fast and efficient retrieval of specific tract systems such as the pyramidal tract, the optic tract or the corpus callosum for medical

application. In Figure 4.3, the application of ROIs with associated Boolean operators for the extraction of the pyramidal tract is demonstrated.

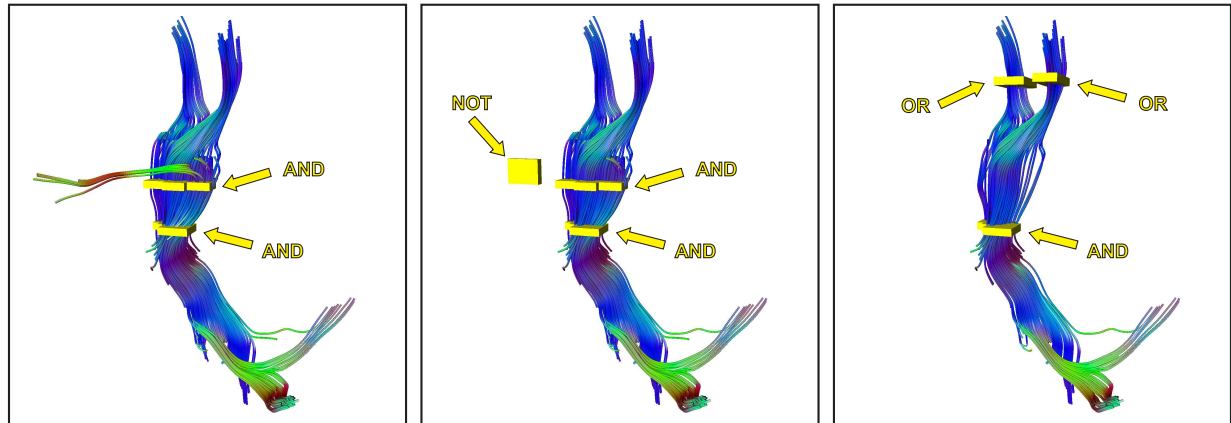


Figure 4.3: The pyramidal tract is reconstructed using ROIs associated with Boolean operators. Application of AND ROIs results in fibers crossing each AND ROI (*left*). The NOT ROI (*middle*) excludes fibers from the tracking result (*compare left and middle*). OR ROIs ensure that the fibers run through one of the specified OR ROIs (*right*).

4.2 Local regularization filters

In contrast to global filters which process the whole tensor dataset prior to fiber reconstruction (Section 3.5), local regularization filters [160] are applied during fiber tracking and move forward as the fibers are constructed. The idea behind local regularization filters is to provide more reliable tracking results by preserving directional consistency and at the same time cross noisy regions and gaps in the data. Compared to global filters, local regularization filters provide more flexibility since the filter parameters can be better adjusted to the data. In order to put more weight on the tensors in the direction of the tracked fiber, a moving filter window of ellipsoidal shape is employed. It is centered around the current end point of the fiber, and points in direction of the current fiber course. The size of the filter window is adjusted depending on the reliability of the local tensor data.

During fiber tracking, a local regularization approach is applied to the tensors in the filter window in order to approximate the local tensor. The resulting regularized tensor is used for tract propagation. For this purpose, a filter window is constructed as outlined in Section 4.2.1. The regularization scheme proposed by [160] is based on Gaussian weighting within the filter window (Section 4.2.2) in combination with a least-squares approximation scheme (Section 4.2.3). Results of local filtering are presented in Section 4.2.4.

4.2.1 Local filter window

In order to provide a convenient method of describing the filter window and all mathematical operations related to filtering, a local frame of reference is employed. Its origin \mathbf{p} corresponds to the center of the filter window, and the axes are aligned according to the semi-axes of the filter ellipsoid. The world coordinates (s_x, s_y, s_z) of a point \mathbf{s} are transformed to the respective local coordinates (ζ, η, θ) based on a rotation and translation transformation according to:

$$\begin{pmatrix} \zeta \\ \eta \\ \theta \end{pmatrix} = \mathbf{R}_p^{-1} \begin{pmatrix} s_x - p_x \\ s_y - p_y \\ s_z - p_z \end{pmatrix} = \mathbf{R}_p^{-1}(\mathbf{s} - \mathbf{p}), \quad (4.5)$$

where \mathbf{R}_p is the rotation matrix formed by the coordinate axes of the local coordinate system. The local filter ellipsoid is oriented according to the interpolated tensor \mathbf{D}_p located at \mathbf{p} , i.e. the rotation matrix $\mathbf{R}_p = \{e_1, e_2, e_3\}$ is formed by the eigenvectors of \mathbf{D}_p . In Figure 4.4, an outline of the filter window is provided, with the local coordinate system indicated in red. The tensor located at \mathbf{p} determines the shape of the local filter window. In order to compute the filtered tensor at \mathbf{p} , sample tensors at varying positions \mathbf{s} within the filter window are used and processed according to one of the approaches described in Section 4.2.2 and 4.2.3.

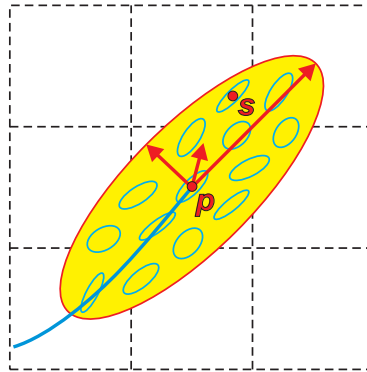


Figure 4.4: Local filter window; the domain of the filter window is indicated in yellow. The filtered tensor at the center \mathbf{p} is computed from tensor samples at different locations \mathbf{s} within the filter window.

4.2.2 Gaussian local regularization filter

In order to weight the tensors within the filter window, a Gaussian weighting function $G(\mathbf{s} - \mathbf{p}; \mathbf{D}_p)$ is introduced [160], which assigns a weight to a point position \mathbf{s} in the vicinity of the center point \mathbf{p} . The weighting function has the effect that tensors located close to the center of the filter window have a higher impact on the regularization result

than tensors at the border of the filter window. In the local frame of reference, the Gaussian weighting function can be expressed in terms of the local coordinates ζ , η and θ according to:

$$G(\mathbf{s} - \mathbf{p}; \mathbf{D}_p) = G(\mathbf{R}_p\{\zeta, \eta, \theta\}; \mathbf{D}_p). \quad (4.6)$$

The shape of the Gaussian filter window is adapted from the tensor ellipsoid associated with the local tensor \mathbf{D}_p at the center point \mathbf{p} . For this reason, a tensor at the coordinate (ζ, η, θ) in the local (translated and rotated) frame of reference is weighted by the Gaussian filter window according to:

$$G(\mathbf{R}_p\{\zeta, \eta, \theta\}; \mathbf{D}_p) = e^{-\left(\left(\frac{\zeta}{\sigma a}\right)^2 + \left(\frac{\eta}{\sigma b}\right)^2 + \left(\frac{\theta}{\sigma c}\right)^2\right)}, \quad (4.7)$$

where σ denotes the scaling factor of the filter ellipsoid and a , b and c the length of the ellipsoid semi-axes. As outlined in Section 3.3.2, the length of the semi-axes of a diffusion ellipsoid is proportional to the square root of the associated eigenvalues of the tensor. Since the Gaussian filter window is adapted to the shape of the local tensor \mathbf{D}_p , its semi-axes are scaled in the same way:

$$a = \sqrt{\lambda_1[\mathbf{D}_p]}, \quad b = \sqrt{\lambda_2[\mathbf{D}_p]}, \quad c = \sqrt{\lambda_3[\mathbf{D}_p]}. \quad (4.8)$$

In order to approximate the tensor $\bar{\mathbf{D}}_p$ at position \mathbf{p} from the tensors in the local neighborhood using the Gaussian filter window in Equation 4.7, the weighted average of the tensors within the filter volume is computed according to:

$$\bar{\mathbf{D}}_p = \frac{1}{V} \int_V \mathbf{D}(\mathbf{p} + \mathbf{R}_p\{\zeta, \eta, \theta\}) \cdot G(\mathbf{R}_p\{\zeta, \eta, \theta\}; \mathbf{D}_p) d\zeta d\eta d\theta, \quad (4.9)$$

where $\mathbf{D}(\mathbf{p} + \mathbf{R}_p\{\zeta, \eta, \theta\})$ refers to the tensor at a position \mathbf{s} with local coordinates (ζ, η, θ) . In order to evaluate the integral, the filter window is sampled and tensors are computed at discrete coordinate positions using component-wise interpolation of the tensor entries (Section 3.4). For fiber tracking, the filtered tensor $\bar{\mathbf{D}}_p$ is used as a substitute for the original, noisy tensor \mathbf{D}_p , resulting in regularized fiber trajectories.

4.2.3 Moving least-squares filter

The local filtering scheme based on Gaussian filtering in Section 4.2.2 is extended by a least-squares approximation within the filter window [160]. Least-squares approximation aims at minimizing an error functional E which measures the quality of a polynomial fit of the data:

$$E(\mathbf{p}) = \frac{1}{V} \int_V G(\mathbf{s} - \mathbf{p}; \mathbf{D}_p) \cdot \left[\mathbf{F}(\mathbf{s} - \mathbf{p}) - \mathbf{D}(\mathbf{s}) \right]^2 d\mathbf{s}^3. \quad (4.10)$$

In order to solve this equation, a low degree polynomial \mathbf{F} has to be found which best approximates the data $\mathbf{D}(\mathbf{s})$ at different locations \mathbf{s} within the filter window centered

around \mathbf{p} . The quality of fit in a least-squares sense is assessed by the functional E , which must be minimized. The impact of a point location on the functional E is controlled by the filter function $G(\mathbf{s} - \mathbf{p}; \mathbf{D}_p)$.

After transforming all point locations to the local frame of reference in Equation 4.5, the polynomial fit in Equation 4.10 can be rewritten as:

$$E(\mathbf{p}) = \frac{1}{V} \int_V G(\mathbf{R}_p\{\zeta, \eta, \theta\}; \mathbf{D}_p) \cdot \left[\mathbf{F}(\mathbf{R}_p\{\zeta, \eta, \theta\}) - \mathbf{D}(\mathbf{p} + \mathbf{R}_p\{\zeta, \eta, \theta\}) \right]^2 d\zeta d\eta d\theta. \quad (4.11)$$

The low degree polynomial \mathbf{F} is a linear combination of tensor basis functions A_{mnp} . For a set of local coordinates (ζ, η, θ) , the weighted sum of the basis functions yields the approximated tensor at this position:

$$\mathbf{F}(\mathbf{R}_p\{\zeta, \eta, \theta\}) = \sum_{mnp}^N A_{mnp} \zeta^m \eta^n \theta^p. \quad (4.12)$$

In order to obtain the tensor basis functions A_{mnp} which provide a smooth approximation of the tensor data in the filter window, Equation 4.11 must be solved. The least-squares fitting procedure is described in more detail in [160].

For fiber tracking, the original, noisy tensor \mathbf{D}_p is approximated with the polynomial fit \mathbf{F} at position \mathbf{p} . Since the position of \mathbf{p} in the local frame of reference corresponds to the origin, the approximated tensor $\bar{\mathbf{D}}_p$ evaluates to the first tensor basis function:

$$\begin{aligned} \bar{\mathbf{D}}_p &= \sum_{mnp} A_{mnp} \zeta^m \eta^n \theta^p \Big|_{\zeta=\eta=\theta=0} = \\ &= A_{000} \underbrace{0^0 0^0 0^0}_{=1} + A_{100} \underbrace{0^1 0^0 0^0}_{=0} + \dots + A_{NNN} \underbrace{0^N 0^N 0^N}_{=0} = \\ &= A_{000}. \end{aligned} \quad (4.13)$$

4.2.4 Results

The local filtering techniques in Section 4.2.2 and Section 4.2.3 were employed in order to reconstruct major tract systems, namely the pyramidal tract, the optic tract and the corpus callosum in various patient and proband datasets. In Figure 4.5, the result of fiber tracking without local filtering (left), with a Gaussian local regularization filter (middle) and with a moving least-squares filter (right) is shown. In each case, streamline propagation using Euler integration (RK-1) was employed. For both local filtering approaches, the moving filter windows were scaled with a factor $\sigma = 50$ and tensor samples within the filter window were taken at a distance of 1 mm for each dimension in 3D space. In the case of the least-squares filter, a polynomial of degree 2 was applied for the approximation.

In order to assess the quality of local filtering using either the Gaussian local regularization filter (Section 4.2.2) or the moving least-squares filter (Section 4.2.3), both

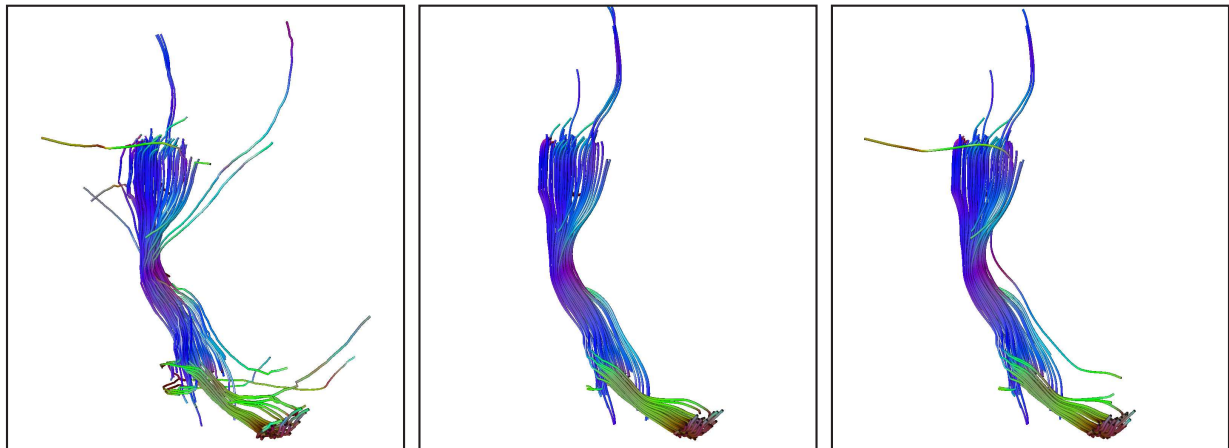


Figure 4.5: Pyramidal tract reconstructed with streamline integration (RK-1) without filtering (*left*), with a Gaussian local regularization filter (*middle*), and with a moving least-squares filter (*right*).

techniques were compared to fiber-tracking results without filtering. For this purpose, streamlines were traced until a termination criterion was reached, and the final sampling point of the fiber was used as the starting point for a reverse fiber, running in the opposite direction. Depending on the quality of the tracking approach applied, the reverse fiber closely follows the original fiber for a certain number of steps, before it diverges from the course of the original fiber. As a consequence, the distance between corresponding sampling points of the original fiber and the reverse fiber indicates the quality of the respective tracking approach. In order to obtain significant results, a set of streamlines and associated reverse fibers was computed and the results were averaged. The diagram in Figure 4.6 (right) shows the averaged divergence between original and reverse fibers for streamline propagation without filtering, with a Gaussian local regularization filter and with a moving least-squares filter. In Table 4.1, the divergence after 50 integration steps as well as the computing times on a PC equipped with an Intel Pentium 4, 3.4 GHz, and 2 GB RAM are provided.

	Time	Divergence		Time	Divergence
RK-1 none	4 sec	8.61 mm	RK-1 none	4 sec	8.61 mm
RK-2 none	11 sec	1.46 mm	RK-1 Gauss	242 sec	5.91 mm
RK-4 none	18 sec	1.27 mm	RK-1 MLS	464 sec	5.88 mm

Table 4.1: For a tracking of the whole brain, the computing time for different integration schemes without filtering (*left*) and with a Gaussian local regularization filter and a moving least-squares filter (*right*) are provided. Additionally, the average divergence between the original fiber and the reverse fiber after 50 integration steps is specified.

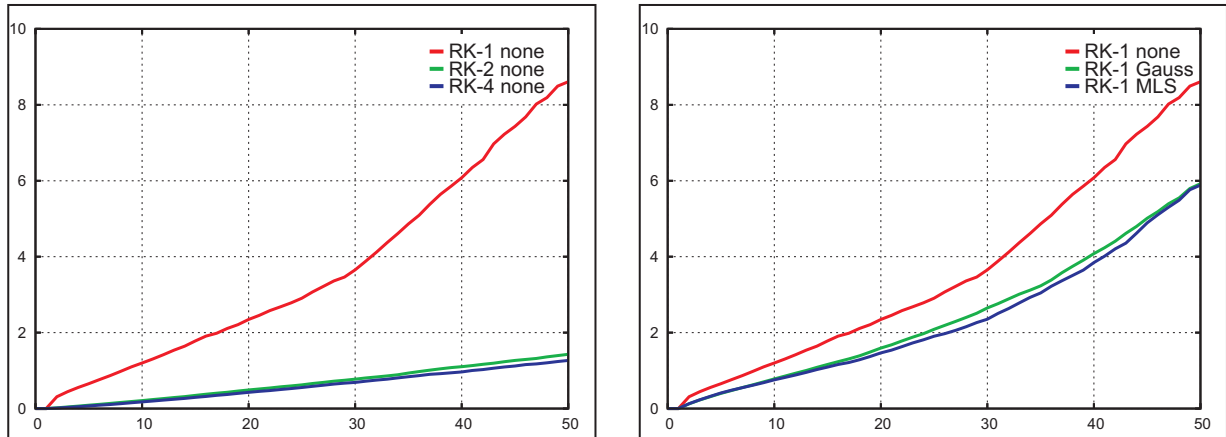


Figure 4.6: Divergence between original fiber and reverse fiber for 50 integration steps, averaged for all fibers in a tracking of the whole brain. *Left*: Comparison of different integration schemes (RK-1, RK-2 and RK-4). *Right*: Comparison of RK-1 integration without local filter (RK-1 none), with local Gaussian filter (RK-1 Gauss) and with moving least-squares filter (RK-1 MLS).

From the diagram in Figure 4.6 (right), it can be concluded that the Gaussian local regularization filter provides similar accuracy to that of the moving least-squares filter, i.e. the computational effort added by the least-squares approximation has only a very slight impact on the accuracy. Taking into account the computing time in Table 4.1 (right), which is much higher in the case of least-squares approximation, it can be concluded that the Gaussian local regularization filter is much more suitable for practical application.

In principle, the local filters improve the tracking accuracy of the respective integration scheme, as shown in Figure 4.6 (right) for streamline tracking based on first order Runge-Kutta integration. However, for a higher-order integration scheme, such as second or fourth order Runge-Kutta in Figure 4.6 (left), even greater accuracy is obtained compared to the lower-order integration in combination with local filters. For this reason, it is more feasible to apply higher-order integration instead of a lower-order integration scheme combined with local filters.

4.3 Fiber tracking using evenly spaced streamlines

Apart from the techniques for propagating fibers through the tensor field presented in the previous section, another important issue in order to obtain meaningful fiber-tracking results is the selection of seed points. In standard fiber tracking, the seed points are commonly positioned in voxels of high FA or in ROIs. However, due to the diverging nature of white matter tract systems, the density of the reconstructed streamlines

varies over the domain in an uncontrolled manner, resulting in sparse areas as well as closely packed regions. In regions containing only a limited number of streamlines, features of the data may remain concealed. Many white matter tracts such as the pyramidal tract ascending from the brain stem to the cortex, diverge as they reach the cortex. As a result, the distribution of generic streamlines becomes sparser as they approach sub-cortical regions of the brain, providing only rare information about the location of white matter. For this reason, the placement of the initial seed points is a critical factor with regard to the effectiveness of fiber-tracking approaches.

To overcome the general problem of seed-point selection, the concept of evenly spaced streamlines for effective user-controlled streamline placement has been presented in the literature [53, 146]. The benefits of this approach were adapted to fiber tracking [147] to obtain uniformly distributed streamlines. In this way, the features contained within the data are better captured. This approach was extended with an adaptive control of the separating distance between single streamlines, depending on the local FA value. In this way, dominant tract systems are visually emphasized and are perceptually more apparent. Additionally, a multi-step technique for ROI-based fiber tracking using evenly spaced streamlines was developed. Both approaches were published in [91].

In this section, an outline of the algorithm for evenly spaced streamlines is provided (Section 4.3.1). The approach for adaptive density control is presented in Section 4.3.2, and special features for extracting separate tract systems using ROIs are covered in Section 4.3.3.

4.3.1 Standard approach for evenly spaced streamlines

The main idea behind evenly spaced streamlines [53, 146] is to propagate trajectories until a user-defined density level is reached. As a result, a regular distribution of fibers is obtained, and areas with an otherwise sparse distribution of trajectories are filled. For the reconstruction of white matter tracts, this is an important characteristic in order to capture all features, i.e. locations of white matter, within the data.

The general outline of the algorithm for evenly spaced streamlines is as follows: First, an initial streamline is computed and new seed points with distance d_{seed} to the initial streamline are defined. Starting at these seed points, new streamlines are propagated in both a forward and backward direction. In order to ensure that streamlines do not come closer to each other than the separating distance d_{sep} , an additional termination criterion is introduced which checks the distance to nearby streamlines after each integration step. Thereby, d_{seed} is slightly higher than d_{sep} to prevent the new streamline from terminating immediately after the first step.

Compared to standard fiber tracking, the algorithm for evenly spaced streamline placement comprises additional processing steps, namely distance control between adjacent fibers and selection of additional seed points, which are outlined in the following. Finally, results are presented which demonstrate the benefit of the approach for the reconstruction of neuronal pathways.

Distance control

The distance check is performed after each propagation step to verify whether the streamline gets too close to another one. In order to obtain acceptable computation times for distance control, only the sample vertices of the streamline are considered. A simple check would test a new streamline vertex p against all sample vertices of all other streamlines, which would be rather inefficient. This is circumvented by using a Cartesian grid with voxel size d_{sep} superimposed on the domain [147]. In order to obtain all vertices that are potentially closer than d_{sep} to p , the voxel containing p as well as the neighboring voxels are determined. For each vertex the distance to p is computed and compared to the separating distance d_{sep} . In the case of a distance less than d_{sep} , streamline propagation is aborted.

The test becomes even more efficient, if the number of distance computations is minimized. For this purpose, the order in which the surrounding voxels and the referred vertices are processed is optimized [91]. For vertices contained within the center voxel, the probability that they are closer to p than d_{sep} is very high, so this voxel is processed first. The voxels sharing a face with the center voxel are processed next, followed by voxels sharing an edge. Finally, the diagonally adjacent voxels only sharing a vertex with the center voxel are examined.

Another point to mention is that the step size for streamline integration and d_{sep} are not fully independent. Since only the distance between sample vertices of the streamlines is computed and not the actual distance to the segments of another streamline, d_{sep} should not be smaller than the step size for fiber tracking. This guarantees that a vertex will not be located much closer to a fiber segment than d_{sep} .

Selection of seed points

In order to fill the domain with equally spaced fibers, new seed points are defined based on existing streamlines. For this purpose, new seed points are determined after completing a streamline, before continuing with another one. The new seed points are defined at a distance d_{seed} from the sample vertices of the current trajectory. They are added to a queue which stores the seed points and controls the order in which seed points are processed.

Since the algorithm for evenly spaced streamlines was originally designed for 2D [53, 146], it has to be extended to three dimensions in order to serve for the reconstruction of neuronal pathways. To obtain new seed points in the vicinity of a sample vertex, the adjacent streamline segments are averaged to obtain the normal of the plane where the new seed points will be placed. The approach for seed-point placement is outlined in more detail in [91]. Finally, the seed-point coordinates are added to the queue, provided that the FA value at each seed point is high enough for tracking.

Results

The approach for evenly spaced streamlines provides fibers equally distributed in white matter regions. In Figure 4.7, a standard fiber tracking of the whole brain (left) in comparison to fiber tracking using evenly spaced streamlines (middle, right) is shown. In the case of standard fiber tracking, seed points were located in voxels with a high FA value. Figure 4.7 clearly shows that standard fiber tracking produces regions of sparse fiber density as well as closely packed areas. Contrarily, fiber tracking incorporating evenly spaced streamlines provides a constant fiber density and therefore an unbiased representation of the data.

The computing time for standard tracking (left) amounted to 8 sec, on a PC equipped with an AMD Athlon (1.2 GHz). In the case of evenly spaced streamlines, the computation time for a spacing of $d_{sep} = 0.5$ mm (middle) was 134 sec. For a spacing of $d_{sep} = 1.5$ mm (right), the computation time amounted to 23 sec.

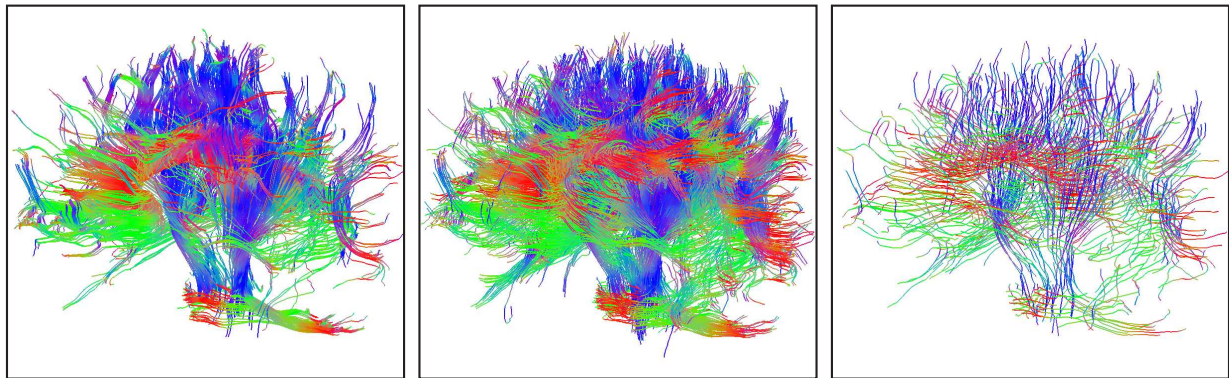


Figure 4.7: Comparison of standard fiber tracking (*left*) and tracking based on evenly spaced streamlines with density $d_{sep} = 0.5$ mm (*middle*) and $d_{sep} = 1.5$ mm (*right*).

4.3.2 Adaptive control of the separating distance

The standard approach for evenly spaced streamlines takes advantage of the separating distance d_{sep} in order to achieve a regular distribution of fibers. However, for surgical application, major tract systems associated with specific function are of primary interest. In a tracking of the whole brain, small peripheral fiber bundles occlude the major pathways and hamper medical interpretation. For this reason, an approach for adaptive distance control is described in this section, which was published in [88].

Since major white matter tracts are composed of dense bundles of coherent nerve fibers, high anisotropic diffusion is encountered in these areas. This information can be used during fiber tracking in order to control the separating distance between the streamlines, resulting in a more comprehensive tracking result. Adaptive density control generates fibers of higher density in areas of anisotropic diffusion, and reduces the

fiber density in more isotropic regions. Thereby, dominant fiber structures characterized by high anisotropic diffusion are visualized with dense streamlines and are still visible in spite of surrounding small fiber bundles. Consequently, attention is drawn to the major fiber bundles, which become visually much more apparent.

From the implementation point of view, some extensions of the original approach for evenly spaced streamlines are required. Since the FA value is in the range between 0 and 1, where high values indicate anisotropic regions, the factor $(1 - FA)$ is used as a distance weight. The values d_{sep-a} and d_{seed-a} for adaptive density control are obtained by multiplying the initial distance control values d_{sep} and d_{seed} with this distance weight. Additionally, a lower limit for d_{sep-a} and d_{seed-a} has to be defined in order to prevent these values from dropping below the step size for fiber tracking. The grid with voxel size d_{sep} superimposed on the domain remains the same, since the adaptive distance d_{sep-a} is less than or equal to d_{sep} . For regions of high density, the grid is in fact coarser than actually required, which leads to a higher number of distance checks than necessary.

Results

A comparison between tracking of the whole brain using evenly spaced streamlines with different levels of adaptive distance control is provided in Figure 4.8. The approach for adaptive spacing ensures that major tract systems with a high anisotropic diffusion are represented with dense streamlines. The pyramidal tract (left, see arrows) as well as the fibers of the corpus callosum (middle, see arrows) can be clearly identified.

In each image, the density d_{sep-a} varies between 0.5 mm which is the step size for fiber tracking and 2 mm (left), 3 mm (middle) and 5 mm (right). On a PC equipped with an AMD Athlon (1.2 GHz), computing times were 142 sec, 98 sec and 58 sec.

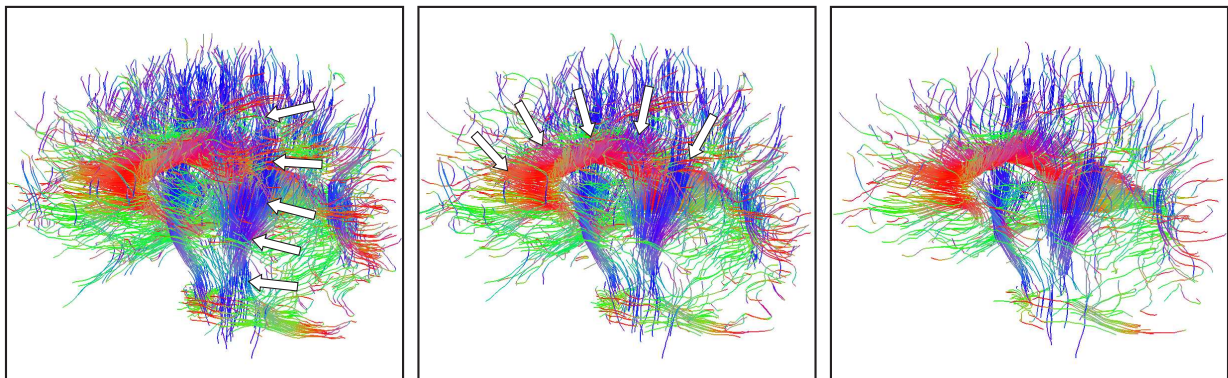


Figure 4.8: Adaptive distance control for tracking using evenly spaced streamlines emphasizes dominant tract systems with dense streamlines. The spacing d_{sep-a} between adjacent streamlines is adjusted depending on the local FA and varies between 0.5 mm and 2 mm (left), 3 mm (middle) and 5 mm (right).

4.3.3 ROI based tracking using evenly spaced streamlines

As outlined in Section 4.1.2, ROIs are an essential technique for obtaining separate tract systems associated with specific function. However, the approach for evenly spaced streamlines is originally not adequate for the combination with ROI tracking because of the following reasons: First of all, the approach for evenly spaced streamlines causes streamlines to terminate early if they get too close to each other. For this reason, only a few streamlines fulfill the ROI conditions, especially if multiple ROIs are used. Additionally, shorter streamlines filling gaps between longer streamlines are not maintained since they do not cross the ROIs themselves.

In order to overcome these problems and to integrate evenly spaced streamlines into standard fiber tracking, the following approach was implemented: In a first iteration, a set of fibers fulfilling the ROI conditions is computed using evenly spaced streamlines. Based on this initial set of fibers, a further generation of evenly spaced streamlines is generated in a second pass. Since these fibers are generated regardless of the ROIs, they are able to fill sparse regions between the initial set of fibers. A second generation of evenly spaced streamlines may be computed based on the first generation, and so on. This iterative process makes it possible to reconstruct a dense white matter bundle based on the initial set of streamlines. However, the number of generations of evenly spaced streamlines should be low to avoid expansion to undesired areas.

Results

In Figure 4.9, the strategy for ROI tracking based on evenly spaced streamlines is shown for the pyramidal tract in a healthy volunteer. In a first step, the initial set of fibers is computed, taking into account the user-defined ROIs for the pyramidal tract (left). In

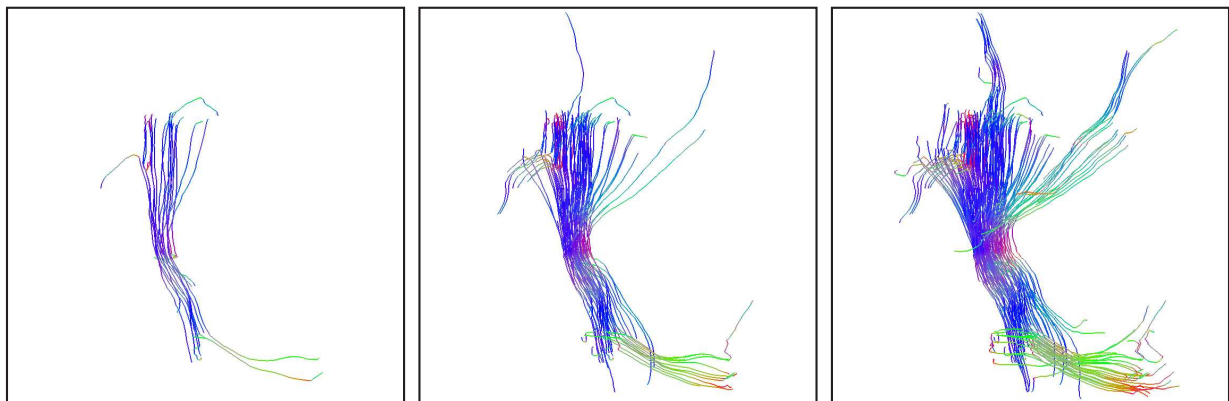


Figure 4.9: ROI tracking of the pyramidal tract (*left*), first (*middle*) and second (*right*) generation of evenly spaced streamlines. Incorporation of evenly spaced streamlines into ROI tracking provides dense tracts.

a second pass, the first generation of evenly spaced streamlines filling sparse regions is generated (middle). A third pass based on the initial fiber bundle and the first generation of evenly spaced streamlines fills the volume further (right). With this technique, the concept of evenly spaced streamlines was adapted to ROI tracking providing dense tracts capturing the features within the data.

4.4 Directional Volume Growing

The fiber-tracking approaches presented in the previous sections generate fiber bundles which approximate the shape and location of major white matter tracts. The reconstructed fiber tracts provide a good impression of the spatial relation of fibers and anatomy and are therefore a valuable supplement for neurosurgical planning. However, even higher-order integration schemes do not prevent the trajectories from drifting away from the exact path due to numerical inaccuracies that accumulate during streamline propagation. Another limitation of fiber tracking is that crossing bundles in areas of planar anisotropy are not comprehensively represented.

For this reason, an alternative approach for reconstructing major tract systems denoted as directional volume growing was developed and published in [87]. The approach is intended to overcome the limitations of fiber tracking by expanding a volume encompassing white matter tracts based on the local tensor information. Instead of a bundle of fibers approximating the shape of the tract system, a volume is generated which contains neuronal structures.

This section is organized as follows: In Section 4.4.1, the strategy for directional volume growing is presented which enables the extraction of separate tract systems. Experimental results using different datasets are provided Section 4.4.2.

4.4.1 Algorithm for directional volume growing

The basic idea of directional volume growing is to expand a volume of interest containing neuronal structures based on the local tensor information. In contrast to standard fiber tracking, where only a single direction is derived in each propagation step, the volume may expand in multiple directions in the case of planar or rather spherical tensors. In this way, the information content provided by rather isotropic tensors is more appropriately processed.

In general, volume-growing algorithms start from a predefined seed region and spread out within the volume until some terminating criterion is reached. In the case of directional volume growing based on diffusion tensor data, the shape of the local tensor controls the direction in which the process expands. The local FA value is used as a threshold in order to prevent the volume from expanding to isotropic regions. The seed regions required for directional volume growing are identical to the ROIs specified for fiber tracking, and are defined based on anatomical landmarks. However, in this case only AND ROIs are possible. In order to expand the volume, the algorithm starts from

each voxel within the ROI and adds neighboring voxels to the initial volume. For this purpose, the diffusion characteristics of the underlying diffusion tensor are taken into account (more details are provided in [87]):

Anisotropic diffusion

In the case of anisotropic tensors with a dominating barycentric space coordinate for linear diffusion c_l , directional volume growing expands the volume in the direction of the principal eigenvector. For this purpose, the algorithm computes all vectors pointing from the center of the current voxel to the centers of the immediate neighboring voxels. A neighboring voxel is added to the growing volume, if two threshold requirements are met:

- (1) The FA value of the neighboring voxel must be above a predefined threshold.
- (2) The angle between the principal eigenvector and the vector pointing to the respective neighboring voxel must be below a specified threshold.

For reasons of symmetry, it is sufficient to check the angle for only 13 of the 26 neighboring voxels. If a neighboring voxel fulfills the angle threshold criterion, this neighboring voxel as well as its opposite voxel is added to the volume.

Isotropic diffusion

In the case of a dominating barycentric space coordinate for planar diffusion c_p , the algorithm tries to enlarge the grown volume in a plane according to the planar shape of the tensor. For this purpose, the third eigenvector is used as a normal vector n of the plane containing the principal and second eigenvector. For each neighboring voxel, the angle between the normal and the vector pointing to the neighboring voxel is determined, and 90 degrees are subtracted in order to obtain the offset angle to the ellipsoid plane. In the same way as for linear diffusion, the associated neighboring voxel is added to the grown volume if this angle is below a specified threshold.

4.4.2 Results

In order to compare fiber tracking based on streamline propagation and directional volume growing, both techniques were applied for the reconstruction of the pyramidal tract in brain tumor patients. On a PC equipped with an Intel Pentium 4, 2.4 GHz, the computing times for directional volume growing were in the range of 40-60 seconds.

In Figure 4.10, conventional volume growing (left) in comparison to iso-surface extraction based on FA values (right) is shown for DTI data of a healthy volunteer. The fragmented nature of the iso-surface makes it difficult to identify clearly connectivity information which is important for surgery. In contrast, conventional volume growing

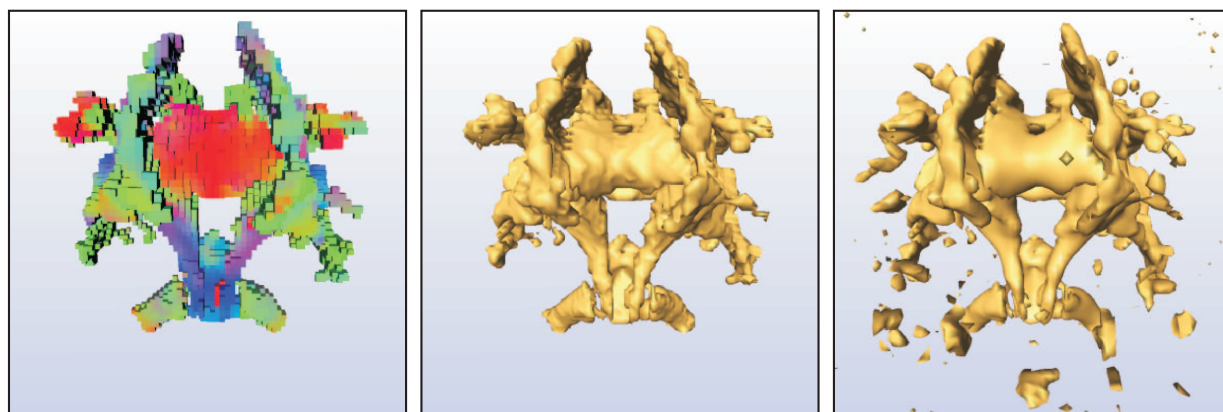


Figure 4.10: Conventional volume growing in healthy volunteer starting from a central seed region: Connected volume of high FA within the whole brain (*left*) and iso-surface extracted from the binary volume (*middle*). Iso-surface extraction of the original FA dataset (*right*).

produces a connected volume without any detached parts. The resulting visualization is further improved after iso-surface extraction based on the binary volume (middle).

In Figure 4.11, fiber tracking and directional volume growing is shown for two tumor patients, where the pyramidal tract passes very close to the tumor. The streamline representation (left) already indicates a close spatial relation between tumor and fiber tract. Additionally, the directional-volume-growing result (middle) clearly shows the volume occupied by white matter in the vicinity of the tumor. A comparison of both representations (right) shows that the tracking algorithm computes streamlines which are completely encompassed by the volume obtained from directional volume growing (in both cases the same FA threshold was applied). This observation indicates that fiber tracking is able to represent the overall shape of the tract, in spite of numerical inaccuracies during line propagation. However, the volume derived by the growing procedure presented occupies more space than revealed by the fiber bundles. Consequently, directional volume growing provides a more conservative estimate of the volume potentially containing fibers.

As demonstrated in the case of different patients, directional volume growing is an adequate tool for estimating the entire volume occupied by white matter tracts within the human brain. The design of the approach aims at obtaining a better evaluation of the tensor information in more isotropic regions, e.g. in voxels containing crossing fibers. In comparison to conventional fiber-tracking approaches, the strategy presented provides a more conservative estimate of the critical volume filled with white matter. For this reason, the resulting representation is of high value for clinical application in neurosurgery.

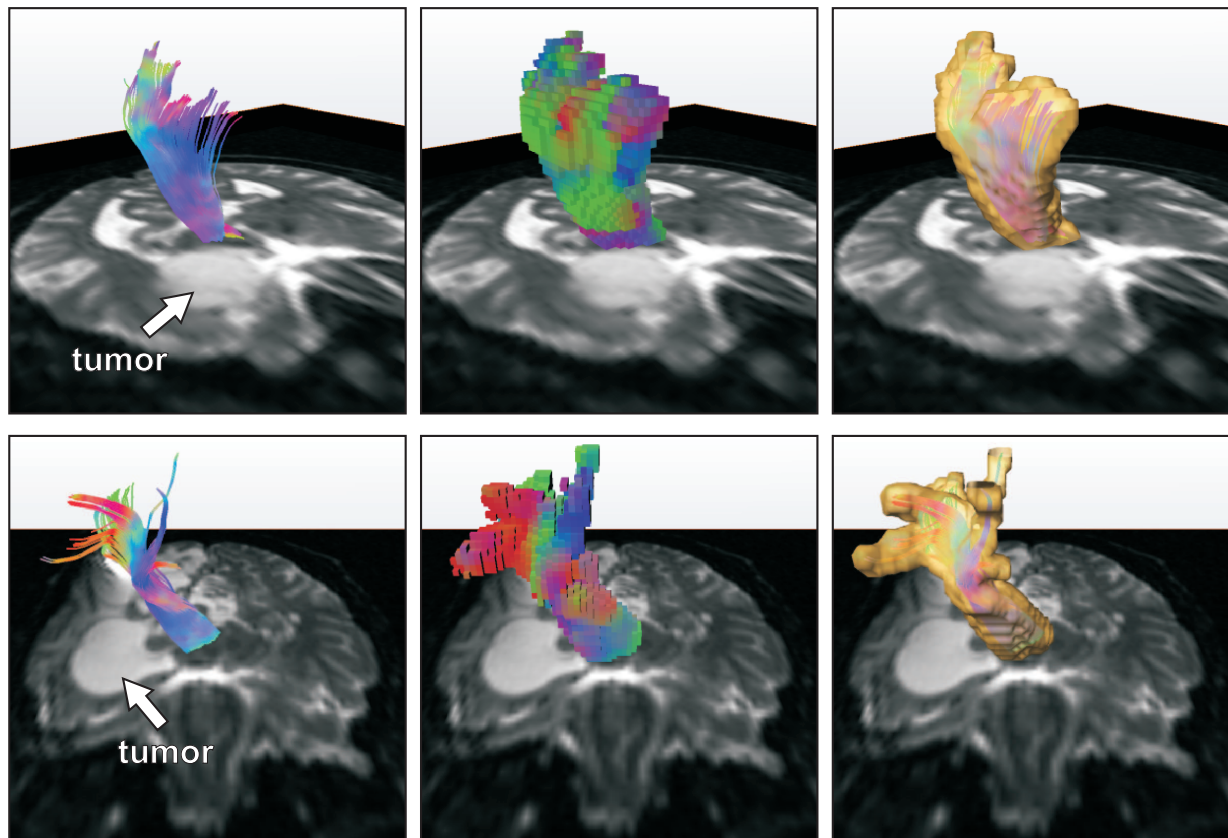


Figure 4.11: Visualization of pyramidal tract in two tumor patients (top/bottom) assigning RGB colors to the x,y,z -coordinates of the normalized principal eigenvector: Fiber tracking (*left*), directional volume growing showing binary volume (*middle*), overlay of fiber tracking and iso-surface derived from binary volume after directional volume growing (*right*).

4.5 Discussion

In this chapter, different approaches for the reconstruction of major white matter tracts were presented and evaluated. These approaches comprise techniques for fiber tracking based on streamline propagation or based on tensor deflection. ROIs defined by the user based on anatomical knowledge are used in order to extract separate tract systems. Oriented filters are used during fiber tracking in order to regularize the tensor field during streamline propagation in a local neighborhood. Another extension for fiber tracking is a mechanism for distance control between single trajectories, which is based on the concept of evenly spaced streamlines. Finally, an approach denoted as directional volume growing is presented, which expands a volume instead of single trajectories. In contrast to fiber tracking, the volume is expanded in multiple directions, depending on the underlying tensor information.

The fiber-tracking approaches presented at the beginning of the chapter are a commonly accepted technique for the reconstruction of major white matter tracts. The resulting fiber bundles approximate the shape of major tract systems and are a valuable source of information for surgical planning. However, in the case of crossing or branching fibers represented by planar or spherical tensors, fiber tracking is not able to model fibers appropriately. In the case of streamline propagation, jagged paths are generated in more isotropic regions because of the flipping direction of the major eigenvector of planar or spherical ellipsoids. The approach for tensor deflection is less sensitive to directional changes of the major eigenvector; in the case of spherical tensors, the direction of propagation is maintained. To sum up the characteristics of streamline propagation and tensor deflection, the advantage of streamline propagation is that it is better able to follow curved pathways, whereas tensor deflection is less sensitive to isotropic regions.

However, in both cases a decision for a single direction is taken, which is not an appropriate interpretation of planar or spherical tensors, where multiple directions of equal probability exist. For this reason, fiber tracking should be restricted to regions of anisotropic diffusion, where the direction of main diffusion is unambiguous. Due to the high anisotropic diffusion encountered in these regions, it is advisable to use fiber tracking based on streamline propagation, which is better able to follow curved paths. For the major tract systems considered in this chapter, strong anisotropic diffusion is encountered. For this reason, fiber-tracking algorithms are capable of recovering the underlying neuronal structures to a satisfactory extent in these cases, as reported in a tracer experiment [28] and in clinical studies [9, 56, 105]. In order to construct neuronal connections in sub-cortical regions, alternative approaches exist, such as the algorithm for connectivity analysis presented in the next chapter.

The approach for oriented filters aims at improving the accuracy of fiber tracking. A local filter window is constructed and evaluated in order to approximate the local tensor, based on the tensor information in a local neighborhood. In this way, the fiber-tracking algorithm is less sensitive to noise, and crossing fibers are better processed. According to the evaluations presented in this chapter, oriented filters improve the accuracy of the respective integration scheme. However, oriented filters require a high level of computational effort, especially for higher-order integration schemes. In the case of Euler integration, the accuracy obtained with oriented filters is achieved just as well with higher-order integration, which involves less computational effort. For this reason, it is more advisable to use a higher-order integration scheme (such as RK-2 or RK-4) instead of RK-1 integration combined with oriented filters.

Apart from line propagation schemes, seed-point selection is another important issue for the reconstruction of fiber bundles. The concept of evenly spaced streamlines, which was originally developed for flow visualization, enables a more comprehensive representation of the data. Evenly spaced placement of seed points as well as early termination of streamlines, if a distance threshold is violated, results in fibers equally dis-

tributed over the domain. In this way, sparse regions are filled and all features within the data are captured. A possible limitation of fiber tracking based on evenly spaced streamlines relates to the step size for tracking. In order to ensure an even spacing between single streamlines, either fiber tracking with fixed step size is required, or at least an upper limit for the maximum step size which is below the separating distance d_{sep} , in the case of tracking with adaptive step size.

The basic approach for evenly spaced streamlines was extended to include a mechanism for adaptive control of the separating distance between single streamlines, and an approach for ROI tracking. Adaptive density control helps to visually emphasize dominant tract systems in areas of high anisotropy, which would otherwise be occluded by more peripheral small fiber tracts. In order to combine the concept of evenly spaced streamlines with ROI-based tracking, a multi-stage approach was presented. Since streamlines are commonly terminated early in order to fulfill the spacing criterion, the fiber bundle resulting from ROI tracking is only sparse. In a first and second iteration, evenly spaced streamlines are generated in order to enhance the reconstructed fiber tract. This approach allows the extraction of separate tract systems based on ROIs, which are generated with the concept of evenly spaced streamlines.

The approach for directional volume growing presented at the end of this chapter, is an extension towards multiple directions. In order to implement expansion to several directions, a volume encompassing neuronal structures is constructed, instead of single trajectories. Limitations of the approach relate to the percentage of planar tensors, which is commonly low in DTI datasets. For this reason, expansion to multiple directions plays only a minor role in the reconstruction of major tract systems. Nevertheless, this technique is a first step towards tract reconstruction taking into account multiple directions per voxel, depending on the underlying tensor information. This idea is pursued further in the next chapter, where a graph structure is built and employed for connectivity analysis between functional regions.

Chapter 5

Connectivity analysis between functional regions

The fiber-tracking techniques presented in the previous chapter are well suited for the reconstruction of major tract systems composed of thick bundles of coherent fibers, such as the pyramidal tract, the optic tract or the corpus callosum. However, in areas near the cortex where small tract systems such as the arcuate fasciculus are located, crossing and branching fibers occur more frequently. As a result, the direction of diffusion is less pronounced resulting in planar and spherical tensor ellipsoids. Consequently, standard approaches for reconstructing fiber tracts are not adequate for connectivity analysis between sub-cortical or cortical regions. For this reason, this chapter presents an alternative technique based on pathfinding. Since pathfinding algorithms are required for various types of search problems, highly efficient solutions such as the A* algorithm [45] exist. For this reason, it is straightforward to adapt pathfinding also in the context of white matter connectivity analysis, which can be considered as an instance of a minimum-cost path problem [51, 40]. The presented approach employs the whole tensor information for connectivity analysis and combines computational efficiency and accuracy. The initial algorithm introducing pathfinding for connectivity analysis was published in [79]; further advances including a more sophisticated cost function and a refined search grid were published in [90].

This chapter starts with a summary of previous work aiming at reconstructing fibers in sub-cortical regions (Section 5.1). Subsequently, an introduction to pathfinding is provided and important parts of the search algorithm as well as efficiency aspects are considered. Finally, pathfinding results for different patient datasets are presented in Section 5.3 and the advantages of the approach are discussed in Section 5.4.

5.1 Previous work

First approaches addressing the problem of connectivity analysis between cortical regions used probabilistic or regularization techniques [8, 11]. Over a large number of

iterations, the process yields a connectivity probability related to the number of probabilistic streamlines found in a volume element. Another class of algorithms derived from level set theory considers arrival times of diffusion fronts [113, 51]. In most recent work based on level sets, the problem of white matter connectivity is modeled as wavefront evolution based on a cost function which depends on the entire diffusion tensor [51]. Considering the arrival times of the wavefront, connections are derived by minimizing the cumulative travel cost along the path. Another recent approach uses global optimization and dynamic programming for fiber reconstruction [40]. A graph is spanned over the domain with assigned cost for each edge connecting two voxels. By means of dynamic programming, connections with the highest probability are computed.

5.2 Connectivity analysis based on pathfinding

Basically, pathfinding algorithms are highly efficient search strategies commonly used in artificial intelligence for problems associated with a state space search. They are designed to derive the minimum-cost path between a start and a goal node based on a cost function [68]. Starting with an initial node, the algorithm builds up a graph consisting of weighted edges leading to successor nodes representing valid steps in solving the search problem. The reliability of a certain edge within the graph is indicated by the costs accumulated up to the current node and estimation of the remaining cost denoted as heuristics. The graph search expands until the goal node is reached.

For connectivity analysis between cortical regions, the A* algorithm [45, 103] is employed in this work. This section provides an introduction to A* pathfinding (Section 5.2.1) and important parts of the algorithm comprising domain restriction, an adequate search grid and an appropriate cost function based on the local tensor information are presented in Sections 5.2.2, 5.2.3 and 5.2.4. The reconstruction of minimum cost paths representing neuronal connections is outlined in Section 5.2.5 and efficiency aspects are considered in Section 5.2.7.

5.2.1 A* algorithm

The A* algorithm [45, 103] was designed for the efficient computation of the path with the lowest cost between a start and a goal node. For this purpose, the algorithm builds up a graph with nodes and edges, where to each edge a local cost is assigned. In each iteration, the path with the lowest cost is expanded until the goal node is reached. An important fact about the A* algorithm is its optimality [29] which guarantees that the best possible solution is found with the smallest computational effort.

In this application, the search area for the A* algorithm is the diffusion tensor dataset. The center points of the voxels in the search area are denoted as 'nodes'. The status of a node may be walkable or unwalkable according to a domain restriction threshold (Section 5.2.2). The search is initialized with a start node and a goal node. Beginning with

```
A-Star-Search(startNode, goalNode) {  
  
    openList.AddNode(startNode);  
  
    while (openList NOT EMPTY) {  
  
        currentNode = openList.RemoveMinCostNode();  
  
        if (currentNode == goalNode)  
            return TraceBackPath(currentNode);  
  
        closedList.AddNode(currentNode);  
        neighbors* = GetNeighbors(currentNode);  
  
        foreach (neighbors) {  
            if (neighbor NOT WALKABLE) continue;  
  
            else if (neighbor NOT ON OPEN OR CLOSED LIST) {  
                neighbor.SetParent(currentNode);  
                neighbor.ComputeCosts();  
                openList.Insert(neighbor);  
  
            } else { // neighbor on open or closed list  
                costG_old = costG(OLD PATH TO NEIGHBOR);  
                costG_new = costG(NEW PATH TO NEIGHBOR);  
  
                if (costG_new < costG_old) {  
                    neighbor.SetParent(currentNode);  
                    neighbor.ComputeCosts();  
                }  
            }  
        }  
    }  
  
    // No path between start and goal found  
    return EmptyPath();  
}
```

Code Example 5.1: Pseudocode for A* algorithm.

the start node, in each step the neighbor nodes of the current node are determined and further processed based on thresholds and costs. To find the path with the lowest cost, the searching process builds up a graph until the goal node is found. A schematic outline of pathfinding in comparison to fiber tracking is found in Figure 5.1.

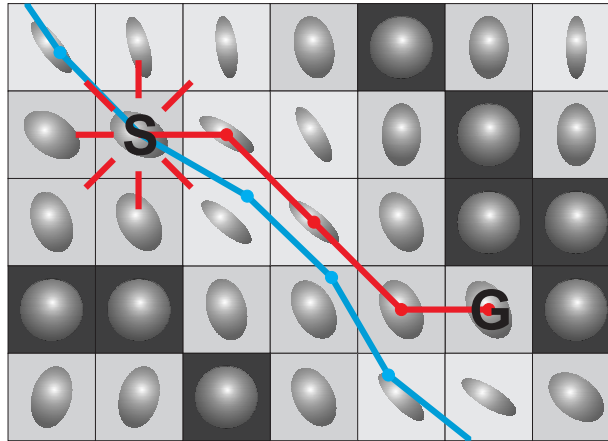


Figure 5.1: Schematic outline of the A* algorithm. For each square in the grid the shape of the tensor ellipsoid is indicated. Squares with a low FA value are not walkable and are denoted by a dark background. An example of fiber tracking (*blue*) as well as a possible pathfinding result (*red*) are shown. Contrary to the fiber, pathfinding is goal oriented and arrives at the goal.

For expanding the search, the algorithm maintains two lists: An open list encompassing all nodes that require further consideration and a closed list of nodes that have already been processed. When starting the search, the open list just contains the start node and the closed list is empty. The start node is taken from the open list and all walkable neighbor nodes are determined and inserted into the open list. Each node maintains a reference pointing to its parent. For each neighbor node on the open list the start node is thus saved as a parent node. As soon as the goal node is reached, the references are used in order to trace the path from the goal back to the start node.

In order to determine the best path, cost functions (Section 5.2.4) are employed. They provide a bias towards neighbor nodes that are more likely to lie on this path and therefore constitute a crucial detail of the algorithm. For a node i of the graph, the following costs are determined:

Movement cost: g_i is the movement cost required to travel along the path to the respective node i and is stored for each node.

Heuristic: h_i provides an estimate of the remaining cost (also called heuristic) to the goal which may optionally be added to direct the search towards the goal making the algorithm more efficient. Otherwise, the search would spread equally in all directions.

It is important to note that h_i does not affect the optimality of A^* as long as h_i is not higher than the actual cost necessary to reach the goal.

Cost function: $f_i = g_i + h_i$ is the overall cost function which is evaluated for each node of the open list in order to decide which one to process next.

The path with the lowest cost is generated by repeatedly selecting the node with the lowest cost f_i from the open list. The walkable neighbors of the current node are determined and added to the open list, provided that they are not yet part of the open or the closed list. Otherwise, the movement costs encountered for reaching the neighbor node via different paths have to be compared and the cheapest alternative is selected. Subsequently, the current node is moved to the closed list. These processing steps are repeated until the goal node is added to the open list and the path with the lowest cost is found. The pseudocode for A^* pathfinding is provided in Code Example 5.1.

5.2.2 Domain restriction

A possible connection between areas within the brain must be restricted to regions of white matter. In order to prevent the algorithm from expanding to regions definitely beyond white matter, the search domain is limited to regions where diffusion exhibits a directional bias due to underlying neuronal structures. For this purpose, diffusion metrics (Section 3.3.3) are employed [51, 40] which classify the properties of local diffusion. These metrics measure the degree of anisotropic diffusion, which is generally agreed to be a characteristic property of white matter. Strongly aligned tissue such as white matter causes anisotropic diffusion resulting in linear diffusion tensors. In the case of crossing or kissing fibers, planar diffusion tensors are observed due to the partial volume effect. Contrarily, in areas of grey matter spherical tensors are mainly encountered. Among the available measures for anisotropy, we selected FA for domain restriction which is also a common fiber propagation threshold for fiber tracking algorithms.

In the context of pathfinding such a threshold is known as a walkability threshold since nodes are thereby classified either as possible successor nodes or as forbidden nodes excluded from further consideration. Due to the restricted search area, the size of the edge weighted graph is considerably reduced. Computation times become faster since the graph expands more restrictively and fewer possible directions have to be processed. Furthermore, a connection is only found if a possible path exists according to the walkability criterion.

5.2.3 Grid for partitioning the search space

For navigating in three-dimensional space, the search algorithm requires a grid which should provide a regular structure uniformly covering the search space and a small step-size between neighbor nodes. The angle between edges should be small to provide enough flexibility to follow the direction of anisotropic diffusion. These requirements

lead to regular polyhedra, the Platonic solids. While grids composed of icosahedra and dodecahedra feature holes, grid structures composed of tetrahedra, hexahedra or octahedra come into question. We choose a grid structure based on hexahedra, where each node is connected to 74 neighbors as shown in Figure 5.2 (left). In comparison to a grid with 26 neighbors, further directions are provided reducing the angle between neighbor edges and offering a considerably improved choice of different directions thus fulfilling the flexibility criterion. The grid size chosen has to be sufficiently small to guarantee a small maximum step-size which should not exceed the grid size of the DTI dataset. The resulting grid is of high resolution and enables a dense sampling of the search space as outlined in Figure 5.2 (middle, right).

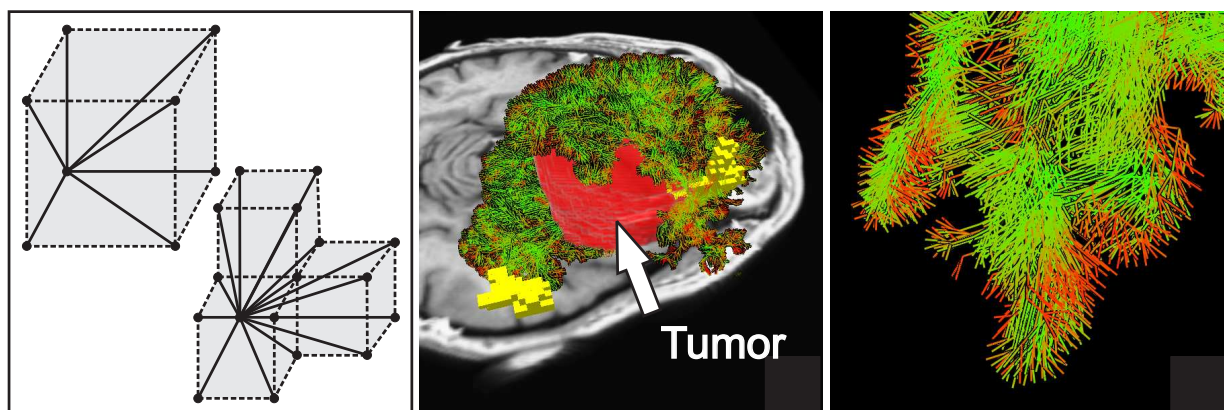


Figure 5.2: Octant of a grid with 26 and 74 neighbors (*left*). Expansion of the search space between Broca's and Wernicke's speech areas using a grid with 74 neighbors and a maximum edge length of 1.5 mm in a brain tumor patient (*middle*). Close-up view showing details of search grid (*right*).

5.2.4 Cost function

The cost function is an integral part of all types of connectivity algorithms since it controls the process of path evolution. In order to overcome the limitations encountered with fiber tracking, where only one direction (principal eigenvector, deflected direction or a combination of both) is considered, connectivity analysis algorithms employ a cost function which incorporates the entire tensor information. For this purpose, the surface of the tensor ellipsoid is commonly used as the probability profile [51, 40, 79]. In order to compute the probability of a fiber following a certain direction, the distance between the center of the ellipsoid located at $(0, 0, 0)^T$ and the intersection point r on the surface of the ellipsoid is determined. For a tensor ellipsoid with semi-axes aligned to the eigenvectors and scaled according to the respective eigenvalues λ_i , $i = 1, 2, 3$, probabilities between 0 and 1 are obtained by normalizing the tensor ellipsoid using λ_1 . Consequently, any segment connecting the center of the ellipsoid with its surface has a

maximum length of 1. As a result, the diffusion probability $p_i(\mathbf{r})$ for any direction can be directly obtained from the profile of the normalized ellipsoid:

$$p_i(\mathbf{r}) = \frac{|\mathbf{r}|}{\lambda_1}. \quad (5.1)$$

However, the resulting probability profile results in a bias towards spherical ellipsoids since they are traversed more easily due to a high probability for all directions. In [51], this is addressed by incorporating fractional anisotropy (FA) [7] into the cost function. In this work, we propose to model the anisotropic characteristic of a tensor by subtracting the isotropic part represented by λ_3 before normalization:

$$p_i(\mathbf{r}) = \frac{|\mathbf{r}| - \lambda_3}{\lambda_1}. \quad (5.2)$$

This is motivated by considering the probability profile of the tensor. In Figure 5.3, the probability profiles for a linear and a spherical tensor are plotted as a function of the azimuthal and polar angle of the corresponding ellipsoid. In the case of Equation 5.1 (left plot in each section), the almost spherical tensor yields very high probabilities for all directions resulting in a bias of isotropic tensors. This is circumvented by the probability profile resulting from Equation 5.2 (right plot in each section) which on the one hand perfectly maintains the shape of the probability profile but cuts the isotropic fraction. In this way, the probability function is solely based on the tensor probability profile and no additional term in the cost function is necessary. The resulting cost function is thus defined as

$$c_i(\mathbf{r}) = 1 - p_i(\mathbf{r}) \quad (5.3)$$

with $p_i(\mathbf{r})$ derived from Equation 5.2. Based on this approach, a more comprehensive probability profile is provided which better captures the tensor properties, making the incorporation of FA into the cost function redundant.

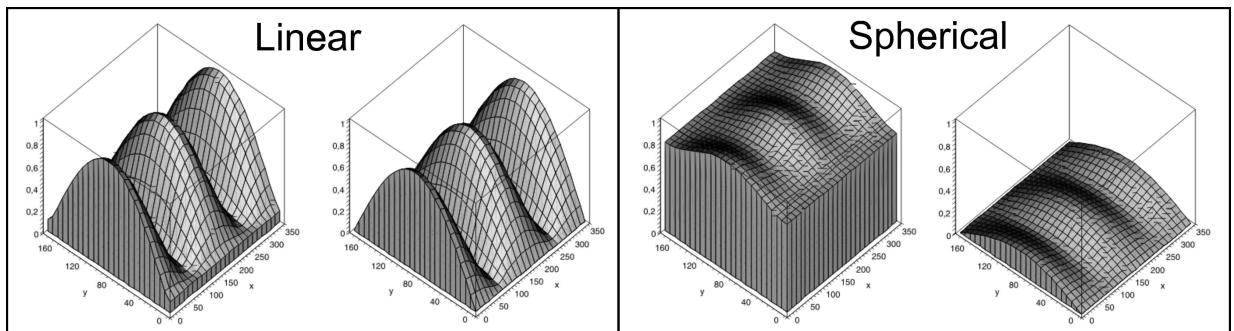


Figure 5.3: Tensor probability profiles (z-axis) of a linear and an almost spherical tensor for Eq. 5.1 (left in each section) and Eq. 5.2 (right in each section), plotted as a function of the azimuthal and polar angle (x- and y-axis) of the corresponding ellipsoid.

5.2.5 Minimum cost path

The theory of tension-based morphogenesis [38] anticipates that neuronal connections are kept optimal during the development of the brain. Under the assumption that this theory is correct, which is supported by numerous examples of evidence, minimum-cost approaches are an appropriate tool for modeling neuronal connectivity. In previous work [51, 40], this concept is used for different types of connectivity algorithms.

In the context of A* pathfinding, minimum-cost connections which approximate neuronal structures are derived. For this purpose, minimum-cost paths are determined by summing up all local movement costs c_j encountered along the path to node i resulting in a global movement cost g_i for the whole path:

$$g_i = \sum_{j=1}^i c_j \rightarrow \min. \quad (5.4)$$

In this way, connections fulfilling the global optimum condition are derived. Thereby, the pathfinding algorithm preferably propagates paths with a low global cost by comparing the cost of all nodes on the open list. As a result, the computed connection between the start and goal region is guaranteed to be optimal.

5.2.6 Multiple start and goal voxels

For connectivity analysis between functional areas, the start and goal region usually comprises more than one voxel. Furthermore, it is desirable to obtain more than one path between the functional regions. For this reason, the start region is divided into a user-defined number of subregions and a path to the goal region is computed for each subregion. So that the search space may be better covered, start and goal region are then switched and connections are computed which run in the opposite direction.

Optionally, it is also possible to continue the search beyond the optimal path, in order to obtain the n best paths. For this purpose, the search is resumed even though a path to the goal region is found, until the desired number of connections is computed.

5.2.7 Heuristic

In order to direct the search towards the goal, the A* algorithm takes advantage of an estimate h_i of the remaining cost, also denoted as the heuristic. If the heuristic overestimates the real cost, it is termed inadmissible. In this case, it is not guaranteed that the algorithm finds the path with lowest cost. If h_i is admissible, i.e. it never overestimates the cost to the goal, then A* is guaranteed to find the path with lowest cost. However, the lower the values of h_i , the more the algorithm expands and the slower it performs. For this reason, the heuristic should be as high as possible, but it should still represent a limit which is lower than the real cost, which has to be estimated.

The heuristic h_i can be considered as an attractor which is employed in the cost function $f_i = g_i + h_i$ in order to direct the search towards the goal. For the connectivity approach presented in this chapter, the following heuristic is employed:

$$h_i = \frac{d_i}{s_{max}} \cdot \hat{c}. \quad (5.5)$$

Thereby, d_i denotes the Euclidean distance of node i to the goal which is normalized according to the maximum step length s_{max} within the grid. The minimum number of steps to the goal d_i/s_{max} is multiplied with the estimated average cost per step \hat{c} which is determined by sampling the data for short connections in regions with high FA. The smallest cost among the samples is then assigned to \hat{c} . This additional term of the cost function f_i directs the search towards the goal. According to my observations, it can be empirically approved that the heuristic is admissible since the resulting paths did not differ from paths computed without heuristic. It was possible to reduce the computing time for the search considerably (for more details see Section 8.3.3).

5.2.8 Efficient implementation

Since the algorithm for connectivity analysis aims at clinical application, strict requirements with respect to computing times are encountered. With increasing distance between start and goal region and with increasing grid resolution, the dimension and complexity of the search grid increases rapidly. For this reason, appropriate data structures and computing schemes are of major importance for an efficient search.

The bulk of the computing time is consumed by operations performed on the open and closed list. Both lists contain a high number of nodes and are frequently accessed for data retrieval and insertion / deletion of nodes. For this reason, different data structures provided by the Standard Template Library (STL) [102] were investigated, as outlined in Table 5.1.

	Vector	Hashtable	Binary Heap	Sorted Vector
IsContained()	$\mathcal{O}(n)$	$\mathcal{O}(1)$	$\mathcal{O}(1)$	$\mathcal{O}(1)$
AddNode()	$\mathcal{O}(1)$	$\mathcal{O}(1)$	$\mathcal{O}(\log(n))$	$\mathcal{O}(\log(n))$
RemoveMinCostNode()	$\mathcal{O}(n)$	$\mathcal{O}(n)$	$\mathcal{O}(\log(n))$	$\mathcal{O}(1)$

Table 5.1: Complexity of different data structures for the operations `IsContained()`, `AddNode()` and `RemoveMinCostNode()`, which are frequently required for the open and closed list.

For the closed list, efficient methods for insertion and access are essential. Since no sorting is required, but fast access to nodes with a specific key for tracing back the final path, a hash table is employed. The hash table provides a complexity of $\mathcal{O}(1)$ for both operations and is therefore the best alternative.

In the case of the open list, a data structure is required which provides fast access to the node with minimum cost f_i , in spite of the large number of nodes contained. For this reason, sorted data structures are required such as a binary heap or a sorted vector. With respect to node insertion, the average expense for *AddNode()* is slightly higher in the case of a sorted vector, since all elements following the position of insertion are repositioned. This is subsumed by the *RemoveMinCostNode()*, which occurs less frequently but is much more efficient in the case of a sorted vector.

The complexity values provided in Table 5.1 denote the upper bounds of the respective operations. In practice, the average computing time for connectivity analysis based on A^* pathfinding is higher, if a sorted vector is used as data structure for the open list. Especially for a large search area, the advantage of the sorted vector over the binary heap becomes apparent.

5.3 Results

For evaluation purposes, two proband and three patient DTI datasets were analyzed. For all datasets, seed regions corresponding to the Broca's and Wernicke's speech areas derived from fMRI were available. From anatomy, it is known that these areas are functionally related by the arcuate fasciculus (Section 2.4). All three patients suffered from lesions located close to the functional areas. However, the speech abilities were unaffected, which indicates that the arcuate fasciculus was intact in each patient.

The approach for connectivity analysis between Broca's and Wernicke's speech area was applied for all datasets. For pathfinding, the 74-neighbor grid introduced in Section 5.2.3 was employed with a maximum step length of 1.5 mm. According to Section 5.2.2, a walkability threshold based on FA was defined in order to restrict the search to regions of white matter only. In all experiments, the walkability threshold amounted to 0.3, excluding nodes with an FA value below the threshold from further processing. The following evaluation investigates the quality of the paths obtained (Section 5.3.1) as well as the computing time (Section 5.3.2).

5.3.1 Quality analysis

In order to investigate the accuracy of the proposed cost function (Equation 5.2) in comparison to a cost function based on the product of the normalized probability profile (Equation 5.1) and the local FA value [51], different measures were evaluated per path. For this purpose, the average probability according to the probability profile of Equation 5.2 and the average FA value were investigated. Additionally, the validity index introduced by Jackowski [51] was recorded. The validity index computes the scalar product between path tangent and major eigenvector for each segment and returns the average value for the whole path. Table 5.2 shows the minimum, maximum and average value for the connections derived between speech areas in two patient datasets. As a result, the cost function achieves better results compared to the normalized tensor

profile commonly employed [51, 40]. In addition to that, the presented approach is as accurate as wavefront evolution [51] with respect to the validity index.

Cost Function: Equation 5.1						
	Patient 1			Patient 2		
<i>Number of fibers</i>	17			21		
	<i>avg</i>	<i>min</i>	<i>max</i>	<i>avg</i>	<i>min</i>	<i>max</i>
Probability Profile	0.68	0.65	0.70	0.63	0.62	0.64
Fractional Anisotropy	0.58	0.54	0.61	0.56	0.55	0.57
Validity Index	0.75	0.69	0.87	0.83	0.82	0.86

Cost Function: Equation 5.2						
	Patient 1			Patient 2		
<i>Number of fibers</i>	19			23		
	<i>avg</i>	<i>min</i>	<i>max</i>	<i>avg</i>	<i>min</i>	<i>max</i>
Probability Profile	0.75	0.73	0.82	0.70	0.69	0.70
Fractional Anisotropy	0.61	0.57	0.68	0.56	0.55	0.57
Validity Index	0.77	0.70	0.88	0.86	0.85	0.87

Table 5.2: Evaluation based on validity index, probability profile and FA represented by average, maximum and minimum value of all fibers.

In order to visualize the local probability according to Equation 5.2, a color transfer function is employed as outlined in Section 8.1. Each segment is color encoded assigning red to a low and green to a high value of the probability profile from Equation 5.2. In Figure 5.4, color coding is used to compare standard fiber tracking based on streamline propagation [99] (RK-4 integration, step size 0.5 mm) and pathfinding with regard to their exactness. The red segments encountered in the case of fiber tracking indicate that spherical tensors were crossed. A more reliable path was obtained using pathfinding which takes into account the entire probability profile of the local tensor and resulted in paths along anisotropic tensors.

5.3.2 Computing time

Since the algorithm aims at clinical application thus requiring fast interaction times, computational cost is of major concern in addition to accuracy. As far as implementation is concerned, an efficient implementation of the open and closed list is instrumental in producing fast processing times since both lists are accessed frequently and have to manage a high number of nodes (Section 5.2.8). Incorporation of the heuristic (Section 5.2.7) directs the search towards the goal, resulting in a smaller search grid and reduced computing times. In both cases, the resulting paths remained the same, since the heuristic is admissible according to empirical observations.

In Table 5.3, results regarding the computing time are presented. Since the computing time directly relates to the expansion of the search tree, the respective node num-

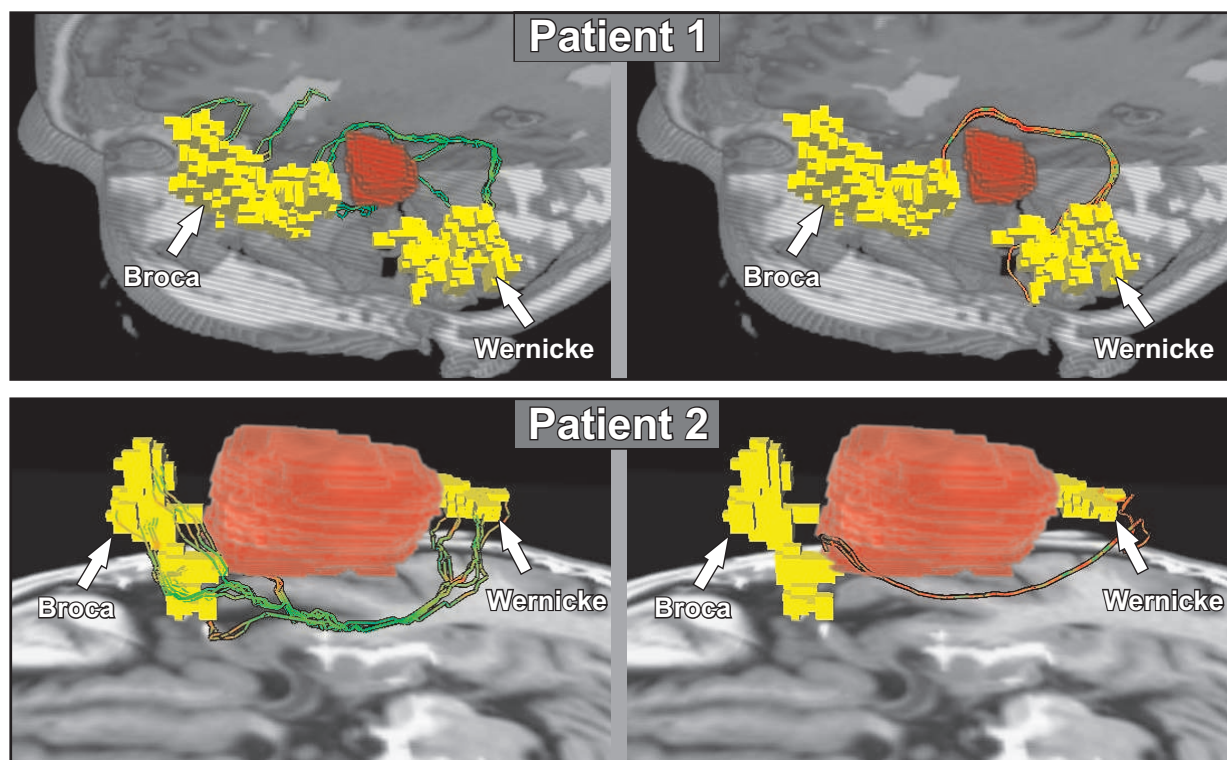


Figure 5.4: *Upper row (Patient 1):* Patient with a cavernoma. *Lower row (Patient 2):* Patient with a glioblastoma multiforme (WHO grade IV) having speech dominance on the right hemisphere. The respective lesion is shown in red in each patient. Pathfinding (*left*) vs. fiber tracking (*right*); color coding shows that pathfinding provides more precise results.

bers were recorded as well. All computations were performed on a PC equipped with an Intel Pentium 4, 3.4 GHz, and 2 GB RAM. For connectivity analysis incorporating a heuristic, the average computing time per path was 14.9 sec for the first patient and 19.5 sec for the second patient. Without heuristic, the computing time is about 70% higher, which illustrates the importance of a heuristic for efficiency reasons. These timings are also reflected by the node numbers of the search tree, which are considerably higher if no heuristic is employed.

Performance	Computing Time		Number of Grid Nodes	
	Patient 1	Patient 2	Patient 1	Patient 2
$f_i = g_i + h_i$	14.9 sec	19.5 sec	106 414	163 586
$f_i = g_i$	42.0 sec	82.8 sec	240 705	318 163

Table 5.3: Average computing time per path and expansion of search grid (number of nodes) for search based on global cost g_i (Eq. 5.2) and speed up encountered with heuristic h_i .

5.4 Discussion

In cortical and sub-cortical regions where the tensor shape deviates from the strongly anisotropic linear type, standard fiber tracking approaches are inappropriate for connectivity analysis, requiring alternative approaches. The advantage of connectivity analysis based on pathfinding over standard fiber tracking is, that a set of multiple directions is considered for each node in the graph. In contrast to standard fiber tracking, only a single fiber direction is computed using streamline integration or tensor deflection. Furthermore, pathfinding is goal oriented, which is another important property in order to compute the course of fibers between functionally related regions. The design of the pathfinding algorithm ensures that the best possible connection between the functional areas is found, whereas fiber tracking initiated from one region is not guaranteed to find the other functional area at all.

In comparison to other approaches aiming at connectivity analysis in cortical or sub-cortical regions, the presented technique offers a number of advantages. First approaches developed in this context are based on probabilistic or regularization techniques and require a huge amount of sampled fibers in order to give evidence about probable connections. Another class of algorithms model connectivity as a minimum-cost problem [51, 40], which is based on the assumption that neuronal connections are kept optimal [38] during brain morphogenesis. They take advantage of a cost or evolution function, which drives the connectivity algorithm. In comparison to the normalized tensor profiles previously employed for this purpose [51, 40], connectivity results were significantly improved using the novel cost function presented in Section 5.2.4, which characterizes both shape and anisotropy of the local tensor. From the algorithmic point of view, pathfinding is computationally more efficient than other graph-based techniques such as [40], since it is possible to prove formally that no other search algorithm which is guaranteed to find the minimum-cost path requires less computational expense than A^* [29]. Apart from that, the presented grid structure provides high resolution and a considerably increased number of neighbor nodes to sample the search space very densely, which is superior compared to the grid used in [40]. Overall, the presented approach provides comparable or even better accuracy compared to other approaches and is, at the same time, much faster than other current approaches.

The presented algorithm could also be combined with higher-order tensor representations derived from high angular resolution diffusion imaging (HARDI) [145]. In order to capture the local diffusion properties more precisely, this technique acquires diffusion datasets with diffusion-weighting gradients applied along many directions, resulting in more complex tensor shapes. Recently, an approach was proposed for tracking lines in higher-order tensor fields based on the direction of largest expansion of the higher-order tensor [49]. The approach presented in this chapter is suited to take advantage of this more complex tensor representation, since a whole set of directions is sampled for constructing the graph, which better exploits the complex tensor information.

Chapter 6

Generation of hulls

The fiber-tracking and connectivity approaches presented in the previous chapters generate fiber bundles which approximate the shape and the course of underlying white matter structures. In neurosurgery, major white matter structures must be spared from injury in order to avoid postoperative neurological deficits. Especially in cases where the tumor is very close to a tract system, or difficult to access, the reconstructed bundles are of great importance. For this reason, essential tract systems such as the optic tract (vision), the pyramidal tract (motor tract system) or the corpus callosum (connection between the two hemispheres) are reconstructed prior to surgery for preoperative planning. The resulting fiber bundles provide valuable information about the location and extent of white matter structures with respect to the surrounding anatomy. In pioneering clinics, they play an important role in planning and navigation in neurosurgery [105, 9].

In spite of the advantages of visualizing fiber bundles in 3D, streamline representations are not adequate for intraoperative visualization. The neuro-navigation system is

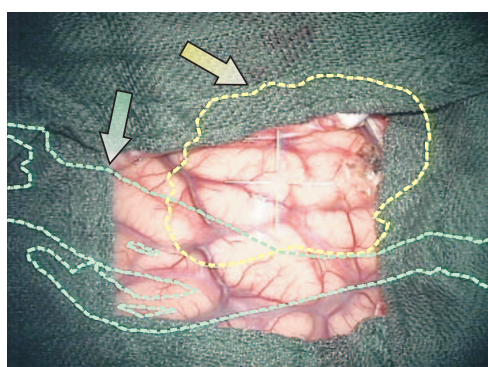


Figure 6.1: View through the OR microscope. The border of the tumor (*yellow*) as well as functional structures such as the optic tract (*green*) are superimposed on the microscope image.

able to superimpose boundary curves of important structures on the OR microscope image in order to guide the surgeon during the intervention. This is shown in Figure 6.1, where the borders of the tumor and the optic tract are superimposed on the microscope view in order to display the relation between tumor tissue and neuronal structures. The boundary curves provide a clear representation and explicitly show the extent of the fiber tract, providing a direct relation between tumor tissue and neuronal structures.

For this purpose, hulls tightly wrapping the fiber bundles are required to serve as a basis for intraoperative visualization. In recent research, a first approach for wrapping fiber tracts was presented [37]. It computes the centerline of the fiber bundle and defines ellipses encompassing the fibers in a series of planes perpendicular to the center line. The ellipses of subsequent planes are then connected using a triangular mesh, resulting in a tube encompassing the fiber tract. This approach has been developed in conjunction with automatic clustering [17] which ensures that single streamlines within a cluster or bundle pursue a similar course. For this reason, the technique is restricted to elongated white matter tracts where the centerline is well-defined. However, for tract systems such as the corpus callosum encompassing fibers with a significantly varying course and direction, the approach will fail. Another problem occurs if the fiber tract branches, which would require a splitting centerline or the definition of several ellipses per plane.

For this reason, two alternative hull algorithms overcoming these drawbacks are presented and discussed in this chapter. The first approach employs tetrahedralization and 3D alpha shapes for hull generation (Section 6.1) and was published in [89]. The second approach for wrapping fibers is based on isosurfaces (Section 6.2).

6.1 Tetrahedralization and 3D Alpha Shapes

The approach based on tetrahedralization and 3D alpha shapes takes advantage of the sampling points of the tracked fibers in order to guarantee high precision. In a first step, a tetrahedral mesh is constructed from the sampling points based on 3D Delaunay tetrahedralization (Section 6.1.1). Since the tetrahedralization process results in the convex hull of the fiber tract, a variation of the 3D-alpha-shape algorithm has to be applied (Section 6.1.2). As a result, the triangles on the surface of the remaining tetrahedral mesh describe a hull precisely encompassing the fiber tract.

6.1.1 3D Delaunay Tetrahedralization

The point set comprising the sampling points of all fibers within the fiber tract is used as the input for the tetrahedralization algorithm. For the reconstruction of a tetrahedral mesh based on this point set, a 3D Delaunay [30] approach is applied. For points in a general position, i.e. no geometric test is ambiguous, this tetrahedralization is uniquely defined and decomposes the convex hull of the point set into tetrahedra [30]. The tetrahedralization of a point set fulfills the 3D Delaunay criterion if each sphere defined by

the four points of a tetrahedron contains no other point of the point set. For implementation purposes, the `vtkDelaunay3D` class of the Visualization ToolKit (VTK) [126] was used. In Figure 6.2 (left), the surface of the initial set of tetrahedra after 3D Delaunay tetrahedralization is shown.

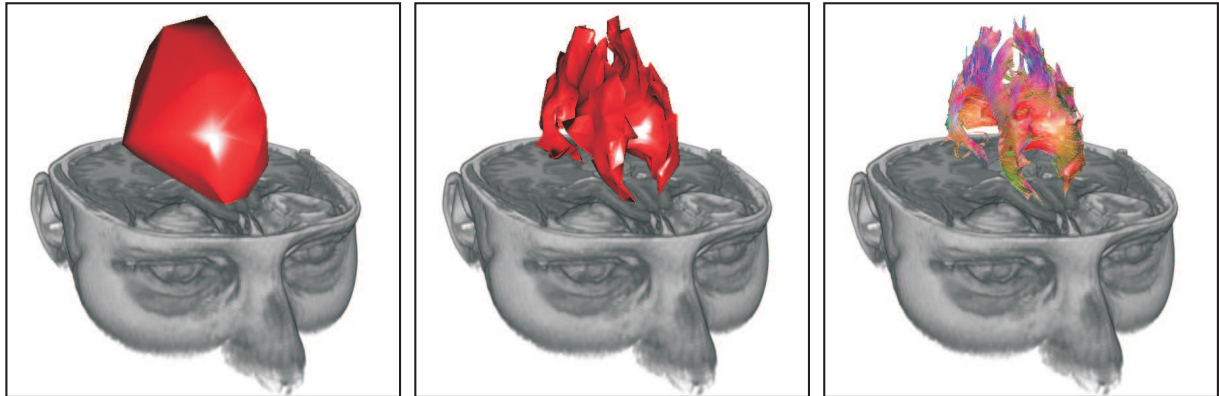


Figure 6.2: 3D Delaunay tetrahedralization based on sampling points of a tract system (corpus callosum) results in the convex hull (*left*). Subset of tetrahedra obtained with 3D alpha shapes for an alpha value of 10 mm (*middle*) and semi-transparent hull for an alpha value of 5 mm displayed with tracked fibers (*right*).

6.1.2 3D Alpha Shapes

The output of the 3D Delaunay algorithm is a tetrahedral mesh filling the convex hull of the point set with volume elements. In order to obtain the subset of tetrahedra tightly enclosing the fiber tract, outer tetrahedra have to be removed in an iterative process. For this purpose, a variation of the 3D-alpha-shape algorithm is applied. The concept of alpha shapes [33] is a generalization of the convex hull, formalizing the intuitive notion of ‘shape’ for spatial point-set data. Depending on the alpha value, which is a real number greater than zero, the alpha shape of an object encompasses only those tetrahedra with a circumsphere smaller than or equal to a sphere with diameter alpha. For sufficiently large alpha, the alpha shape is identical to the convex hull which is the original tetrahedral mesh. For decreasing values of alpha, approaching the step size used for fiber tracking, the alpha shape shrinks and gradually reveals the shape of the fiber tract.

When applying the alpha-shape concept to the tetrahedral meshes obtained from 3D Delaunay tetrahedralization, holes may occur due to the removal of inner tetrahedra. For this reason, a variation of the 3D-alpha-shape algorithm is used, where tetrahedra are only removed according to the alpha criterion if they are on the surface of the current tetrahedral mesh. This is implemented by setting an alpha-flag for all tetrahedra which

should be removed according to the alpha value, and a boundary-flag for all tetrahedra on the surface. In an iterative procedure, surface tetrahedra with a valid alpha-flag are removed, and the boundary-flag of their neighboring elements is set. Sweeping through the tetrahedra data structure continues, as long as tetrahedra requiring to be removed are found.

After applying the 3D-alpha-shape algorithm, a tetrahedral mesh remains which corresponds to the intuitive shape of the fiber tract. The triangular hull mesh is constructed from the outer faces of the surface tetrahedra. For dense fiber bundles, the resulting hull tightly wraps the fiber tract, as shown in Figure 6.3.

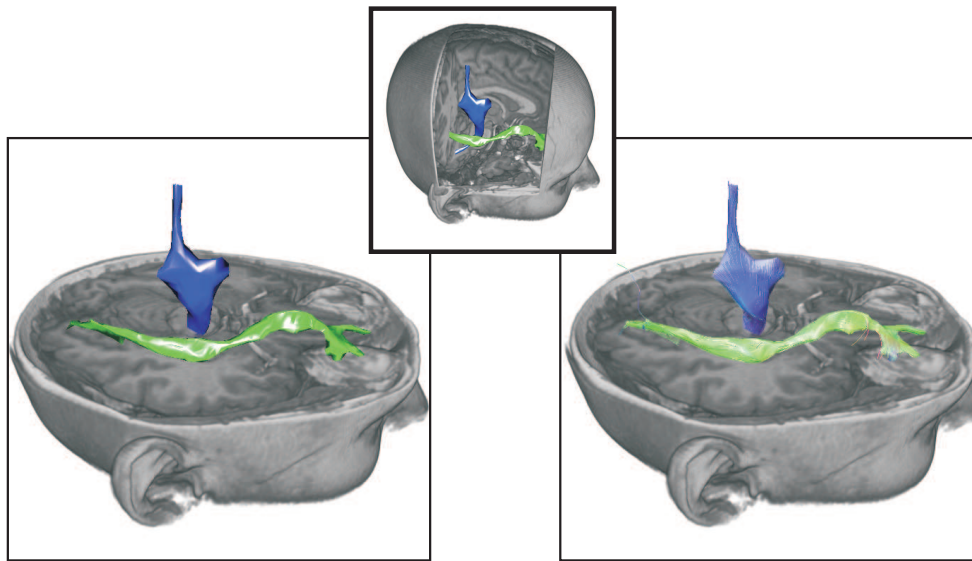


Figure 6.3: Hulls obtained from tetrahedralization and 3D alpha shapes for an alpha value of 5 mm for the pyramidal (*blue*) and the optic tract (*green*). Semi-transparent visualization of the hulls in combination with the fibers (*right*) shows the high precision of the approach.

6.1.3 Results

The hull approach based on tetrahedralization and 3D alpha shapes was applied to different tract systems, as shown in Figures 6.2 and 6.3. For the tract systems presented, the computing times for 3D Delaunay tetrahedralization are between 2 and 80 seconds on a PC equipped with a P4 3.0 GHz and 2 GB RAM. The remaining computations required in order to eliminate unnecessary tetrahedra (Section 6.1.2) are in the range of a few seconds. Computing times could be lowered by a coarser sampling of the fibers, or by advanced tracking strategies controlling the density of single fibers, both resulting in a smaller point set.

For all tract systems, the algorithm succeeded in generating precise hulls following the shape of the fiber bundle, as shown in Figures 6.2 and 6.3. The technique presented provides high precision which is due to the fact that points originating from fiber tracking are directly used for tetrahedralization and remain after application of 3D alpha shapes. As a result, the hulls tightly fit the underlying fiber structure.

6.2 Isosurfaces

The idea behind the hull approach based on isosurfaces is to raster the fibers and to generate an isosurface encompassing the fiber tract. For this purpose, a series of processing steps has to be accomplished. First, the fiber tracts are rasterized (Section 6.2.1) and a volume filter is applied (Section 6.2.2). The Marching Cubes algorithm is then applied in order to extract an isosurface (Section 6.2.3), which is finally smoothed using surface filters (Section 6.2.4).

6.2.1 Rasterization

In order to encompass the fiber bundle with a wrapping surface, the volume occupied in 3D-space is determined in a first step which is achieved with rasterization. For this purpose, the Bresenham algorithm [16] is employed, which is a standard concept for rasterization, originally designed for lines in 2D discrete space. This approach is based on integer arithmetic and takes advantage of the implicit representation of a line for efficient drawing.

For rasterization in 3D space, the Bresenham algorithm has been adapted to three dimensions [57]. The 3D version of the Bresenham algorithm projects the 3D line on 2D planes and executes the 2D Bresenham algorithm on each plane. As a result, a consistent volume comprising the tracked fibers is extracted. Since the fiber bundles consist of multiple streamlines which are composed of a series of line segments, the 3D Bresenham algorithm is executed for each line segment by taking the start- and endpoint of the line segment as input values. The rasterization result is a binary volume that approximates the fiber bundle in 3D discrete space. With respect to the resolution of the grid, two contradicting criteria are encountered: The grid must be fine enough in order to maintain the shape of the tract after rasterization, but at the same time, the tract should be represented by connected rasterized voxels without holes. Depending on the density of fibers representing the whole tract, a good trade-off between these criteria is provided by a grid size of about 1 mm edge length or less.

For a maximum fiber-tracking step size below the rasterization resolution, it would be equally possible to mark voxels containing a tract vertex. However, rasterization based on the 3D Bresenham algorithm ensures that streamlines with arbitrary sampling features, such as an adaptive step size or a step size above the grid resolution, are correctly processed.

6.2.2 Volume filtering

The binary volume generated with the 3D Bresenham algorithm needs further preprocessing, in order to serve as an input for a surface extraction algorithm, since its discrete nature would result in jaggies. A commonly used technique used to reduce these aliasing artifacts is to apply filter operations on the volume. For this purpose, a 3D Gaussian filter is applied. This filter kernel suppresses high frequencies in the spatial domain and smooths the rasterized volume. In Figure 6.4, the effect of Gaussian volume filtering is shown for a coronal slice of the corpus callosum.

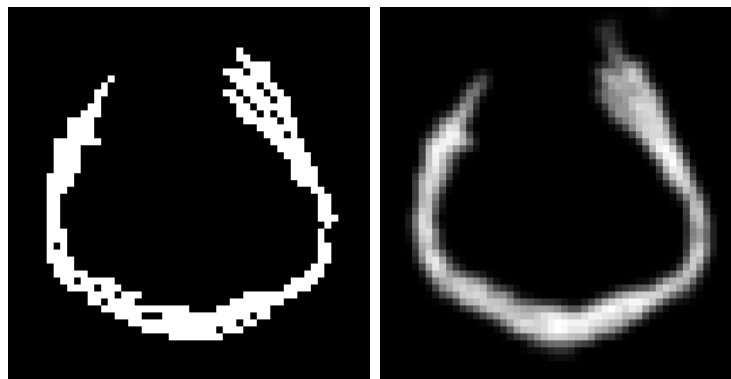


Figure 6.4: Comparison of volume after rasterization using 3D Bresenham (*left*) and additional Gaussian volume filtering (*right*), shown for a coronal slice of the corpus callosum.

Application of the 3D Gaussian filter not only smooths the volume, but also results in a slight volume expansion. However, this is tolerable if an appropriate value for iso-surface extraction is used, or is compensated later by surface filters, which cause a slight volume shrinkage. In order to maintain important details during volume filtering, it is advisable to use a small Gaussian kernel of size $3 \times 3 \times 3$. In addition to Gaussian volume filtering, morphological operations could be applied in order to fill potential holes and to smooth the volume further. However, for the processed tract systems consisting of dense fiber bundles, application of the Gaussian volume filter was sufficient.

6.2.3 Surface Extraction

Based on the rasterized and filtered volume, surface extraction is applied. For this purpose, the Marching Cubes algorithm [73] is employed, which is an effective technique for extracting a triangular surface from a volume dataset. For surface extraction, an iso-value is specified that indicates at which grey level of the input volume the boundary surface has to be computed. In order to extract an iso-surface encompassing all fibers, a low iso-value has to be selected. The rasterized and Gaussian-filtered volume comprises grey values between 0 and 255; for iso-surface extraction an iso-value between 0

and 10 is advisable. In Figure 6.5, an iso-surface extracted by Marching Cubes based on a rasterized and Gaussian-filtered volume is shown. Even though the Marching Cubes algorithm works on a filtered volume, the extracted surface features terracing artifacts. For this reason, surface filtering is applied in the next step in order to attenuate these artifacts resulting in a smooth hull.

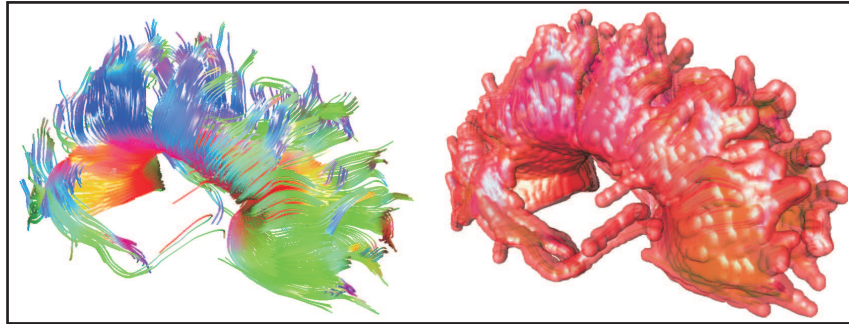


Figure 6.5: Initial iso-surface extracted with Marching Cubes for an iso-value of 1.

6.2.4 Surface filtering

In spite of volume filtering, the hulls resulting from iso-surface extraction suffer from unevenness and consequently lack tightness. For this reason, three surface filters are presented in this section, which are based on the umbrella operator [64]. The filter parameters are adjusted by the user in order to generate tight and smooth hulls.

Laplace Filter: A discrete Laplace filter based on angle weights was originally proposed by [119]. In the meantime, the Laplace filter has become a standard approach for mesh smoothing [2, 32, 59, 64]. Based on the topological neighborhood, each vertex is repositioned and the mesh gets smoother within a few iterations. In each iteration, the Laplace filter traverses all surface vertices and moves each vertex \mathbf{p} towards the geometric center of the n topological neighboring vertices \mathbf{q}_i . Since this approach leads to a considerable shrinkage of the surface, a weighting factor λ is commonly applied. This factor has the effect that \mathbf{p} is not completely moved to the center of its topological neighbors, but only for a portion λ of the movement vector. Accordingly, the smoothed position \mathbf{p}' of vertex \mathbf{p} is computed as follows:

$$\mathbf{p}' = \mathbf{p} + \lambda \frac{1}{n} \sum_{i=0}^{n-1} (\mathbf{q}_i - \mathbf{p}) \quad (6.1)$$

Taubin Filter: The main idea of the Taubin filter [143] is to reduce volume shrinkage encountered with the Laplace filter by applying a positive (λ_1) and a negative weighting factor (λ_2) alternately. The new position \mathbf{p}' of a vertex is computed according to:

$$\mathbf{p}' = \mathbf{p} + \lambda_{1/2} \sum_{i=0}^{n-1} w_i (\mathbf{q}_i - \mathbf{p}) \quad (6.2)$$

The weighting factors w_i sum up to 1 and can be used to weight the influence of a neighboring vertex. A common setting is to use $w_i = 1/n$, which is equivalent to the standard Laplace filter. The absolute value of the negative weight $|\lambda_2|$ is chosen slightly bigger than $|\lambda_1|$, e.g. $\lambda_2 = -1.02 \lambda_1$ as suggested by [143]. Alternating application of the factors λ_1 and λ_2 in subsequent iterations alternately shrinks and expands the volume. As a result, the Taubin filter preserves the volume much better than the Laplace filter.

Scale-Dependent Laplace Filter: The previously introduced filters based on the umbrella operator do not take into account the angles between triangles or the edge length, which leads to the same smoothing result for different neighborhood configurations. However, the length of edges in the neighborhood provides more information about the configuration of a triangulation, which is important for good smoothing results. For this reason, the scale-dependent Laplace filter [32] scales the umbrella operator with the sum E of the lengths of all neighboring edges. The resulting filter computes the smoothed position \mathbf{p}' of a vertex from its old position \mathbf{p} and its neighbors \mathbf{q}_i as described previously, but the vectors to the neighboring vertices are normalized and the sum of edge lengths E is used in order to scale the resulting movement vector:

$$\mathbf{p}' = \mathbf{p} + \frac{\lambda}{E} \sum_{i=0}^{n-1} \frac{(\mathbf{q}_i - \mathbf{p})}{|\mathbf{q}_i - \mathbf{p}|}, \quad \text{with } E = \sum_{i=0}^{n-1} |\mathbf{q}_i - \mathbf{p}| \quad (6.3)$$

In Figure 6.6, smoothing results obtained with the scale-dependent Laplace filter are shown. Depending on the number of iterations, a slight but constant volume shrinkage is observed. At the same time, the surface gets smoother and terracing artefacts disappear. The filter parameter λ as well as the number of iterations is controlled by the user in order to obtain a hull surface tightly fitting the underlying fiber tract. In addition to the iso-value, the filter parameters thus allow fine-tuned fitting of the hull in order to obtain the desired surface quality.

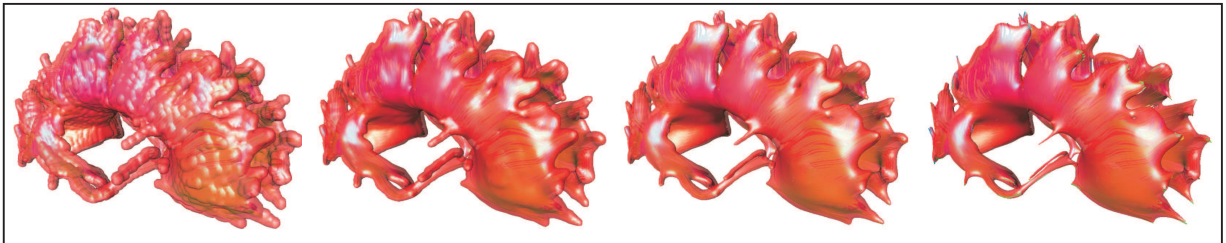


Figure 6.6: Surface filtering with a scale-dependent Laplace filter after 0, 25, 50 and 75 iterations and a filter value $\lambda = 0.5$ (from left to right).

6.2.5 Results

Based on fiber bundles obtained with fiber tracking (Section 4) or connectivity analysis (Section 5), hulls were generated by means of rasterization, volume filtering, iso-surface extraction and surface smoothing, as outlined in the previous sections. The computing times for the hull surfaces presented were between ten seconds and three minutes (on a PC equipped with a P4 3.0 GHz and 2 GB RAM), depending on the number of fibers which have to be rasterized and the number of iterations chosen for the surface filter. From various experiments, the following parameters proved to be adequate for generating isosurface-hulls tightly fitting the underlying fiber tract:

- Voxel size of rasterization volume: $1 \times 1 \times 1 \text{ mm}^3$
- Size of Gaussian filter kernel: $3 \times 3 \times 3$
- Iso-value for Marching Cubes: 0-10
- Surface filter: Scale-dependent Laplace filter
- Filter parameter λ : 0.5
- Number of filter iterations: 10-60

One neurosurgeon and two medical students (neurosurgery) applied the approach to several tract systems in different patients, namely the arcuate fasciculus, the pyramidal tract, the optic tract, and the corpus callosum. In Figure 6.7, a hull wrapping the arcuate fasciculus obtained from connectivity analysis is shown. In Figure 6.8, hulls for the corpus callosum and the pyramidal tract are shown for a brain-tumor patient. The

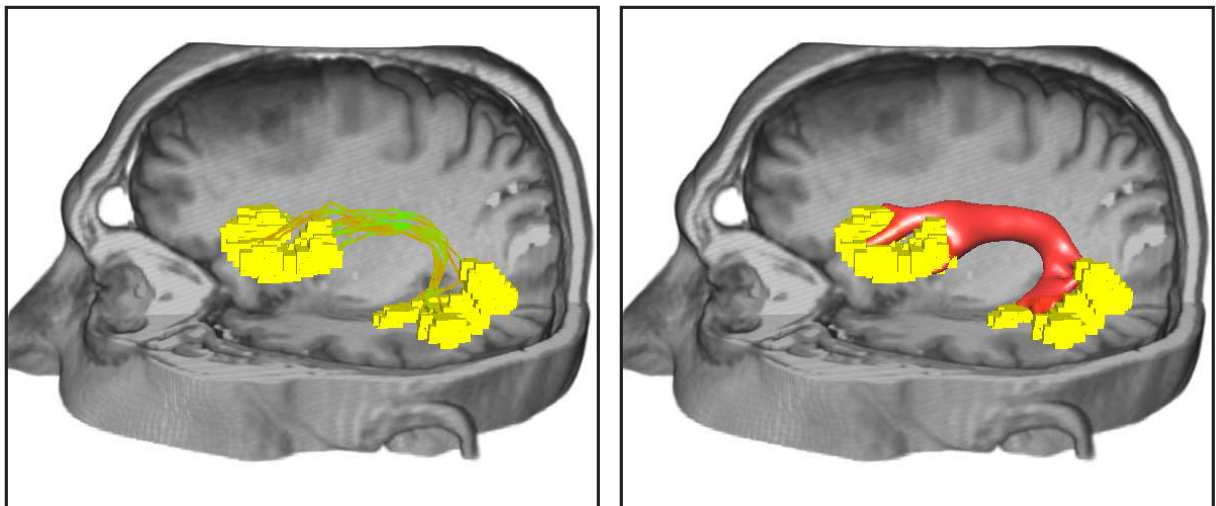


Figure 6.7: Arcuate fasciculus in a brain-tumor patient undergoing surgery. Based on the results obtained from connectivity analysis (*left*), a hull was generated (iso-value 5, Taubin filter with $\lambda = 0.4$, 40 iterations) (*right*).

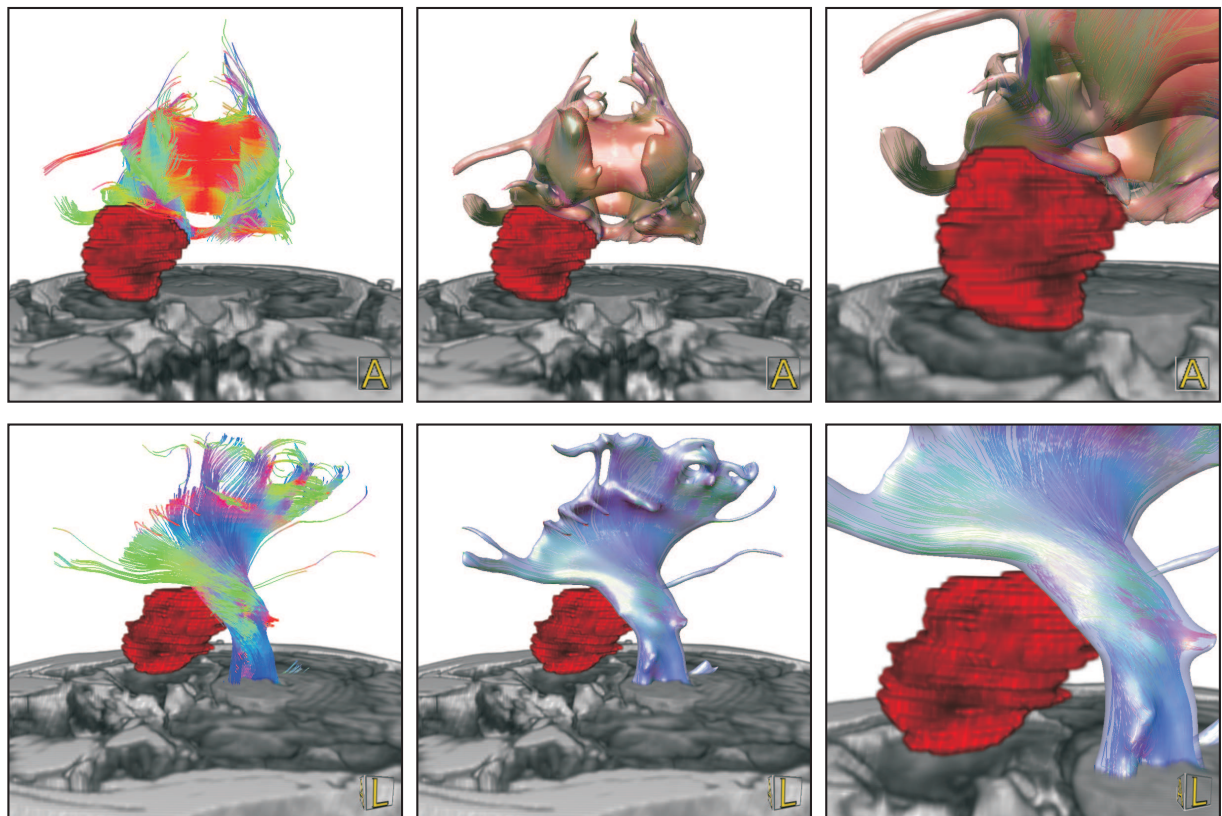


Figure 6.8: Brain-tumor patient, the corpus callosum (*upper row*) and the pyramidal tract (*lower row*) are very close to the tumor (*red*), as indicated by fiber tracking (*left*). A hull wrapping the corpus callosum and the pyramidal tract was generated (iso-value 1, scale-dependent Laplace filter with $\lambda = 0.5$, 40 iterations) which tightly fits the underlying fiber tracts (*middle*). Zoomed views of the tumor region (*right*).

tumor was manually segmented and is shown in red. Since the tract systems presented are very close to the lesion, intraoperative visualization of the respective hulls provides surgical guidance and supports safe resection. In Figure 6.9, the pyramidal tract in four patients is investigated, and the hulls as well as a semi-transparent representation are shown. The quality of the hulls was visually confirmed by the medical experts based on semi-transparent hull visualization.

The quality of a hull resulting from a specific parameter set can be visually investigated by simultaneous visualization of the fiber tract and the respective hull. In this way, the hull extraction parameters are easily adjusted in order to obtain tight hulls wrapping the underlying fiber tract.

In order to support quality control further and to provide a quantitative measure, it is also possible to measure the tightness of a hull with respect to the underlying tract system. For this purpose, the distance of each surface point to the nearest tract vertex

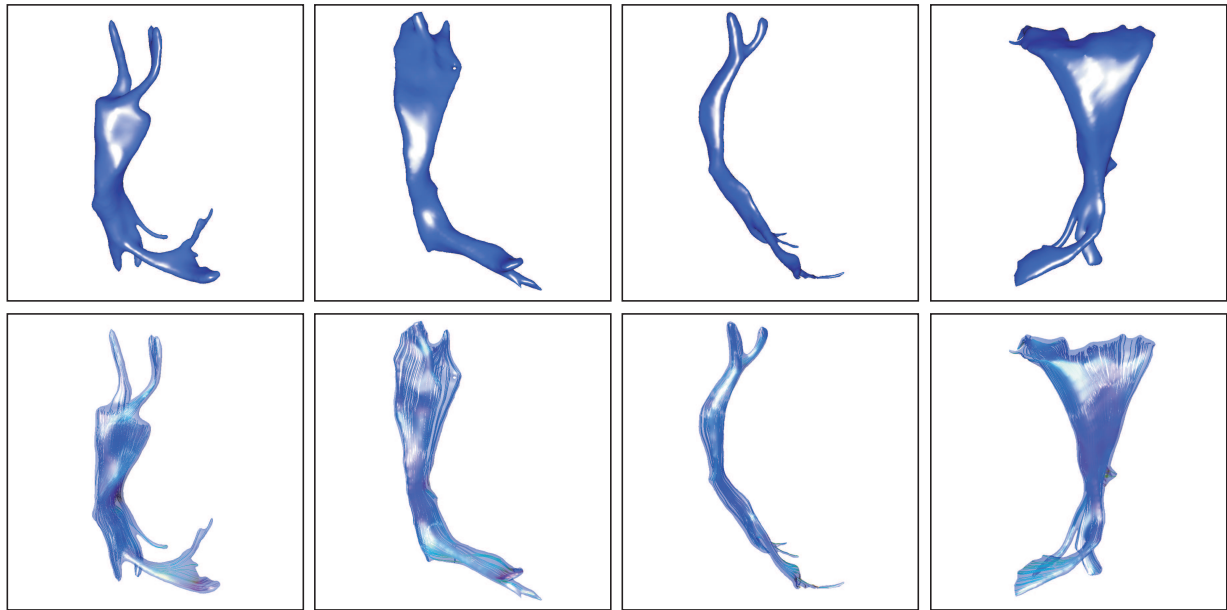


Figure 6.9: Pyramidal tract of different brain-tumor patients undergoing surgery. Based on the fiber-tracking results, hulls were generated (iso-value 5, scale-dependent Laplace filter with $\lambda = 0.5$, 50 iterations) (*upper row*). Semi-transparent visualization of the hull in combination with the fiber-tracking results (*lower row*) facilitates the adjustment of the surface extraction parameters in order to obtain tight hulls.

is computed and evaluated (average and maximum value of all surface vertices). In order to compute the minimum distance for each surface vertex efficiently, the volume is decomposed into cubes with edge length 4 mm, and the tract vertices are assigned to the respective cube. For each surface vertex, the corresponding cube is determined and the minimum distance between the surface vertex and all tract vertices within the cube is computed. If the surface vertex is very close (< 1 mm) to one of the sides of the cube, the tests are also performed for the tract vertices contained within the respective adjacent cube. As a result, the distance between a surface vertex with respect to the fiber tract is assessed. In Table 6.1, the results for the pyramidal tract for the five patients are presented, depending on the number of iterations for the surface filter (the remaining parameter settings were in accordance with the recommendation above, with an iso-value of 5). For each patient, hulls for the pyramidal tract were extracted after 40, 50 and 60 surface-filter iterations, and the average and maximum distance value for all surface points was determined.

Visual inspection of the hulls showed that the hulls enclosed the pyramidal tracts completely; only in the case of 60 iterations did the tips of the tract systems protrude slightly. The distance measurements further confirm the quality of the hulls, with an average distance between hull and tract of about 1 mm. Moreover, these measurements

		Pyramidal tract	
		avg [mm]	max [mm]
40 iter	Patient 1	0.96	1.81
	Patient 2	1.09	1.97
	Patient 3	0.86	1.79
	Patient 4	0.92	1.89
	Patient 5	1.12	2.33
50 iter	Patient 1	0.89	1.75
	Patient 2	1.02	1.90
	Patient 3	0.80	1.74
	Patient 4	0.83	1.82
	Patient 5	1.06	2.05
60 iter	Patient 1	0.79	1.63
	Patient 2	0.96	1.85
	Patient 3	0.78	1.71
	Patient 4	0.75	1.77
	Patient 5	1.01	1.97

Table 6.1: In five patients, the pyramidal tract was reconstructed and wrapped with hulls (iso-value 5, scale-dependent Laplace filter with $\lambda = 0.5$). The number of iterations for the surface filter was varied between 40, 50 and 60 iterations. For each hull, the average and maximum distance of all surface points to the nearest tract vertex was computed.

are an upper limit of the real distance. Since the fiber-tracking step size was set to 1 mm, the real distance between surface vertex and fiber streamline may be up to 0.5 mm less than the computed value. Nevertheless, the distance measures provide additional information about the tightness of the hulls and enable a quantitative assessment of their quality.

6.3 Construction of a safety margin

The wrapping approaches previously described provide hulls encompassing the fiber bundles and are an important prerequisite for intraoperative visualization. Based on these hulls, the boundary curves of white matter tracts are displayed within the focus plane of the OR microscope in order to guide the surgeon during the intervention. In this way, a direct relation between tumor tissue and eloquent structures is provided.

Additionally, an expanded surface providing a safety distance around the white matter tract is highly desirable for preoperative planning as well as for surgery. For this purpose, an offset surface is computed based on the initial hull by shifting all vertices of

the surface in the direction of the respective point normal n . A surface point p is repositioned by a distance d in the direction of the point normal resulting in the expanded position p' according to:

$$p' = p + d \cdot \frac{n}{|n|} \quad (6.4)$$

This technique provides smooth offset hulls as shown in Figure 6.10 for the pyramidal (blue) and optic (green) tract, where expanded safety hulls with a distance of 8 mm are presented.

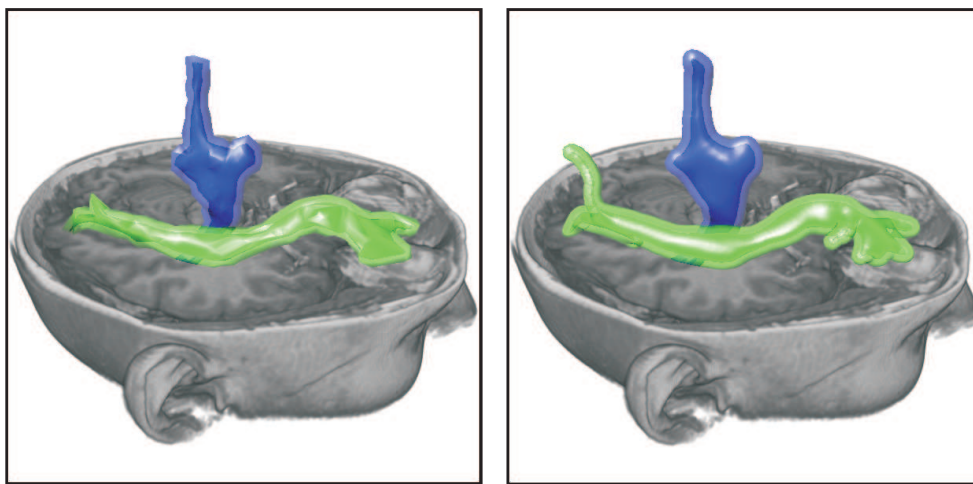


Figure 6.10: Hull surfaces and expanded surfaces for the optic (*green*) and pyramidal (*blue*) tract obtained from the approach based on tetrahedralization (*left*) and based on isosurfaces (*right*). The expanded surfaces serve as safety margins.

In principle, this simple approach for safety hulls might result in self-intersections of the outer hull. However, for different reasons, with respect to clinical application this is no real limitation: First of all, the required safety distances are in the range of a few millimeters (1-5 mm), resulting in non-intersecting safety hulls for the majority of reconstructed tract systems. Moreover, self-intersections may only occur in regions near the cortex where the tract systems terminate and where single fibers may fan out in different directions. For surgery of brain tumors, which are most frequently located near the internal capsule, deep-seated regions are of major interest, where thick bundles composed of coherent fibers are located. Finally, it is not difficult to interpret a boundary curve resulting from a self-intersecting hull correctly. In this case, only the outer contour is relevant, and inner loops have to be ignored (which can be further assessed, if the inner hull is displayed as well).

6.4 Discussion

The primary objective of the approaches presented in this section was to improve fiber-tract visualization for medical application by providing smooth hulls tightly fitting the underlying fiber tracts. Since streamline representations only illustrate a direction, the shape of a streamline bundle as a whole can only be estimated. Furthermore, hulls are necessary for intraoperative visualization, where the boundary curves of hulls are displayed in the focus plane of the OR microscope for neuronavigation. As a result, for neuronal structures within the brain, image-guided surgery based on hulls considerably reduces the risk of postoperative deficits, which is of high value for neurosurgery.

The initial approach for wrapping fiber bundles [36] suffers from a number of limitations, which are addressed by the alternative techniques presented. Developed in conjunction with automatic clustering of fibers, the initial geometric approach is restricted to elongated tract systems where a centerline is well-defined. For tract systems such as the corpus callosum encompassing fibers with a significantly varying direction, the approach will fail. Another problem is the precision of the approach. The ellipses defined per plane provide only limited precision in the case of concavities which are not correctly modeled.

In comparison to the initial approach for wrapping fibers, the approach based on tetrahedralization and 3D alpha shapes [89] provides high precision, which is an essential feature for the intended application. This is due to the fact that points originating from fiber tracking are directly used for tetrahedralization and remain after application of 3D alpha shapes. Additionally, the algorithm is able to wrap branching fiber tracts or tract systems with diverging fiber directions and it succeeded in generating precise hulls following the shape of the fiber bundle. A limitation of the approach relates to sparse bundles, where holes may occur if the threshold for tetrahedra removal is too low or if an adaptive step size has been applied during fiber tracking. In addition to that, the surface of the resulting hull is not very smooth, which makes the generation of an extended hull difficult.

The approach based on isosurfaces produces smooth hulls that tightly fit the underlying fiber bundles. The processing steps for hull generation have been thoroughly investigated and are harmonized with each other in order to provide smooth hulls of high accuracy. In a first processing step, the fibers are rasterized and a volume filter is applied to the rasterized volume. In this way, the occurrence of holes during further processing steps is circumvented. In a second step, a hull surface is extracted using the Marching Cubes algorithm. The resulting surface is smoothed using surface filtering approaches, where the number of iterations is used to control volume shrinkage and the tightness of the fitted hull. As a result, the technique presented is able to wrap fiber bundles of arbitrary shape and density. Even single streamlines diverging from the bundle and sparse regions are wrapped. The usability and adjustment of hulls was tested by a neurosurgeon and two medical students (neurosurgery), who applied the approach to several tract systems in different patients. They appreciated the flexibility of the approach, which makes it possible to generate the desired hulls by varying

mainly two parameters (the iso-value and the number of filter iterations). According to the distance measurements, the hulls generated by the medical experts wrap the tract systems with an average distance of about 1 mm to the underlying fibers. With respect to accuracy, this slight average expansion is tolerable for surgery. In recent research, it was even suggested that a worst-case safety distance of about 5 mm [110] should be adhered to, in order to compensate for effects influencing the precision of location, such as brain shift and image distortions inherent to DTI data. As a result, tight and smooth hulls are generated for arbitrary tract shapes, which are very well-suited for application in surgery. Due to their smoothness, they are also an appropriate basis for computing an expanded hull.

Overall, both approaches presented are able to wrap fiber tracts of any shape, and at the same time provide high wrapping precision. The hulls generated with the isosurface-based approach feature a higher degree of smoothness, which is important if expanded hulls are desired. For medical application as well as intraoperative visualization in neurosurgery, the approaches are of high value.

Chapter 7

Distortion correction

In Chapters 4 and 5, different methods for deriving fiber tract information from DTI data are described. The resulting fiber bundles play an important role in surgical planning, especially in relation to surgery of tumors near eloquent brain areas. Knowledge about the course and location of white matter tracts supports optimal resection while avoiding postoperative neurological deficits [43, 66, 109]. However, DTI measurements based on single-shot echo planar imaging (EPI) suffer from image distortions, primarily eddy-current-induced image distortions, chemical shift, and susceptibility artifacts. Consequently, the fiber tract information included in an anatomical MR dataset for neuronavigation is spatially displaced with respect to anatomical structures. For this reason, this chapter presents a method for correcting the distortions of DTI data based on non-linear registration. The approach was first published in [88]; a more detailed outline of the registration framework and an evaluation comprising the quality of registration as well as experimental results were published in [94]. Details about the registration strategy developed by Soza *et al.* are available in [132].

The chapter starts with an overview of image distortions inherent to DTI data in Section 7.1. Recent work addressing the correction of DTI-EPI artifacts is reviewed in Section 7.2. In Section 7.3, the registration framework and its main components are described. The experimental setup for distortion correction is outlined in Section 7.4 and registration results are presented in Section 7.5. Finally, the registration approach and its relevance for clinical application are discussed in Section 7.6.

7.1 Distortion artifacts of DTI-EPI data

During acquisition of DTI-EPI data, several sources of distortions exist; primarily eddy-current-induced image distortions, chemical shift and susceptibility artifacts.

Eddy currents are induced by the switching of the diffusion gradients in diffusion-weighted pulse sequences. They decay during the sampling period and produce time-varying magnetic fields. Consequently, the k -space data is not correctly sampled, which

results in a geometric distortion. Eddy-current-induced image distortions and patient motion cause a spatial misalignment of the diffusion-weighted volumes and are a common problem in clinical DTI acquisitions. For this reason, gradient preemphasis schemes are currently implemented in most MRI scanners, which is a very effective method of reducing the impact of eddy currents. Alternatively, post-acquisition strategies using image-based registration [121, 128, 76] or cross-correlation-based correction schemes [14] have been presented. The advantage of such schemes is that they do not rely on a properly calibrated gradient pre-emphasis.

Chemical shift and susceptibility artifacts can be attributed to the small bandwidth of the EPI sequence in phase-encoding direction. Differences in chemical shift or susceptibility cause slight differences in the proton resonant frequency resulting in positional shifts and distortions when the positions of the signal are mapped onto the image by frequency. To minimize the image distortions originating from chemical shift, the EPI scans are usually acquired with lipid suppression. For this purpose, a saturating pulse is commonly applied to the fat resonance prior to data acquisition [150]. Another promising approach is to combine chemical shift and slice selective excitation [95].

Susceptibility artifacts [52] resulting from microscopic gradients or variations in the magnetic field strength are observed at the interface of tissues with different magnetic susceptibility. They appear in the proximity of the skull base and near other air-filled spaces such as the brainstem and the frontal lobe and cause severe distortions implying a displacement of anatomical structures.

While the problem of eddy currents and chemical shift artifacts is eliminated with gradient pre-emphasis schemes and lipid suppression, the susceptibility artifacts inherent to EPI data remain an open problem. A short review of strategies that aim at correcting the respective distortions is provided in the next section.

7.2 Previous work

First attempts to account for susceptibility artifacts inherent to EPI use non-linear registration schemes. Hellier *et al.* [48] proposed a hierarchical multigrid algorithm, where a deformation field is estimated. This is achieved by minimizing a cost function based on mutual information using Powell's optimization scheme [120]. Another approach for correcting EPI distortions presented by Kybic *et al.* uses a higher-order spline model for warping and a similarity measure based on squared differences [67]. In their work, Kybic *et al.* encounter the problem of local minima, which they identified as a potential source of error in their approach. To overcome this problem, the registration algorithm applied in this work employs the SPSA optimization strategy [136] which is explicitly designed to overcome the problem of local minima more efficiently. Since the low resolution of the DTI-B0 dataset makes registration more difficult, a robust optimization technique is essential in order to obtain sufficient registration quality.

7.3 Non-linear registration

In this section, an intensity-based registration approach is presented which is applied in order to correct image distortions due to susceptibility artifacts inherent to DTI-EPI data. During non-linear registration, a transformation is computed which maps the reference B0 image onto the anatomical MR scan. In order to assess the quality of alignment, a similarity measure is required. For this purpose, normalized mutual information is employed as outlined in Section 7.3.1. Another essential part of the registration framework is the optimization strategy. Important characteristics of an optimization strategy are robustness in order to overcome local minima, and high convergence rates reducing the overall computational cost. The SPSA optimization strategy outlined in Section 7.3.2 combines both features and is therefore well-suited for non-linear registration. Both similarity measure and optimization are combined with a deformation model in order to compute the registration transformation. For this purpose, a control point grid is superimposed on the B0 dataset and a 3D free-form deformation model is employed for warping, as described in Section 7.3.3. Since the non-linear registration approach requires repeated resampling of the dataset according to the current transformation, hardware-based techniques enabling an efficient implementation are employed for the free-form deformation. In this way, the high computational cost for non-linear registration is considerably reduced, which is an important aim for clinical application.

7.3.1 Similarity measure

For intensity-based image registration, a similarity measure is required in order to assess the quality of alignment. For this purpose, an information theory approach denoted as mutual information (MI) was introduced for medical image registration [23, 151]. MI is based on the Shannon entropy $H(I)$ [127], which is a measure of the diversity of the intensity distribution in an image I . The quantity measured by MI is the statistical dependency between intensities in two datasets, which has to be minimized during registration. Since MI does not directly depend on the intensity values, it is an adequate similarity measure for datasets of different modalities, as required for distortion correction. The normalized version of MI denoted as normalized mutual information (NMI) [142] is currently the most frequently used similarity measure. For a source image I_s and a target image I_t with joint entropy $H(I_s, I_t)$, NMI is defined as

$$NMI(I_s, I_t) = \frac{MI(I_s, I_t)}{H(I_s, I_t)} + 1 = \frac{H(I_s) + H(I_t)}{H(I_s, I_t)}, \quad (7.1)$$

where MI is normalized with respect to the joint entropy. NMI overcomes the problem of MI sensitivity to changes in the image overlap region and is therefore used for the registration framework.

7.3.2 Optimization

Optimization is an iterative process, where the transformation mapping the source to the target dataset is computed. In each iteration, the set of parameters is updated based on the NMI value obtained for the current transformation. For a control point grid of $7 \times 7 \times 7$ free vertices and x, y and z coordinate for each vertex, 1029 parameters have to be adjusted during optimization in order to assess the optimal transformation. For this reason, the robustness and performance of an optimization strategy are crucial in order to arrive at the global minimum with minimal computational expenses. A very efficient optimization strategy applied for this purpose is the *simultaneous perturbation stochastic approximation* (SPSA) [136] method for multivariate optimization. In comparison to other optimization approaches, SPSA provides equal or greater efficiency in terms of overall cost as outlined in [78, 134, 135]. Additionally, SPSA proved to be more robust than other optimization schemes due to simultaneous perturbation of the optimized parameters and due to estimated gradient information [132]. In each iteration $k + 1$, the vector \mathbf{t}_{k+1} containing the translational offsets for all optimization parameters is updated according to

$$\mathbf{t}_{k+1} = \mathbf{t}_k - a_k \mathbf{g}_k(\mathbf{t}_k), \quad (7.2)$$

where for varying k , a_k is a scalar sequence and $\mathbf{g}_k(\mathbf{t}_k)$ is the estimate of the gradient of the optimized NMI function [136]. The gradient approximation requires only two measurements of the NMI for the perturbed parameter vector \mathbf{t}_k , irrespective of the dimension of the parameter domain. Essentially, the gradient approximation and simultaneous perturbation of all optimized parameters are the specific merits of SPSA optimization, leading to a significant reduction of the optimization cost compared to other optimization approaches such as Powell's direction search method [120]. Further implementation details and considerations relating to the SPSA optimization scheme are available in [132, 94].

7.3.3 3D free-form deformation

In order to deform the source dataset according to the shifts of the control points determined during optimization, a free-form deformation (FFD) model based on 3D Bézier functions is employed. The main principle of FFD is to warp the space surrounding an object, which will be warped implicitly. In order to obtain an elastic deformation, Bézier functions are employed which enable a smooth deformation of soft tissue by repositioning the control points.

Deformation model

In order to define a deformation function D , a trivariate tensor product of Bézier functions is employed. The respective basis functions B_i^l, B_j^m, B_k^n are the Bernstein polynomials of order l, m and n . The dataset is embedded in a lattice of 3D control points b_{ijk} ,

where $i = 0, \dots, l$, $j = 0, \dots, m$, $k = 0, \dots, n$. The associated deformation function D assigning a 3D coordinate position to a point with parameter space coordinates (s, t, u) is defined as:

$$D(s, t, u) = \sum_{i=0}^l \sum_{j=0}^m \sum_{k=0}^n B_i^l(s) B_j^m(t) B_k^n(u) b_{ijk}. \quad (7.3)$$

By moving the control points b_{ijk} within the lattice, the deformation function is changed, resulting in a shifted position of $D(s, t, u)$. The design of the Bézier basis functions ensures that the deformation function smoothly follows the movement of the control points, showing an intuitive behavior on positional changes of the control points. Due to the convex hull property inherent to the basis functions, it is possible to prevent the deformation function from taking values outside the image volume, by moving only inner control points and by setting the border control points fix. As a result, this FFD model makes it possible to model smooth, elastic deformations according to the movements of the control points.

Hardware-accelerated free-form deformation

The fact that a deformed dataset has to be generated in each iteration during optimization in order to measure the alignment using NMI involves a high computational cost. In order to speed-up the computation of the deformed dataset, the fast interpolation capabilities available on modern graphics hardware were utilized. For this purpose, the image data is loaded to the 3D texture memory of the graphics adapter in order to employ the texture processing unit. The control points, which are uniformly distributed at the beginning, i.e. $b_{ijk} = (i/l, j/m, k/n)$, correspond to respective texture coordinates. According to the current optimization input defined by the translation vector t_k , the control points are shifted to new locations.

Based on the deformed control point grid, classical approaches [122] explicitly calculate the new coordinate for every object point. In order to circumvent this computational expense, the deformation function D is only evaluated for a limited set of parameter values (s, t, u) which uniformly sample the parameter space. For an adequate approximation of the original shape of the deformation function, the sampling points are set more densely than the control lattice. For registration of DTI-EPI and anatomical MR data, a control lattice of $9 \times 9 \times 9$ control points ($7 \times 7 \times 7$ free control points) and a grid of $17 \times 17 \times 17$ sampling points provides the required flexibility. Based on the sampled values of D , the deformation is propagated onto the whole volume using trilinear interpolation. For this purpose, the deformation function is approximated with a 3D piecewise linear model [132, 47]. This approach is computationally less expensive since there is no need to process the whole volume to obtain new intensity values, which is necessary in software approaches. Instead, graphics hardware is employed to reduce the execution time of these expensive operations.

7.3.4 Registration framework

Before non-linear registration, an initial transformation is computed based on rigid registration [46] which is used as an initial estimate. This step may be omitted if the DTI-EPI and the anatomical MR dataset were acquired successively, without a positional change of the patient. In order to refine the registration result gradually, a three-stage multiresolution approach is employed. First, a non-linear registration is performed at a coarse resolution level. The resulting transformation serves as input for the second stage at a higher resolution level, et cetera. The third stage of the multiresolution approach corresponds to the original resolution of the datasets. With increasing resolution, the registration result is gradually improved on each hierarchy level. This technique helps to overcome local minima and the computational effort is reduced, since the total number of iterations required to achieve the optimum global value is generally reduced [132].

On each hierarchy level, the source dataset is loaded into texture memory and is embedded in a uniform lattice of control points. In an iterative procedure, the inner control points of the lattice are perturbed until the source dataset aligns with the target data. The manipulation of the free control points is controlled by the SPSA optimizer, which estimates the optimal position in each iteration by stochastic perturbation. The new deformed volume is generated by evaluating the deformation function at discrete parameter values and by approximating it linearly at intermediate positions. Depending on the quality of alignment, the registration algorithm terminates if the similarity measure does not change significantly over time, or if a maximum number of iterations is reached.

7.4 Experimental setup

In order to assess the quality of the registration framework, different experiments based on a known transformation and based on landmarks were performed. The experimental setup as well as respective results are documented in detail in [94]. This general verification is necessary in order to ensure that the transformation field obtained from non-linear registration reliably corrects the distortion artifacts inherent to the data.

After verifying the quality of registration, the presented approach was applied in order to evaluate the impact of susceptibility distortions on the location of white matter tracts. For this purpose, the pyramidal tract was investigated, which is an important tract system commonly monitored during surgery by means of functional neuronavigation. In this context, the potential misalignment due to susceptibility artifacts is of great interest to the surgeon.

For this purpose, datasets of 14 patients suffering from either gliomas or cavernoma were investigated in a retrospective study. Preoperative anatomical MR as well as DTI-EPI data were available for each patient. In order to leverage the impact of eddy currents and to eliminate chemical shift, gradient emphasis as well as lipid suppression were enabled during EPI acquisition. The remaining susceptibility artifacts were then

addressed using the presented approach for non-linear registration.

If necessary, the datasets are rigidly registered after image acquisition. Afterwards, they are prepared for non-linear registration by extracting the brain from the scan datasets, which is automatically accomplished using the Brain Extraction Tool (BET) software [130] from the FMRIB Software Library (FSL). This segmentation is of special importance for intraoperative datasets where the intraoperative head holder is visible as well as artifacts from the metal screws. In general, brain extraction prevents rigid structures such as skull bone from undesired deformation. The quality of the segmentation result is adjusted by the fractional intensity threshold and verified for each dataset.

In order to assess the spatial distortion of the pyramidal tract in each patient, the tract system is reconstructed using a ROI-based fiber-tracking approach, as outlined in Chapter 4. Subsequently, a marked B0 dataset is generated, where the grey value of all voxels containing fibers is set to a predefined, unambiguous value. Additionally, the non-linear registration approach is applied for mapping the B0 onto the anatomical MR dataset in order to compensate for the susceptibility artifacts. The resulting deformation field is then applied to the marked B0 dataset in order to correct the spatial displacement of the marked voxels. In Figure 7.1, the shift of marked voxels in areas where distortions were present in the B0 data is illustrated. The distortions inherent to DTI data due to susceptibility artifacts are clearly visible, as well as the effect of distortion correction on the position of the marked pyramidal tract.

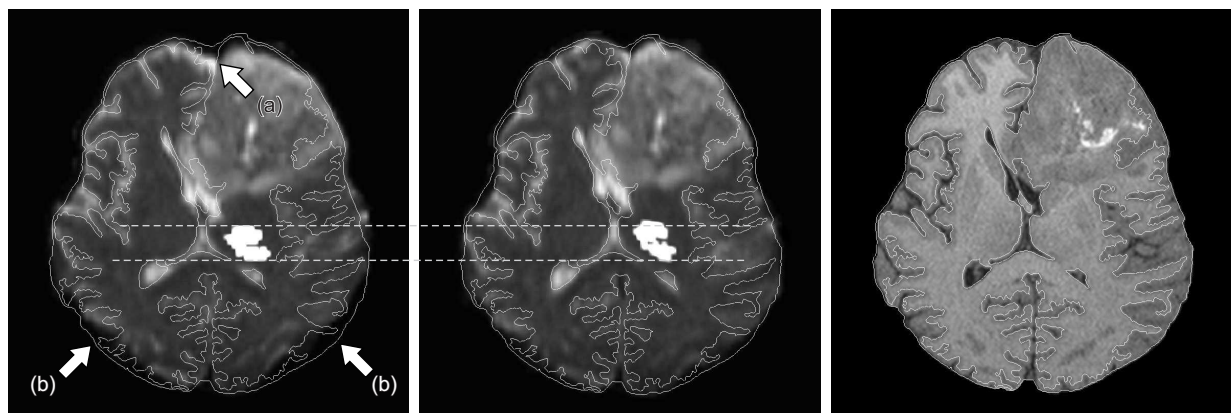


Figure 7.1: Patient with a right frontal astrocytoma (WHO grade III). Axial slice of the distorted B0 image with the marked pyramidal tract before (*left*) and after (*middle*) registration, and anatomical MR slice (*right*). The dashed line makes it possible to investigate displacement. (*a*) denotes susceptibility distortions, (*b*) indicates distortions due to the metal screws of the intraoperative head holder.

For evaluation of the susceptibility distortions, the displacement of the marked pyramidal tract was investigated. In this context, the measurement of distortions in anterior-posterior (A-P) directions is of major interest, since EPI distortions mainly occur in

phase-encoding direction, which corresponds to the A-P direction. For this reason, the left-right (L-R) distortions are expected to be minor. With respect to the z-direction, no distortions occur since MR acquisition is performed in slice selection mode. Consequently, the extent of distortions is evaluated by analyzing corresponding axial slices of the marked B0 dataset before and after applying the non-linear registration transformation. For this purpose, the maximum displacement of the fibers was determined by measuring the offset of marked voxels in every second axial slice. As outlined in Figure 7.2 (right), the maximum distance between two corresponding boundary points is determined in A-P and L-R direction.

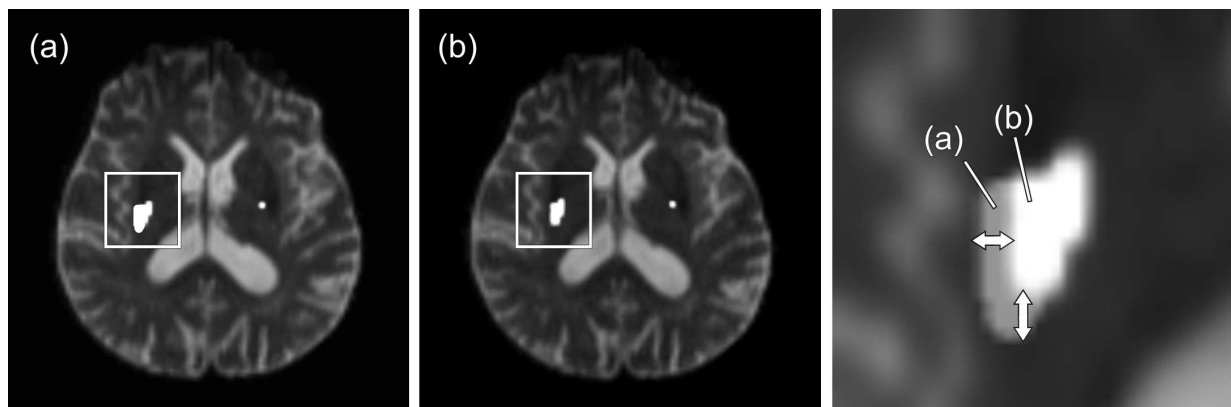


Figure 7.2: Patient with a right temporo-mesial WHO grade III anaplastic astrocytoma. Axial slice of B0 dataset with marked voxels representing the right pyramidal tract before (*left*) and after (*middle*) registration and transparent overlay analysis (*right*). Arrows indicate the maximal displacement in L-R and A-P direction.

In order to summarize roughly the distortion measurements in all 14 patients, the axial slices in each dataset are renumbered in order to provide a cross-alignment between the different patient datasets. For this purpose, the axial slice containing the upper boundary of the lateral ventricles is determined in each dataset and assigned a common slice number, and all other slices are renumbered accordingly. As a result, anatomical structures as well as areas of major distortions are located in slices with a common number in all patient datasets. This makes it possible to average the measured distortions in A-P and L-R direction per slice number.

7.5 Results

For each individual patient, distortion correction based on non-linear registration was applied and the offset of the marked voxels was measured. The computing time for all processing steps comprising data conversion, brain extraction, fiber tracking, marking of voxels, linear and non-linear registration was about 1.5 h on a PC equipped with an

Intel Pentium 4 (2.4 GHz). The main part is consumed by the non-linear registration approach, which is in the region of 50 minutes.

In a first step, the measurements for each patient were evaluated individually by plotting the distance measurements in A-P and L-R direction. For this purpose, the displacement of the pyramidal tract is plotted for the respective slice, as visualized in Figure 7.3 for A-P direction. In each patient, major distortions were observed in A-P direction, whereas the L-R distortions were considerably smaller. This is in accordance with previous expectations, taking into account that susceptibility distortions mainly occur in phase-encoding direction. Another distinct feature observed in all individual A-P evaluations was the distribution of distortions, depending on the slice location in z-direction. While prominent distortions mainly occurred near the cortex and at the brainstem, the intermediate part around the internal capsule was much less affected.

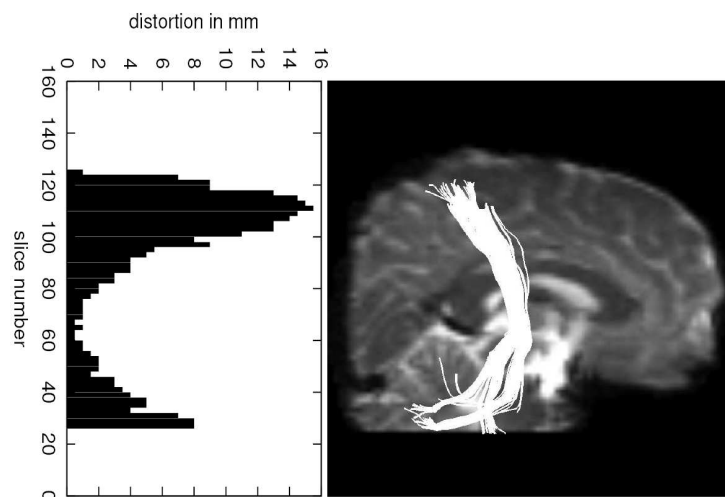


Figure 7.3: Patient with a cavernoma located in the postcentral gyrus. For each second axial slice, the measured distortions for the pyramidal tract in A-P direction are presented. Distinct distortions occur near the cortex and the brainstem.

In a second step, the results were summarized, based on the evaluations for each individual patient, by aligning the datasets. For this purpose, the slices were renumbered in such a way, that the slice number denoting the frontal base of the brain is identical in all datasets. This alignment makes it possible to compare the distortions in A-P and L-R direction in different individuals to some extent. The respective results for all patient datasets are summarized in Figure 7.3, where the averaged distortions in A-P and L-R direction are presented. In each diagram, the maximum and minimum, as well as the mean value \pm standard deviation of the distortion measurements is displayed. In line with the observations made in relation to the individual measurements, the averaged evaluation yielded major distortions in A-P direction, which were most prominent at the brainstem and near the cortex, whereas the distortions in L-R direction were less

significant.

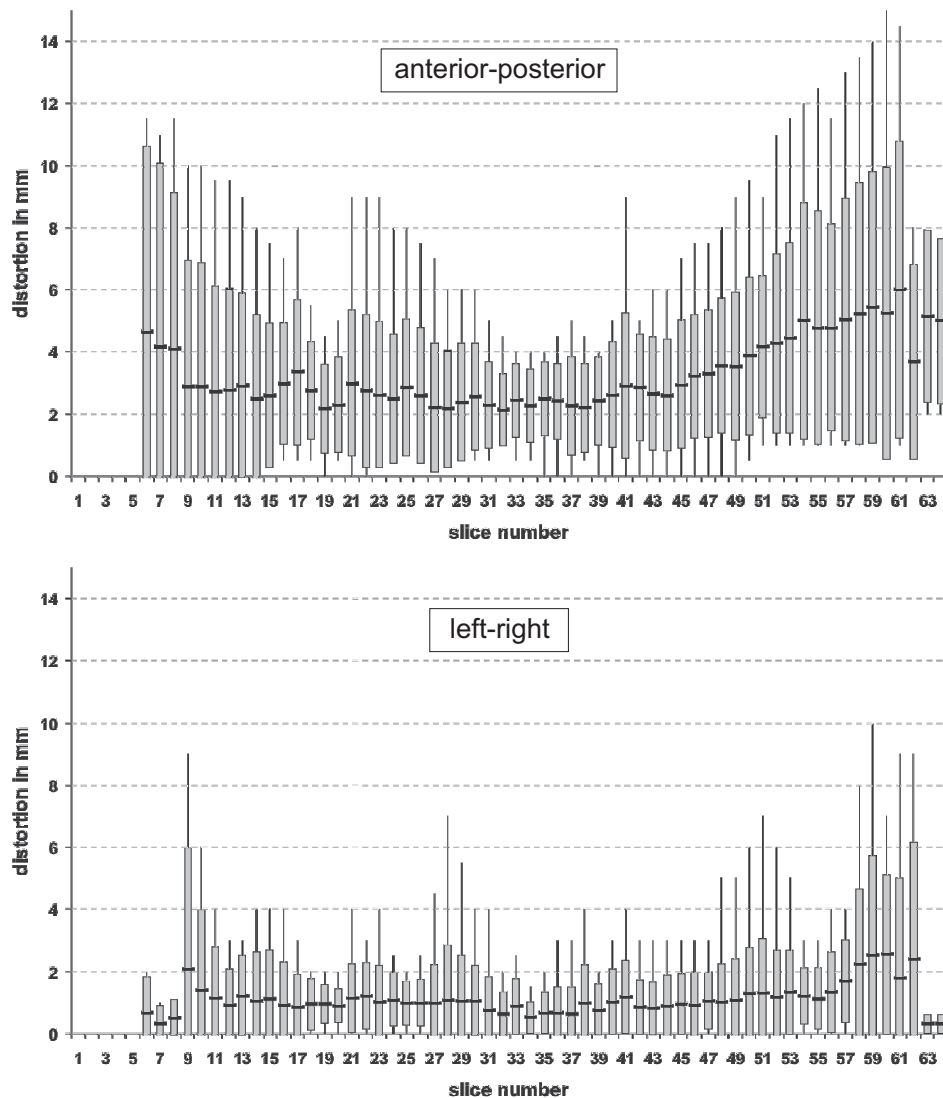


Figure 7.4: The patient datasets are aligned according to the frontal base of the brain. Slice numbering starts at the brainstem level. Average distortion \pm standard deviation, as well as minimum and maximum distortions for corresponding axial slices averaged for all 14 patients denoted in mm.

Finally, the evaluations from Figure 7.4 were further subsumed by classifying the slices into three groups, according to their location near the cortex, the internal capsule or the brainstem. The measurements were averaged per group, resulting in the summarized distortions presented in Table 7.1. As a result, the measured susceptibility artifacts

in A-P direction are most prominent at the cortex and the brainstem, where the mean distortion amounted to 4.0 mm and 3.2 mm. In the area of the internal capsule which is frequently the zone undergoing tumor resection, the mean distortion was limited to 2.4 mm.

	anterior-posterior			left-right		
	min [mm]	max [mm]	mean \pm sd [mm]	min [mm]	max [mm]	mean \pm sd [mm]
cortex	0	15	4.0 \pm 2.8	0	10	1.3 \pm 1.4
internal capsule	0	9	2.4 \pm 1.7	0	7	0.9 \pm 0.9
brainstem	0.5	11.5	3.2 \pm 3.5	0	9	1.0 \pm 1.5

Table 7.1: Minimum (min), maximum (max), and mean distortion \pm standard deviation (sd) in A-P (phase-encoding) and L-R direction measured for different areas of the brain in 14 patients.

7.6 Discussion

Susceptibility artifacts resulting in a spatial displacement of anatomical structures are a problem when fiber tract data has to be integrated into anatomical data for neuro-navigation. In principle, there exist different strategies in order to account for distortions inherent to DTI-EPI data: In modern functional scanning tools, field maps are implemented to identify and mark areas where the image information can no longer be trusted. However, a correction of image distortions is not provided with this technique. Another strategy concerns DTI sequences such as diffusion-weighted single-shot STEAM MR imaging [111] which exhibit significantly fewer image distortions. However, this MRI technique suffers from other drawbacks such as a coarser resolution, a lower signal-to-noise ratio and an increased measurement time, which mean that its clinical use is still problematic. For these reasons, EPI remains essential for clinical DTI, requiring alternative strategies for distortion correction.

For this reason, non-linear registration approaches were proposed for correction of susceptibility artifacts [48, 67, 88]. In particular, the presented registration strategy provides robustness and efficiency due to SPSA optimization and due to the implementation of the deformation model based on graphics hardware. SPSA has equal or greater efficiency in terms of overall cost compared to other optimization approaches [78, 134, 135] and is therefore an excellent method for both local and global optimization. Additionally, the SPSA optimization method is much better suited to overcome local minima, due to simultaneous perturbation of the optimized parameters and due to the fact that the gradient of the similarity measure is estimated, which contributes to the robustness of the registration framework. As a result, the presented registration algorithm enables

registration of DTI-EPI and anatomical MR data in spite of the low resolution encountered for DTI-EPI data.

In this work, the non-linear registration approach is used in order to compute a displacement field, which is applied to the DTI dataset, resulting in a shift of fibers represented by marked voxels. This indirect approach relying on precomputed fibers and marked voxels is necessary due to the geometric nature of the tensor information. Non-linear registration of DTI data would require a re-orientation of the respective tensors for full correction, which is overcome by the suggested technique. Furthermore, approaches currently available for tensor re-orientation [44, 123, 129] suffer from significantly increased computing times due to their algorithmic complexity. In addition to that, these techniques have not yet been fully quantified and theoretically proven. For this reason, re-orientation of tensors is circumvented in the presented approach.

For clinical application, distortion correction of susceptibility artifacts inherent to DTI-EPI data is of great interest. In order to minimize the risk of neurological deficits, the location of functional brain areas and white matter tracts is determined preoperatively. Currently, functional brain areas identified with fMRI are integrated into an anatomical MR dataset which is used for stereotactic guidance in functional neuronavigation [43, 109, 107]. In order to integrate white matter structures into a stereotactic setup as well [56, 63, 21, 22], techniques for correcting susceptibility artifacts are required.

In order to evaluate the impact of susceptibility distortions for medical application, the approach was applied in the case of 14 patients. After distortion correction, the displacement of the pyramidal tract was assessed. In accordance with previous expectations, distinct distortions were measured near the cortex and in the area of the brainstem. For all patients, the main displacement occurred in A-P direction, which is the phase-encoding direction, whereas the left-right displacements proved to be less dominant. These general observations are also supported by the summarized results obtained from roughly aligning the different patient datasets. For medical application, these observations are of major importance, showing that a displacement of up to 15 mm is possible in A-P direction for the pyramidal tract. However, in spite of these general tendencies, differences between the patients were apparent. For this reason, distortion correction based on non-linear registration has to be applied separately for individual patient datasets in order to obtain precise results. This is of special importance for patients where the lesion is close to the pyramidal tract in order to prevent injury of this tract system. Nevertheless, the presented evaluations show that susceptibility artifacts are most prominent near the cortex and in the brainstem and affect the position of the pyramidal tract primarily in A-P direction.

However, with respect to intraoperative application, limitations are encountered due to the computational expense of the approach. During surgical intervention, brain shift effects and tumor removal require an update of the navigation system with intraoperative data [108, 105] to compensate for these effects [104]. In spite of acceleration based on graphics hardware and a highly efficient optimization strategy, the non-linear registration approach is still too time-consuming for intraoperative use. However, the

problem of updating the navigation after brain shift or tissue removal also holds for fMRI data which have to be acquired preoperatively. In current research, this problem is addressed by simulation approaches aiming at prediction of intraoperative deformations [133]. Another possible method for locating functional regions is subcortical electrical stimulation, which may serve as an additional source of information. However, this technique is merely adequate to support neuronavigation, since permanent deficits remain when electrical stimulation is applied alone [58]. For this reason, correction of susceptibility artifacts is an important aim for neurosurgical interventions. The presented approach improves spatially correct preoperative planning and integration of fiber-tracking data into the neuronavigation system, resulting in safer resection.

Part III

Visualization

Chapter 8

Visualization of fibers

For the reconstruction of fiber tracts based on DTI data, various approaches exist, as outlined in Chapters 4 and 5. In order to provide an efficient and meaningful visualization, different visualization strategies for reconstructed fiber bundles are presented and discussed in this chapter. For medical application, a comprehensive visualization of the reconstructed fiber tracts is important in order to support inspection of the data for surgical planning. Since the amount of streamlines may be immense in the case of tracking the whole brain, and since at the same time interactive visualization is necessary for medical investigation, appropriate techniques are required. The topics addressed in this context comprise color schemes as well as rendering techniques for the fibers. Color schemes are an important tool in order to convey additional information about the local tensor field. In conjunction with the approach for connectivity analysis, different color transfer functions were presented, which were published in [79, 90]. For efficient rendering of fibers, different renderers were developed. Fiber tracts are frequently visualized based on line rendering, which was enhanced with an approach for adaptive transparency depending on the local FA values. An alternative technique based on triangle strips and point sprites provides improved visual quality and was published in [93, 92].

The chapter starts with an overview of different color transfer functions in Section 8.1. Subsequently, the approach for line rendering is outlined in Section 8.2 and adaptive transparency depending on the local FA value is presented. Finally, a hybrid visualization technique based on triangle strips and point sprites is described in Section 8.3.

8.1 Color transfer functions

The fiber bundles obtained from fiber tracking or connectivity analysis represent the shape and the course of the underlying white matter structures. In addition to this spatial information, color transfer functions provide the possibility to convey additional information, depending on the local tensor information. In principle, different scalar

measures such as the local FA value, the barycentric space coordinates or the local cost function may serve as a basis for the mapping function. For practical application, three techniques proved to be of major interest:

Map major eigenvector components to RGB: The standard strategy for color encoding of fibers [25, 55, 115] utilizes the normalized principal eigenvector of the local trilinear interpolated tensor. The vector components are mapped to RGB values, i.e. the x component of the vector is taken as R value, the y component as G value and the z component as B value. As a result, the orientation of fibers is highlighted by color, and fibers of similar direction are visually bundled. In the case of fiber tracking, directional information of the major eigenvector is already represented with streamline directions, which is further supported by this color mapping scheme.

FA value: Mapping of the FA value [79, 90] assigns green to $FA = 1$ and red to $FA = 0$, and intermediate values to the face diagonal of the RGB cube connecting red and green. Since the FA value relates to the anisotropy of diffusion, the FA value adds further information about the local coherence of underlying nerve structures. In the case of fiber tracking, the mapped FA value is also an indicator of the reliability of the fiber-tracking results. Since a high FA value visualized in green indicates an elongated tensor with highly anisotropic diffusion characteristic, the reliability of fiber tracking based on the major eigenvector is high in these regions. Contrarily, for fiber segments with a reddish appearance, the underlying tensors are rather spherical. This implies that the fiber-tracking results might be less reliable in these regions.

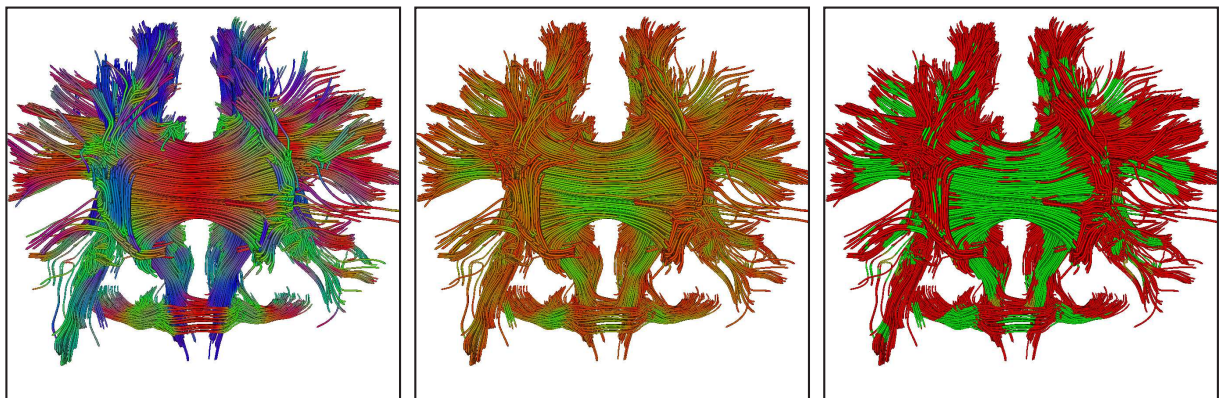


Figure 8.1: Color transfer functions for fiber visualization. *Left:* The xyz -components of the normalized major eigenvector are mapped to RGB color values. *Middle:* The FA value is mapped to green for a high, and red for a low value. *Right:* Mapping of the barycentric space coordinates: Linear tensors are mapped to green, planar tensors to brown and spherical tensors to red.

Barycentric space coordinates: The barycentric space coordinates c_l , c_p and c_s separate the shape of a tensor into linear, planar and spherical components, which classify the tensor properties. The barycentric space color mapping identifies the largest of the three values and assigns green to a tensor with dominant c_l value, brown to a tensor with major c_p value and red to a tensor with highest c_s component. Similarly to mapping of the FA value, regions of high anisotropic diffusion where linear tensors dominate can be identified. The barycentric space color mapping thus conveys additional information about the underlying tensors, with respect to their shape classification.

In Figure 8.1, the different techniques for color encoding are shown. Color encoding of the major eigenvector (left) supports spatial perception of the fiber-tracking result and provides visual clustering of similar fiber directions. FA mapping (middle) provides additional information about the local anisotropy of diffusion. Since the FA value serves as a threshold for fiber tracking, zones with green and orange color occur, but no red zones. The mapping technique based on the barycentric space coordinates c_l , c_p and c_s reveals that for most tensors, the linear (green) and spherical (red) barycentric space coordinates dominate, whereas only a few tensors feature a primary planar characteristic (brown).

8.2 Visualization based on lines

In order to visualize the trajectories obtained from fiber tracking or connectivity analysis, line-based representations are frequently used. In this way, real-time rendering of a large number of trajectories is possible, which is important for practical application, since fiber trackings may result in several thousands of streamlines. For rendering of fibers, the trajectories were stored in a vertex buffer object (VBO) and were rendered using the OpenGL API. In order to improve visual perception, illuminated streamlines were implemented as outlined in Section 8.2.1. The approach for adaptive transparency presented in Section 8.2.2 was developed in order to make major tract systems occluded by peripheral fibers visible.

8.2.1 Illuminated streamlines

In general, illumination is important in order to support the spatial interpretation, thus improving insight into the data. For surface primitives characterized by a distinct outward normal vector, illumination is provided by the hardware shading capabilities of modern graphics cards. However, in the case of line primitives, no unique normal directions exist. For this reason, an approach for illuminated streamlines presented by [162, 75] is employed and extended, which is based on the Phong reflection model.

Phong lighting model

The reflection model of Phong [117] is composed of different terms which are based on the light direction L , the normal vector N and the reflection vector R . The ambient fraction I_{amb} is a global term which represents the overall light intensity in the environment due to multiple reflections. The diffuse term I_{diff} describes diffuse reflection according to Lambert's law, where the reflected intensity is independent of the viewing direction V . The specular term I_{spec} generates specular highlights with maximum intensity in the direction of the reflection vector. The exponent n controls the shininess, i.e. the width of the highlights. The terms are weighted with respective constants k_a , k_d and k_s , which characterize the reflection properties of the material. As a result, the equation for Phong illumination is defined as follows:

$$\begin{aligned} I &= I_{amb} + I_{diff} + I_{spec} \\ &= k_a + k_d L \cdot N + k_s (V \cdot R)^n. \end{aligned} \quad (8.1)$$

Line illumination

However, in the case of line primitives, no unique normal vector is defined, since all vectors in a plane perpendicular to the fiber tangent T come into question. The normal plane containing potential normal vectors is shown in Figure 8.2 (left). A possible solution to the problem of ambiguous normal directions suggested by [3] maximizes the scalar products for the diffuse and specular term in Equation 8.1. According to [162], the diffuse term reaches its maximum, if the normal N is perpendicular to T and coplanar to T and L , as shown in Figure 8.2. Using Pythagoras' theorem, the scalar product

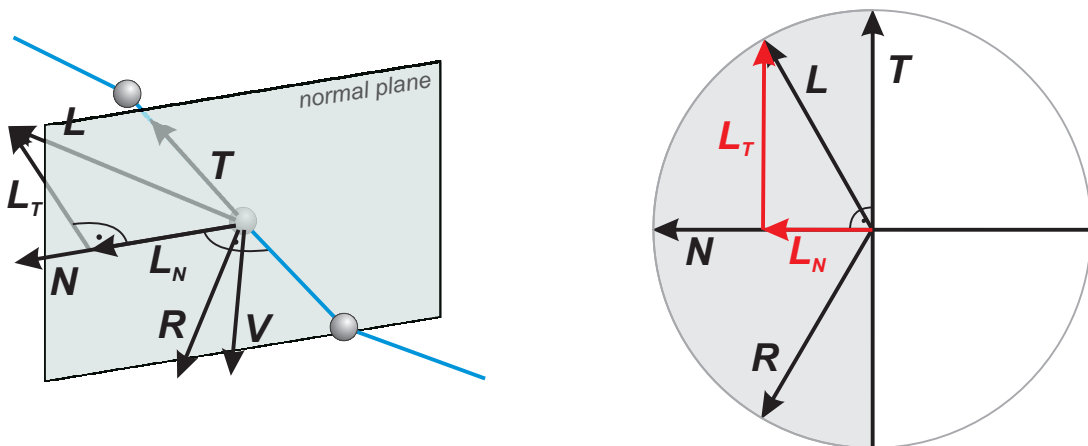


Figure 8.2: *Left:* The light vector L can be decomposed into two orthogonal components L_T and L_N . *Right:* Plane containing the vectors V and T , with coplanar normal vector N and reflection vector R .

required for the diffuse term in Phong's reflection model can be rewritten as follows (see Figure 8.2 (right) for comparison):

$$\mathbf{L} \cdot \mathbf{N} = |\mathbf{L}_N| = \sqrt{1 - |\mathbf{L}_T|^2} = \sqrt{1 - (\mathbf{L} \cdot \mathbf{T})^2}. \quad (8.2)$$

Similarly, the scalar product required for the specular term can be expressed in terms of \mathbf{L} , \mathbf{V} and \mathbf{T} . In [162, 75], the following derivation is provided, which is adapted to the vector directions employed in Figure 8.2:

$$\begin{aligned} \mathbf{V} \cdot \mathbf{R} &= \mathbf{V} \cdot (\mathbf{L}_N - \mathbf{L}_T) \\ &= \mathbf{V} \cdot ((\mathbf{L} \cdot \mathbf{N})\mathbf{N} - (\mathbf{L} \cdot \mathbf{T})\mathbf{T}) \\ &= (\mathbf{L} \cdot \mathbf{N})(\mathbf{V} \cdot \mathbf{N}) - (\mathbf{L} \cdot \mathbf{T})(\mathbf{V} \cdot \mathbf{T}) \\ &= \sqrt{1 - (\mathbf{V} \cdot \mathbf{T})^2} \sqrt{1 - (\mathbf{L} \cdot \mathbf{T})^2} - (\mathbf{L} \cdot \mathbf{T})(\mathbf{V} \cdot \mathbf{T}). \end{aligned} \quad (8.3)$$

In order to replace $(\mathbf{L} \cdot \mathbf{N})$, the result from Equation 8.2 is applied, which is also adapted in order to resolve $(\mathbf{V} \cdot \mathbf{N})$. An alternative possibility to express $(\mathbf{V} \cdot \mathbf{R})$ in terms of \mathbf{L} , \mathbf{V} and \mathbf{T} is derived as follows:

$$\begin{aligned} \mathbf{V} \cdot \mathbf{R} &= \mathbf{V} \cdot (\mathbf{L}_N - \mathbf{L}_T) \\ &= \mathbf{V} \cdot ((\mathbf{L} - \mathbf{L}_T) - \mathbf{L}_T) \\ &= \mathbf{V} \cdot (\mathbf{L} - 2\mathbf{L}_T) \\ &= \mathbf{V} \cdot (\mathbf{L} - 2(\mathbf{L} \cdot \mathbf{T})\mathbf{T}) \\ &= (\mathbf{V} \cdot \mathbf{L}) - 2(\mathbf{L} \cdot \mathbf{T})(\mathbf{V} \cdot \mathbf{T}). \end{aligned} \quad (8.4)$$

The presented result in Equation 8.4 needs fewer operations and is therefore more efficient than the derivation provided in Equation 8.3. In the case of a headlight located at the same position as the camera, i.e. $\mathbf{V} = \mathbf{L}$, Equation 8.3 and 8.4 can be further simplified, which yields the following result:

$$\mathbf{V} \cdot \mathbf{R} = 1 - 2(\mathbf{L} \cdot \mathbf{T})^2. \quad (8.5)$$

In Table 8.1, the frame rates for the different techniques to compute the specular term $(\mathbf{V} \cdot \mathbf{R})$ are provided. For benchmarking a PC equipped with a P4 3.0 GHz, 2 GB RAM and a NVidia Geforce 6800 Ultra graphics card with 256 MB graphics memory was used. The viewport for all renderings was 600×800 pixels and the displayed set of lines, generated by fiber tracking within the whole brain, consisted of approximately 300000 segments originating from about 4500 fibers. For rendering of illuminated lines, the approach suggested by [162, 75] (Equation 8.3) is the least efficient one and achieves only 88 % performance compared to the alternative technique presented in Equation 8.4. Simplification of the equations by using a headlight with $\mathbf{V} = \mathbf{L}$ provides a further gain in performance, which is in the range of 22 % compared to the improved approach in Equation 8.4.

Visualization technique	Frame rate
Lines, no illumination	232.5 fps
Illuminated lines, Equation 8.3	135.4 fps
Illuminated lines, Equation 8.4	153.3 fps
Illuminated lines (headlight), Equation 8.5	187.7 fps

Table 8.1: Frame rates in fps (frames per second) for illuminated lines, depending on the implementation of the diffuse term according to Equation 8.3, 8.4 or 8.5.

Tangent interpolation

The lighting results obtained from the technique described above generate the intended illumination effects and are automatically interpolated along each single line segment. However, the highlights sometimes change abruptly and have an unnatural appearance, which is due to sudden changes of the fiber direction. A possible solution in order to improve lighting results is interpolation of the normal and color information between an enlarged number of sampling vertices of the streamline. Alternatively, it is also possible to interpolate the respective tangent directions, which is more efficient since the tangents must be computed anyway. In order to achieve a smooth transition between highlights, weighted interpolation between five adjacent tangents according to

$$\begin{aligned}
 \mathbf{t}_i &= 1/10 (\mathbf{t}_{i-2} + 2\mathbf{t}_{i-1} + 4\mathbf{t}_i + 2\mathbf{t}_{i+1} + \mathbf{t}_{i+2}) \\
 &= 1/10 (\mathbf{t}_{i-2} + \mathbf{t}_{i+2} + 2(\mathbf{t}_{i-1} + \mathbf{t}_{i+1} + 2\mathbf{t}_i))
 \end{aligned} \tag{8.6}$$

is suggested. The resulting tangent direction is transferred to the vertex program and serves as a basis for computing the local illumination. The difference between lighting without and with tangent averaging is shown in Figure 8.3.

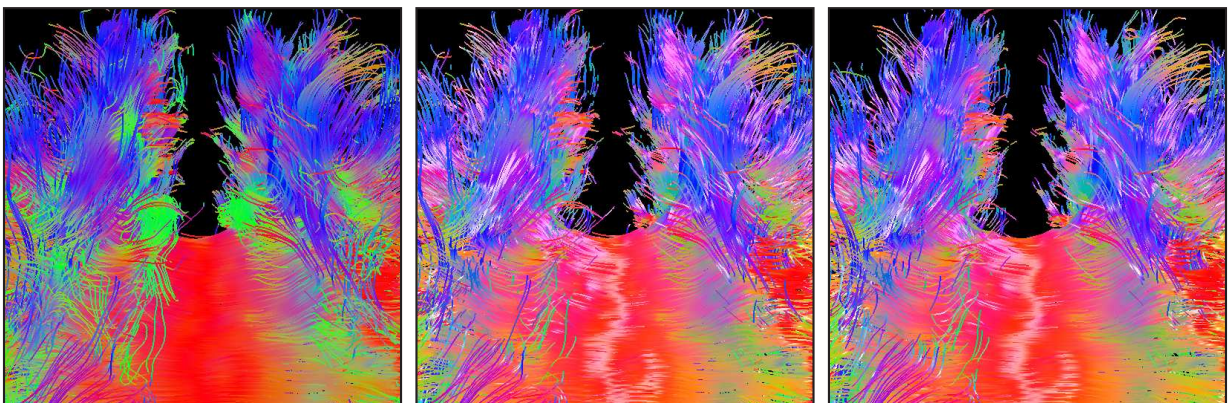


Figure 8.3: *Left*: Line rendering without illumination. *Middle*: Approach for illuminated streamlines. *Right*: Tangent interpolation leads to smoother illumination results.

Implementation

The above results for streamline illumination are implemented based on programmable graphics hardware. The vertex program evaluates Equation 8.2 and 8.4 for each vertex, based on the local tangent direction and the light vector. Instead of a normal, the averaged tangent direction is submitted to the vertex program, and the light vector is transferred for each draw command as a global variable. The resulting factors $L \cdot N$ for diffuse and $(V \cdot R)^n$ for specular illumination are passed to the fragment program, which computes the final color for each pixel based on the initial color and the material properties.

8.2.2 Adaptive transparency

In visualization applications, transparency is used in order to make occluded structures visible. In the case of a tracking of the whole brain, important tract systems are often occluded by smaller, peripheral fibers. For this reason, transparent rendering of the fibers with small FA value is applied in order to reveal the underlying major tract systems. This is achieved by an adaptive transparency value, depending on the local FA features.

In general, the depth-buffer test is not sufficient for transparent rendering, since in the case of transparency, occluded objects may be visible as well. For this reason, transparent rendering requires depth-sorting in order to combine different objects correctly. Additionally, intersecting objects must be divided into sub-objects which are sorted anew. Since the sorting of objects depends on the view direction, the current sorting order depends on the camera position.

For the streamlines obtained from fiber tracking, the objects which have to be sorted are the line segments. Since the line segments are short and seldom overlap, an intersection test can be omitted. Specifically, in the case of fiber tracking based on evenly spaced streamlines (Section 4.3), it is guaranteed that streamline segments do not intersect. In order to sort the line segments, the Euclidean distance between the camera and the center point of the line segment could be used as a distance measure. However, a more efficient measure is provided by the point distance function based on the Hessian normal form. The distance d of a point p to a plane E is computed by inserting p into the plane equation of E in Hessian normal form:

$$d = \langle n|p \rangle - \langle n|x_0 \rangle . \quad (8.7)$$

Thereby, the plane E with unit normal vector n and point x_0 is taken as the reference plane. The sign of d indicates, on which side of E the point p is located. In order to utilize this equation for sorting the line segments, n is chosen parallel to the viewing direction. For simplification, E is chosen as plane through the origin, i.e. $\langle n|x_0 \rangle = 0$. As a result, the distance of a fiber point p to the plane through the origin can be computed with one single inner product $d = \langle n|p \rangle$, which is much more efficient than the Euclidean distance and equally suited for sorting.

Based on the computed distances, the segments are sorted using the STL sort algorithm, which is based on introsort [101] with a worst case complexity of $\mathcal{O}(n \log(n))$. In order to reduce the computational effort encountered for sorting and to provide realtime-rendering, a popular technique is to precompute the sorting order for different directions. During rendering, the precomputed sorting associated with the direction closest to the current viewing direction is chosen. For this purpose, the fiber segments are sorted for a set of eight viewing directions (aligned with the four diagonals of a cube, with two possible orientations for each diagonal). As a result, frame rates of about 90 fps are achieved on a NVidia Geforce 6800 Ultra graphics card with 256 MB graphics memory, compared to 7 fps without precomputed sorting sequences.

Instead of a constant transparency for all fibers, an adaptive value per fiber segment is determined. As a result, small and peripheral tract systems which are less dense and pronounced are rather transparent, whereas major tract systems are more opaque and are visually dominant. The transparency ramp can be adjusted by the user, as shown in Figure 8.4. As a result, dominant tract systems are no longer occluded by small fiber bundles and regions with high local FA are visually emphasized, which is clearly apparent in Figure 8.4 (see marked regions).

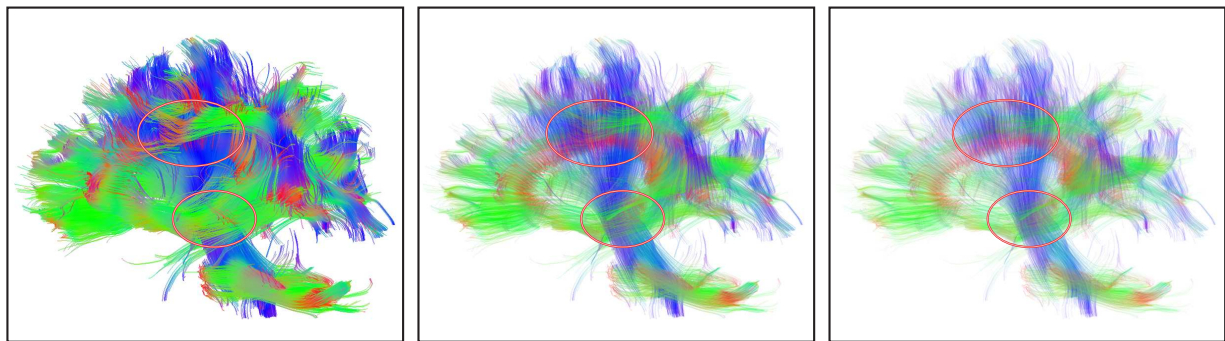


Figure 8.4: Streamlines visualized with adaptive transparency depending on the local FA value, with a maximum alpha value of 0.5, 0.1 and 0.05 (from left to right). Transparency depending on the FA value makes important tract systems visible, which would otherwise be occluded by peripheral fibers (see marked areas).

The visualization technique based on adaptive transparency is therefore an alternative approach to color encoding based on FA and is also related to evenly spaced streamlines with adaptive density, depending on the FA value (Section 4.3.2). In order to intensify the perception of local FA variations, these techniques can also be combined.

8.3 Visualization based on triangle strips and point sprites

The line rendering technique presented in the previous section provides interactive rendering times, which is of major interest for a large number of fibers. However, simple

line rendering implies several disadvantages, such as gaps between neighboring segments which are visible if the lines are wider than one pixel. Additionally, the depth perception is lost due to a constant width irrespective of the distance to the camera. These limitations are not encountered using tubes, which provide a significantly improved visualization. However, the complex geometry of tubes makes rendering much more time-consuming and therefore restricts interactivity.

In order to overcome these limitations, an alternative visualization technique for fiber bundles is presented in this section, which is based on a combination of textured triangle strips and point sprites. As a result, a visualization very similar to tubes is obtained and the number of primitives is significantly reduced enabling interactive rendering. For this reason, the presented strategy is of major interest for medical application in neurosurgery.

8.3.1 Previous work

The fiber bundles obtained from fiber tracking are commonly visualized using line-based representations such as illuminated streamlines [162, 75]. To improve the visual perception and in order to provide a better overall impression, lines were extended to streamtubes [159]. Alternative approaches utilize hyperstreamlines [31, 156] to convey further tensor information through the shape of the tube in order to increase the information content. As a drawback, the resulting rendering times are considerably slower than in the case of lines since complex geometry is necessary to model tubes or hyperstreamlines. In recent work, a more efficient technique for a tube-like visualization has been presented [141], combining a GPU-based approach using quad strips with a CPU-based tessellation in regions where artifacts occur. A speed-up of about 2.4 was achieved in comparison to approaches solely based on tessellated tubes. However, to meet the performance requirements encountered when rendering dense fiber tracts, this approach is still not fast enough due to a time-consuming CPU stage. An alternative technique for interactive visualization of many streamlines employs cylindrical billboards [124], which provides good results as long as thin streamlines are rendered. However, artifacts due to flipping triangles occur in regions where the fiber direction is nearly parallel to the viewing direction.

8.3.2 Hybrid visualization approach

Current visualization techniques for streamlines either provide high visual quality, but are too slow to handle trackings of the whole brain, or reduced quality has to be accepted to obtain interactivity. For this reason, a hybrid approach combining triangle strips and point sprites is presented which meets the clinical requirements for visualizing a large number of fiber tracts. As a result, real-time rendering is achieved and at the same time the visualization quality is comparable to geometry-based tubes.

Visualization using triangle strips

The crucial advantage of triangle strips over tube-based representations is the fact that the geometry is considerably reduced. Instead of modeling a tracking segment with triangles forming a tube, only two triangles per segment are required in our approach. The triangles are rotated towards the camera by a vertex program and are textured in order to obtain a tube-like appearance. Furthermore, the applied triangle strips provide a depth-dependent width which supports the visual perception.

The reconstruction of the triangle strip is outlined in Figure 8.5. Starting from each sampling point \mathbf{p}_i of the streamline, two new vertices are generated which are used as boundary vertices of the triangle strip. For this purpose, the cross product $\mathbf{d}_i = \mathbf{v}_i \times \mathbf{t}_i$ between viewing direction \mathbf{v}_i and streamline tangent \mathbf{t}_i is computed providing the direction \mathbf{d}_i which is used to place the new nodes. The width of the tube is defined by the user by choosing the radius r . \mathbf{d}_i is normalized and the new nodes $\mathbf{p}_{i,north}$, $\mathbf{p}_{i,south}$ necessary to construct the triangle strip are generated:

$$\mathbf{p}_{i,north/south} = \mathbf{p}_i \pm r \cdot \mathbf{d}_i \quad \text{with} \quad \mathbf{d}_i = \frac{\mathbf{v}_i \times \mathbf{t}_i}{|\mathbf{v}_i \times \mathbf{t}_i|} \quad (8.8)$$

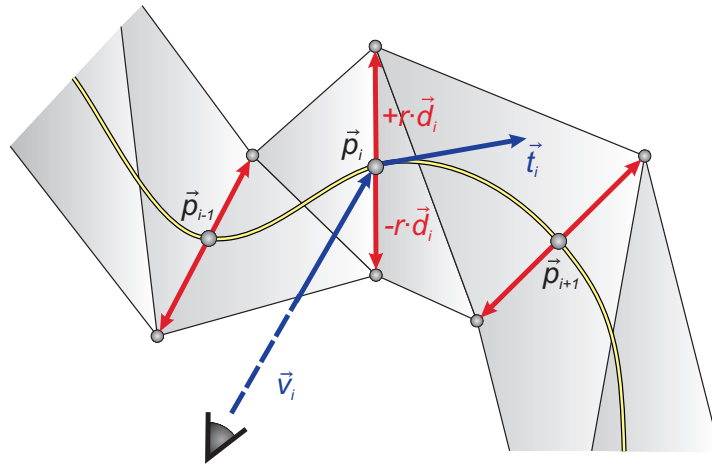


Figure 8.5: Construction of a triangle strip. Based on sampling nodes of streamline (yellow), nodes for modeling the triangle strip are generated.

The construction of the triangle strip is efficiently computed using graphics hardware. For this purpose, the triangle strip contains each node \mathbf{p}_i twice since the shifted node locations are computed for each frame within the vertex program. For each copy of \mathbf{p}_i , a 2D texture coordinate is stored where the first coordinate corresponds to a 1D texture used for simulating tube-like illumination. The second 2D texture coordinate contains a flag which is 1 if the node is shifted to north resulting in $\mathbf{p}_{i,north}$ and -1 if the node is shifted to south, respectively. In Figure 8.6, the texture coordinates are given in brackets for each node of the triangle strip.

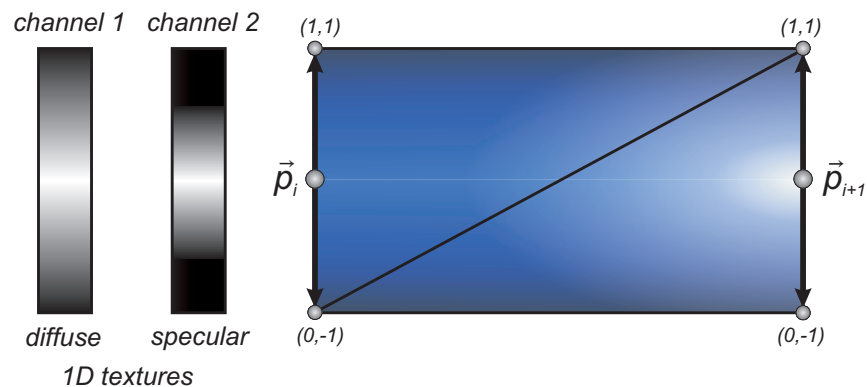


Figure 8.6: A 1D texture is used to simulate tube-like illumination. The luminance channel is used for diffuse illumination; the alpha channel stores the specular term.

An essential component for a tube-like appearance of a triangle strip is adequate texturing which simulates illumination of a tube. For this purpose, a 1D texture with a luminance and an alpha channel is employed. The luminance channel stores the diffuse illumination whereas the alpha channel contains the specular term. In order to simulate illumination of a tube, the textures have to get darker when approaching the border of the triangle strip. In the case of diffuse illumination, a sine function for angles between 0 and 180 degrees provides an appropriate decay. For specular highlights, the bright spot has to be focused. Natural results were obtained by raising the values for diffuse illumination to a power of 16. Figure 8.6 shows both channels of the texture on the left and a textured triangle strip segment on the right. In order to obtain a smooth illumination effect, the normals in viewing direction at two adjacent sampling points p_i and p_{i+1} are interpolated.

The underlying color of the textures is based on one of the color transfer functions outlined in Section 8.1. For efficient rendering using OpenGL, all tracked streamlines are drawn by invoking `GL_TRIANGLE_STRIP` only once. In order to obtain separated streamlines at the end, degenerate triangles are employed which connect two streamlines by positioning all triangle points on a line since OpenGL excludes these triangles from rendering. For optimum rendering performance, the nodes and their attributes are stored interleaved using a vertex buffer object (VBO).

The presented approach based on triangle strips provides good results as long as the direction of a line segment does not come close to the viewing direction. Otherwise, flipping artifacts occur when viewing and segment direction are nearly parallel. Artifacts arising from flipping triangles are shown in Figure 8.11.

Visualization using point sprites

Point sprites are particularly suitable for the visualization of line segments which are nearly parallel to the viewing direction. In this case, they provide a natural, tube-like

visualization since they resemble the cross section of a tube. A point sprite corresponds to a textured square which is always oriented towards the camera and which is efficiently visualized based on the OpenGL extension for point sprites. Similar to textured triangle strips, a 64×64 2D-RGB-texture is used to draw and illuminate them (see Figure 8.7). The R-channel is used as alpha channel to obtain a spherical shape of the point sprite. The G- and B-channel are used to simulate diffuse and specular illumination.

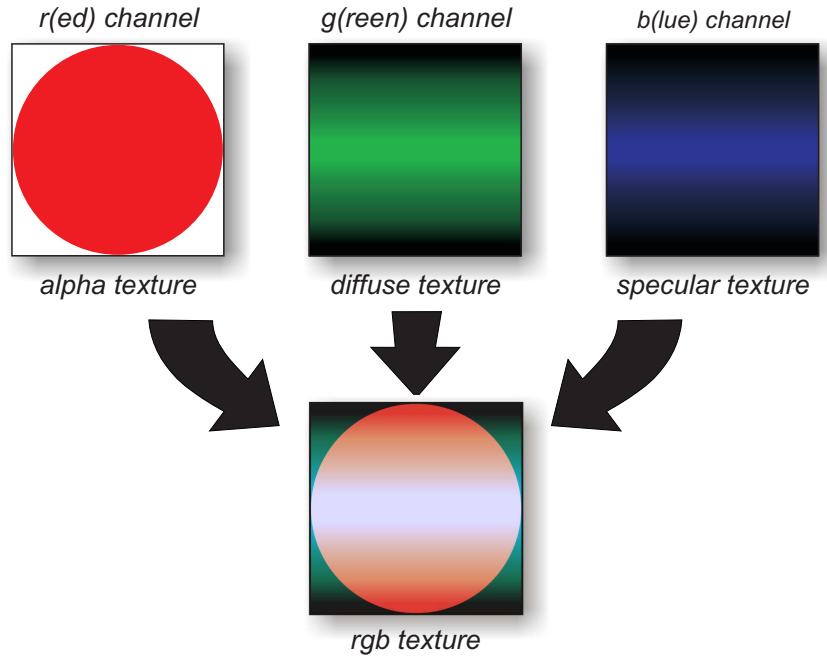


Figure 8.7: The channels of a RGB-texture are used to draw and illuminate a point sprite. The R-channel is used as alpha channel; the G- and B-channel are used to simulate diffuse and specular illumination.

In order to obtain a tube-like appearance, the point sprites have to be rotated according to the direction of the streamline segments. This is achieved by rotating the texture coordinates of the point sprite. The rotation of a point sprite positioned at location P_1 depends on the direction of the tangent at this streamline point. In order to obtain the factors needed for rotation, the tangent t at point P_1 has to be projected to the image plane resulting in t_p (compare Figure 8.8). This is achieved by first multiplying P_1 and $P_2 = P_1 + t$ with the model view projection matrix $\mathbf{M}_{4 \times 4}$:

$$P_{1p}.xyzw = \mathbf{M}_{4 \times 4} \cdot P_1.xyzw , \quad (8.9)$$

$$P_{2p}.xyzw = \mathbf{M}_{4 \times 4} \cdot P_2.xyzw . \quad (8.10)$$

The projection t_p of the tangent vector t into the image plane is then obtained by dehomogenization and conversion to screen coordinates:

$$\mathbf{t}_p \cdot xy = \begin{pmatrix} P_{2p}.x/P_{2p}.w - P_{1p}.x/P_{1p}.w \\ -P_{2p}.y/P_{2p}.w + P_{1p}.y/P_{1p}.w \end{pmatrix}. \quad (8.11)$$

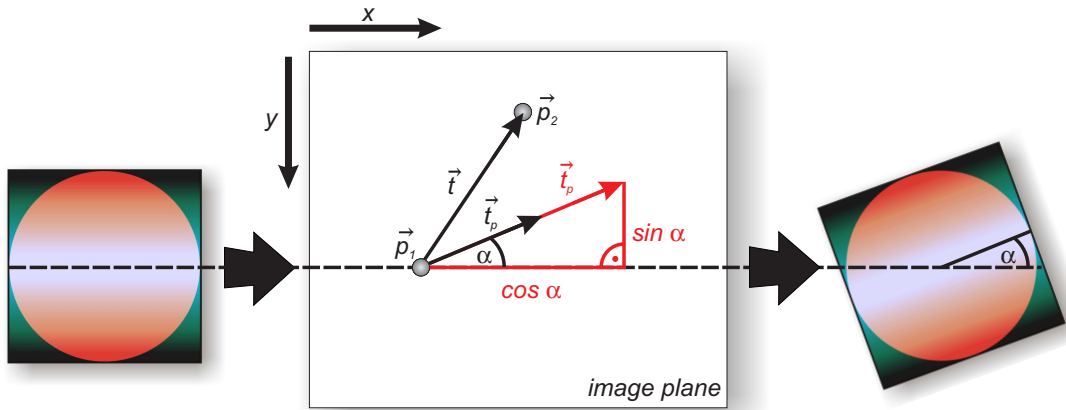


Figure 8.8: Rotation of the 2D texture coordinates depending on angle α . The factors for computing the rotation are obtained from the tangent vector \mathbf{t} which is projected into the image plane and normalized resulting in \mathbf{t}_p^0 .

Normalization of \mathbf{t}_p results in a vector $\mathbf{t}_p^0 = \begin{pmatrix} \cos \alpha \\ \sin \alpha \end{pmatrix}$ where the angle α denotes the rotation of the segment with respect to the x-axis (see Figure 8.9). The components of \mathbf{t}_p^0 which are computed by a vertex program are then used within a fragment program to compute the rotation of the texture coordinates. Since the texture coordinates $T.xy$ are defined within $[0;1]^2$ and the rotation is defined within $[-1;1]^2$, each texture coordinate is first translated by $(-0.5; -0.5)$. Once the rotation has been applied, they are shifted back to their original domain:

$$\begin{aligned} T_{new}.x &= \left(\mathbf{t}_p^0.y \cdot (T.y - 0.5) + \mathbf{t}_p^0.x \cdot (T.x - 0.5) \right) + 0.5, \\ T_{new}.y &= \left(\mathbf{t}_p^0.y \cdot (T.x - 0.5) - \mathbf{t}_p^0.x \cdot (T.y - 0.5) \right) + 0.5. \end{aligned}$$

The rotation is computed for each fragment resulting in correctly oriented point sprites. The approach provides a good visual representation for segments where the viewing direction is nearly parallel to the segment direction as illustrated in Figure 8.9.

Combined visualization using triangle strips and point sprites

As long as a streamline is oriented perpendicular to the viewing direction, the profile of the tube is rectangular (Figure 8.10, left), which is appropriately visualized using triangle strips. However, if the viewing direction is nearly parallel to the direction of a

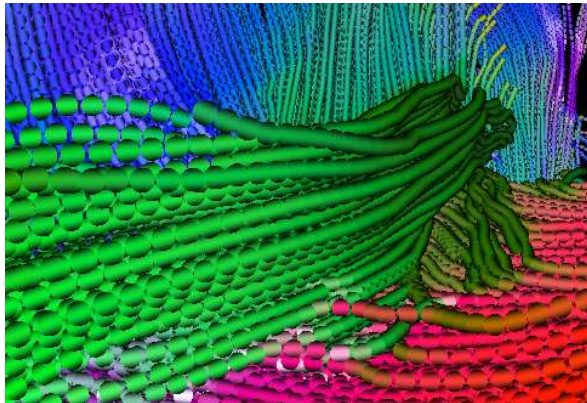


Figure 8.9: Visualization of fiber tracts using point sprites. Good visual results are obtained for segments nearly parallel to the viewing direction, the quality decreases for more perpendicular segments.

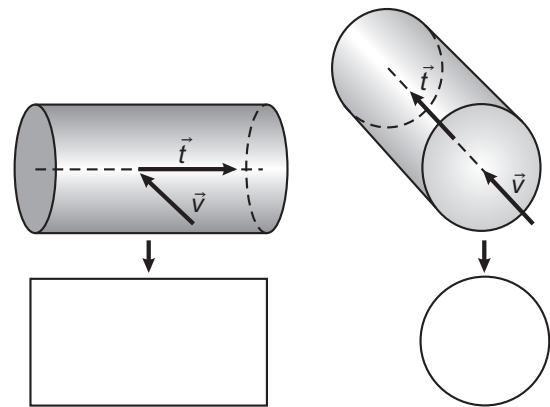


Figure 8.10: Profile of a tube depending on viewing direction: Rectangular when viewing direction v perpendicular to fiber tangent t (left), spherical in the case of viewing direction v parallel to tangent t (right).

segment, the profile of a tube is better represented using a circle (Figure 8.10, right) or a point sprite, respectively. For this reason, the presented hybrid approach combines the advantages of triangle strips and point sprites leading to a comprehensive and efficient visualization.

Within the hybrid approach, the size of the point sprite is computed to fit the width of the triangle strip. Accordingly, the point sprite is scaled to the required size within the vertex program using `glPointSize()`. Depending on the scalar product $\langle t, v \rangle$ between tangent vector t and viewing direction v , a decision is made as to whether the point sprite is displayed or not. More precisely, the point sprite is visualized if the scalar product is greater than 0.93, otherwise the homogeneous coordinate of the point is set to zero and the point is clipped within the rendering pipeline. In order to obtain an overlap region of point sprites and triangle strips, the latter are displayed if the scalar product is less than 0.98. Otherwise, drawing of triangle strips is suppressed by setting the A component of the RGBA color value to zero. The transparency value (A value) is checked for each fragment using `glAlphaFunc` preventing the visualization of flipping triangles. As a result, rendering based on triangle strips alone leads to flipping artifacts whereas the hybrid approach incorporating point sprites provides a tube-like visualization without artifacts (see Figure 8.11).

The presented technique provides a natural appearance which is very similar to tubes. However, at the beginning and the end of each fiber, the representation lacks realism since a tube-like ending is missing and the flat geometry of the triangle strip becomes apparent. In order to overcome this drawback, a terminating textured quad is used at both ends of each fiber (compare Figure 8.12).

8.3.3 Results

The algorithms developed in this work were implemented using OpenGL and GLSL. For benchmarking a PC equipped with an Intel Pentium 4, 3.0 GHz, 2 GB RAM and a NVidia Geforce 6800 Ultra graphics card with 256 MB graphics memory was used. The viewport for all renderings was 600×800 pixels and the displayed set of lines, generated by fiber tracking within the whole brain, consisted of approximately 300 000 segments originating from about 4 500 fibers.

Table 8.2 gives a detailed overview of the performance results of the presented methods. Lines and tubes are the geometrical approaches where a single tube segment consists of 16 triangles. They were compared to triangle strips, point sprites and the presented combination of these two techniques. All approaches were analyzed with respect to Vertex Buffer Objects (VBOs) provided by OpenGL for optimized geometry transfer. Illumination implemented in a fragment program was considered separately for each strategy. According to the performance measurements provided in Table 8.2, the presented hybrid approach achieves interactive frame rates regardless of the massive load of 300 000 segments encountered for a whole brain tracking.

Using geometrically modeled tubes, the geometry load was about 4.8 million triangles per frame which led to 4.2 million vertices in the case of triangle strip rendering. According to our observations, the sampling rate for tubes should not be less than 8 resulting in an octagon profile in order to obtain acceptable rendering quality. A further increase of the resolution leading to a higher number of triangles would significantly reduce the rendering performance since the vertex load becomes the limiting factor. Similarly, a higher number of fibers, which is encountered in the case of probabilistic tracking techniques or for dense fiber trackings, would decrease the rendering performance even more if geometry-based tube representations are used.

In comparison to geometric tubes, rendering times are about six (with illumination) to eight (no illumination) times faster using the suggested hybrid approach enabling

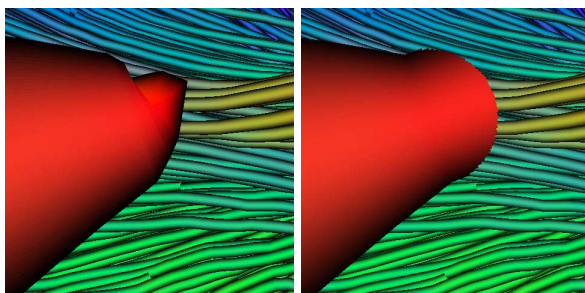


Figure 8.11: Flipping triangles for a segment in viewing direction (*left*). These artifacts are overcome with the hybrid approach incorporating point sprites (*right*).

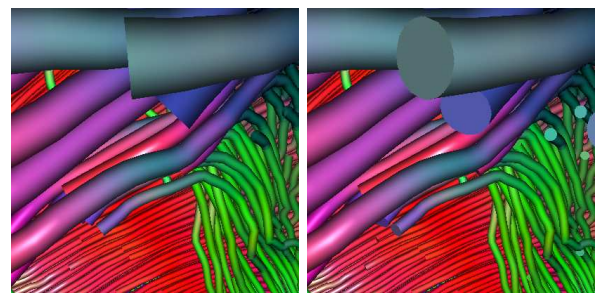


Figure 8.12: More realistic representation: Hybrid approach without (*left*) and with terminating textured quads at both ends of each fiber (*right*).

Visualization technique	Frame rate
Lines (no illumination)	242.5 fps
Lines (illuminated)	153.3 fps
Tubes (no illumination)	7.5 fps
Tubes (illuminated)	7.5 fps
Triangle strips (no illumination)	85.3 fps
Triangle strips (illuminated)	65.4 fps
Point sprites (no illumination, no rotation)	203.2 fps
Point sprites (illumination, rotation)	89.5 fps
Triangle strips & point sprites (no illumination)	57.5 fps
Triangle strips & point sprites (illumination)	42.5 fps

Table 8.2: Frame rates in fps (frames per second) depending on the visualization technique and illumination.

interactive visualization at high quality. The high number of triangles necessary in the case of conventional tube representations is reduced by a factor of eight, which leads to lower data requirements and consequently to improved performance. As a result, the purely GPU-based approach presented overcomes the limitations of standard geometry-based approaches and provides a further speed-up compared to a hybrid CPU-GPU-based approach [141].

Considering practical application, accelerated rendering of tube-like streamlines is an important prerequisite for a fusion with anatomical data based on direct volume rendering (DVR). Since DVR is very demanding in terms of rasterization power, it is essential to reduce the effort for additional rendering tasks (e.g. geometry) to a minimum. Due to the significantly reduced amount of data using the presented hybrid visualization technique, multimodal inspection of functional and anatomical information is possible in real-time. An important result is that functional data such as fiber tracts are explored within their anatomical context. Critical areas (e.g. a tumor in the immediate neighborhood of neuronal pathways) can be investigated in a convenient way, which improves diagnosis and therapy planning.

As can be seen in Figure 8.13, multimodal visualization combining function and surrounding anatomy were applied in a patient with a brain tumor. The overview figures show the global location of the tumor whereas the zoomed views provide details of white matter structures surrounding the tumor. Investigating such a multimodal representation, the surgeon is able to verify whether important tract systems are located in the vicinity of the tumor. Based on this information, an appropriate surgery plan can be developed. Since the neuronal structures have to remain intact to avoid postoperative neurological deficits, their real-time visualization together with anatomical data is an important aid to safer surgery. Overall, the presented technique provides visualization of high quality and at the same time enables better inspection due to high frame rates. It is a valuable supplement for medical application in neurosurgery.

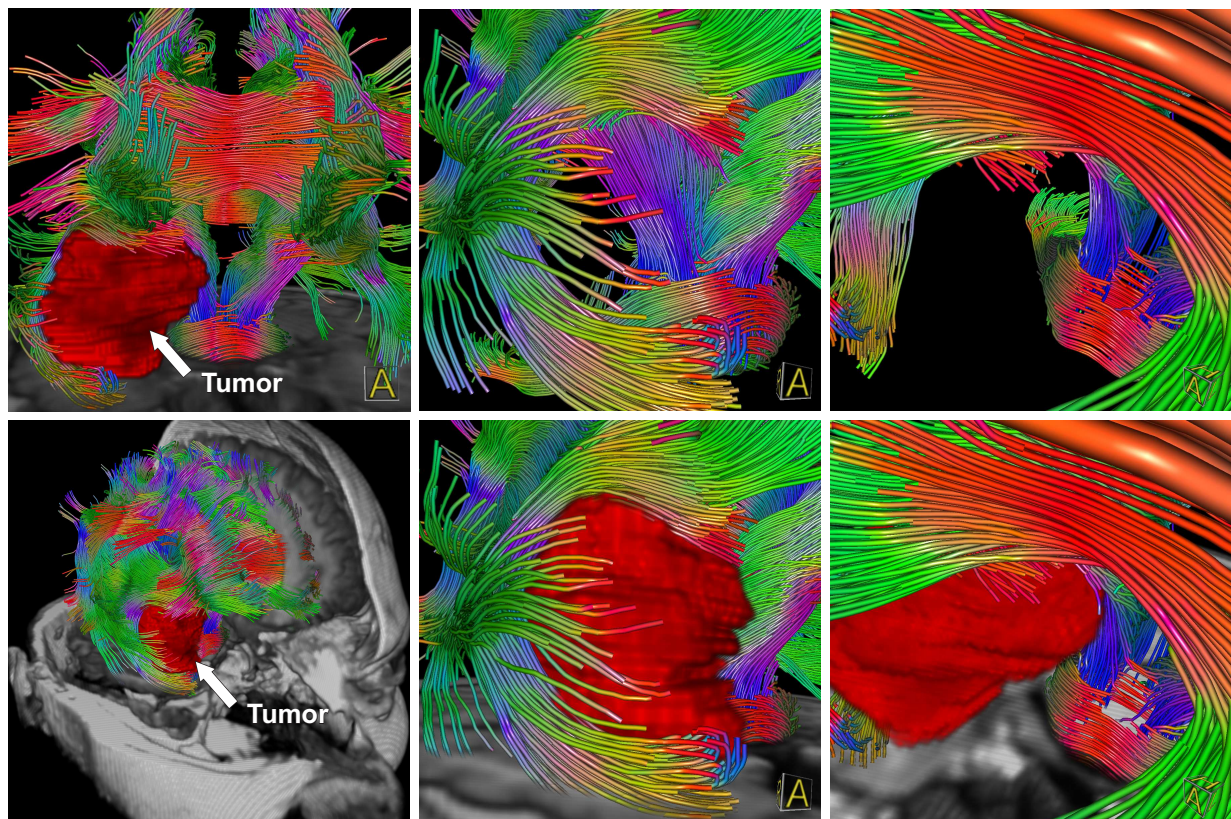


Figure 8.13: Fiber tracking in a patient with a brain tumor (*red*) rendered with the presented hybrid approach. Additionally, direct volume rendering of anatomical data provides background information about the location of the neuronal pathways with respect to the tumor and other anatomy. Close-up views of fibers surrounding the tumor (*middle, right*) and comparison of rendering with and without tumor (*compare upper and lower row*) provide important information for surgery planning.

8.4 Discussion

In this section, different approaches for the visualization of fibers for medical application have been presented. A major concern for the applied techniques are interactive frame rates, which is important for integration into a clinical workflow. The line rendering approach as well as the hybrid technique based on triangle strips and point sprites fulfill these criteria.

Additionally, different approaches for color encoding of the fiber bundles were presented in order to convey additional information such as local FA values. This approach makes it possible to identify major tract systems where higher FA values are present. In the case of fiber tracking, color encoding also helps to estimate the reliability of the tracking result. In regions of major white matter tracts where dense, coherent fibers are

located, the direction of the major eigenvector corresponds well with the fiber direction and results in a more reliable fiber-tracking result. Color encoding based on the FA value provides information about the local tensor shape and consequently about the reliability of the fiber-tracking result.

Another tool for visually emphasizing dominant tract systems is the presented approach for adaptive transparency. Depending on the local FA value, the opacity of the fibers is adjusted and dominant tract systems are no longer occluded by small fiber bundles. For this reason, the approach is an alternative to evenly spaced streamlines with adaptive spacing. However, adaptive transparency addresses occlusion of dominant tract systems during visualization, whereas the approach for evenly spaced streamlines with adaptive spacing considers this issue during streamline generation.

The illumination of streamlines is another important topic covered in this chapter. In general, illumination improves depth perception and is therefore a valuable tool in visualization applications. However, illumination also adulterates the original colors, which is an unwanted effect in conjunction with color encoding, where colors convey additional information. For this reason, illumination should be used carefully, especially when color encoding is applied.

Chapter 9

Visualization of hulls

The generation of hulls is an initial step towards boundary curves which are displayed in the focus plane of the OR microscope. Nevertheless, the visualization of hulls in 3D is also helpful for different purposes: First of all, 3D visualization of hulls is required in order to investigate the quality of the hull with respect to the reconstructed fiber bundles which approximate the underlying white matter structures. Additionally, hulls provide a more comprehensive representation of a fiber tract and the spatial relation between anatomical structures and tract system is more easily estimated. In the visualization of hulls, lighting as well as transparency play an important role, which is further outlined in Section 9.1 and 9.2.

9.1 Lighting

Lighting plays an important role in investigating the structure of the hull surfaces. For this reason, shading is essential for a meaningful visualization. In general, good shading results are already obtained with Gouraud shading, due to the fine tessellation of the

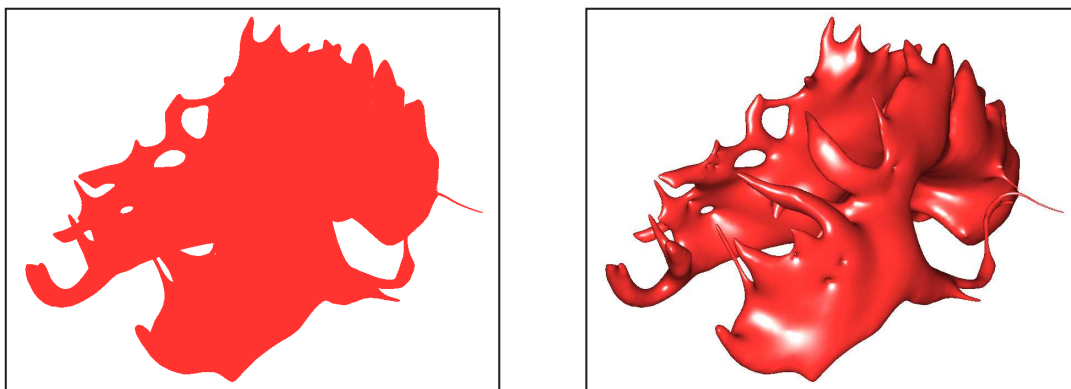


Figure 9.1: No illumination (*left*), per-pixel Phong illumination (*right*).

hulls. A better alternative is per-pixel shading, based on the Phong reflection model, which is accomplished with shader programs which are supported by current graphics hardware. Lighting results for per-pixel shading are shown in Figure 9.1.

9.2 Transparency

Transparency is applied for quality control and provides excellent support for comparing the generated surfaces with the underlying streamlines. Furthermore, the inner hull tightly wrapping the fiber tract and expanded hulls can be combined during visualization, as shown in Figure 9.2.

For semi-transparent rendering using OpenGL, blending is used in order to combine the color in the framebuffer with the color of an incoming primitive. In principle, correct rendering of opaque and semi-transparent objects requires two rendering passes. Opaque objects are rendered first, and then transparent objects are rendered from back to front in a second pass. Correct blending during rendering requires depth sorting of the transparent objects on the triangle level. However, sorting causes significant additional costs which prevents interactive frame rates. For this reason, rendering of semi-transparent hulls with different expansion levels enclosing the same tract is achieved by performing front-face culling in a first pass and back-face culling in a second pass. In the first pass, the surfaces are rendered in a descending order of expansion. Afterwards, ascending order and enabled back face culling are used. In this way, sorting artifacts are only seldom visible and have no significant visual impact on the visualization result. As a result, interactive visualization is possible, which is of great importance for medical application. In Figure 9.2, semi-transparent visualization is demonstrated for hulls wrapping the pyramidal tract.

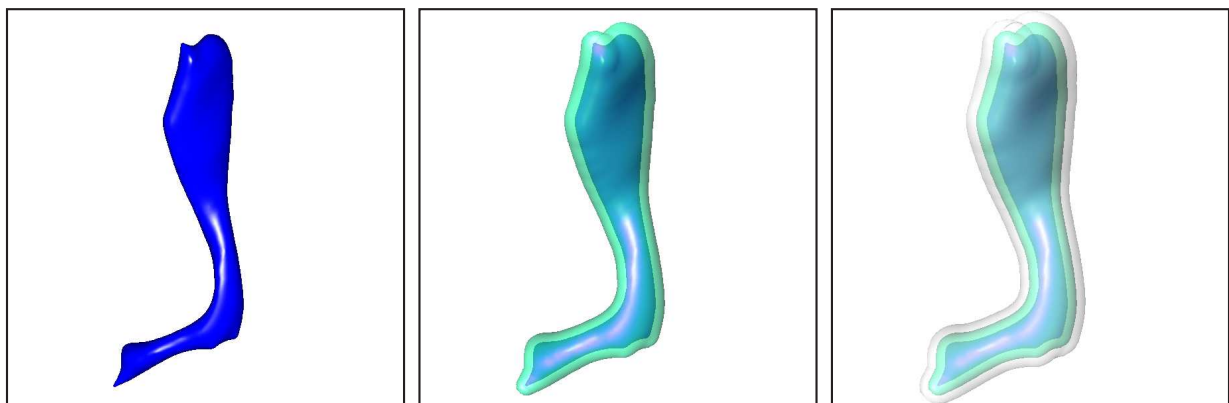


Figure 9.2: Opaque hull of the pyramidal tract (*left*) visualized in combination with a semi-transparent expanded hull with distance 4 mm (*middle*) and another semi-transparent hull with distance 8 mm (*right*) to the inner hull.

Chapter 10

Multimodal visualization of DTI- and MR-Data

Fiber tracts and hulls reconstructed from DTI data provide a comprehensive representation of white matter structures. However, for application in surgical planning, a combined visualization of fiber tracts and anatomy is necessary, which is outlined in more detail in this chapter. The concurrent display of anatomy and fibers enables the surgeon to assess the location of fibers in relation to anatomical landmarks. This is of major importance in patients with space-occupying lesions which may cause a displacement of fibers and other anatomical structures. To avoid postoperative neurological deficits a surgeon must be able to estimate the spatial relation between tumor and vital white matter structures. For this reason, an integrated visualization of fiber tracts and anatomical data is a valuable contribution to safer surgery.

The visualization techniques applied for this purpose are described in Section 10.1 and comprise direct volume rendering incorporating tagged volumes (Section 10.1.1) as well as volume clipping (Section 10.1.2). In Section 10.1.3, important aspects for the fusion of the fibers and anatomical data are considered. Performance results are presented in Section 10.2 and the benefit of the presented techniques for medical application is discussed in Section 10.3. The combination of the presented techniques and their benefit for visualization in neurosurgery were published in [83].

10.1 Multimodal visualization based on direct volume rendering

Direct volume rendering is applied in order to visualize anatomical MR data in combination with fibers or hulls. It is supported by the capabilities of current PC graphics hardware, which is capable of handling volume data as 3D textures for interactive visualization. For this reason, 3D volume rendering of clinical data is suited for preoperative planning and is therefore a valuable tool in brain tumor surgery.

10.1.1 Tagged volumes

However, the visualization of MR data based on direct volume rendering is difficult for different reasons: First of all, the dynamic range of the intensity values is low, making separation of different tissues difficult. Additionally, different anatomical structures such as skin and brain tissue are represented by the same intensity value which prevents the separation of different structures using intensity-based transfer functions. Therefore, tagged volumes are an alternative strategy for visualizing and investigating the spatial relation of fibers and anatomy or brain tumors. For this purpose, relevant structures such as the ventricles or a brain tumor were segmented in a preprocessing step. A second dataset containing tag IDs for each segmented structure is generated, which makes it possible to assign specific transfer functions to each sub-volume. Figure 10.1 shows a brain tumor and the ventricles rendered as tagged volumes.

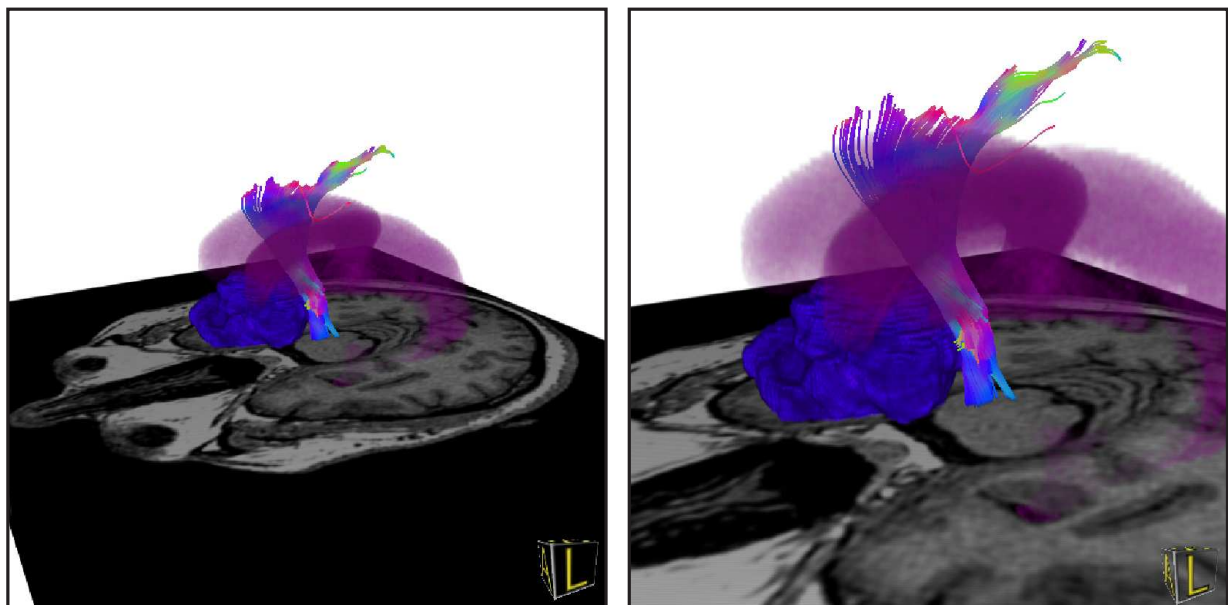


Figure 10.1: Tagged volume visualization makes it possible to apply separate transfer functions for a tumor (*blue*) and ventricles (*purple*). Additionally, an axial slice of the anatomical dataset is visualized as well as fibers of the pyramidal tract.

10.1.2 Volume clipping

In addition to tagged volumes, clipping is essential in order to suppress entire areas from rendering, giving direct visual access to hidden structures. Therefore, hardware accelerated clipping of arbitrary geometry as introduced by [149] was incorporated in order to mask uninteresting areas. In comparison to rendering a 2D slice as shown in Figure 10.1, volume clipping provides more flexible access to the underlying anatomical

structures, as shown in Figure 10.2. As a result, tagged volumes in combination with clipped volume rendering make it possible to investigate segmented structures and surrounding anatomy. In addition, this method may be combined with rendered fibers.

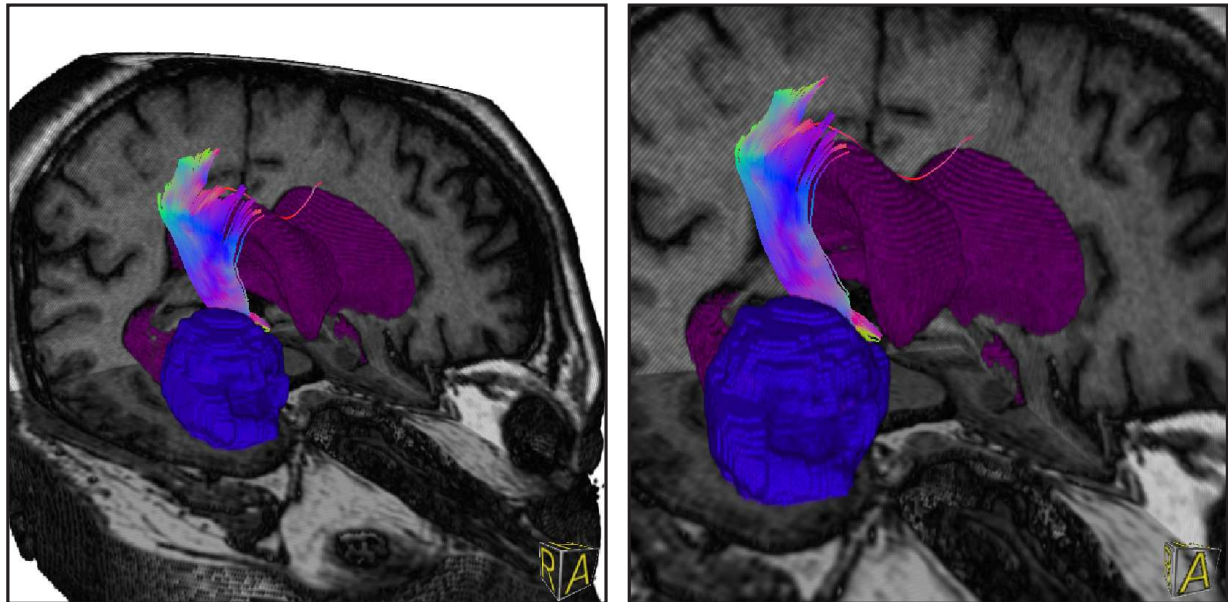


Figure 10.2: Volume rendering based on tagged data and volume clipping combined with fibers of the pyramidal tract. The resulting visualization supports orientation in 3D and shows the spatial relation between tumor and fibers as well as surrounding anatomy.

10.1.3 Fusion

Rendering of fibers and hulls in combination with the volume is accomplished in a step-by-step manner. After activating the depth buffer and rendering all opaque fibers and hulls, the anatomical dataset is rendered back-to-front. The depth-test ensures that parts of the volume which are concealed by fibers or hulls are suppressed.

Apart from the technical aspects of combined rendering, another important issue is the coherence of the base datasets. For a combined visualization of the reference DTI dataset with derived fibers, this coherence is granted per se. However, for true multimodal visualization where fibers from DTI data are rendered together with an anatomical MR scan, registration has to be applied prior to visualization to adjust the datasets. Rigid registration is thereby sufficient for many registration tasks dealing with undistorted image data. However, in the case of DTI data, non-linear registration has to be performed to account for image distortions, as outlined in Chapter 7. Non-linear registration thus ensures that fibers computed from the distorted DTI images are positioned properly within the undistorted dataset showing anatomy.

10.2 Results

The approaches presented in this chapter for an integrated visualization of diffusion tensor fiber tracts and anatomical data were adapted to the requirements for application in surgery. An important aim therefore was to enable interactive manipulation and comfortable handling of the tools. Due to extensive use of the programming capacities of current graphics hardware, volume rendering and application of transfer functions, tagged volumes and clipping run interactively. The frame rates for different setups comprising datasets of varying resolution and different tract systems are presented in Table 10.1.

For the measurements, fiber trackings of the pyramidal tract, the optic tract and the corpus callosum were generated and rendered with the hybrid approach based on triangle strips and point sprites presented in Section 8.3. For volume rendering, datasets of different resolution levels were employed, namely a DTI reference dataset ($128 \times 128 \times 60$ voxel), and MPRAGE anatomical datasets at different resolutions ($256 \times 256 \times 128$ and $512 \times 512 \times 128$ voxel). Based on this data, the frame rates for displaying different tract systems in combination with a DTI reference dataset and MPRAGE anatomical datasets were measured on a PC equipped with a P4 3.0 GHz, 2 GB RAM and a NVidia GeForce 6800 Ultra graphics card with 256 MB graphics memory. The viewport for all measurements was 600×800 pixels.

The presented results show that multimodal visualization of anatomical data and fibers is possible at interactive frame rates. For clinical application, this is of major importance due to limited time in clinical workflows, which greatly influences the acceptance of medical tools.

	Pyramidal tract <i>7 443 sampling points</i>	Optic tract <i>20 139 sampling points</i>	Corpus Callosum <i>70 352 sampling points</i>
DTI 128	36.5 fps	32.2 fps	29.3 fps
MPRAGE 256	19.2 fps	18.5 fps	17.9 fps
MPRAGE 512	9.8 fps	8.7 fps	7.5 fps

Table 10.1: Frame rates for multimodal visualization in fps (frames per second), for different setups including datasets of varying resolution and different tract systems.

10.3 Discussion

The presented approach for multimodal visualization of diffusion tensor fiber tracts in combination with anatomical data was adapted to application in surgery. Compared to the visualization of 2D slice images for planning in surgery, direct volume rendering permits a better understanding of 3D anatomy.

However, it is hardly possible to discover inner structures of the human brain using intensity-based transfer functions. This is due to the low dynamic range of the grey val-

ues of MR data and also to the fact that different anatomical structures are represented by identical grey values, such as different tissues. For this reason, volume clipping plays an important role in the investigation of inner structures. Interactive adjustment of the clip volume thereby provides fast and precise access to respective anatomical structures. As a result, combined rendering of clipped anatomical data and fibers makes it possible to investigate the course of fibers and nearby anatomy simultaneously.

Additionally, a 3D representation of certain structures is desirable in order to show clearly the location and volume of these structures. For this purpose, the desired areas are segmented by a clinical expert and are rendered as tagged volumes. For the visualization of brain tumors, this approach is superior to a transfer-function-based visualization, since brain tumors often have no clear border due to infiltration with other tissue. Consequently, in order to show clearly the volume of the lesion, tumor visualization based on segmentation and tagged volumes is more reliable. For this reason, rendering of tagged volumes is an important strategy for investigating the spatial relation of tumor, fibers and anatomy.

Overall, multimodal visualization based on direct volume rendering, including well-established techniques such as volume clipping and tagged volumes, provides a comprehensive representation of the complex 3D data and fiber anatomy. Additionally, interactive frame rates are achieved, which meets the requirements for clinical application.

Part IV

Conclusion

Chapter 11

Summary

In recent years, neurosurgical procedures have been revolutionized by the invention of navigation systems and preoperative planning software, which support the surgeon during the planning process as well as intraoperatively. The neuronavigation system tracks the operating microscope during the intervention and makes it possible to relate preoperative planning data spatially with the operating site. In this way, the results of comprehensive preoperative examinations, such as information about the location of functional areas, are directly available during surgery. This makes it possible to conduct the resection of diseased tissue more precisely and effectively and to reduce the risk of postoperative deficits for the patient.

Further important developments supporting surgical planning are novel MR imaging sequences, such as the DTI imaging technique developed about a decade ago. The possibility of assessing information about the location and course of white matter tracts *in vivo* thus available, provides a high degree of potential for neurosurgical planning and intervention. Another important imaging technique applied in neurosurgery is functional imaging based on fMRI, which was introduced about 15 years ago and which is used for localizing functional areas. The use of DTI and fMRI data for preoperative planning as well as intraoperatively in conjunction with the neuronavigation system, enables precise planning and execution of interventions. However, for this purpose, appropriate software tools are required for preparing and evaluating the data obtained, in order to make it usable for clinical application.

This thesis presents a series of different approaches for reconstructing and visualizing neuronal pathways from DTI data, which were developed in order to support neurosurgical interventions, including preoperative planning. In general, the working areas in this thesis can be divided into two major stages: The reconstruction of neuronal structures on the one hand, followed by the visualization of the reconstruction results on the other. This provides the basis for the respective parts of this thesis, which comprises the introduction and motivation (*Part I*), a section dealing with reconstruction approaches (*Part II*), and visualization techniques (*Part III*). In the following, the contents of these parts are summarized, hereby focusing on the main contributions.

The first part of this work provides fundamental knowledge about the medical background. Beginning with a short review of the history of neurosurgery, this part provides an introduction to disease patterns necessitating neurosurgical intervention, followed by information about neurosurgical interventions and neuroanatomy. Finally, the different MR acquisition techniques referred to in this thesis are described. The boundary conditions and fundamentals presented in this part of the thesis are an important prerequisite for understanding the medical requirements.

The second part of this thesis starts with a review of tensor reconstruction and quantification. Subsequently, a novel method for filtering the diffusion tensors is presented, which follows the design of video filters.

Based on the reconstructed and filtered tensor data, fiber-tracking algorithms are presented in the next chapter. For the reconstruction of single tract systems for clinical application, an approach based on regions of interest (ROIs) with associated Boolean operators was developed, which enables flexible and patient-specific extraction of separate tract systems. Furthermore, an approach for oriented filters was implemented and evaluated with respect to accuracy aspects. As a result, even though oriented filters are potentially able to achieve better processing of fiber crossings, they proved to be less appropriate for clinical application. This is due to the high computational cost encountered for only a slight gain in accuracy. In addition, a novel approach based on the concept of evenly spaced streamlines is presented, which is used for adaptive distance control between streamlines. From a clinical point of view this is of high value since the tract systems relevant for the surgeon are clearly visible and are not occluded by small peripheral fibers. Another approach developed for reconstructing neuronal pathways is directional volume growing. The approach can be regarded as a transition from fiber tracking to connectivity analysis, since both approaches consider several potential directions of expansion per voxel.

The subsequent chapter deals with connectivity analysis between speech areas. Since these fiber tracts are part of the more peripheral tract systems and are difficult to reconstruct using conventional approaches, an algorithm based on A*-pathfinding was developed. Based on a cost function, it is possible to analyze multiple possible directions per voxel, depending on the underlying tensor information. The advantage of the approach is an adequate representation of the information content provided by planar or spherical tensors, where multiple directions of equal probability exist. In clinical application, it was possible to provide a reliable reconstruction of speech pathways in tumor patients. Currently, the approach is undergoing thorough evaluation in a clinical study.

The subsequent chapter addresses the generation of hull surfaces wrapping fiber bundles. The reconstructed pathways serve as a basis for preoperative planning. However, for intraoperative visualization of boundary curves displayed in the focus plane of the OR microscope, the tracts must at first be converted to hulls. For this purpose, two alternative approaches are presented: On the one hand, a technique using tetrahedralization and 3D alpha shapes; on the other hand an approach based on rasterization and isosurfaces. For clinical application, the second approach is more appropriate, since it

makes it possible to control the tightness of the resulting hull. These approaches are of crucial importance in order to make the reconstruction results available for intraoperative application.

Another important topic which is addressed in a further chapter, is the correction of distortion artifacts. Due to susceptibility artifacts, the DTI data is distorted, resulting in a misplacement of the reconstructed structures. With the help of non-linear registration, the distortions were corrected and the influence of distortions on the position of tract systems was measured. For clinical application, this correction approach is of major importance in order to estimate the impact of distortions on the tract location and to correct the distortion artifacts.

A further important part of this work deals with appropriate visualization strategies in order to visualize the structures reconstructed in Part II. Essentially, this comprises the visualization of reconstructed tract systems, the display of hulls, and the multimodal visualization of anatomical MR data in conjunction with reconstructed structures.

An important issue for the visualization of pathways is coloring, which makes it possible to convey additional information content. For this reason, a set of different color transfer functions was developed. Furthermore, an efficient visualization of fiber-tracking results in real-time is essential in order to assure acceptance by the clinical user. A basic approach which meets this requirement is rendering of lines. In order to illuminate the lines, the approach for illuminated streamlines was implemented and further improved. In addition, it was possible to suppress small tract systems visually in regions of low FA by means of adaptive transparency. As a result, attention is drawn to the major tract systems, which are of superior relevance for surgery. As an alternative to line rendering, a hybrid approach based on triangle strips and point sprites was developed and presented, which provides a number of visual advantages compared to lines. The approaches provided for the visualization of fiber bundles enable flexible real-time visualization of neuronal pathways for clinical application.

A further chapter addresses the visualization of hulls for preoperative planning. Even though hulls are intended as an initial step towards a 2D representation of neuronal pathways for the OR microscope, their 3D visualization is at least necessary for quality control during hull generation. By means of semi-transparent visualization, it is possible to compare the hull with the underlying fiber tract and to assess its accuracy.

The subsequent chapter is about multimodal visualization of reconstructed structures as well as anatomical or functional data. For the visualization of anatomical MR data, direct volume rendering is used, whereby tumors are segmented in a pre-processing step and rendered as tagged volumes with individual transfer functions, in order to distinguish them from other types of tissue. For preoperative planning, multimodal visualization is of major interest in order to visualize neuronal structures and functional areas in their anatomical context.

Most of the DTI data processing and visualization approaches developed in this thesis have been tested in clinical applications and have been partly evaluated by clinical experts, providing encouraging results. Thus the investigations contribute to the research efforts in this field, and help to lower the risk of neurosurgical interventions for the patient.

Chapter 12

Outlook

In spite of the intense research processes in the field of DTI, various open questions and areas requiring further investigation remain. Two major spheres of activity can be distinguished: The field of imaging physics and sequence development on the one hand, and data processing and visualization strategies on the other. In the following, future challenges and possible fields of activity in both areas are summarized:

Origin of anisotropic diffusion in white matter: The varying diffusion properties of water in tissue, in particular diffusion anisotropy, is the basic effect measured with DTI. However, from the point of view of physics, the phenomenon of diffusion anisotropy in white matter has not yet been fully understood. According to experimental results reviewed in [112], myelination is not required for diffusion anisotropy, and cell membranes are relatively permeable to water. For this reason, research into the origin of these biophysical barriers is required in order to achieve a more precise interpretation of the measured diffusion patterns and, in turn, of the biological structures.

Accuracy and reliability of reconstruction approaches: A closely related issue refers to the accuracy of filtering and regularization techniques as well as to the reliability of tract-reconstruction algorithms. Without knowing how reconstructed tract systems map to neuronal structures, it is very difficult to assess their reliability. In the case of fiber-tracking algorithms, the question remains as to the extent to which real neuronal structures are represented by reconstructed fiber bundles. A first step in this direction is a paper published in [28], where reconstructed fiber tracts are compared to the pathways identified by a neuronal-tract tracer in histological sections. Due to the complexity of brain structure and due to biophysical limitations, it can be assumed that the reconstructed models are merely an approximation of the real neuronal structures. Nevertheless, for the application of reconstruction algorithms, it is important to know the limitations of the model compared to the real structures.

Improved resolution of DTI data: With respect to image acquisition in DTI, a higher resolution of the data is desirable in order to determine the local diffusion characteristics

more precisely. However, an increased spatial resolution is associated with an increase in noise, which reduces the reliability of the measurement. An alternative method to improve the signal-to-noise ratio (SNR) is provided by MR scanners with an increased field strength, such as the upcoming 3T scanners which are already installed at some institutes.

Undistorted DTI data: Another issue for future research relates to improved imaging sequences, which eliminate undesired effects such as the susceptibility artifacts outlined in Chapter 7. The STEAM MR imaging technique [111] is an example of an MR sequence which exhibits significantly fewer image distortions. For the application of imaging data in neurosurgery in conjunction with a neuronavigation system, distortion-free sequences are of great interest since, in this case, complex correction procedures can be circumvented.

More precise assessment of local diffusion characteristics: In current research, an imaging technique denoted as high angular resolution diffusion imaging (HARDI) [145] was presented, which aims at overcoming certain limitations of DTI. The main idea behind this imaging sequence is to apply diffusion-weighting gradients in many directions, distributed almost isotropically on the surface of a unit sphere. According to [41], the measured distribution of diffusivities is used to reconstruct a higher-order tensor which provides a better representation of the local diffusion characteristics. Even though some techniques known from DTI reconstruction and processing can easily be adapted to suit higher-order tensors, e.g. fiber tracking [49] or the approach for connectivity analysis presented in Chapter 5, special requirements have to be considered. For example, new scalar metrics characterizing areas of anisotropic diffusion are required, as well as adequate tract-reconstruction algorithms which exploit the more precise information content provided by HARDI tensors. The possibility of obtaining more comprehensive information about the local diffusion properties paves the way for more precise reconstruction techniques, which is an interesting topic for future research.

Clinical evaluation of the approaches: Another important issue is the clinical evaluation of the implemented algorithms. One neurosurgeon and two medical students currently work with the DTI software developed in this thesis. Of special interest are the algorithms for fiber tracking and for connectivity analysis as well as the hull-generation approaches, which are currently being evaluated in retrospective studies. For the future, additional evaluation studies are planned in order to further verify the accuracy and reliability of the developed algorithms in clinical application.

Bibliography

- [1] AKERS, D., SHERBONDY, A., MACKENZIE, R., DOUGHERTY, R., AND WANDELL, B. Exploration of the brain's white matter pathways with dynamic queries. In *Proc. IEEE Visualization (VIS)* (2004), pp. 377–384.
- [2] BADE, R., HAASE, J., AND PREIM, B. Comparison of fundamental mesh smoothing algorithms for medical surface models. In *Proc. Simulation and Visualization (SimVis)* (2006), T. Schulze, G. Horton, B. Preim, and S. Schlechtweg, Eds., SCS Publishing House e.V., pp. 289–304.
- [3] BANKS, D. Illumination in diverse codimensions. In *Proc. Computer Graphics and Interactive Techniques (SIGGRAPH)* (1994), pp. 327–334.
- [4] BASSER, P., MATTIELLO, J., AND LE BIHAN, D. Estimation of the effective self-diffusion tensor from the NMR spin echo. *Journal of Magnetic Resonance, Series B*, 103, 3 (1994), 247–254.
- [5] BASSER, P., MATTIELLO, J., AND LE BIHAN, D. MR diffusion tensor spectroscopy and imaging. *Biophysical Journal* 66, 1 (1994), 259–267.
- [6] BASSER, P., PAJEVIC, S., PIERPAOLI, C., DUDA, J., AND ALDROUBI, A. In vivo fiber tractography using DT-MRI data. *Magnetic Resonance in Medicine* 44, 4 (2000), 625–632.
- [7] BASSER, P., AND PIERPAOLI, C. Microstructural and physiological features of tissues elucidated by quantitative diffusion tensor MRI. *Journal of Magnetic Resonance, Series B*, 111, 3 (1996), 209–219.
- [8] BEHRENS, T., JOHANSEN-BERG, H., WOOLRICH, M., SMITH, S., WHEELER-KINGSHOTT, C., BOULBY, P., BARKER, G., SILLERY, E., SHEEHAN, K., CICCARELLI, O., THOMPSON, A., BRADY, J., AND MATTHEWS, P. Non-invasive mapping of connections between human thalamus and cortex using diffusion imaging. *Nature Neuroscience* 6, 7 (2003), 750–757.
- [9] BERMAN, J., BERGER, M., MUKHERJEE, P., AND HENRY, R. Diffusion-tensor imaging-guided tracking of fibers of the pyramidal tract combined with intraoperative cortical stimulation mapping in patients with gliomas. *Neurosurgery* 101, 1 (2004), 66–72.

- [10] BHAGAT, Y., EMERY, D., SHUAIB, A., SHER, F., RIZVI, N., AKHTAR, N., CLARE, T., LEATHERDALE, T., AND BEAULIEU, C. The relationship between diffusion anisotropy and time of onset after stroke. *Journal of Cerebral Blood Flow and Metabolism* 26, 11 (2006), 1442–1450.
- [11] BJÖRNEMO, M., BRUN, A., KIKINIS, R., AND WESTIN, C.-F. Regularized stochastic white matter tractography using diffusion tensor MRI. In *Proc. Medical Image Computing and Computer Assisted Intervention (MICCAI)* (2002), pp. 435–442.
- [12] BLAAS, J., BOTHA, C., VOS, F., AND POST, F. Fast and reproducible fibre bundle selection in DTI visualization. In *Proc. IEEE Visualization (VIS)* (2005), pp. 59–64.
- [13] BLOCH, F. Nuclear induction. *Physical Review* 70 (1946), 460–474.
- [14] BODAMMER, N., KAUFMANN, J., KANOWSKI, M., AND TEMPELMANN, C. Eddy current correction in diffusion-weighted imaging using pairs of images acquired with opposite diffusion gradient polarity. *Magnetic Resonance in Medicine* 51, 1 (2004), 188–193.
- [15] BOZZALI, M., FALINI, A., FRANCESCHI, M., CERCIGNANI, M., ZUFFI, M., SCOTTI, G., COMI, G., AND FILIPPI, M. White matter damage in Alzheimer’s disease assessed in vivo using diffusion tensor magnetic resonance imaging. *Journal of Neurology, Neurosurgery and Psychiatry* 72, 6 (2002), 742–746.
- [16] BRESENHAM, J. Algorithm for computer control of a digital plotter. *IBM System Journal* 4, 1 (1965), 25–30.
- [17] BRUN, A., KNUTSSON, H., PARK, H., SHENTON, M., AND WESTIN, C.-F. Clustering fiber tracts using normalized cuts. In *Proc. Medical Image Computing and Computer Assisted Intervention (MICCAI)* (2004), pp. 368–375.
- [18] BUTCHER, J. *The numerical analysis of ordinary differential equations: Runge-Kutta and general linear methods*. John Wiley and Sons Inc., 1987.
- [19] CARANO, R., LI, F., IRIE, K., HELMER, K., SILVA, M., FISHER, M., AND SOTAK, C. Multispectral analysis of the temporal evolution of cerebral ischemia in the rat brain. *Journal of Magnetic Resonance Imaging* 12, 6 (2000), 842–858.
- [20] CASTANO-MORAGA, C., RODRIGUES-FLORIDO, M., ALVAREZ, L., WESTIN, C.-F., AND RUIZ-ALZOLA, J. Anisotropic interpolation of DT-MRI data. In *Proc. Medical Image Computing and Computer Assisted Intervention (MICCAI)* (2004), pp. 343–350.
- [21] CLARK, C., BARRICK, T., MURPHY, M., AND BELL, B. White matter fiber tracking in patients with space-occupying lesions of the brain: A new technique for neurosurgical planning? *NeuroImage* 20, 3 (2003), 1601–1608.

- [22] COENEN, V., KRINGS, T., MAYFRANK, L., POLIN, R., REINGES, M., THRON, A., AND GILSBACH, J. Three-dimensional visualization of the pyramidal tract in a neuronavigation system during brain tumor surgery: First experiences and technical note. *Neurosurgery* 49, 1 (2001), 86–92.
- [23] COLLIGNON, A., MAES, F., DELAERE, D., VANDERMEULEN, D., SUETENS, P., AND MARCHAL, G. Automated multimodality image registration using information theory. In *Proc. Information Processing in Medical Imaging (IPMI)* (1995), pp. 263–274.
- [24] CONTURO, T., LORI, N., CULL, T., AKBUDAK, E., SNYDER, A., SHIMONY, J., MCKINSTRY, R., BURTON, H., AND RAICHLE, M. Tracking neuronal fiber pathways in the living human brain. *Proceedings of the National Academy of Sciences of the United States of America* 96, 18 (1999), 10422–10427.
- [25] COREMANS, J., LUYPAERT, R., VERHELLE, F., STADNIK, T., AND OSTEAX, M. A method for myelin fiber orientation mapping using diffusion-weighted MR images. *Magnetic Resonance Imaging* 12, 3 (1994), 443–454.
- [26] COROUGE, I., FLETCHER, T., JOSHI, S., GILMORE, J., AND GERIG, G. Fiber tract-oriented statistics for quantitative diffusion tensor MRI analysis. In *Proc. Medical Image Computing and Computer Assisted Intervention (MICCAI)* (2005), pp. 131–139.
- [27] COULON, O., ALEXANDER, D., AND ARRIDGE, S. Diffusion tensor magnetic resonance image regularization. *Medical Image Analysis* 8, 1 (2004), 47–67.
- [28] DAUGUET, J., PELED, S., BEREZOVSKII, V., DELZESCAUX, T., WARFIELD, S., BORN, R., AND WESTIN, C.-F. 3D histological reconstruction of fiber tracts and direct comparison with diffusion tensor MRI tractography. In *Proc. Medical Image Computing and Computer Assisted Intervention (MICCAI)* (2006), pp. 109–116.
- [29] DECHTER, R., AND PEARL, J. Generalized best-first search strategies and the optimality of A*. *Journal of the ACM* 32, 3 (1985), 505–536.
- [30] DELAUNAY, B. Sur la sphère vide. *Bulletin of Academy of Sciences of the USSR (VII)* (1934), 793–800.
- [31] DELMARCELLE, T., AND HESSELINK, L. Visualizing second-order tensor fields with hyperstreamlines. *IEEE Computer Graphics and Applications* 13, 4 (1993), 25–33.
- [32] DESBRUN, M., MEYER, M., SCHRÖDER, P., AND BARR, A. Implicit fairing of irregular meshes using diffusion and curvature flow. In *Proc. Computer Graphics and Interactive Techniques (SIGGRAPH)* (1999), pp. 317–324.
- [33] EDELSBRUNNER, H., AND MÜCKE, E. Three-dimensional alpha shapes. *ACM Transactions on Graphics* 13, 1 (1994), 43–72.

- [34] ENDERS, F., ISERHARDT-BAUER, S., HASTREITER, P., NIMSKY, C., AND ERTL, T. Hardware-accelerated glyph based visualization of major white matter tracts for analysis of brain tumors. In *Proc. SPIE Medical Imaging (2005)*, R. Galloway and K. Cleary, Eds., SPIE – The International Society for Optical Engineering, pp. 504–511.
- [35] ENDERS, F., MERHOF, D., HASTREITER, P., STAMMINGER, M., FAHLBUSCH, R., AND NIMSKY, C. DTI-based visualization strategies for the pyramidal tract. *GMS CURAC 1 (2006)*, Doc07, 1–11.
- [36] ENDERS, F., MERHOF, D., HASTREITER, P., STAMMINGER, M., AND NIMSKY, C. Enhanced visualization of diffusion tensor data for neurosurgery. In *Proc. Bildverarbeitung für die Medizin (BVM) (2005)*, H.-P. Meinzer, H. Handels, A. Horsch, and T. Tolxdorff, Eds., Springer, pp. 272–276.
- [37] ENDERS, F., SAUBER, N., MERHOF, D., HASTREITER, P., NIMSKY, C., AND STAMMINGER, M. Visualization of white matter tracts with wrapped streamlines. In *Proc. IEEE Visualization (VIS) (2005)*, pp. 51–58.
- [38] ESSEN, D. A tension-based theory of morphogenesis and compact wiring in the central nervous system. *Nature 385*, 6614 (1997), 313–318.
- [39] FLETCHER, T., AND JOSHI, S. Riemannian geometry for the statistical analysis of diffusion tensor data. *Signal Processing 87*, 2 (2007), 165–1684.
- [40] FOUT, N., HUANG, J., AND DING, Z. Visualization of neuronal fiber connections from DT-MRI with global optimization. In *Proc. ACM Symposium on Applied Computing (SAC) (2005)*, pp. 1200–1206.
- [41] FRANK, L. Characterization of anisotropy in high angular resolution diffusion-weighted MRI. *Magnetic Resonance in Medicine 47*, 6 (2002), 1083–1099.
- [42] FRIEBE, M., AND KAUP, A. Low complexity two classes Gauss weighting filter for noise reduction in mobile received analog TV signals. In *Proc. European Signal Processing Conference (EUSIPCO) (2005)*, pp. 1–4.
- [43] GANSLANDT, O., BUCHFELDER, M., HASTREITER, P., GRUMMICH, P., FAHLBUSCH, R., AND NIMSKY, C. Magnetic source imaging supports clinical decision making in glioma patients. *Clinical Neurology and Neurosurgery 107*, 1 (2004), 20–26.
- [44] GUIMOND, A., GUTTMANN, C., WARFIELD, S., AND WESTIN, C.-F. Deformable registration of DT-MRI data based on transformation invariant tensor characteristics. In *Proc. IEEE International Symposium on Biomedical Imaging (ISBI) (2002)*.

- [45] HART, P., NILSSON, N., AND RAPHAEL, B. A formal basis for the heuristic determination of minimum cost paths. *IEEE Transactions on Systems Science and Cybernetics* 4, 2 (1968), 100–107.
- [46] HASTREITER, P., AND ERTL, T. Integrated registration and visualization of medical image data. In *Proc. Computer Graphics International (CGI)* (1998), pp. 78–85.
- [47] HASTREITER, P., REZK-SALAMA, C., SOZA, G., BAUER, M., GREINER, G., FAHLBUSCH, R., GANSLANDT, O., AND NIMSKY, C. Strategies for brain shift evaluation. *Medical Image Analysis* 8, 4 (2004), 447–464.
- [48] HELLIER, P., AND BARILLOT, C. Multimodal non-rigid warping for correction of distortions in functional MRI. In *Proc. Medical Image Computing and Computer Assisted Intervention (MICCAI)* (2000), pp. 512–520.
- [49] HLAWITSCHKA, M., AND SCHEUERMANN, G. Hot-lines: Tracking lines in higher order tensor fields. In *Proc. IEEE Visualization (VIS)* (2005), pp. 27–34.
- [50] JACKOWSKI, M., KAO, C., QIU, M., CONSTABLE, R., AND STAIB, L. Estimation of anatomical connectivity by anisotropic front propagation and diffusion tensor imaging. In *Proc. Medical Image Computing and Computer Assisted Intervention (MICCAI)* (2004), pp. 663–670.
- [51] JACKOWSKI, M., KAO, C., QIU, M., CONSTABLE, R., AND STAIB, L. White matter tractography by anisotropic wavefront evolution and diffusion tensor imaging. *Medical Image Analysis* 9, 5 (2005), 427–440.
- [52] JEZZARD, P., AND CLARE, S. Sources of distortion in functional MRI data. *Human Brain Mapping* 8, 2-3 (1999), 80–85.
- [53] JOBARD, B., AND LEFER, W. Creating evenly-spaced streamlines of arbitrary density. In *Proc. Eurographics Workshop on Visualization in Scientific Computing (EUROGRAPHICS)* (1997), pp. 43–56.
- [54] JONES, D., SYMMS, M., CERCIGNANI, M., AND HOWARD, R. The effect of filter size on VBM analyses of DT-MRI data. *NeuroImage* 26, 2 (2005), 546–554.
- [55] JONES, D., WILLIAMS, S., AND HORSFIELD, M. Full representation of white-matter fibre direction in one map via diffusion tensor analysis. In *Proc. International Society for Magnetic Resonance in Medicine (ISMRM)* (1997), p. 1743.
- [56] KAMADA, K., TODO, T., MASUTANI, Y., AOKI, S., INO, K., TAKANO, T., KIRINO, T., KAWAHARA, N., AND MORITA, A. Combined use of tractography-integrated functional neuronavigation and direct fiber stimulation. *Journal of Neurosurgery* 102, 4 (2005), 664–672.

- [57] KAUFMAN, A., AND SHIMONY, E. 3D scan-conversion algorithms for voxel-based graphics. In *Proc. ACM Workshop on Interactive 3D Graphics* (1986), pp. 45–76.
- [58] KELES, G., LUNDIN, D., LAMBORN, K., CHANG, E., OJEMANN, G., AND BERGER, M. Intraoperative subcortical stimulation mapping for hemispherical perirolandic gliomas located within or adjacent to the descending motor pathways: Evaluation of morbidity and assessment of functional outcome in 294 patients. *Journal of Neurosurgery* 100, 3 (2004), 369–375.
- [59] KIM, B., AND ROSSIGNAC, J. GeoFilter: Geometric selection of mesh filter parameters. *Computer Graphics Forum* 24, 3 (2005), 295–302.
- [60] KINDLMANN, G. Superquadric tensor glyphs. In *Proc. Joint Eurographics - IEEE TVCG Symposium on Visualization (VisSym)* (2004), pp. 147–154.
- [61] KINDLMANN, G., AND WEINSTEIN, D. Hue-balls and lit-tensors for direct volume rendering of diffusion tensor fields. In *Proc. IEEE Visualization (VIS)* (1999), pp. 183–189.
- [62] KINDLMANN, G., WEINSTEIN, D., AND HART, D. Strategies for direct volume rendering of diffusion tensor fields. *IEEE Transactions on Visualization and Computer Graphics* 6, 2 (2000), 124–138.
- [63] KINOSHITA, M., YAMADA, K., HASHIMOTO, N., KATO, A., IZUMOTO, S., BABA, T., MARUNO, M., NISHIMURA, T., AND YOSHIMINE, T. Fiber-tracking does not accurately estimate size of fiber bundle in pathological condition: Initial neurosurgical experience using neuronavigation and subcortical white matter stimulation. *NeuroImage* 25, 2 (2005), 424–429.
- [64] KOBELT, L., CAMPAGNA, S., VORSATZ, J., AND SEIDEL, H.-P. Interactive multi-resolution modeling on arbitrary meshes. In *Proc. Computer Graphics and Interactive Techniques (SIGGRAPH)* (1998), pp. 105–114.
- [65] KOBER, H., MÖLLER, M., NIMSKY, C., VIETH, J., FAHLBUSCH, R., AND GANSLANDT, O. New approach to localize speech relevant brain areas and hemispheric dominance using spatially filtered magnetoencephalography. *Human Brain Mapping* 14, 4 (2001), 236–250.
- [66] KOBER, H., NIMSKY, C., MÖLLER, M., HASTREITER, P., FAHLBUSCH, R., AND GANSLANDT, O. Correlation of sensorimotor activation with functional magnetic resonance imaging and magnetoencephalography in presurgical functional imaging: A spatial analysis. *NeuroImage* 14, 5 (2001), 1214–1228.
- [67] KYBIC, J., THÉVENAZ, P., NIRKKO, A., AND UNSER, M. Unwarping of unidirectionally distorted EPI images. *IEEE Transactions on Medical Imaging* 19, 2 (2000), 80–93.

- [68] LATOMBE, J.-C. *Robot Motion Planning*. Kluwer Academic Publishers, 1991.
- [69] LAZAR, M., AND ALEXANDER, A. Divergence/convergence effects on the accuracy of white matter tractography algorithms. In *Proc. International Society for Magnetic Resonance in Medicine (ISMRM)* (2003), p. 2160.
- [70] LAZAR, M., AND ALEXANDER, A. An error analysis of white matter tractography methods: Synthetic diffusion tensor field simulations. *NeuroImage* 20, 2 (2003), 1140–1153.
- [71] LAZAR, M., WEINSTEIN, D., TSURUDA, J., HASAN, K., ARFANAKIS, K., MEYER, E., BADIE, B., ROWLEY, H., HAUGHTON, V., FIELD, A., AND ALEXANDER, A. White matter tractography using diffusion tensor deflection. *Human Brain Mapping* 18, 4 (2003), 306–321.
- [72] LE BIHAN, D., BRETON, E., LALLEMAND, D., GRENIER, P., CABANIS, E., AND LAVAL-JEANTET, M. MR imaging of intravoxel incoherent motions: Application to diffusion and perfusion in neurologic disorders. *Radiology* 161, 2 (1986), 401–407.
- [73] LORENSEN, W., AND CLINE, H. Marching cubes: A high resolution 3D surface reconstruction algorithm. In *Proc. Computer Graphics and Interactive Techniques (SIGGRAPH)* (1987), pp. 163–169.
- [74] M. MARTIN-FERNANDEZ, C.-F. WESTIN, C. A.-L. 3D Bayesian regularization of diffusion tensor MRI using multivariate Gaussian Markov random fields. In *Proc. Medical Image Computing and Computer Assisted Intervention (MICCAI)* (2004), pp. 351–359.
- [75] MALLO, O., PEIKERT, R., SIGG, C., AND SADLO, F. Illuminated lines revisited. In *Proc. IEEE Visualization (VIS)* (2005), pp. 19–25.
- [76] MANGIN, J., POUPON, C., CLARK, C., LE BIHAN, D., AND BLOCH, I. Distortion correction and robust tensor estimation for MR diffusion imaging. *Medical Image Analysis* 6, 3 (2003), 191–198.
- [77] MARTIN-FERNANDEZ, M., ALBEROLA-LOPEZ, C., RUIZ-ALZOLA, J., AND WESTIN, C.-F. Regularization of diffusion tensor maps using a non-Gaussian Markov random field approach. In *Proc. Medical Image Computing and Computer Assisted Intervention (MICCAI)* (2003), pp. 92–100.
- [78] MARYAK, J., AND CHIN, D. Global random optimization by simultaneous perturbation stochastic approximation. In *Proc. of the American Control Conference Arlington* (2001), pp. 756–762.

- [79] MERHOF, D., ENDERS, F., HASTREITER, P., GANSLANDT, O., FAHLBUSCH, R., NIMSKY, C., AND STAMMINGER, M. Neuronal fiber connections based on A*-pathfinding. In *SPIE Medical Imaging (2006)*, A. Manduca and A. Amini, Eds., SPIE – The International Society for Optical Engineering, pp. 6143, 1S, 1–8.
- [80] MERHOF, D., ENDERS, F., HASTREITER, P., STAMMINGER, M., FAHLBUSCH, R., AND NIMSKY, C. Reconstruction of neural pathways based on diffusion tensor imaging. In *Proc. Deutsche Gesellschaft für Computer- und Roboterassistierte Chirurgie (CURAC) (2004)*, pp. C1–12.
- [81] MERHOF, D., ENDERS, F., STAMMINGER, M., NIMSKY, C., AND HASTREITER, P. Rekonstruktion und Visualisierung Neuronaler Bahnen. *Medizintechnik in Bayern - Profile, Porträts, Perspektiven 1 (2006)*, 40–42.
- [82] MERHOF, D., ENDERS, F., STAMMINGER, M., NIMSKY, C., AND HASTREITER, P. Reconstruction and visualization of neuronal pathways. *Medical Technology in Bavaria - Profiles, Portraits, Perspectives 1 (2007)*, 40–42.
- [83] MERHOF, D., ENDERS, F., VEGA, F., HASTREITER, P., NIMSKY, C., AND STAMMINGER, M. Integrated visualization of diffusion tensor fiber tracts and anatomical data. In *Proc. Simulation and Visualization (SimVis) (2005)*, T. Schulze, G. Horton, B. Preim, and S. Schlechtweg, Eds., SCS Publishing House e.V., pp. 153–164.
- [84] MERHOF, D., GROSSO, R., AND TREMEL, U. Anisotropic quadrilateral meshing: An indirect approach. In *Proc. Engineering Computational Structures (ECT) (2004)*, B. Topping and C. M. Soares, Eds., Civil-Comp Press, pp. 47,1–12.
- [85] MERHOF, D., GROSSO, R., TREMEL, U., AND GREINER, G. Local surface approximation and its application to smoothing in three-dimensional indirect mesh generation. Tech. Rep. TR2/2004, Computer Graphics Group, University of Erlangen-Nuremberg, 2004.
- [86] MERHOF, D., GROSSO, R., TREMEL, U., AND GREINER, G. Anisotropic quadrilateral mesh generation: An indirect approach. *Advances in Engineering Software* 38, 11-12 (2007), 860–867.
- [87] MERHOF, D., HASTREITER, P., NIMSKY, C., FAHLBUSCH, R., AND GREINER, G. Directional volume growing for the extraction of white matter tracts from diffusion tensor data. In *Proc. SPIE Medical Imaging (2005)*, R. Galloway and K. Cleary, Eds., SPIE – The International Society for Optical Engineering, pp. 165–172.
- [88] MERHOF, D., HASTREITER, P., SOZA, G., STAMMINGER, M., AND NIMSKY, C. Non-linear integration of DTI-based fiber tracts into standard 3D MR data. In *Proc. Vision, Modeling and Visualization (VMV) (2004)*, B. Girod, M. Magnor, and H.-P. Seidel, Eds., Akademische Verlagsgesellschaft Aka GmbH, pp. 371–377.

- [89] MERHOF, D., MEISTER, M., BINGÖL, E., HASTREITER, P., NIMSKY, C., AND GREINER, G. Generation of hulls encompassing neuronal pathways based on tetrahedralization and 3D alpha shapes. In *Proc. Bildverarbeitung für die Medizin (BVM)* (2007), A. Horsch, T. Deserno, H. Handels, H.-P. Meinzer, and T. Tolxdorff, Eds., Springer, pp. 308–312.
- [90] MERHOF, D., RICHTER, M., ENDERS, F., HASTREITER, P., GANSLANDT, O., BUCHFELDER, M., NIMSKY, C., AND GREINER, G. Fast and accurate connectivity analysis between functional regions based on DT-MRI. In *Proc. Medical Image Computing and Computer Assisted Intervention (MICCAI)* (2006), pp. 225–233 (Part II).
- [91] MERHOF, D., SONNTAG, M., ENDERS, F., HASTREITER, P., FAHLBUSCH, R., NIMSKY, C., AND GREINER, G. Visualization of diffusion tensor data using evenly spaced streamlines. In *Proc. Vision, Modeling and Visualization (VMV)* (2005), G. Greiner, J. Hornegger, H. Niemann, and M. Stamminger, Eds., Akademische Verlagsgesellschaft Aka GmbH, pp. 79–86.
- [92] MERHOF, D., SONNTAG, M., ENDERS, F., NIMSKY, C., HASTREITER, P., AND GREINER, G. Hybrid visualization for white matter tracts using triangle strips and point sprites. *IEEE Transactions on Visualization and Computer Graphics* 12, 5 (2006), 1181–1188.
- [93] MERHOF, D., SONNTAG, M., ENDERS, F., NIMSKY, C., HASTREITER, P., AND GREINER, G. Streamline visualization of diffusion tensor data based on triangle strips. In *Proc. Bildverarbeitung für die Medizin (BVM)* (2006), H. Handels, J. Ehrhardt, A. Horsch, H.-P. Meinzer, and T. Tolxdorff, Eds., Springer, pp. 271–275.
- [94] MERHOF, D., SOZA, G., STADLBAUER, A., GREINER, G., AND NIMSKY, C. Correction of susceptibility artifacts in diffusion tensor data using non-linear registration. *Medical Image Analysis* 11, 6 (2007), 588–603.
- [95] MEYER, C., PAULY, J., MACOVSKI, A., AND NISHIMURA, D. Simultaneous spatial and spectral selective excitation. *Magnetic Resonance in Medicine* 15, 2 (1990), 287–304.
- [96] MISHRA, A., LU, Y., MENG, J., ANDERSON, A., AND DING, Z. Unified framework for anisotropic interpolation and smoothing of diffusion tensor images. *NeuroImage* 31, 4 (2006), 1525–1535.
- [97] MITELMAN, S., NEWMARK, R., TOROSJAN, Y., CHU, K., BRICKMAN, A., HAZNEDAR, M., HAZLETT, E., TANG, C., SHIHABUDDIN, L., AND BUCHSBAUM, M. White matter fractional anisotropy and outcome in schizophrenia. *Schizophrenia Research* 87, 1-3 (2006), 138–159.

- [98] MOBERTS, B., VILANOVA, A., AND VAN WIJK, J. Evaluation of fiber clustering methods for diffusion tensor imaging. In *Proc. IEEE Visualization (VIS)* (2005), pp. 65–72.
- [99] MORI, S., CRAIN, B., CHACKO, V., AND VAN ZIJL, P. Three dimensional tracking of axonal projections in the brain by magnetic resonance imaging. *Annals of Neurology* 45, 2 (1999), 265–269.
- [100] MORI, S., AND VAN ZIJL, P. Fiber tracking: Principles and strategies – a technical review. *NMR in Biomedicine* 15 (2002), 468–480.
- [101] MUSSER, D. Introspective sorting and selection algorithms. *Software Practice and Experience* 27, 8 (1997), 983.
- [102] MUSSER, D., DERGE, G., AND SAINI, A. *STL Tutorial and Reference Guide, Second Edition: C++ Programming with the Standard Template Library*. Addison-Wesley Longman Publishing Co., Inc., 2001.
- [103] NILSSON, N. *Principles of Artificial Intelligence*. Tioga Publishing Company, 1980.
- [104] NIMSKY, C., GANSLANDT, O., CERNY, S., HASTREITER, P., GREINER, G., AND FAHLBUSCH, R. Quantification of, visualization of, and compensation for brain shift by intraoperative magnetic resonance imaging. *Neurosurgery* 47, 5 (2000), 1070–1080.
- [105] NIMSKY, C., GANSLANDT, O., ENDERS, F., MERHOF, D., AND FAHLBUSCH, R. Visualization strategies for major white matter tracts identified by diffusion tensor imaging for intraoperative use. In *Proc. Computer Assisted Radiology and Surgery (CARS)* (2005), H. Lemke, K. Inamura, K. Doi, M. Vannier, and A. Farman, Eds., Elsevier B.V., pp. 793–797.
- [106] NIMSKY, C., GANSLANDT, O., ENDERS, F., MERHOF, D., HAMMEN, T., AND BUCHFELDER, M. Visualization strategies for major white matter tracts for intraoperative use. *International Journal of Computer Assisted Radiology and Surgery (CARS)* 1, 1 (2006), 13–22.
- [107] NIMSKY, C., GANSLANDT, O., AND FAHLBUSCH, R. Functional neuronavigation and intraoperative MRI. *Advances and Technical Standards in Neurosurgery* 29 (2004), 229–263.
- [108] NIMSKY, C., GANSLANDT, O., HASTREITER, P., WANG, R., BENNER, T., SORENSEN, A., AND FAHLBUSCH, R. Intraoperative diffusion-tensor MR imaging: Shifting of white matter tracts during neurosurgical procedures - initial experience. *Radiology* 234, 1 (2004), 218–225.

- [109] NIMSKY, C., GANSLANDT, O., KOBER, H., MÖLLER, M., ULMER, S., TOMANDL, B., AND FAHLBUSCH, R. Integration of functional magnetic resonance imaging supported by magnetoencephalography in functional neuronavigation. *Neurosurgery* 44, 6 (1999), 1249–1256.
- [110] NIMSKY, C., GANSLANDT, O., MERHOF, D., SORENSEN, G., AND FAHLBUSCH, R. Intraoperative visualization of the pyramidal tract by DTI-based fiber tracking. *NeuroImage* 30, 4 (2006), 1219–1229.
- [111] NOLTE, U., FINSTERBUSCH, J., AND FRAHM, J. Rapid isotropic diffusion mapping without susceptibility artifacts: Whole brain studies using diffusion-weighted single-shot STEAM MR imaging. *Magnetic Resonance in Medicine* 44, 5 (2000), 731–736.
- [112] NORRIS, D. The effects of microscopic tissue parameters on the diffusion weighted magnetic resonance imaging experiment. *NMR in Biomedicine* 14, 2 (2001), 77–93.
- [113] O'DONNELL, L., HAKER, S., AND WESTIN, C.-F. New approaches to estimation of white matter connectivity in diffusion tensor MRI: Elliptic PDEs and geodesics in a tensor-warped space. In *Proc. Medical Image Computing and Computer Assisted Intervention (MICCAI)* (2002), pp. 459–466.
- [114] OKUGAWA, G., NOBUHARA, K., MINAMI, T., TAKASE, K., SUGIMOTO, T., SAITO, Y., YOSHIMURA, M., AND KINOSHITA, T. Neural disorganization in the superior cerebellar peduncle and cognitive abnormality in patients with schizophrenia: A diffusion tensor imaging study. *Progress in Neuro-Psychopharmacology and Biological Psychiatry* 30, 8 (2006), 1408–1412.
- [115] PAJEVIC, S., AND PIERPAOLI, C. Color schemes to represent the orientation of anisotropic tissues from diffusion tensor data: Application to white matter fiber tract mapping in the human brain. *Magnetic Resonance Imaging* 42, 3 (1999), 526–540.
- [116] PARKER, G. Tracing fiber tracts using fast marching. In *Proc. International Society for Magnetic Resonance in Medicine* (2000), p. 85.
- [117] PHONG, B. Illumination for computer generated pictures. *Communications of the ACM* 18, 6 (1975), 311–317.
- [118] PIERPAOLI, C., AND BASSER, P. Toward a quantitative assessment of diffusion anisotropy. *Magnetic Resonance in Medicine* 36, 6 (1996), 893–906.
- [119] PINKALL, U., AND POLTHIER, K. Computing discrete minimal surfaces and their conjugates. *Experimental Mathematics* 2, 1 (1993), 15–36.

- [120] PRESS, W., TEUKOLSKY, S., VETTERLING, W., AND FLANNERY, B. *Numerical Recipes in C++*. Cambridge University Press, 2002.
- [121] ROHDE, G., BARNETT, A., BASSER, P., MARENCO, S., AND PIERPAOLI, C. Comprehensive approach for correction of motion and distortion in diffusion-weighted MRI. *Magnetic Resonance in Medicine* 51, 1 (2004), 103–114.
- [122] RUECKERT, D., SONODA, L., C. HAYES, D. H., LEACH, M., AND HAWKES, D. Nonrigid registration using free-form deformations: Application to breast MR images. *IEEE Transactions on Medical Imaging* 18, 8 (1999), 712–721.
- [123] RUIZ-ALZOLA, J., WESTIN, C.-F., WARFIELD, S., ALBEROLA, C., MAIER, S., AND KIKINIS, R. Nonrigid registration of 3D tensor medical data. *Medical Image Analysis* 6, 2 (2002), 143–161.
- [124] SCHIRSKI, M., KUHLEN, T., HOPP, M., ADOMEIT, P., PISCHINGER, S., AND BISCHOF, C. Virtual tubelets - efficiently visualizing large amounts of particle trajectories. *Computers & Graphics* 29, 1 (2005), 17–27.
- [125] SCHLÖSSER, R., NENADIC, I., WAGNER, G., GÜLLMAR, D., VON CONSRUCH, K., KÖHLER, S., SCHULTZ, C., KOCH, K., FITZEK, C., MATTHEWS, P., REICHENBACH, J., AND SAUER, H. White matter abnormalities and brain activation in schizophrenia: A combined DTI and fMRI study. *Schizophrenia Research* 89, 1-3 (2007), 1–11.
- [126] SCHROEDER, W., MARTIN, K., AND LORENSEN, B. *The Visualisation ToolKit*. Kitware, 2002. , URL: <http://www.vtk.org>.
- [127] SHANNON, C., AND WEAVER, W. *The Mathematical Theory of Communication*. University of Illinois Press, 1949.
- [128] SHEN, Y., LARKMAN, D., COUNSELL, S., PU, I., EDWARDS, D., AND HAJNAL, J. Correction of high-order eddy current induced geometric distortion in diffusion-weighted echo-planar images. *Magnetic Resonance in Medicine* 52, 5 (2004), 1184–1189.
- [129] SIERRA, R. Nonrigid registration of diffusion tensor images. Master's thesis, Swiss Federal Institute of Technology Zurich, 2001. SPL Technical Report 207.
- [130] SMITH, S. Fast robust automated brain extraction. *Human Brain Mapping* 17, 3 (2002), 143–55.
- [131] SORENSEN, A., WU, O., COPEN, W., DAVIS, T., GONZALEZ, R., KOROSHETZ, W., REESE, T., ROSEN, B., WEDEEN, V., AND WEISSKOFF, R. Human acute cerebral ischemia: Detection of changes in water diffusion anisotropy by using MR imaging. *Radiology* 212, 3 (1999), 785–792.

- [132] SOZA, G. *Registration and Simulation for the Analysis of Intraoperative Brain Shift*. PhD thesis, Computer Graphics Group, Computer Science Department, University of Erlangen-Nuremberg, 2005.
- [133] SOZA, G., GROSSO, R., NIMSKY, C., GREINER, G., AND HASTREITER, P. Estimating mechanical brain tissue properties with simulation and registration. In *Proc. Medical Image Computing and Computer Assisted Intervention (MICCAI)* (2004), pp. 276–283.
- [134] SPALL, J. Adaptive stochastic approximation by the simultaneous perturbation method. *IEEE Transactions on Automatic Control* 45, 10 (2000), 1839–1853.
- [135] SPALL, J., HILL, S., AND STARK, D. Theoretical comparisons of evolutionary computation and other optimization approaches. In *Proc. IEEE Congress on Evolutionary Computation (CEC)* (1999), pp. 1398–1405.
- [136] SPALL, J. C. Multivariate stochastic approximation using a simultaneous perturbation gradient approximation. *IEEE Transactions on Automatic Control* 37, 3 (1992), 332–341.
- [137] STAEMPFLI, P., JAERMANN, T., CRELIER, G., KOLLIAS, S., VALAVANIS, A., AND BOESIGER, P. Resolving fiber crossing using advanced fast marching tractography based on diffusion tensor imaging. *NeuroImage* 30, 1 (2006), 110–120.
- [138] STAHL, R., DIETRICH, O., TEIPEL, S., HAMPEL, H., REISER, M., AND SCHOENBERG, S. White matter damage in Alzheimer disease and mild cognitive impairment: Assessment with diffusion-tensor MR imaging and parallel imaging techniques. *Radiology* 243, 2 (2007), 483–492.
- [139] STEJSKAL, E. Use of spin echoes in a pulsed magnetic-field gradient to study anisotropic, restricted diffusion and flow. *Journal of Chemical Physics* 43, 10 (1965), 3597–3603.
- [140] STEJSKAL, E., AND TANNER, J. Spin diffusion measurements: Spin echoes in the presence of a time-dependent field gradient. *Journal of Chemical Physics* 42, 1 (1965), 288–292.
- [141] STOLL, C., GUMHOLD, S., AND SEIDEL, H.-P. Visualization with stylized line primitives. In *Proc. IEEE Visualization (VIS)* (2005), pp. 695–702.
- [142] STUDHOLME, C., HILL, D., AND HAWKES, D. An overlap invariant entropy measure of 3D medical image alignment. *Pattern Recognition* 32, 1 (1999), 71–86.
- [143] TAUBIN, G. A signal processing approach to fair surface design. In *Proc. Computer Graphics and Interactive Techniques (SIGGRAPH)* (1995), pp. 351–358.

- [144] TORREY, H. Bloch equations with diffusion terms. *Physical Review* 104, 3 (1956), 563–565.
- [145] TUCH, D., WEISKOFF, R., BELLIVEAU, J., AND WEDEEN, V. High angular resolution diffusion imaging of the human brain. In *Proc. International Society for Magnetic Resonance in Medicine (ISMRM)* (1999), p. 321.
- [146] TURK, G., AND BANKS, D. Image-guided streamline placement. In *Proc. Computer Graphics and Interactive Techniques (SIGGRAPH)* (1996), pp. 453–460.
- [147] VILANOVA, A., BERENSCHOT, G., AND VAN PUL, C. DTI visualization with streamsurfaces and evenly-spaced volume seeding. In *Proc. Joint Eurographics - IEEE TVCG Symposium on Visualization (VisSym)* (2004), pp. 173–182.
- [148] WEINSTEIN, D., KINDLMANN, G., AND LUNDBERG, E. Tensorlines: Advection-diffusion based propagation through diffusion tensor fields. In *Proc. IEEE Visualization (VIS)* (1999), pp. 249–253.
- [149] WEISKOPF, D., ENGEL, K., AND ERTL, T. Volume clipping via per-fragment operations in texture-based volume visualization. In *Proc. IEEE Visualization (VIS)* (2002), pp. 93–100.
- [150] WEISSKOFF, R. Improved hard-pulse sequences for frequency-selective presaturation in magnetic resonance. *Journal of Magnetic Resonance* 86, 1 (1990), 170–175.
- [151] WELLS, W., VIOLA, P., ATSUMI, H., NAKAJIMA, S., AND KIKINIS, R. Multimodal volume registration by maximization of mutual information. *Medical Image Analysis* 1, 1 (1997), 35–51.
- [152] WESTIN, C.-F., MAIER, S., KHIDHIR, B., EVERETT, P., JOLESZ, F., AND KIKINIS, R. Image processing for diffusion tensor magnetic resonance imaging. In *Proc. Medical Image Computing and Computer Assisted Intervention (MICCAI)* (1999), pp. 441–452.
- [153] WESTIN, C.-F., MAIER, S., MAMATA, H., NABAVI, A., JOLESZ, F. A., AND KIKINIS, R. Processing and visualization for diffusion tensor MRI. *Medical Image Analysis* 6, 2 (2002), 93–108.
- [154] WESTIN, C.-F., PELED, S., GUBJARTSSON, H., KIKINIS, R., AND JOLESZ, F. Geometrical diffusion measures for MRI from tensor basis analysis. In *Proc. International Society for Magnetic Resonance in Medicine (ISMRM)* (1997), p. 1742.
- [155] WIEGELL, M., LARSSON, H., AND WEDEEN, V. Fiber crossing in human brain depicted with diffusion tensor MR imaging. *Radiology* 217, 3 (2000), 897–903.

- [156] WÜNSCHE, B., AND LOBB, R. The visualization of diffusion tensor fields in the brain. In *Proc. Mathematics and Engineering Techniques in Medicine and Biological Science (METMBS)* (2001), pp. 498–504.
- [157] XIE, S., XIAO, J., GONG, G., ZANG, Y., WANG, Y., WU, H., AND JIANG, X. Voxel-based detection of white matter abnormalities in mild Alzheimer disease. *Neurology* 66, 12 (2006), 1845–1849.
- [158] ZHAN, W., STEIN, E., AND YANG, Y. Mapping the orientation of intravoxel crossing fibers based on the phase information of diffusion circular spectrum. *NeuroImage* 23, 4 (2004), 1358–1369.
- [159] ZHANG, S., DEMIRALP, C., AND LAIDLAW, D. Visualizing diffusion tensor MR images using streamtubes and streamsurfaces. *IEEE Transactions on Visualization and Computer Graphics* 9, 4 (2003), 454–462.
- [160] ZHUKOV, L., AND BARR, A. Oriented tensor reconstruction: Tracing neural pathways from diffusion tensor MRI. In *Proc. IEEE Visualization (VIS)* (2002), pp. 387–394.
- [161] ZLOKOLICA, V., PHILIPS, W., AND VAN DE VILLE, D. A new non-linear filter for video processing. In *Proc. IEEE Benelux Signal Processing Symposium (SPS)* (2002), pp. S02-1 – S02-4.
- [162] ZÖCKLER, M., STALLING, D., AND HEGE, H.-C. Interactive visualization of 3D-vector fields using illuminated stream lines. In *Proc. IEEE Visualization (VIS)* (1996), pp. 107–113.

Rekonstruktion und Visualisierung
neuronaler Bahnen aus Diffusionstensor-Daten

Kurzfassung

Für die Diagnose und die OP-Planung sind Aufnahmen mittels Magnetresonanztomographie (MRT) eine wichtige Informationsquelle. Vor etwa einem Jahrzehnt wurde eine neue MRT-Technik entwickelt, die sogenannte Diffusionstensor-MRT (DT-MRT). Dieses Bildgebungsverfahren ermöglicht Rückschlüsse auf die Lage und den Verlauf von Gewebe mit faseriger Struktur, so z.B. den neuronalen Strukturen im Gehirn. Da dies *in vivo* bisher nicht möglich war, ist das Interesse an DT-MRT in verschiedenen Forschungsgebieten stark gewachsen.

In der Neurochirurgie ist DT-MRT von großem Wert, da zusätzlich zu den MRT-Daten, welche anatomische Strukturen zeigen, Informationen über den Verlauf neuronaler Bahnen gewonnen werden können. Neuronale Bahnen sind wichtige Strukturen im Gehirn, die integrativen Funktionen, z.B. im Bereich der Motorik oder Sensorik, zugeordnet sind. Bei einer Gehirnoperation im Falle pathologischer Veränderungen (Tumor) dürfen diese Nervenbahnen nicht verletzt werden, um neurologischen Defizite zu vermeiden.

Die Rekonstruktion neuronaler Strukturen aus DT-MRT-Daten ist jedoch aufgrund der Komplexität der vorliegenden Tensor-Information nicht trivial. Aus diesem Grund wurde in den letzten Jahren intensiv an Verfahren zur Rekonstruktion und Visualisierung basierend auf DT-MRT-Tensordaten gearbeitet.

Die vorliegende Arbeit trägt zur aktuellen Forschung in diesem Bereich bei, indem neue Techniken zur Rekonstruktion und Visualisierung neuronaler Bahnen vorgestellt werden. Die verschiedenen Ansätze wurden in Zusammenarbeit mit Neurochirurgen entwickelt mit dem Ziel, die präoperative Planung und die intraoperative Visualisierung bei neurochirurgischen Operationen zu unterstützen. Zu diesem Zweck wurde ein DT-MRT-Programmpaket mit einer Vielzahl an Algorithmen zur Verarbeitung von DT-MRT-Daten entwickelt. Dazu zählen die Rekonstruktion von Tensoren, globale Filterungstechniken, Fiber Tracking und Konnektivitätsanalyse, Algorithmen zur Generierung von Hüllen und verschiedene Visualisierungstechniken.

Die in diesem Forschungsbereich erzielten Ergebnisse werden in Zukunft dazu beitragen, die Planung neurochirurgischer Eingriffe weiter zu verbessern und das Risiko postoperativer neurologischer Defizite für die Patienten zu verringern.

Inhaltsverzeichnis

Kurzfassung	i
Inhaltsverzeichnis	vi
Abbildungsverzeichnis	viii
Tabellenverzeichnis	ix
Verzeichnis der Programmbeispiele	xi
Danksagung	xiii
I Einleitung	2
1 Hintergrund und Überblick	3
1.1 Motivation	3
1.2 Beiträge der Arbeit	4
1.3 Überblick	6
2 Neurochirurgie: Geschichte, Krankheitsbilder und OP-Durchführung	9
2.1 Geschichte der Neurochirurgie	9
2.2 Behandelte Krankheitsbilder	10
2.3 Neurochirurgische Eingriffe	11
2.3.1 Klinischer Aufbau und Ablauf im Operationssaal	11
2.3.2 Navigation in der bildgestützten Neurochirurgie	12
2.4 Neuroanatomie	14
2.5 Bildgebende Verfahren in der Neurochirurgie	16
2.5.1 Physikalischer Hintergrund	16
2.5.2 Magnet-Resonanz-Tomographie (MRT)	18
2.5.3 Funktionelle MRT (fMRT)	19

2.5.4	Diffusions-Tensor-MRT (DT-MRT)	20
2.5.5	Bildgebungsparameter und Bilddaten	20
II	Rekonstruktion neuronaler Strukturen	24
3	Tensor-Rekonstruktion und -Verarbeitung	25
3.1	Die Stejskal-Tanner-Gleichung	25
3.2	Berechnung der Tensoren	26
3.3	Quantifizierung der Tensorform	27
3.3.1	Eigensystem des Tensors	27
3.3.2	Diffusions-Ellipsoide	28
3.3.3	Skalare Metriken	28
3.3.3	Spur des Tensors	29
3.3.3	Fraktionale Anisotropie	29
3.3.3	Koordinaten im Baryzentrischen Raum	29
3.4	Tensor-Interpolation	30
3.5	Filtern von Tensoren	31
3.5.1	Gauss-Filter	32
3.5.2	Zwei-Klassen-Gauss-Filter	33
3.5.3	Best-Neighbor-Filter	34
3.5.4	Ergebnisse	35
3.6	Diskussion	36
4	Fiber-Tracking-Verfahren	39
4.1	Grundlagen zu Fiber-Tracking	39
4.1.1	Verfolgung von Strömungslinien und Tensor-Deflection	40
4.1.2	Verfahren zur Selektion von Traktsystemen	44
4.2	Lokale Filter	45
4.2.1	Lokales Filter-Fenster	46
4.2.2	Lokaler Gauss-Filter	46
4.2.3	Moving-Least-Squares-Filter	47
4.2.4	Ergebnisse	48
4.3	Fiber-Tracking mit Abstandskontrolle	50
4.3.1	Verfahren zur Abstandskontrolle	51
4.3.2	Adaptive Abstandskontrolle	53
4.3.3	Fiber-Tracking mit Abstandskontrolle und Regions-of-Interest	55
4.4	Gerichtetes Volumenwachstum	56
4.4.1	Algorithmus für gerichtetes Volumenwachstum	56
4.4.2	Ergebnisse	57
4.5	Diskussion	59

5	Konnektivitätsanalyse zwischen funktionellen Zentren	63
5.1	Bisherige Arbeiten	63
5.2	Konnektivitätsanalyse mittels Pfadsuche	64
5.2.1	Der A*-Algorithmus	64
5.2.2	Begrenzung des Suchraums	67
5.2.3	Gitter zur Partitionierung des Suchraums	67
5.2.4	Kostenfunktion	68
5.2.5	Kostengünstigster Pfad	70
5.2.6	Mehrere Start- und Zielvoxel	70
5.2.7	Heuristik	70
5.2.8	Effiziente Implementierung	71
5.3	Ergebnisse	72
5.3.1	Qualitätsanalyse	72
5.3.2	Rechenzeit	73
5.4	Diskussion	75
6	Generierung von Hüllen	77
6.1	Tetraedrisierung und 3D-Alpha-Shapes	78
6.1.1	3D-Delaunay-Algorithmus	78
6.1.2	3D-Alpha-Shapes	79
6.1.3	Ergebnisse	80
6.2	Isoflächen	81
6.2.1	Rasterisierung	81
6.2.2	Volumenfilter	82
6.2.3	Oberflächenextraktion	82
6.2.4	Glättung der Oberfläche	83
6.2.5	Ergebnisse	85
6.3	Konstruktion einer Sicherheitshülle	88
6.4	Diskussion	90
7	Korrektur von Verzerrungen	93
7.1	Verzerrungsartefakte in DTI-EPI Daten	93
7.2	Bisherige Arbeiten	94
7.3	Nichtlineare Registrierung	95
7.3.1	Ähnlichkeitsmaß	95
7.3.2	Optimierung	96
7.3.3	3D-Freiform-Deformation	96
7.3.4	Registrierungs-Framework	98
7.4	Experimentelle Durchführung	98
7.5	Ergebnisse	100
7.6	Diskussion	103

III	Visualisierung	108
8	Visualisierung der berechneten Bahnstrukturen	109
8.1	Transferfunktionen für die Farbgebung	109
8.2	Visualisierung durch Linien	111
8.2.1	Beleuchtete Linien	111
8.2.2	Adaptive Transparenz	115
8.3	Visualisierung durch Dreieckstreifen und Point-Sprites	116
8.3.1	Bisherige Arbeiten	117
8.3.2	Hybrides Visualisierungsverfahren	117
8.4	Diskussion	125
9	Visualisierung der Hüllen	127
9.1	Beleuchtung	127
9.2	Transparenz	128
10	Multimodale Visualisierung von DT-MRT- und MRT-Daten	129
10.1	Multimodale Visualisierung mittels Volumen-Rendering	129
10.1.1	Markierte Volumina	130
10.1.2	Volumen-Clipping	130
10.1.3	Fusion	131
10.2	Ergebnisse	132
10.3	Diskussion	132
IV	Abschließende Bemerkungen	136
11	Zusammenfassung	137
12	Ausblick	141
	Literaturverzeichnis	143

Teil I

Einleitung

Kapitel 1

Hintergrund und Forschungsbeitrag

1.1 Motivation

Die heute verfügbaren bildgebenden Verfahren in der Medizin sind ein wichtiges Werkzeug, um grundlegende anatomische und physiologische Zusammenhänge zu erkennen und um eine zuverlässige und reproduzierbare Diagnose zu ermöglichen. Aus diesem Grund sind moderne bildgebende Verfahren für eine Vielzahl medizinischer Anwendungen von großer Bedeutung. Die Magnet-Resonanz-Tomographie (MRT) ist beispielsweise ein nicht-invasives Bildgebungsverfahren, mit dem vorzugsweise Organe und Gewebe dargestellt werden. Für diagnostische Zwecke, bei der Planung von Operationen sowie für navigierte Eingriffe leisten MRT-Daten wertvolle Dienste. Für die Verarbeitung und Visualisierung von MRT-Daten stehen eine Vielzahl verschiedener Techniken zur Verfügung, beispielsweise Verfahren zur 3D Volumenvisualisierung oder unterschiedliche Segmentierungsverfahren.

Während des letzten Jahrzehnts hat sich ein weiteres MRT-Bildgebungsverfahren etabliert, die sogenannte *Diffusions-Tensor-MRT (DT-MRT)*. Mit DT-MRT wird die Diffusion von Wasser gemessen, die auf zufällige Bewegungen der Moleküle aufgrund ihrer thermischen Energie zurückzuführen ist. In faserigem Gewebe wie beispielsweise der weißen Substanz¹ des zentralen Nervensystems ist die Diffusion auf eine Vorzugsrichtung beschränkt. Aus der Diffusionsmessung sind daher Rückschlüsse auf die Struktur des darunter liegenden Gewebes möglich. Dies eröffnet die Möglichkeit, die Funktion und Struktur des Gehirns *in vivo* zu analysieren, was für verschiedene Forschungsgebiete und in der medizinischen Anwendung von großem Interesse ist. Die mittels DT-MRT gemessenen Diffusionseigenschaften unterstützen die Diagnose von Schlaganfällen, degenerativen Erkrankungen des Gehirns oder psychischen Erkrankungen wie beispielsweise Schizophrenie. In der Neuroanatomie und Neurochirurgie dienen DT-MRT-Messungen als Basis zur Rekonstruktion von Bahnsystemen der weißen Substanz.

Die Verarbeitung und Visualisierung von DT-MRT-Daten ist jedoch aufgrund der

¹Die weiße Substanz enthält Nervenbündel (Axone), die der Weiterleitung von Informationen dienen. Die Axone sind von Myelin umgeben, das eine weißliche Färbung besitzt.

Komplexität der Daten sehr anspruchsvoll. Anstatt eines skalaren Wertes ist bei DT-MRT pro Voxel ein kompletter Tensor verfügbar, der die lokalen Diffusionseigenschaften beschreibt. Die Herausforderungen bei der Rekonstruktion und Visualisierung neuronaler Bahnen liegen darin, aussagekräftige skalare Metriken, sowie geeignete Rekonstruktionsverfahren und umfassende Visualisierungstechniken zu entwickeln.

In dieser Arbeit werden Rekonstruktions- und Visualisierungsverfahren basierend auf DT-MRT-Daten vorgestellt, welche auf die Anforderungen in der Neurochirurgie zugeschnitten sind. DT-MRT-Daten bieten großes Potential zur Verbesserung von Diagnose und Planung in der Neurochirurgie. Ziel dabei ist es, wichtige Strukturen der weißen Substanz bei Operationen zu erhalten und so postoperativ neurologische Defizite zu vermeiden. Aus diesem Grund haben erste Kliniken damit begonnen, im Rahmen von Forschungsprojekten die DT-MRT-Bildgebung für die präoperative Planung und auch zur intraoperativen Visualisierung im Rahmen der Neuronavigation einzusetzen.

Das Ziel dieser Arbeit war es, die sich widersprechenden Vorgaben der Neurochirurgie besser zu verbinden. Zum einen wird beispielsweise die möglichst vollständige Resektion von Gehirntumoren angestrebt, zum anderen gilt es, wichtige Funktionen wie Motorik oder Sprache zu erhalten. Zu diesem Zweck wurden neue Verfahren zur Rekonstruktion und Visualisierung entwickelt, die den Neurochirurgen sowohl bei der präoperativen Planung als auch intraoperativ unterstützen.

1.2 Beiträge der Arbeit

Die Beiträge der Arbeit umfassen verschiedene Techniken zur Rekonstruktion und Visualisierung von Traktsystemen der weißen Substanz. Die Forschungsergebnisse wurden auf einschlägigen Konferenzen und in Zeitschriften veröffentlicht [79-95]. Im Wesentlichen werden folgende Beiträge in dieser Arbeit vorgestellt und diskutiert:

(1) REKONSTRUKTION – FILTERUNG VON TENSOREN

Trotz der Verwendung von Bildgebungs-Protokollen, bei denen verschiedene Messungen gemittelt werden, sind DT-MRT-Daten mit Rauschen behaftet. Um das Rauschen zu verringern, wurden Filter eingesetzt, die aus der Videoverarbeitung bekannt sind. Da eine Videosequenz und eine Sequenz von Schichtbildern eine gewisse Parallele aufweisen, wurden die Vorteile der Videofilter zur Filterung von DT-MRT-Daten eingesetzt.

(2) REKONSTRUKTION – FIBER-TRACKING

Zur Rekonstruktion von Traktsystemen aus DT-MRT-Daten werden für gewöhnlich sogenannte *Fiber-Tracking-Verfahren* verwendet. In diesem Zusammenhang wurde das Konzept der *Evenly-Spaced-Streamlines* adaptiert und verwendet, um die Dichte der einzelnen Strömungslinien in Abhängigkeit der lokalen Anisotropiewerten zu steuern. Außerdem wurde ein alternatives Verfahren zur Rekonstruktion von Traktsystemen entwickelt, das auf gerichtetem Volumenwachstum basiert.

(3) REKONSTRUKTION – KONNEKTIVITÄTSANALYSE

In Bereichen nahe des Kortex sind kleinere, sich verzweigende Bahnen angesiedelt, so dass die Richtungsinformation aus den Tensorwerten weniger deutlich ausgeprägt ist. Aus diesem Grund wurde ein alternatives Verfahren zur Rekonstruktion von Bahnen zwischen funktionellen Zentren entwickelt. Der auf A*-Pfadsuche basierende Algorithmus sowie weitere Verbesserungen durch eine ausgereifere Kostenfunktion und ein verfeinertes Suchgitter werden vorgestellt und diskutiert.

(4) REKONSTRUKTION – HÜLLEN

Fiber-Tracking- und Konnektivitätsanalyse-Verfahren erzeugen im Allgemeinen Bündel von Kantenzügen, welche die Form eines Traktsystems approximieren. Für die intraoperative Visualisierung in Verbindung mit einem Neuronavigationssystem sind jedoch Hüllflächen besser geeignet, da sie als Grundlage für Randkurven dienen können, die ins OP-Mikroskop eingeblendet werden. Basierend auf Erfahrungen im Bereich Netzgenerierung [84-86] konnten verschiedene Techniken zur Generierung von Hüllen entwickelt werden, darunter ein Ansatz basierend auf Tetraedrisierung und ein Verfahren, das Isoflächen nutzt.

(5) REKONSTRUKTION – VERZERRUNGSKORREKTUR

Für die Akquisition von DT-MRT-Daten werden im allgemeinen EPI-Sequenzen verwendet, die jedoch zu Verzerrungsartefakten führen. Die rekonstruierten Traktsysteme sind daher ebenfalls verschoben. Um die Verzerrungen zu korrigieren und die DT-MRT-Daten für die Neuronavigation nutzen zu können, wurde ein Verfahren zur nicht-linearen Registrierung verwendet. Die Verarbeitungsschritte und Ergebnisse aus dieser Vorgehensweise wurden evaluiert und werden diskutiert.

(6) VISUALISIERUNG – FIBER-TRACKING

Zur Visualisierung der rekonstruierten Traktsysteme wurden verschiedene Verfahren entwickelt. Abhängig von den Anisotropie-Werten der lokalen Diffusion wurde die Transparenz der einzelnen Fibers reguliert, so dass dominante Traktsysteme visuell deutlicher hervortreten. Außerdem wurde in Verbindung mit dem Verfahren zur Konnektivitätsanalyse verschiedene Farb-Transferfunktionen vorgestellt, welche die lokalen Kosten oder Anisotropie-Werte kodieren. Für die Visualisierung der Fibers wurde ein hybrides Verfahren entwickelt, das auf Dreiecksstreifen und Point-Sprites basiert. Die resultierende Visualisierung ist von hoher visueller Qualität, gleichzeitig kann aber auch eine große Menge von Fibers in Echtzeit dargestellt werden.

(7) VISUALISIERUNG – HÜLLEN

Zur Visualisierung der Hüllen wurden Per-Pixel-Lighting und Transparenz eingesetzt. Dadurch ist es möglich, die Struktur der Hüllen genau zu analysieren und die Qualität der Hüllen visuell zu überprüfen. Die Techniken zur Visualisierung

von Hüllen wurden in Verbindung mit den Rekonstruktionsverfahren für Hüllen entwickelt.

(8) VISUALISIERUNG – MULTIMODALE VISUALISIERUNG

Um die rekonstruierten Traktsysteme, die zugehörigen Hüllen sowie funktionelle Zentren aus fMRI gleichzeitig in ihrem anatomischen Kontext zu visualisieren, ist eine multimodale Visualisierung mit anatomischen MR-Daten erforderlich. Die entsprechenden Visualisierungstechniken und ihre Vorzüge für den Einsatz in der Neurochirurgie wurden untersucht.

Die Entwicklung von Rekonstruktions- und Visualisierungstechniken für DT-MRT-Daten ist ein aktives Forschungsgebiet. Aus diesem Grund sind die vorgestellten Algorithmen und Visualisierungsverfahren nicht als endgültige Lösung bestehender Fragestellungen zu verstehen, sondern als aktuelle Forschungsbeiträge im Rahmen einer fortlaufenden Entwicklung. Die einzelnen Kapitel stellen verschiedene Verfahren zur Verarbeitung von DT-MRT-Daten vor, die im Hinblick auf Anwendungsmöglichkeiten in der Neurochirurgie entwickelt wurden. Der potentielle Nutzen des jeweiligen Verfahrens wird am Ende eines jeden Kapitels diskutiert. Die Ergebnisse sind vielversprechend, eine umfassende klinische Evaluation befindet sich momentan jedoch noch in Bearbeitung.

1.3 Überblick

In dieser Arbeit wird eine Reihe neuer Methoden zur Rekonstruktion und Visualisierung von Traktsystemen der weißen Substanz, basierend auf DT-MRT-Daten, vorgestellt. Die Arbeit gliedert sich in drei Hauptteile: Der erste Teil (Kapitel 1 und 2) beginnt mit einer Einleitung und erläutert den medizinischen Hintergrund neurochirurgischer Eingriffe. Der zweite Teil (Kapitel 3 bis 7) beschreibt verschiedene Rekonstruktionsverfahren basierend auf DT-MRT-Daten. Im dritten Teil (Kapitel 8 bis 10) werden Visualisierungsverfahren vorgestellt, die der geeigneten Darstellung der rekonstruierten Strukturen im medizinischen Umfeld dienen.

Teil I – Kapitel 2 behandelt den medizinischen Hintergrund neurochirurgischer Eingriffe. Das Kapitel beginnt mit einem kurzen Abriss der Geschichte der Neurochirurgie, beschreibt dann verschiedene Krankheitsbilder, die eine neurochirurgische Behandlung erfordern, und gibt einen Einblick in die Ausrüstung des OPs und zur Anwendung des Neuronavigationssystem. Beendet wird das Kapitel mit einer Einführung in die verschiedenen Bildgebungsmodalitäten, die in der Neurochirurgie bevorzugt Anwendung finden.

Teil II – Kapitel 3 erläutert zunächst die Grundlagen der Tensor-Rekonstruktion. Im weiteren Verlauf werden Verfahren zur Quantifizierung der Tensor-Form, zur Tensor-Interpolation und zur Filterung vorgestellt. Dieses Kapitel beinhaltet fundamentale In-

formationen zur Tensor-Rekonstruktion und -Verarbeitung, die als Grundlage für die folgenden Kapitel dienen.

Teil II – Kapitel 4 bietet eine Einführung zu den sog. *Fiber-Tracking*-Algorithmen. Dabei werden zwei grundlegende Verfahren vorgestellt: Zum einen die Verfolgung von Strömungslinien, zum anderen ein Verfahren basierend auf *Tensor-Deflection*. Außerdem werden verschiedene Möglichkeiten zur Selektion einzelner Traktsysteme aufgezeigt. Im weiteren Verlauf des Kapitels werden fortgeschrittene Verfahren beschrieben, darunter ein Konzept zur adaptiven Abstandskontrolle zwischen einzelnen Fibers, sowie eine Alternative zum *Fiber-Tracking* basierend auf gerichtetem Volumenwachstum.

Teil II – Kapitel 5 beschreibt ein Verfahren zur Rekonstruktion neuronaler Verbindungen zwischen funktionellen Zentren, wie z.B. zwischen dem Broca- und Wernicke-Sprachzentrum. Da in kortikalen und subkortikalen Bereichen die anisotrope Diffusion weniger ausgeprägt ist, wird ein alternatives Verfahren vorgestellt, das die komplette Tensorinformation nutzt. Das Verfahren basiert auf Pfadsuche und verwendet einen Suchbaum und eine Kostenfunktion, die auf der lokalen Tensor-Information basiert, um mögliche neuronale Verbindungen zu rekonstruieren.

Teil II – Kapitel 6 widmet sich der Fragestellung, wie die rekonstruierten Bahnen aus Kapitel 4 und 5 für den intraoperativen Einsatz genutzt werden können. Da das direkte Einblenden der Linienrepräsentation ins OP-Mikroskop eher verwirrend als nützlich ist, wird eine alternative Darstellung benötigt. Zu diesem Zweck werden in diesem Kapitel verschiedene Ansätze zur Generierung von Hüllen um die rekonstruierten Bahnen vorgestellt. Die Hüllen dienen als Basis für Randkurven, welche in die Fokus-Ebene des OP-Mikroskops eingeblendet werden und die für den intraoperativen Einsatz wesentlich besser geeignet sind.

Teil II – Kapitel 7 beschäftigt sich mit der Korrektur von Verzerrungen, welche durch die Aufnahmetechnik bei der DT-MRT-Bildgebung bedingt sind, da üblicherweise EPI-Sequenzen verwendet werden. Zu Beginn des Kapitels werden die im Zusammenhang mit EPI-Sequenzen entstehenden Bildgebungsartefakte beschrieben. Im weiteren Verlauf des Kapitels wird ein nicht-lineares Verfahren zur Registrierung erläutert, das zur Verzerrungskorrektur eingesetzt wurde. Zum Abschluß des Kapitels werden Ergebnisse der Verzerrungskorrektur vorgestellt und diskutiert, welche die Vorteile der Korrektur zeigen.

Teil III – Kapitel 8 stellt verschiedene Verfahren zur Visualisierung von Bahnen vor, die durch *Fiber-Tracking* oder Konnektivitätsanalyse gewonnen wurden. Zunächst wird adaptive Transparenz in Abhängigkeit von den lokalen Diffusionseigenschaften vorgestellt, wodurch dominante Bahnsysteme visuell hervortreten, während kleine Bahnen transparenter werden. Auf diese Weise wird die Aufmerksamkeit auf die wichtigen Bahnsysteme gelenkt und sichergestellt, dass sie nicht durch kleine Bahnen verdeckt werden. Ein weiterer Aspekt der in diesem Kapitel betrachtet wird, ist die Farbgebung der Bahnen. Um Informationen wie beispielsweise die Werte der lokalen Anisotropie oder Kostenfunktion visuell zu vermitteln, werden geeignete Farbschemata vorgestellt. Abgerundet wird das Kapitel durch ein hybrides Verfahren zur Visualisierung von Bah-

nen, das auf Dreiecksstreifen und Point-Sprites basiert und das sich durch visuelle Qualität bei gleichzeitig hohen Frameraten auszeichnet.

Teil III – Kapitel 9 beschreibt die Visualisierung von Hüllen. Beleuchtung und Transparenz sind wichtige Werkzeuge, um die Form und Qualität der Hülle bezüglich der zugrunde liegenden Fiber-Tracking-Ergebnisse darzustellen.

Teil III – Kapitel 10 präsentiert und diskutiert Ansätze zur multimodale Visualisierung, bei der anatomische MR-Daten zusammen mit Bahnen und Hüllen aus DT-MRT sowie funktionellen Arealen dargestellt werden. Für die präoperative Planung liefert die gleichzeitige Visualisierung anatomischer MR-Daten mit Strukturen der weißen Substanz wichtige Informationen über die Lage und den Verlauf der Bahnen bezüglich benachbarter Anatomie.

Teil IV

Abschließende Bemerkungen

Kapitel 11

Zusammenfassung

In den letzten Jahren wurden neurochirurgische Eingriffe durch die Entwicklung von Navigationssystemen sowie durch Software für die präoperative Planung revolutioniert, welche den Chirurgen sowohl bei der Planung als auch intraoperativ unterstützen. Das Neuronavigations-System nutzt optisches Tracking, um die Position des OP-Mikroskops während der OP zu verfolgen. Damit wird es möglich, den räumlichen Bezug präoperativer Planungsdaten zum OP-Situs herzustellen. Auf diese Weise können die Ergebnisse umfangreicher Untersuchungen direkt während der OP genutzt werden, z.B. Informationen über die Position funktioneller Zentren. Somit kann tumoröses Gewebe präziser und effektiver entfernt und das Risiko postoperativer Defizite für den Patienten erheblich vermindert werden.

Weitere wichtige Entwicklungen zur Unterstützung neurochirurgischer Eingriffe sind neue MR-Bildgebungsverfahren wie beispielsweise das DT-MRT-Verfahren, welches vor ungefähr einem Jahrzehnt entwickelt wurde. Die sich damit eröffnenden Möglichkeiten, die Lage und den Verlauf neuronaler Bahnen *in vivo* zu ermitteln, stellen ein großes Potential für die neurochirurgische Planung und OP-Durchführung dar. Ein anderes wichtiges Bildgebungsverfahren in der Neurochirurgie ist die funktionelle Bildgebung mit fMRI, die vor ungefähr 15 Jahren eingeführt wurde und die der Lokalisation funktioneller Zentren dient. Der Einsatz von DT-MRT und fMRI für die präoperative Planung und intraoperativ in Verbindung mit dem Neuronavigations-System ermöglicht eine zielgenaue Planung und Durchführung von OPs. Zu diesem Zweck ist jedoch geeignete Software zur Aufbereitung und Auswertung der Daten erforderlich, mit der die gemessenen Daten erst klinisch nutzbar werden.

In dieser Arbeit werden eine Reihe verschiedener Ansätze zur Rekonstruktion und Visualisierung neuronaler Bahnen aus DT-MRT-Daten vorgestellt, welche die Planung und Durchführung neurochirurgischer Eingriffe unterstützen. Generell lassen sich die Arbeitsbereiche in zwei aufeinander aufbauende Stufen unterteilen, die einerseits die Rekonstruktion neuronaler Strukturen, andererseits die Visualisierung der Rekonstruktions-Ergebnisse umfassen. Daraus ergeben sich die Teile dieser Arbeit, welche eine Einführung und Motivation (*Teil I*), die Rekonstruktions- (*Teil II*) sowie die Visualisierungs-

verfahren (*Teil III*) beinhaltet. Im Folgenden werden die einzelnen Teile zusammengefasst, mit Fokus auf den wesentlichen Beiträgen der Arbeit.

Im ersten Teil der Arbeit wird fundamentales Wissen zum medizinischen Hintergrund vermittelt. Beginnend mit einem kurzen Rückblick in die Geschichte der Neurochirurgie, bietet dieser Teil eine Einführung zu Krankheitsbildern, neuro-anatomischen Strukturen und neurochirurgischen Eingriffen. Schließlich werden die verschiedenen MR-Bildgebungsverfahren vorgestellt, auf die in der Arbeit verwiesen wird. Die in diesem Teil präsentierten Randbedingungen und Grundlagen sind eine wichtige Voraussetzung für das Verständnis der medizinischen Fragestellungen.

Der zweite Teil der Arbeit beginnt mit einer Ausführung über Tensor-Rekonstruktion und -Quantifizierung. Im Anschluss daran wird ein neues Verfahren zur Filterung von Tensoren vorgestellt, das in Anlehnung an Video-Filter entwickelt wurde.

Basierend auf den rekonstruierten und gefilterten Tensoren werden im darauffolgenden Kapitel Fiber-Tracking-Algorithmen zur Rekonstruktion von Bahnsystemen vorgestellt. Zur Rekonstruktion einzelner Bahnsysteme für den klinischen Einsatz wurde ein Verfahren basierend auf Regions-of-Interest (ROIs) entwickelt, welche mit Bool'schen Operatoren verknüpft werden. Damit wurde eine flexible, patientenspezifische Extraktion einzelner Bahnsysteme möglich. Des Weiteren wurde das Verfahren der orientierten Filter implementiert und in einer Auswertung der Genauigkeitsgewinn beim Fiber-Tracking untersucht. Als Fazit lässt sich festhalten, dass orientierte Filter aufgrund der hohen Rechenzeiten im Verhältnis zum Genauigkeitsgewinn für den klinischen Einsatz eher weniger geeignet sind, auch wenn Kreuzungsstellen potentiell besser berücksichtigt werden. Außerdem wird ein neues Verfahren vorgestellt, das auf dem Konzept der Evenly-Spaced-Streamlines beruht und zur adaptiven Abstandskontrolle zwischen einzelnen Fibers eingesetzt werden kann. Aus klinischer Sicht ist dies von großer Bedeutung, da die für den Chirurgen relevanten Bahnsysteme auf diese Weise gut sichtbar sind und nicht von kleinen, peripheren Bahnen verdeckt werden. Als weiteres Verfahren zur Rekonstruktion von Bahnen wurde das Directional-Volume-Growing entwickelt. Das Verfahren stellt einen Übergang zur Konnektivitätsanalyse dar, da in beiden Fällen pro Voxel mehrere mögliche Expansionsrichtungen in Betracht gezogen werden.

Das nächste Kapitel beschäftigt sich mit der Verbindungsanalyse zwischen Sprachzentren. Da es sich hierbei um kleine Bahnsysteme handelt, die mit konventionellen Verfahren nur schwer zu rekonstruieren sind, wurde ein Algorithmus basieren auf A*-Pfadssuche entwickelt. Mit Hilfe einer Kostenfunktion ist es möglich, pro Voxel mehrere geeignete Richtungen zu analysieren, je nach lokaler Tensor-Information. Der Vorteil des Verfahrens ist, dass der Informationsgehalt planarer und sphärischer Tensoren adäquat wiedergegeben wird, indem mehrere gleich wahrscheinliche Expansionsrichtungen ausgewertet werden. Im klinischen Einsatz konnten damit bei Tumor-Patienten zuverlässig Sprachbahnen rekonstruiert werden. Das Verfahren wird momentan noch eingehend klinisch evaluiert.

Im darauf folgenden Kapitel wird die Generierung von Hüllen behandelt. Die re-

konstruierten Bahnen dienen als Grundlage für die OP-Planung. Um die Bahnen jedoch auch intraoperativ im OP-Mikroskop in Form von Randkurven darstellen zu können, werden zunächst Hüllen um die Bahnen benötigt. Zu diesem Zweck wurden zwei alternative Verfahren vorgestellt: Zum einen eine Technik, die Tetraedrisierung und 3D-Alpha-Shapes nutzt, zum anderen ein Ansatz basierend auf Rasterisierung und Isoflächen. Für den klinischen Einsatz ist das zweite Verfahren besser geeignet, da der Benutzer mehr Einflussmöglichkeiten auf die Passgenauigkeit der resultierenden Hülle hat. Diese Verfahren sind von entscheidender Bedeutung, um die Rekonstruktionsergebnisse auch intraoperativ verfügbar zu machen.

Ein anderes wichtiges Thema, das in einem weiteren Kapitel behandelt wird, ist die Korrektur von Verzerrungsartefakten. Aufgrund von Suszeptibilitätsartefakten sind die DT-MRT-Daten verzerrt, so dass die rekonstruierten Strukturen nicht korrekt platziert sind. Mit Hilfe von nicht-linearer Registrierung wurden die Verzerrungen korrigiert und der Einfluss der Verzerrungen auf die Lage von Bahnen gemessen. Für die klinische Anwendung sind diese Messergebnisse und Korrekturmöglichkeiten von großer Bedeutung, um die Auswirkungen der Verzerrungsartefakte einschätzen und korrigieren zu können.

Ein weiterer wichtiger Teil der Arbeit ist die geeignete Visualisierung der in Teil II rekonstruierten Strukturen. Im Wesentlichen geht es dabei um die Visualisierung der rekonstruierten Bahnen, die Darstellung der Hüllen und die multimodale Visualisierung von anatomischen MR-Daten mit rekonstruierten Strukturen.

Bei der Visualisierung von Bahnen spielt zum einen die Farbgebung eine Rolle, mit der zusätzliche Informationen vermittelt werden können. Aus diesem Grund wurden eine Reihe verschiedener Farb-Transferfunktionen entwickelt. Des Weiteren ist die effiziente Visualisierung von Fiber-Tracking-Ergebnissen in Echtzeit essentiell, um die Akzeptanz durch die klinischen Benutzer zu gewährleisten. Ein einfaches Verfahren, das dieser Anforderung entspricht, ist das Rendern von Linien. Zur Beleuchtung der Linien wurde das Verfahren der Illuminated-Streamlines implementiert und weiter verbessert. Durch adaptive Transparenz ist es außerdem möglich, kleine Bahnsysteme in Bereichen mit niedriger FA visuell zu unterdrücken, so dass das Augenmerk auf die besonders relevanten Bahnen gelenkt wird. Alternativ zum Linien-Rendern wurde ein hybrides Verfahren basierend auf Dreiecksstreifen und Point-Sprites entwickelt und vorgestellt, das gegenüber den Linien eine Reihe visueller Vorteile besitzt. Mit den verfügbaren Verfahren ist eine flexible, echtzeitfähige Visualisierung von Bahnen für die klinische Anwendung gewährleistet.

Ein weiteres Kapitel behandelt die Visualisierung von Hüllen für die präoperative Planung. Auch wenn das Ziel der Hüllen darin besteht, rekonstruierte Bahnen geeignet im OP-Mikroskop darzustellen, ist eine 3D Visualisierung für die Qualitätskontrolle bei der Erstellung der Hülle notwendig. Durch Transparenz ist der Vergleich einer Hülle mit der umhüllten Bahn noch besser möglich.

Das darauf folgende Kapitel beschäftigt sich mit der multimodalen Darstellung rekonstruierter Strukturen und anatomischer oder funktioneller Daten. Zur Visualisie-

rung der anatomischen MR-Daten wird direktes Volumen-Rendering verwendet, wobei Tumore vorsegmentiert und als Tagged-Volumes durch eigene Transferfunktion hervorgehoben werden können. Für die präoperative Planung ist eine multimodale Visualisierung von großer Bedeutung, um neuronale Strukturen und funktionelle Zentren in ihrem anatomischen Kontext betrachten zu können.

Ein Großteil der in dieser Arbeit entwickelten Verfahren zur Verarbeitung und Visualisierung von DT-MRT-Daten wurde im klinischen Umfeld getestet und teilweise durch klinischen Experten evaluiert, mit vielversprechendem Ergebnis. Die vorgestellten Verfahren leisten damit einen Beitrag zur Forschung in diesem Gebiet, wodurch in Zukunft das Risiko neurochirurgischer Eingriffe für den Patienten verringert werden kann.

Kapitel 12

Ausblick

Trotz der exzessiven Forschungsaktivitäten im Bereich DT-MRT gibt es eine Reihe offener Fragen sowie weiterführende Betätigungsfelder. Im Wesentlichen können zwei große Forschungsbereiche unterschieden werden, zum einen das Gebiet der Bildgebungsphysik und Sequenzentwicklung, zum anderen die Verarbeitung und Visualisierung der resultierenden Tensor-Daten. Im Folgenden werden zukünftige Herausforderungen und mögliche Betätigungsfelder in beiden Gebieten vorgestellt:

Ursache der gerichteten Diffusion in der weißen Substanz: Mit Hilfe von DT-MRT werden Variationen der Diffusion von Wasser im Gewebe gemessen, insbesondere die Richtungsabhängigkeit der Diffusion, was das Grundprinzip dieser MR-Technik darstellt. Nach dem Stand heutiger Literatur ist das Phänomen gerichteter Diffusion in der weißen Substanz aus physikalischer Sicht jedoch noch nicht vollständig erforscht. Entsprechend den Versuchsergebnissen, die in [112] zusammengefasst sind, ist die Umhüllung der Nerven durch Myelin keine Voraussetzung für gerichtete Diffusion, ebensowenig wie das Vorhandensein von Zellmembranen, die sich durchaus als wasserdurchlässig erwiesen. Aus diesem Grund ist es wünschenswert, den genauen Ursprung dieser biophysikalischen Barrieren zu erforschen, um wiederum genauere Rückschlüsse von den gemessenen Werten auf die biologischen Strukturen ziehen zu können.

Genauigkeit und Zuverlässigkeit von Rekonstruktionsverfahren: Ein benachbartes Forschungsgebiet ist die Bestimmung der Genauigkeit von Filterungs- und Regularisierungstechniken, ebenso die Analyse der Zuverlässigkeit von Rekonstruktionsalgorithmen. Ohne Kenntnis darüber, ob die rekonstruierten Strukturen mit den neuronalen Strukturen übereinstimmen, lässt sich schwer eine Aussage über ihre Zuverlässigkeit treffen. Im Fall von Fiber-Tracking-Algorithmen besteht die Fragestellung darin, in welchem Umfang neuronale Bahnen durch die rekonstruierten Strukturen repräsentiert werden. Ein erster Schritt in diese Richtung wird von einer Arbeit geleistet, die in [28] publiziert wurde. Darin werden rekonstruierte Bahnsysteme mit den neuronalen Bahnen verglichen, die im Rahmen einer Tracer-Untersuchung in histologischen Schnitten identifiziert werden konnten. Aufgrund der Komplexität der Strukturen im Gehirn und

aufgrund biophysikalischer Grenzen kann jedoch davon ausgegangen werden, dass die rekonstruierten Modelle nur eine Annäherung an reale Strukturen sind. Trotzdem ist es für den Einsatz von Rekonstruktionsverfahren wichtig zu wissen, wie gut diese Annäherungen die realen Strukturen widerspiegeln.

Verbesserung der Auflösung von DT-MRT-Daten: Im Hinblick auf die Bildgebung ist eine höhere Auflösung der Daten wünschenswert, um die lokalen Diffusionseigenschaften genauer bestimmen zu können. Eine Verbesserung der räumlichen Auflösung geht jedoch einher mit einem Anstieg des Rauschens, was die Zuverlässigkeit der Messwerte verringert. Eine Alternative zur Verbesserung des Signal-zu-Rausch-Verhältnisses (SNR) bieten MR-Scanner mit höheren Feldstärken, wie z.B. die neuen 3T Scanner, welche bereits an einigen Instituten installiert wurden.

Verzerrungsfreie DT-MRT-Sequenzen: Ein weiterer Punkt für zukünftige Forschung sind verbesserte Bildgebungs-Sequenzen, bei denen unerwünschte Effekte wie die Suszeptibilitätsartefakte in Kapitel 7 vermieden werden. Die STEAM-Sequenz [111] ist ein Beispiel für eine solche MR-Sequenz, die wesentlich geringere Verzerrungsartefakte aufweist. Für den Einsatz der Bilddaten in der Neurochirurgie sind verzerrungsfreie Sequenzen von großem Interesse, da in diesem Fall auf aufwändige Korrekturverfahren verzichtet werden kann.

Lokale Diffusionseigenschaften präziser erfassen: In der aktuellen Forschung wurde ein Bildgebungsverfahren vorgestellt, das mit High Angular Resolution Diffusion Imaging (HARDI) bezeichnet wird [145]. Dabei handelt es sich um ein Verfahren, bei dem die Gradienten zur Diffusionsmessung in viele verschiedene Richtungen ausgerichtet werden, welche möglichst gleichmäßig auf der Oberfläche einer Einheitskugel verteilt sind. Nach [41] werden die gemessenen Diffusionswerte zur Rekonstruktion eines Tensors höheren Rangs verwendet, der die lokalen Diffusionseigenschaften besser repräsentiert. Auch wenn sich einige aus der DT-MRT-Rekonstruktion und -Verarbeitung bekannten Verfahren ohne weiteres auf Tensoren höherer Ordnung übertragen lassen, z.B. Fiber Tracking [49] oder das Verfahren zur Konnektivitätsanalyse in Kapitel 5, müssen besondere Anforderungen berücksichtigt werden. Beispielsweise werden neue skalare Metriken zur Charakterisierung von Regionen mit anisotroper Diffusion benötigt, ebenso adäquate Rekonstruktions-Algorithmen, welche den höheren Informationsgehalt von HARDI-Tensoren nutzen. Die Möglichkeit, umfassendere Informationen über die lokalen Diffusionseigenschaften zu gewinnen, ebnet den Weg für präzisere Rekonstruktions-Verfahren, was ein interessantes Aufgabengebiet für die zukünftige Forschung ist.

Klinische Evaluierung der Verfahren: Ein weiterer wichtiger Aspekt ist die klinische Evaluierung der implementierten Algorithmen. Damit wurde bereits durch einen Neurochirurgen und zwei Medizinstudenten begonnen, welche mit der DT-MRT-Software arbeiten, die im Rahmen dieser Arbeit entwickelt wurde. Von besonderem Interesse sind dabei die Algorithmen für Fiber-Tracking und Konnektivitätsanalyse, ebenso das

Verfahren zur Generierung von Hüllen, die momentan in einer retrospektiven Studie evaluiert werden. Für die Zukunft sind weitere Auswertungen geplant, um die Genauigkeit und Zuverlässigkeit der Algorithmen im klinischen Einsatz zu überprüfen.

Lebenslauf

NAME, VORNAME: Merhof, Dorit
GEBURTSDATUM: 04.09.1978
GEBURTSORT: Erlangen
STAATSANGEHÖRIGKEIT: deutsch

1985 – 1989	Grundschule am Lichtenstein, Pommelsbrunn
1989 – 1998	Paul-Pfinzing-Gymnasium, Hersbruck
06/98	Abitur
10/98 – 09/03	Studium der Informatik an der Universität Erlangen-Nürnberg
09/03	Diplom in Informatik
10/03 – 12/07	Wissenschaftliche Mitarbeiterin am Lehrstuhl für Graphische Datenverarbeitung
	10/03 – 12/05 Stipendiatin des Graduiertenkollegs Dreidimensionale Bildanalyse und -Synthese
	01/06 – 12/07 Mitarbeiterin im Teilprojekt C9, Sonderforschungsbereich 603
29.06.2007	Antrag auf Zulassung zur Promotion
08.10.2007	Tag der Promotion

